CORA Cork Open Research Archive
Cartlann Taighde Oscailte Chorcaí

Title	Electronic excitation and atomic forces in optically excited group V semimetals
Authors	O'Mahony, Shane M.
Publication date	2020-09-02
Original Citation	O'Mahony, S. M. 2020. Electronic excitation and atomic forces in optically excited group V semimetals. PhD Thesis, University College Cork.
Type of publication	Doctoral thesis
Rights	© 2020, Shane M. O'Mahony. - https://creativecommons.org/licenses/by-nc-nd/4.0/
Download date	2026-09-15 02:47:25
Item downloaded from	https://hdl.handle.net/10468/10587

UCC
University College Cork, Ireland
Coláiste na hOllscoile Corcaigh

Electronic excitation and atomic forces in optically excited group V semimetals

Shane M. O'Mahony
BSc
111369431

NATIONAL UNIVERSITY OF IRELAND, CORK

SCHOOL OF SCIENCE

DEPARTMENT OF PHYSICS

Thesis submitted for the degree of Doctor of Philosophy

2 September 2020

Head of Department: Prof. John McInerney

Supervisors: Prof. Stephen Fahy
Dr Felipe Murphy-Armando

Research supported by Irish Research Council and Science Foundation Ireland

Contents

List of Figures iv
List of Tables vii
Abstract x
Acknowledgements xii
. xiv

1 Introduction **1**
1.1 Thesis outline 3

2 Experimental background and properties of Group V semimetals **5**
2.1 Pump-probe experiments 5
2.1.1 Types of probe pulse 6
2.2 Physical processes involved in pump-probe experiment 8
2.3 Group V semimetals 9
2.3.1 Rhombohedral A7 structure 11
2.3.2 Electronic structure and phonons of Group V semimetals 14
2.4 Displacive excitation of coherent phonons 17
2.5 Stimulated Raman scattering picture 19
2.5.1 Finite lifetime charge density fluctuations 21

3 Theoretical background and methods **23**
3.1 Many-body Hamiltonian 23
3.2 Many-body fermionic wavefunction as Slater determinant . . . 24
3.3 Variational principle and Hartree-Fock theory 26
3.4 Density functional theory 28
3.4.1 Kohn-Sham equations 29
3.5 Physical interpretation of Kohn-Sham eigenvalues 31
3.5.1 Approximations to exchange and correlation 32
3.5.2 Plane-wave based methods 34
3.6 Pseudopotentials 35
3.7 Lattice dynamics in three-dimensional crystals 37
3.7.1 Dynamical matrix 38
3.8 Electron-phonon scattering 40
3.9 Hamiltonian for electron-phonon interaction 40
3.9.1 Quantising the Phonon Coordinates 42
3.10 Electronic scattering rate 43
3.10.1 Change in electron and phonon occupations 45
3.11 Equilibrium lifetime of electronic state 46
3.12 Validity on short time scales 47
3.13 Atomic forces from electron-phonon matrix elements 49
3.14 Density functional perturbation theory 50
3.14.1 Conventions within the ABINIT code 53
3.15 Wannier interpolation 54
3.15.1 Maximally localised Wannier functions 54

3.15.2 Gauge freedom . . . 56
3.15.3 Generalisation to multiple bands . . . 56
3.15.4 The spread functional in real space . . . 57
3.15.5 Reciprocal space representation . . . 58
3.15.6 Entangled bands . . . 59
3.15.7 Interpolation of electronic band structure . . . 61
3.15.8 Interpolation of electron-phonon matrix elements. . . . 63
3.16 Photoexcited electrons: Constrained DFT . . . 66
3.16.1 Fast electron-hole recombination . . . 67
3.16.2 Slow electron-hole recombination . . . 68
3.16.3 Two-temperature model . . . 69
3.17 Photoexcitation: Electron-Photon interaction . . . 70
3.17.1 Modification due to finite lifetime of electronic states. . 73
3.17.2 Computing photoinduced driving forces on coherent modes 74
3.17.3 Polarization dependence and symmetry-breaking 75

4 Photoinduced reversal of Peierls distortion in Antimony 77
4.1 Introduction . . . 77
4.2 Constrained DFT calculations of photoexcited potential energy of A_{1g} mode in Antimony . . . 78
4.2.1 Isentropic dynamics . . . 79
4.2.2 Numerical approach . . . 80
4.2.3 Results . . . 80
4.3 Comparison with experiment . . . 84
4.3.1 Reversal of Peierls distortion . . . 86
4.4 Calculations of anharmonic decay of A_{1g} mode in Sb. . . . 90
4.5 Summary . . . 95

5 Ultrafast relaxation of symmetry-breaking photo-induced atomic forces 96
5.1 Introduction . . . 97
5.2 Theoretical framework and methodology . . . 99
5.3 Results . . . 102
5.3.1 Reinterpretation of experimental results given partial decay of A_{1g} force. . . . 104
5.3.2 Comparison with experimental E_g force lifetimes. . . . 108
5.4 Conclusions . . . 113

6 Conclusions 115

7 Outlook: Ultrafast thermalisation of non-equilbrium excited electronic distributions. 117
7.1 Coulomb matrix elements . . . 119
7.2 Dielectric function in the random phase approximation . . . 120

A Comparison of slow and fast electron-hole recombination within constrained DFT 123

B Wannier interpolation of Group V semimetal bandstructures 125

C Convergence of E_g force lifetime. 128

D Numerical Implementation 130
D.0.1 Electron and Phonon Occupations 130
D.0.2 Hartree atomic units and dimensional analysis 131

E Comparison of DFPT and frozen-phonon methods for Bismuth 132
E.1 Frozen-phonon calculation of electron-phonon matrix elements 132
E.1.1 Extracting the electron-phonon matrix elements 132
E.1.2 ABINIT wavefunctions including spin-orbit interaction . 133
E.1.3 Overlap of ABINIT wavefunctions in terms of fourier coefficents 134
E.1.4 Setting up the supercell 136
E.1.5 Freezing in the X phonon 137
E.1.6 Results 137

List of Figures

1.1 Schematic of the coherent phonon modes in the group V semimetals. 3

2.1 Schematic representation of a pump-probe experiment 6
2.2 Optical pump-probe measurements showing reflectivity oscillations corresponding to the coherent modes in Bi and Sb. 7
2.3 Optical pump- x-ray probe data for Bi, showing oscillations of the x-ray structure factor corresponding to the A_{1g} coherent mode. 8
2.4 Section of the periodic table showing the locations of the group V semimetals: Bi, Sb and As. 10
2.5 Plot showing the trends in spin-orbit splitting of the outermost p-orbital versus atomic number for a selection of elements. . . . 10
2.6 Illustration of the unit cell of the group V semimetals: Bi, Sb, and As. 11
2.7 Schematic of the band structure of a monovalent 1-D atomic chain with and without a Peierls distortion. 12
2.8 A 1-D monatomic solid with a half filled band will spontaneously double its period, saving energy by lowering the energy of occupied states near the half way point of the BZ. 13
2.9 The first Brillouin zone of the A7 rhombohedral materials. . . . 14
2.10 Electronic structure of the Group V semimetals. 16
2.11 Phonon dispersions of the group V semimetals calculated by Density functional perturbation theory (DFPT). 17
2.12 Schematic of the DECP model of coherent phonon excitation. . 18
2.13 Schematic showing how photoinduced charge density fluctuations couple to coherent modes in the group V semimetals. 21
2.14 Measured lifetime of the force driving the low-symmetry E_g force in Bi and Sb. 22

3.1 Schematic comparing the full Coulomb potential and real wavefunction of a material with the pseudopotential and pseudowavefunction. 36
3.2 Feynman diagrams showing the allowed first order electron-phonon scattering processes. 45
3.3 Illustration of energy conservation violation in a scattering event between states with energy E_1 and E_2 and linewidths $2\,\mathrm{Im}\{\Sigma_1\}$ and $2\,\mathrm{Im}\{\Sigma_2\}$. 48
3.4 Schematic of the Wannier interpolation procedure. 62
3.5 The real space representation of the electron-phonon matrix element $\langle \mathbf{0}_e | \partial_{\mathbf{q}\mu} V | \mathbf{R}_e \rangle$ in the basis of Wannier functions. 65
3.6 Schematic of photoexcited electronic occupations assuming that the electrons are in a hot Fermi-Dirac distribution with a single chemical potential for all bands. 68

3.7 Schematic of photoexcited electronic occupations assuming that the electrons have hot Fermi-Dirac distributions with equal temperatures, but with different chemical potentials for electrons and holes. 69
3.8 A schematic of a direct transition involving the absorption of a photon of energy $\hbar\omega$. 72
3.9 Schematic showing the regions of the first Brillouin zone of the Group V semimetals which have the largest concentration of excited electrons following photoexciation. 75

4.1 The surface describing the potential of the A_{1g} mode in Sb as a function of photoexcited carrier density n_c. 81
4.2 (a) Shows the harmonic and anharmonic frequencies and (b) shows the equilibrium value(s) of the A_{1g} mode coordinate x_0 as a function of photoexcited carrier concentration. 82
4.3 Potential energy curves of the A_{1g} mode for three important values of photoexcited carrier concentration n_c. 83
4.4 Time traces of transient reflectivity $\Delta R/R$ from single shot optical pump-optical probe measurements. 85
4.5 Comparison between the experimental and calculated harmonic frequency of the Sb A_{1g} mode. 87
4.6 Comparison between calculated and measured harmonic frequency, anharmonic frequency and range of motion. 87
4.7 Experimentally measured A_{1g} mode decay for several values of incident fluence. 88
4.8 Simulations of the coherent A_{1g} mode component of the transient reflectivity obtained by solving the classical equations of motion in a time-dependent potential as described in Eq. (4.11). 89
4.9 Simulated time-dependent A_{1g} mode displacement for the two highest fluences in the experiment. 90
4.10 (a): Calculated time evolution of the A_{1g} mode coordinate x_0 at an excitation density of $n_c = 1\%$ valence electrons excited to the conduction bands and (b): Calculated and measured A_{1g} mode decay rates as a function of fluence. 93
4.11 Transient reflectivity trace from pump-probe measurements in Ref. [1]. 94

5.1 The crystal structure of the A7 rhombohedral structures Bi, Sb and As with coherent modes indicated. 99
5.2 Comparison of Gaussian and Lorentian lineshapes of the same spectral weight. 101
5.3 The E_g and A_{1g} driving forces in Bi, Sb and As as functions of time-delay, following the absorption of 0.1 photons of energy $\hbar\omega = 1.5$ eV per unit cell. 103
5.4 Phase difference between A_{1g} and E_g mode of Bi and Sb as a function of temperature. 106

5.5 Corrections to the experimentally derived E_g force lifetimes reported in Ref. [1] taking into account the calculated partial decay of the A_{1g} driving force. 107
5.6 Lifetime of driving force on E_g mode as a function of lattice temperature for Bi, Sb and As for a pump photon energy of 1.5 eV. 108
5.7 The E_g force decay rate with and without the addition of a corrective temperature-independent scattering rate via Matthiessen's rule for (a): Sb and (b): Bi. 109
5.8 (a): Inverse electronic lifetimes of Bi, Sb and As as a function of energy at 300K. (b): Electronic density of states for same three materials. 110
5.9 Initial driving force and lifetime of driving force on E_g mode as a function of pump photon energy. 111
5.10 Comparison of experimentally measured photon dependence of reflectivity oscillation amplitude with the calculated photon energy dependence of the product of initial force and force lifetime of E_g mode. 112

7.1 Snapshots of excited electronic distribution in Bi, evolving under the influence of electron-phonon scattering. 118

A.1 Comparison of the effects of slow and fast electron-hole recombination on the harmonic frequency and the equilibrium coordinate of the A_{1g} mode as a function of photoexcited carrier concentration. 124

B.1 Comparison of Bi DFT bands with those obtained by Wannier interpolation. 126
B.2 Comparison of Sb DFT bands with those obtained by Wannier interpolation. 126
B.3 Comparison of As DFT bands with those obtained by Wannier interpolation. 127

C.1 Convergence of low-temperature (0.1 K) E_g force lifetime in Bi with respect to N_k and σ assuming an absorbed photon energy of 1.5 eV. 129

List of Tables

2.1 Structural parameters of Bi, Sb and As including lattice constant a_0, rhombohedral angle α and internal atomic displacement parameter z. Data taken from Ref. [2]. 12

5.1 Comparison of initial (F^i_{A1g}) and final A_{1g} force (F^f_{A1g}) with those obtained in a two-chemical potential CDFT calculation ($F^{2\mu}_{A1g}$) [3] and those obtained in a one-chemical potential calculation ($F^{1\mu}_{A1g}$). The forces are computed assuming an absorbed fluence of 0.1 photons of energy 1.5 eV per unit cell. 104

E.1 Comparison of phonon frequencies at $\mathbf{X}$ in the Brillouin zone calculated by DFPT and frozen-phonon methods. 137

E.2 Comparison of squared matrix elements calculated by DFPT and frozen-phonon method. 138

List of abbreviations

DECP ..... Displacive Excitation of Coherent Phonons.

TSRS ..... Transient Stimulated Raman Scattering.

DFT ..... Density Functional Theory.

DFPT ..... Density Functional Perturbation Theory.

CDFT ..... Constrained Density Functional Theory.

TDDFT ..... Time-Dependent Density Functional Theory.

LDA ..... Local Density Approximation.

GGA ..... Generalised Gradient Approximation.

BZ ..... Brillouin Zone.

XFEL ..... X-ray Free Electron Laser.

SCF ..... Self Consistent Field.

HOMO ..... Highest Occupied Molecular Orbital.

HGH ..... Hartwigsen-Goedecker-Hutter.

MLWF ..... Maximally Localised Wannier Functions.

scBE ..... self consistent Boltzmann Equation.

This is to certify that the work I am submitting is my own and has not been submitted for another degree, either at University College Cork or elsewhere. All external references and sources are clearly acknowledged and identified within the contents. I have read and understood the regulations of University College Cork concerning plagiarism.

Shane M. O'Mahony

Abstract

The main focus of this work is to investigate how electronic excitation changes the forces between atoms in materials, causing large amplitude collective atomic motion, referred to as coherent phonon motion. The recent development of ultrafast optical spectroscopy has greatly advanced our understanding of these phenomena. However, many aspects of ultrafast phenomena are still poorly understood. For instance, experiments on a variety of different materials have shown that symmetry-breaking coherent modes have a much smaller amplitude than fully symmetric coherent modes. Recent experimental work in the group V semimetals have shown that the symmetry-breaking E_g mode is driven by a force which decays in ~ 10 fs, a timescale much shorter than the period of the mode, explaining its small amplitude. However, the exact mechanism for this decay has remained unclear. We show that the E_g force in optically excited group V semimetals decays due to coupling of the excited electrons to thermal vibrations. We propose a method for increasing the impact of photoexcitation on symmetry-breaking modes by a suitable choice of photon energy, which would apply to a variety of materials. We are also interested in the dynamics of the coherent phonons themselves. Recently, it has been shown that optical excitation can drive collective structural transformations to phases that do not exist on the equilibrium phase diagram of materials as diverse as transition metal oxides, transition metal chalcogenides, and the group V semimetals. Experimentally reaching many of these states requires a high degree of photoexcitation, with a significant fraction (1-5%) of the valence electrons excited to the conduction bands. We use first-principles calculations to simulate coherent phonon dynamics in Sb, and show that at high enough excited carrier concentration, Sb undergoes a reversal of its Peierls distortion. Our results are in good agreement with pump-probe experiments carried out by our experimental collaborators, providing good evidence that such a reversal can be induced by optical excitation.

To my parents

Acknowledgements

First and foremost, I would like to thank my supervisor, Prof. Stephen Fahy, whose depth of knowledge and enthusiasm still impresses me to this day. He allowed me to evolve as an independent researcher while providing key insights along the way, which would often be crucial to solving whatever problem I was working on at the time. In a time when a lot of PhD projects are narrowly focused, Stephen strongly believed in providing his students with a well rounded physics education. Now, as I'm moving in to a different field of physics, I'm especially grateful for this approach. He shared my enthusiasm for physics in general, and as such, we often had very interesting discussions about areas of physics not directly related to my project. Stephen's guidance and supervision were crucial, not only to the success of my PhD project, but also to my development as a scientist.

I'd also like to thank my co-supervisors. Firstly, Eamonn Murray was my official co-supervisor for just 4 months, as his career took him to Imperial College London at the end of 2015, but throughout my PhD he always responded to my questions and was willing to lend his expertise. Without his advice, several steps in my PhD would have taken longer. Felipe Murphy-Armando - or Philip, as we all call him him - was my co-supervisor for the remaining 3 and a half years of my PhD. I cannot say enough about Philip. He was always available for impromptu meetings and often dropped what he was doing to work on my project with me. Many problems were solved in his office, or at the whiteboard of the adjacent meeting room. We had many interesting discussions over pints, or in the hallways of Tyndall A block. Often, we would discuss politics or fundamental physics. Philip really enriched my PhD experience. I would also like to thank the other members of the materials theory group for their advice, collaboration and support.

I would like to thank me thesis examiners, Prof. Frank Peters and Prof. Roberto Merlin for giving me a very fair viva examination, and for making suggestions that have undoubtedly made this a better thesis.

I'd like to thank my future wife, Amy Kirwan, for putting up with my research induced mood swings and always managing to put a smile on my face, no matter how frustrated I would get. She always put things in perspective for me, and would regularly remind me that there are more important things in life than research. Lets hope Covid-19 doesn't delay our wedding again.

I thank my parents, Orla and Terry, and my sister, Kate for always believing in me and for keeping me grounded. I never would have made it this far without their love and support.

A big thank you to my UCC physics friends: Amy, Tom, Seb, Kev, Kieran, Anna, Grainne, Gerard, Sharon, Hugh, Ed, Steve, Daire and Luke. Even though some of us have gone our separate ways, we still regularly keep in touch to this day. You

have been some of my best friends over the past 9 years. We've went for coffee too many times to count, competed in Pokemon speed runs (I'll win one some day, Tom), gotten way too competitive with CS:GO and gathered for a Christmas dinner/party 9 years in a row. Here's to many more years of friendship.

I would also like to acknowledge the many friends I have made in Tyndall: Djordje, Christian, Jose, Aoife Murphy, Ransell, Jiang, Anna, Shima, Chris, Aoife Lucid, Saroj, Sarita and others. You have all contributed to making my time at Tyndall extremely pleasant.

"Enthusiasm is followed by disappointment and even depression, and then by renewed enthusiasm"

– Murray Gell-Mann

Chapter 1

Introduction

The generation and control of atomic forces in optically excited molecules and materials is important for a number of areas including photocatalysis [4] [1], laser annealing [2] and the study of photo-assisted phase transitions [5, 6, 7] [3], with applications that include the development of efficient renewable energy [8] and phase-change memories [9, 10] [4]. The development of ultrafast optical spectroscopy has greatly advanced our understanding of electron and phonon dynamics in optically excited materials, with time resolution on the tens-of-femtoseconds scale readily accessible [11, 12, 13]. More recently, time-resolved x-ray diffraction and time-resolved photoemission spectroscopy have allowed the direct observation of atomic motion and electronic dynamics on timescales shorter than a picosecond following photoexcitation [14, 15, 16, 17], providing insight into the physics of strongly correlated and charge density wave systems [18, 19].

Photoexcitation with a laser pulse of duration much less than the fastest phonon period can be used to launch large amplitude, collective atomic vibrations in a variety of materials and molecules [14]. These collective atomic vibrations involve atoms throughout the material oscillating in phase with one another and are therefore referred to as coherent phonons. The study of coherent phonons, and the photoinduced forces driving them were a major focus of this thesis. An

[1] The acceleration of chemical reactions by optical excitation of one or more of the reacting species.

[2] A technique which allows the colouring of the surfaces of certain metals. e.g. steel, titanium and stainless steel.

[3] Phase transitions driven or assisted by optical excitation.

[4] This is a type of random access memory in which information is written to the medium by optically inducing a phase transition from a crystalline structure to an amorphous one. For the materials used, the amorphous phase has a very different optical absorption spectrum.

early aim of this thesis was to calculate from first principles the coherent phonon dynamics in antimony and to investigate the possibility of inducing a structural phase transition by optical excitation in this material. These were phenomena which have recently been explored in bismuth [20, 6], but remained unresolved in Sb.

However, the main aim of this thesis is to understand how the excitation, and subsequent relaxation, of electrons in materials affects the atomic forces and gives rise to coherent phonon motion. The coherent phonon modes which can be excited in a given material will either preserve the symmetry of the crystal or break that symmetry. In principle, photoexcitation can excite both of these types of coherent phonon, if the polarisation of the pump pulse is chosen correctly, as discussed in section 3.17. However, symmetry-breaking coherent atomic motion generated by above-gap excitation has been shown experimentally to have an amplitude orders of magnitude less than that of symmetry-preserving coherent atomic motion in a variety of materials [5] [1, 22, 23, 24]. In fact, symmetry-breaking mode oscillations often go undetected in pump-probe experiments. Furthermore, the amplitudes of symmetry-breaking modes decrease strongly with increasing sample temperature, whereas high-symmetry mode amplitude is relatively insensitive to temperature, indicating very different aspects of the ultrafast dynamics affecting the two cases. In this thesis, we provide a quantitative explanation for this discrepancy by performing first-principles electronic structure calculations on the prototypical Group V semimetals: Bi, Sb and As. We focus on these materials due to their large vibrational response to optical excitation [25, 26, 27, 28]. Fig. 1.1 depicts the allowed coherent phonon modes in the group V semimetals: the symmetry-preserving A_{1g} mode and the symmetry-breaking E_g mode [6]. The symmetry-breaking E_g mode in all three materials is driven by a short-lived imbalance in the excited occupations of symmetry equivalent regions of the Brillouin zone. We performed first-principles calculations of electron-phonon scattering

[5] This is not always the case for below-gap excitation, for example in transparent materials [21]. However, in this thesis we focus on above gap (absorptive) excitation.

[6] The labels A_{1g} and E_g are from group theory. They describe the symmetries of the vibrational modes. For the A_{1g} mode, the A indicates that the mode is singly degenerate and symmetric with respect to the highest order rotation about the principle symmetry axis of the crystal (For the group V semimetals, this is threefold rotation about the z-axis as shown in Fig. 1.1) and the g subscript indicates that the mode has even (**g**erade in German) parity. The 1 subscript indicates that the mode is symmetric with respect to twofold rotation about an axis perpendicular to the principle axis. For the E_g mode, the E indicates that the mode is doubly degenerate and is not symmetric with respect to the highest order rotation about the principle axis. For more details, see Ref. [29].

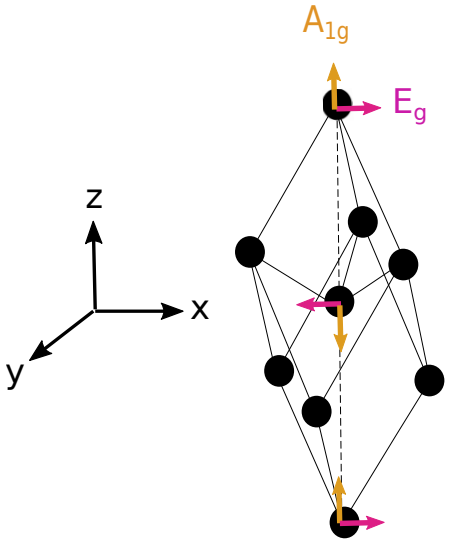

Figure 1.1: Schematic of the coherent phonon modes in the group V semimetals, shown within the primitive cell of the rhombohedral structure. (see section 2.3.1). Since these are coherent modes, the motion in all neighbouring primitive cells are in phase with one another.

of the excited electrons, which show that electron-phonon scattering between these symmetry equivalent regions causes the excited electronic distribution to regain full symmetry, causing the driving force on the E_g mode to decay rapidly ($\sim$ 10 fs). Comparison with the experimentally measured lifetime of the E_g force [1] allow us to conclude that electron-phonon scattering is the primary relaxation mechanism for this force in Bi and Sb. The E_g force lifetime in As has not yet been measured, so our calculated value serves as a prediction. Having identified the dominant scattering mechanism limiting the generation of symmetry-breaking coherent modes, we then suggest a method for maximising the impact of photoexcitation on these modes by suitable choice of photon energy [30].

1.1 Thesis outline

The chapters of this thesis are laid out in the following way. Chapter 2 outlines the experimental developments and results which motivated this work, as well as introducing important properties of the group V semimetals. It also discusses the two main models which describe the excitation of coherent phonons: displacive excitation of coherent phonons (DECP) [31] and impulsive Raman scattering [26]. In chapter 3, we introduce the background theory and methods

which were used throughout this thesis. Chapter 4 contains a detailed examination of coherent phonon dynamics and Peierls distortion reversal in photoexcited Sb, including a combination of constrained density functional theory (CDFT) calculations and single shot pump-probe experimental measurements. In chapter 5, we present our calculations of the phonon assisted time-evolution of photoinduced atomic forces in Bi, Sb and As, showing that the low-symmetry E_g decays primarily due to electron-phonon scattering and suggesting a method for maximising the impact on symmetry-breaking modes. The major conclusions of this work are discussed in chapter 6 and in chapter 7 we outline our first steps towards first-principles calculations of electron thermalisation following photoexcitation, including the effects of electron-electron scattering, and argue that this is an interesting next step for the work presented here.

The work presented in chapter 5 has been published in the following paper:

- **S. M. O'Mahony**, F. Murphy-Armando, E. D. Murray, J. D. Querales-Flores, I. Savic, and S. Fahy, "Ultrafast relaxation of symmetry-breaking photoinduced atomic forces," Phys. Rev. Lett., vol. 123, p. 087401, Aug 2019.

The work presented in chapter 3 is being prepared for publication:

- S. W. Teitelbaum, **S. M. O'Mahony**, Y. Cheng, F. Gao, M. Plankl, S. Fahy and K. A. Nelson, "Photoinduced Bond Softening and Barrier Crossing in Antimony," (in preparation).

I also contributed to the following two publications during my PhD:

- S. W. Teitelbaum, T. Henighan, Y. Huang, H. Liu, M. P. Jiang, D. Zhu, M. Chollet, T. Sato, E. D. Murray, S. Fahy, **S. O'Mahony**, T. P. Bailey, C. Uher, M. Trigo, and D. A. Reis, "Direct measurement of anharmonic decay channels of a coherent phonon," Phys. Rev. Lett., vol. 121, p. 125901, Sep 2018.
- S. W. Teitelbaum, T. C. Henighan, H. Liu, M. P. Jiang, D. Zhu, M. Chollet, T. Sato, E. D. Murray, S. Fahy, **S. O'Mahony**, T. P. Bailey, C. Uher, M. Trigo, and D. A. Reis, "Measurements of nonequilibrium interatomic forces in photoexcited bismuth," ArXiV preprint (under review at Phys. Rev. Lett.)

Chapter 2

Experimental background and properties of Group V semimetals

2.1 Pump-probe experiments

Pump-probe experiments are among the most useful methods available for studying the ultrafast excitation of materials and molecules [11]. Figure. 2.1 shows a schematic of a pump-probe experiment. In these experiments, the sample is initially illuminated by an extremely short and intense laser pulse, referred to as the pump, which is typically < 100 fs in duration with a fluence $\sim$ few mJ/cm^2. In most cases the photon energy exceeds the band gap of the material, leading to promotion of valence electrons to the conduction bands. [1] The system is allowed to evolve for a delay time t and then probed with a much less intense pulse, whose reflected/transmitted intensity gives us snapshot of some optical constant of the material. The reflectivity will vary with the optical dielectric function, which depends on both the positions of the atoms in the sample, and the excited electronic distribution. The oscillatory part of the reflectivity corresponds to coherent phonon motion, which is a type of atomic motion in which all atoms in a material undergo large amplitude in-

[1] The transmission geometry is primarily used in the study of transparent materials, or few layered samples of opaque materials. It involves an intense pump pulse being transmitted through the materials followed by a much less intense probe pulse at a fixed time delay. The excitation of electrons and coherent atomic vibrations caused by the pump pulse results in absorption/optical gain of the probe pulse leading to modulations of the probe transmittance. Studying the transmittance as a function of time-delay allows us to observe the excited electronic and coherent phonon dynamics [21]. In this thesis, we focus exclusively on the reflection geometry as we are interested in bulk Bi, Sb and As, which are opaque materials.

phase oscillations, modulating the optical dielectric function in the process. This process is repeated for different time delays, allowing the sample to relax between pump-probe pairs. Compiling the results we obtain a time-resolved

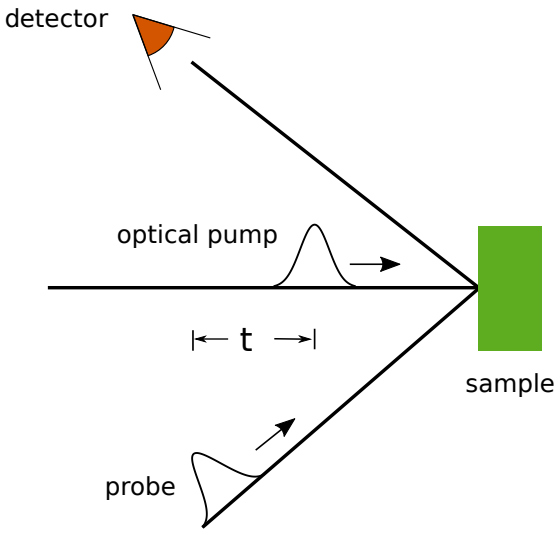

Figure 2.1: Schematic representation of a pump-probe experiment. Firstly, the sample is excited by an optical pump pulse. After some time-delay t, the sample is hit with the much less intense probe pulse. The changes in the reflected probe pulse intensity are measured as a function of time-delay f.

picture of this optical constant. The most common method for producing time-delayed pump-probe pairs is to split a single femtosecond laser pulse into two separate pulses: a pump and a probe. This works for pump - probe experiments in which we want the pump and probe pulses to have the same wavelength. However, probe pulses of other wavelengths may also be used, by introducing a second laser source or by up- or down-converting the original pulse in a non-linear amplifier. For instance, in optical pump - x-ray probe experiments. In optical probe experiments, the delay time t is controlled by varying the path length of the probe. X-ray probe experiments are typically performed using an x-ray free electron laser, where the x-ray pulse is generated in an undulator, separately from the optical pump pulse. In these experiments, controlling the relative timing of the pump and probe pulses is significantly more challenging, though not intractable. For more details, refer to the review in Ref. [32].

2.1.1 Types of probe pulse

A common approach to pump-probe spectroscopy is to pump and probe the system with optical pulses. In this case, the probe pulse measures the transient

change in optical reflectivity of the sample. The optical reflectivity varies with the dielectric function of the material, which itself depends on the atomic positions and electronic distribution following photoexcitation. The electronic and vibrational contributions to the reflectivity can be separated, with the latter resulting in damped oscillations of $\Delta R/R$ and the former giving rise to an overall exponential decay as follows [6]:

$$\frac{\Delta R}{R} = Ae^{-\Gamma t}\cos(\Omega t + \phi) + Be^{-\gamma_c t} + C, \tag{2.1}$$

where γ_c is the decay rate of the photoexcited electronic distribution. The third term in this equation is a constant shift related to the change in atomic equilibrium position upon photoexcitation. Fig. 2.2 shows an example of an optical pump- optical probe experiment on Bi and Sb in which the transient reflectivity displays oscillations corresponding to the A_{1g} and E_g coherent modes.

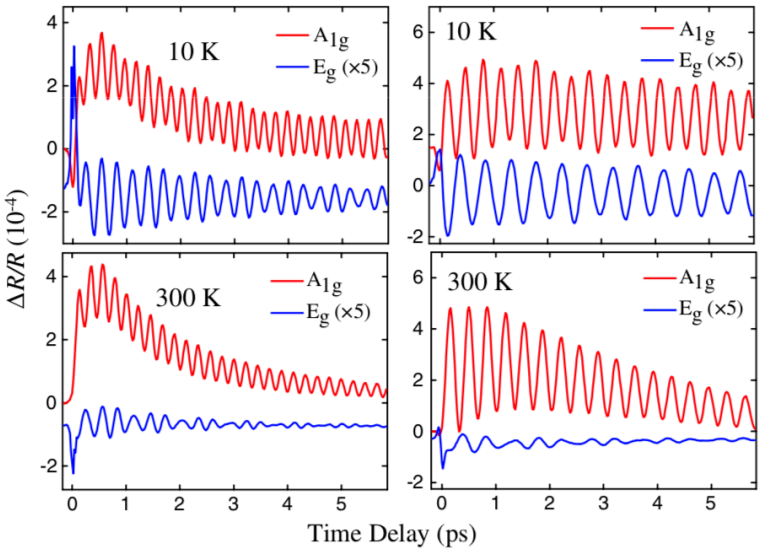

Figure 2.2: Optical pump- optical probe measurements for sample temperatures of 10 K and 300 K, showing oscillations of transient reflectivity which correspond to the high-symmetry A_{1g} and low-symmetry E_g coherent modes. The left panels are measurements of Sb and the right panels are measurements of Bi. Figure reproduced from Ref. [1]

A more recently introduced alternative to optical probes are x-ray probes generated by x-ray free electron lasers (XFELs) [32]. For these probes, the quantity that we measure is the time-dependent change in the x-ray structure factor, which directly relates to changes in the atomic positions. This is a major advantage of x-ray probe experiments over optical probe experiments, since the quantity measured using the latter, transient reflectivity, can have many contributions, making

it more difficult to extract information about atomic displacements. Fig. 2.3 shows an optical pump- x-ray probe experiment performed on bismuth [14]. The oscillations of the x-ray structure factor coincide with oscillations of the A_{1g} coherent mode. The data in the inset demonstrates that the frequency of the A_{1g} mode decreases with increasing fluence, which is a well known effect in these materials [33].

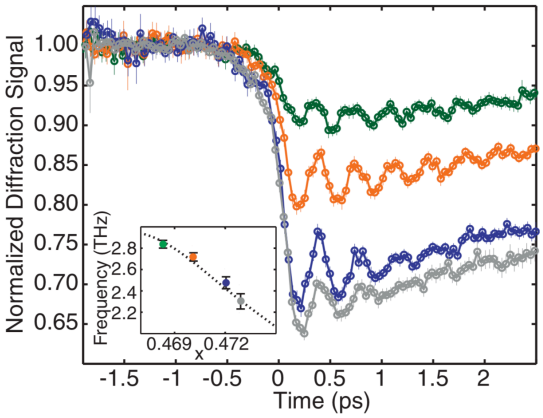

Figure 2.3: Optical pump- x-ray probe data for Bi, showing oscillations of the x-ray structure factor corresponding to the A_{1g} coherent mode. The experiment was performed with excitation fluences of 0.7(green), 1.2(orange), 1.7(blue) and 2.3 mJ/cm^2 (grey). The inset shows the frequency and equilibrium coordinate of the A_{1g} mode for the four fluences considered. Figure reproduced from Ref. [14]

2.2 Physical processes involved in pump-probe experiment

Many physical processes take place during a pump-probe experiment, each of which must be carefully treated theoretically using appropriate approximations. The first of these processes is the initial excitation of electrons to higher energy states by the pump pulse. This produces a non-equilibrium distribution of electrons and holes, which becomes a thermal distribution as a result of electron-electron and electron-phonon scattering on timescales much shorter than a phonon period. Electron-electron scattering is effective at relaxing the energy of the photoexcited electrons and electron-phonon scattering relaxes the momentum. This thermalisation process is often assumed to establish a well defined electronic temperature in tens to hundreds of fs [34, 35], but the precise timescale is not known. However, some progress towards a fully first-principles

simulation of this process in the semiconductor silicon [36, 37, 38] has been made by Andrea Marini and collaborators. In chapter 7 we outline the first steps towards the more challenging problem of simulating thermalisation of electrons in *semimetals* from first principles.

The presence of excited electrons and holes alters the forces between the atoms in the unit cell, launching large amplitude coherent phonon oscillations [2]. These coherent phonons either preserve the symmetry of the crystal (symmetry-preserving) or break this symmetry (symmetry-breaking). The measured amplitude of symmetry-breaking modes is usually found to be much smaller than symmetry-preserving modes. For example, a large difference in amplitude has been observed in bismuth and antimony [15, 1], tellurium [23, 24], bismuth telluride [22] and titanium oxide [31]. In chapter 5, we show from first-principles calculation that this originates primarily through the rapid momentum relaxation of the photoexcited electron-hole plasma by electron-phonon scattering [30].

On longer timescales ($\sim$ few ps), the excited coherent phonons decay, primarily from anharmonic coupling to other phonons [39, 40, 41]. The most common decay mechanism is the Klemens' channel [39], whereby the coherent phonons transfer their energy to pairs of acoustic modes with opposite momenta and whose energies sum to the coherent phonon energy. This has been shown experimentally to account for the decay of the A_{1g} mode in Bi [41]. The anharmonic decay of coherent phonons has also been shown to produce squeezing oscillations of the mean square displacement of these target acoustic modes at twice their harmonic frequency [40, 41].

Another process which occurs on picosecond timescales is the diffusion of photoexcited carriers away from the surface of the sample. Throughout this thesis, our calculations will treat photoexcited systems as possessing a spatially homogeneous plasma that is coupled to the atomic degrees of freedom.

2.3 Group V semimetals

In this work we focus on the prototypical group V materials: bismuth, antimony and arsenic. These materials are highly stable to radioactive decay. Bismuth, antimony and arsenic have atomic masses of ~ 208.98, 121.76 and 74.92 g/mol

[2] Coherent phonons are collective oscillations where atoms vibrate in phase with their neighbours.

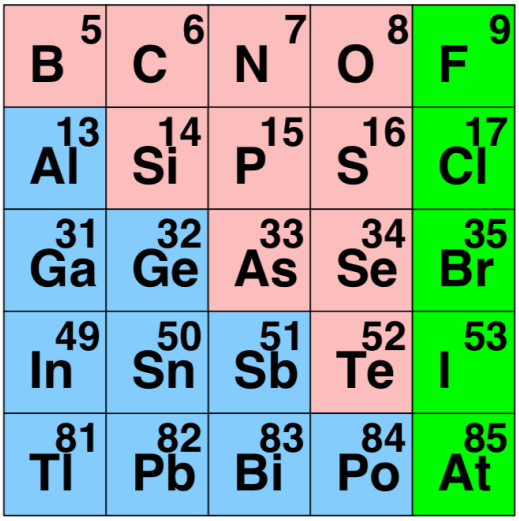

Figure 2.4: Section of the periodic table showing the locations of the group V semimetals: Bi, Sb and As.

respectively. While antimony and arsenic are known to be highly toxic, bismuth's toxicity is much lower than that of it neighbours on the periodic table. They

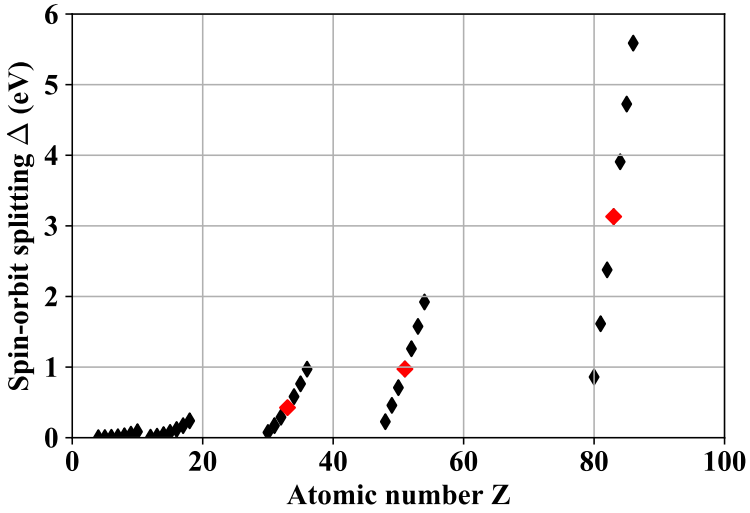

Figure 2.5: Plot showing the trends in spin-orbit splitting of the outermost p-orbital versus atomic number for a selection of elements. The general trend suggests that heavier atoms will have a larger spin orbit splitting. Bi($Z = 83$), Sb($Z = 51$) and As($Z = 33$) have been highlighted with bigger red diamonds. The data is from Ref. [42]

are pentavalent semimetals with an overlap of valence and conduction bands in their equilibrium states. This overlap results in these materials having some free carriers in the ground state. However, bismuth has fewer than 2×10^{-5} carriers per unit cell, antimony has fewer than 3×10^{-3} and arsenic has fewer than 10^{-2} making all three materials poor conductors [2]. These materials also possess

a significant spin-orbit interaction. Since the strength of this interaction scales with atomic mass, bismuth is found to have very strong spin-orbit coupling (see Fig. 2.5 and Ref. [42]).

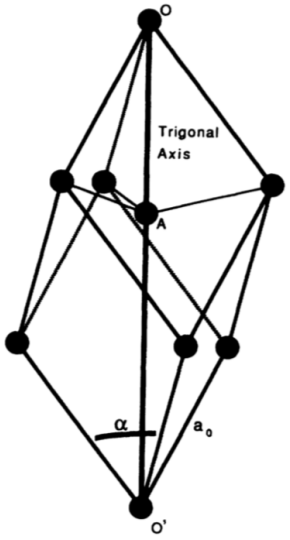

Figure 2.6: This picture shows the unit cell of the Bi, Sb and As. They each crystallise in the rhombohedral structure with two atoms per unit cell. Figure reproduced from Ref. [2]. The crystal parameters, taken from Ref. [2], are listed in Table. 2.1

2.3.1 Rhombohedral A7 structure

The group V semimetals; Bi, Sb and As each crystallise in the A7 rhombohedral structure [2] with two atoms per unit cell. The unit cell is depicted in Fig. 2.6. It's primitive lattice vectors can be expressed in cartesian coordinates as

$$\mathbf{a}_1 = (a, 0, c), \quad \mathbf{a}_2 = (-a/2, a\sqrt{3/4}, c), \quad \mathbf{a}_3 = (-a/2, -a\sqrt{3/4}, c), \tag{2.2}$$

where $a_0 = \sqrt{a^2 + c^2}$ is the length of the basis vector shown in Fig. 2.6 (lattice constant), and a and c are lattice parameters which depend on the angle α that the lattice vectors make with each other:

$$a = a_0 \left[\frac{2}{3}(1 - \cos\alpha)\right]^{\frac{1}{2}}, \tag{2.3}$$

$$c = a_0 \left[\frac{1}{3}(2\cos\alpha + 1)\right]^{\frac{1}{2}}. \tag{2.4}$$

The crystal structure can be specified fully using only the lattice constant a_0 and the rhombohedral angle α. There are two atoms in the unit cell, one of which we take to be at the origin and the other is a fractional distance (z, z, z) along the trigonal axis, as expressed in terms of the primitive lattice vectors in Eq. (2.2). We refer to z as the internal atomic displacement factor. The A7

Table 2.1: Structural parameters of Bi, Sb and As including lattice constant a_0, rhombohedral angle α and internal atomic displacement parameter z. Data taken from Ref. [2].

	Bi	Sb	As
a_0 (Å)	4.7236	4.4898	4.1018
α (deg)	57.53	57.233	54.554
z	0.46814	0.46724	0.45528

structure can be viewed as a distorted simple cubic structure. In fact, if we set $\alpha = 60°$ and $z = 1/2$, we would have a simple cubic structure with one atom per unit cell. However, the lowest energy structure for Bi, Sb and As is one where z is slightly perturbed from $z = 1/2$. This is due to the existence of a Peierls distortion [43] in all three materials. A Peierls distortion occurs when

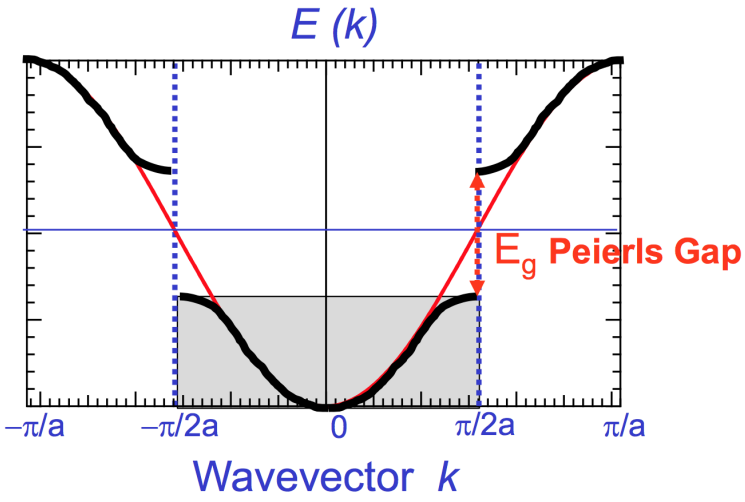

Figure 2.7: Schematic of the band structure of a monovalent 1-D atomic chain with (black) and without (red) a Peierls distortion. It is apparent that the Peierls distortion is energetically favourable in the ground state of this system where the band is 1/2 filled.

electronic states that are degenerate in the fully symmetric system can be split by a lowering of symmetry in such a way that only the lower state in the splitting is occupied. This results in a lowering of the total energy of the system [3]. As

[3] This is because unoccupied states do not contribute to the total energy.

long as the energy saving from lowering this symmetry outweighs the elastic energy required to re-arrange the atoms, the Peierls distorted structure will be the stable one. This was first explained for a simple model: a 1-D crystal comprised of equally spaced atoms, each contributing 1 electron to the system, leading to a half-filled band with electronic states being occupied up to values of $ka = \pm\pi/2$ (Half the radius of the Brillouin zone (BZ)). As we can see in Fig. 2.7, it is energetically favourable to introduce further gaps at $ka = \pm\pi/2$, since only the lower energy state in this splitting will be occupied. This opening of a gap half way into the BZ, corresponds to a doubling of the periodicity of the structure as depicted in Fig. 2.8. This model of a 1-D crystal supplies some intuition for understanding the distortion along the trigonal direction occurring in the group V semimetals. The rhombohedral structure can be derived from a simple cubic lattice by a slight pairing of hexagonal planes along one of the body diagonals. This pairing is directly analogous to the Peierls distortion in a 1-D lattice, with the hexagonal planes playing the role of the atoms in this chain. The degree of pairing of these planes is encapsulated by the internal atomic displacement parameter z, which quantifies the fractional displacement of the second atom in the unit cell with respect to the first. More generally, internal atomic displacement parameters exist as free parameters of the crystal point group.

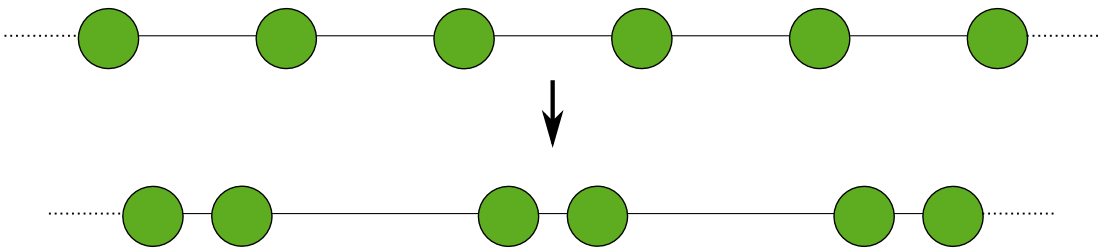

Figure 2.8: A 1-D monatomic solid with a half filled band will spontaneously double its period, saving energy by lowering the energy of occupied states near the half way point of the BZ. In the group V semimetals, the same argument holds, but with the hexagonal planes lying along the trigonal axis replacing the role of the atoms.

The internal atomic displacement z is highly dependent on the number of electrons excited to the conduction band, with z moving closer to $1/2$ as the number of excited carriers is increased. This is due to the diminishing energy advantage of the lower symmetry structure as the upper energy levels, which would be degenerate with the lower levels in the symmetric structure, become more occupied. Recent experimental and theoretical studies of bismuth have revealed precisely which interatomic force constants are strengthened and weakened dur-

ing photoexcitation, providing a more quantitative picture of why $z \to 1/2$ upon photoexcitation [44, 45]. The sensitivity of z to carrier density means that Peierls distorted structures, such as the group V semimetals, exhibit a pronounced vibrational response to photoexcitation. As a consequence, photoexcitation can launch large amplitude oscillations of z, by suddenly shifting its equilibrium value. (see Fig. 2.12). These oscillations are referred to as A_1 or A_{1g} coherent phonons as they fully preserve the crystal's point group symmetry. However, under the correct circumstances, photoexcitation can also launch coherent phonons which break this symmetry, albeit with a much lower amplitude. In sections 2.4 and 2.5 we will briefly introduce the two main theories which describe the excitation of coherent phonons: DECP [27, 31] and transient stimulated raman scattering (TSRS) [21, 25, 1]. However, we will first describe the electronic band structure and phonons of the group V semimetals.

2.3.2 Electronic structure and phonons of Group V semimetals

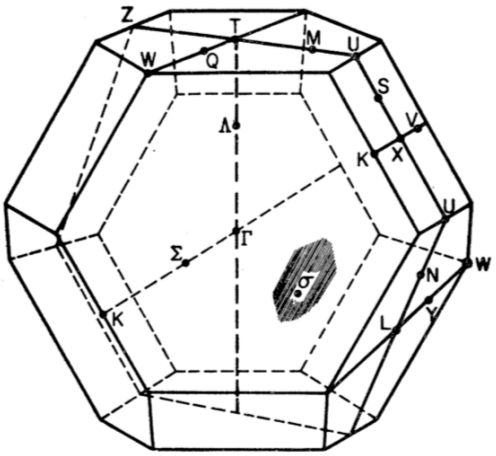

Figure 2.9: The first Brillouin zone of the A7 rhombohedral materials is a truncated octahedron which is slightly stretched along the $\Gamma - \mathrm{T}$ direction. Figure reproduced from Ref. [46].

The group V materials bismuth, antimony and arsenic are all semimetals, characterised by a conduction band minimum which is *lower* in energy than the valence band maximum, leading to some finite density of carriers (electrons and holes) in the ground state. However, unlike metals, semimetals have an extremely small, but finite density of states at the Fermi level [4], leading to finite

[4]The Fermi level gives the energy at which states are half-filled i.e. $f(\varepsilon_{\mathrm{F}}) = 1/2$.

but poor electrical conductivity. Fig. 2.10 shows the electronic bandstructure of Bi, Sb and As for energies within 6 eV of the Fermi level, calculated within the framework of density functional theory (DFT, see section 3.4) [5] and plotted along selected high-symmetry directions in the Brillouin zone (see Fig. 2.9). Broadly speaking, all three materials have similar band structures. However, going from As to Sb and Bi, the spin-orbit interaction increases, the cell becomes less Peierls distorted from simple cubic and the lattice constant increases, leading to some quantitative differences in the electronic structure of these materials. The most striking difference is in the concentration of free carriers in the ground state. The right panels (b), (d) and (f) demonstrate that the free carrier density of the Group Vs increases moving up the periodic table, with arsenic being the most metallic of the three. Theoretical and experimental studies have shown that Sb has ~ 100 times more free carriers than Bi, and As has ~ 3 times more free carriers than Sb [2, 47, 48]. Another notable difference between the three materials is the locations of the electron and hole pockets which comprise the Fermi surface. All three of the materials possess pockets of free electrons centred on their L points. However, the holes occur in different areas of the Brillouin zone for the three materials. In bismuth, there is a single hole pocket at the T point, whereas in antimony and arsenic the holes occur in 6 pockets centred around the lower symmetry H points, which lie on the σ reflection planes of the Brillouin zone as depicted in Fig. 2.9 and Fig. 3 of Ref. [47].

In addition to the electronic structure of these materials, we are interested in their phonons. Fig. 2.11 shows the phonon dispersions of the Bi, Sb and As calculated using density functional perturbation theory (DFPT, see section 3.14). The three materials have qualitatively similar phonon dispersions, with the less massive materials having higher frequency modes throughout the Brillouin zone. The coherent modes, which are a major focus of this thesis, correspond to the optical modes at Γ, with the highest frequency mode in each material being the high-symmetry A_{1g} mode, closely followed in energy by the doubly degenerate low-symmetry E_g mode.

Structurally, the A_{1g} mode interpolates between the Peierls distorted A7 rhombohedral phase and an undistorted phase with one atom per unit cell by modulating the internal atomic displacement parameter z. Since this undistorted phase has only one atom per unit cell, it does not admit any optical modes. As we remove the Peierls distortion, the zone centre A_{1g} mode softens, eventually becoming a

[5] These calculations were performed using the local density approximation to exchange and correlation. (see section 3.5.1)

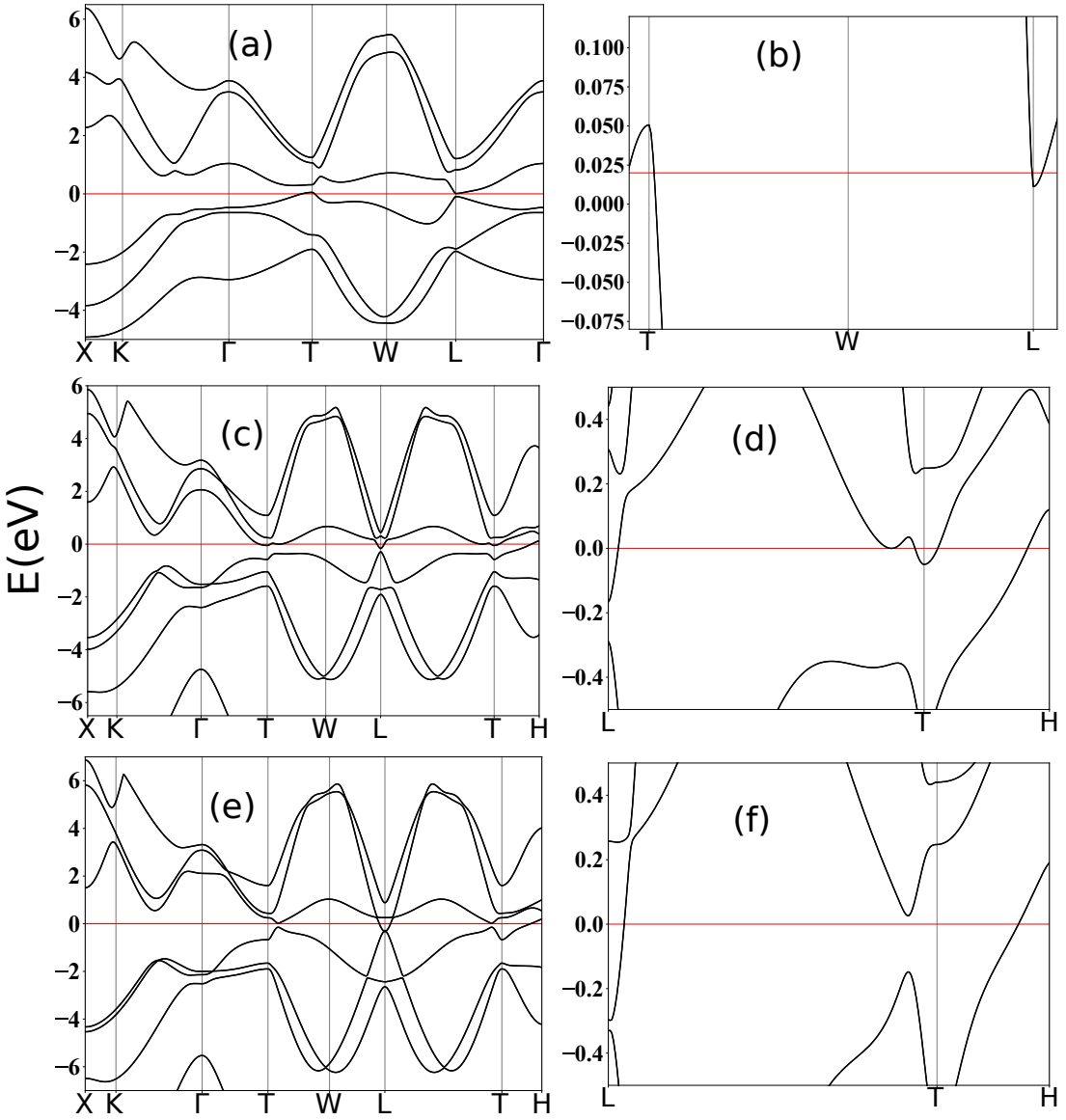

Figure 2.10: Electronic structure of the Group V semimetals. Figures (a), (c) and (e) show the electronic band structure of Bi, Sb and As respectively. Figures (b), (d) and (e) show the band structures of Bi, Sb and As zoomed in close to the electron and hole pockets near the Fermi level. It is clear that bismuth is the least metallic and arsenic the most.

zone boundary mode of the one atom unit cell. This can be seen in Fig. 2.11 (d), where the phonon dispersions of the three materials are scaled such that each of the materials have the same atomic mass as Bi:

$$\tilde{\omega}_j = \sqrt{\frac{m_j}{m_{\mathrm{Bi}}}}\omega_j, \tag{2.5}$$

where j indexes the atomic species. This shows that the more distorted the structure is from the undistorted phase, the higher the A_{1g} mode frequency.

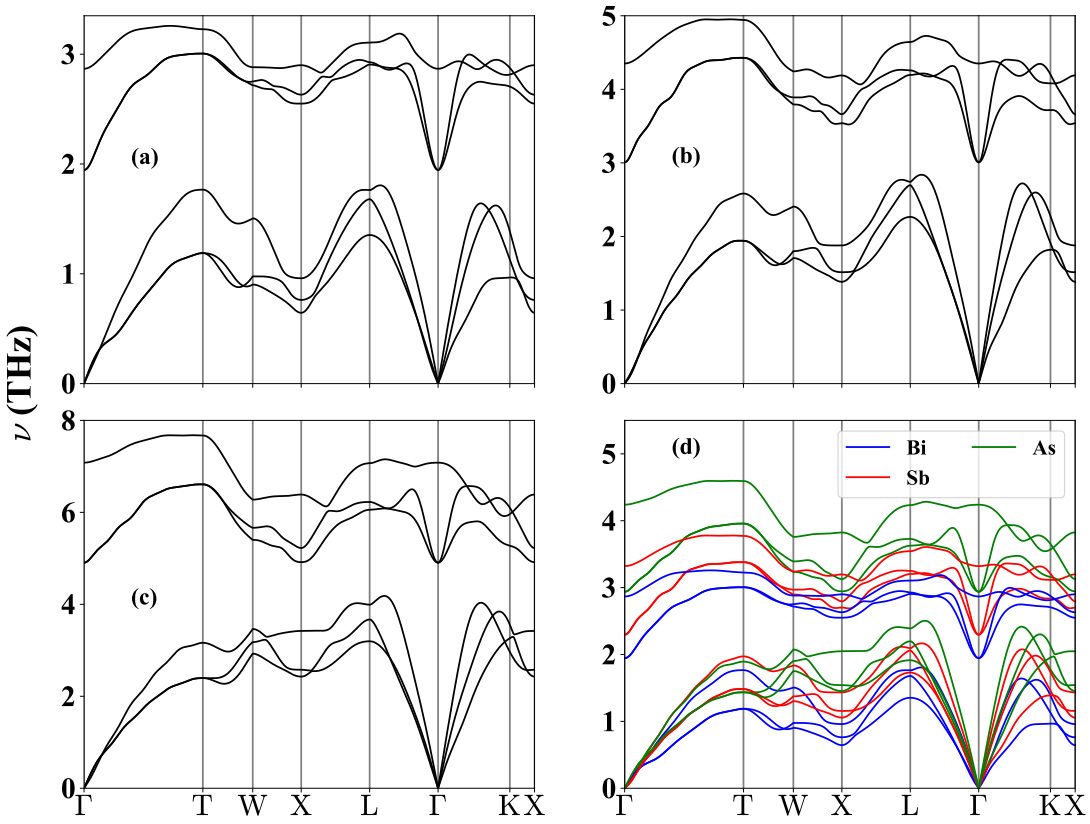

Figure 2.11: Phonon dispersions of (a): Bi, (b): Sb and (c): As calculated within the framework of density functional perturbation theory (DFPT, see section 3.14). The phonon dispersions of all three materials, scaled to the atomic mass of Bi (Eq. (2.5)) are shown in (d). The scaled A_{1g} mode frequency increases going from Bi to Sb and As, consistent with an increasingly large Peierls distortion.

2.4 Displacive excitation of coherent phonons

The DECP theory was first introduced by Dresselhaus and collaborators in 1992 [31] to explain the fact that only fully-symmetric modes were observed when optically exciting the first set of materials that people studied with pump-probe techniques. For example, Peierls distorted materials undergo oscillations of their internal atomic displacement parameter z which correspond to a coherent phonon of A_1 symmetry. In this theory, photoexcitation excites a number of carriers n_C which quickly establish a quasi-equilibrium distribution through scattering on a timescale much shorter than the period of the A_1 coherent mode. This causes a sudden shift in the equilibrium A_1 coordinate, launching coherent cosine-like oscillations about the new equilibrium position as illustrated in Fig. 2.12. [6] The excitation of these coherent phonons is described by the

[6] This is directly analogous to what would happen to a relaxed vertically hanging spring if the gravitational force acting on it were suddenly changed $g \rightarrow g + \delta g$.

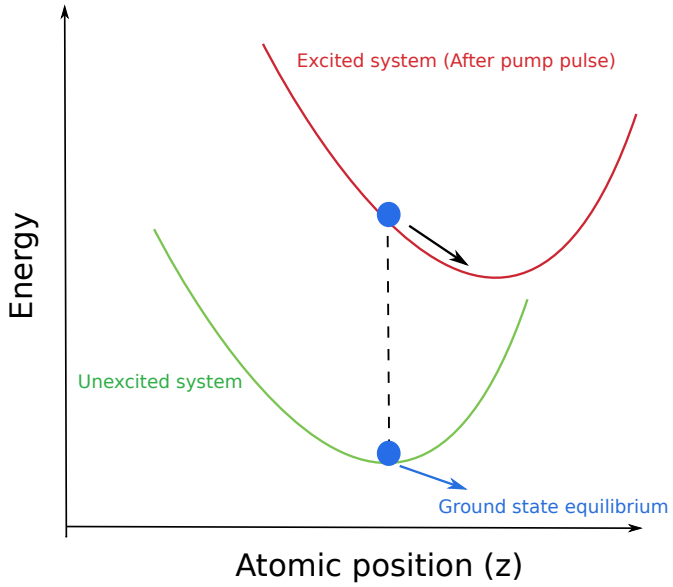

Figure 2.12: Schematic of the DECP model of coherent phonon excitation. The pump pulse suddenly shifts the equilibrium coordinate of the phonon, leading to a cosine-like oscillation.

following system of equations:

$$\dot{n}_C(t) = \rho P(t) - \beta n_C(t), \tag{2.6}$$

$$Q_0(t) = \kappa n_C(t), \tag{2.7}$$

$$\ddot{Q}(t) = -\Omega_0^2[Q(t) - Q_0(t)] - 2\gamma\dot{Q}(t), \tag{2.8}$$

where the first term in Eq. (2.6) gives the rate of generation of carriers which is proportional to the power density (energy/time/area at surface) $P(t)$ of the pump pulse. The second term in Eq. (2.6) gives the rate of decay of carriers back to the ground state. Eq. (2.7) comes from assuming that the equilibrium mode coordinate $Q_0(t)$ depends linearly on the carrier density and Eq. (2.8) is the equation of motion of a harmonic oscillator with damping constant γ. The step-function shift in Q_0 upon photoexcitation provides a driving force $F(t)/\mu = \Omega_0^2 Q_0(t)$ in Eq. (2.8) and produces oscillations of the coherent mode which are proportional to $\cos(\Omega_0 t)$, where Ω_0 is the mode frequency. [7].

The DECP mechanism has proved very useful in describing the dynamics of fully-symmetric (A_1) coherent phonons. However, non-fully symmetric modes,

[7] In reality, photoexcitation reduces the mode frequency from its ground state value. For low levels of excitation, this can be ignored.

such as the E_g mode in Bi, Sb [15, 1], the E mode in Te [23] and the T_{2g} mode in Si [49] have also been observed in pump-probe experiments, albeit with a much smaller amplitude, indicating that the DECP model cannot be a complete description. Furthermore, these symmetry-breaking modes are observed to oscillate as $\sin(\Omega t)$ rather than $\cos(\Omega t)$, indicating an impulsive driving force, similar to the case of a harmonic oscillator driven by a delta-function force. To describe these excitations, we must draw upon a different theory of coherent phonon excitation. Namely, the theory of stimulated Raman scattering.

2.5 Stimulated Raman scattering picture

The generation of coherent phonons by photoexcitation can also be described within semiclassical stimulated Raman scattering theory as described in Refs. [21, 25, 1]. The incident electric field $\mathbf{E}(t)$ is treated classically and the Hamiltonian written:

$$\hat{H} = \frac{1}{2}\hat{P}^2 + \frac{1}{2}\Omega_0^2\hat{Q}^2 + \hat{H}_e - \Xi\hat{Q} - \hat{\mathbf{\Delta}} \cdot \mathbf{E}(t), \tag{2.9}$$

where the first 2 terms correspond to the unperturbed phonon Hamiltonian, $\hat{H}_e$ is the unperturbed electron Hamiltonian, $\Xi\hat{Q}$ is the electron-phonon interaction and $\hat{\mathbf{\Delta}} \cdot \mathbf{E}(t)$ is the interaction between the electrons and the classical electric field. This Hamiltonian gives us an equation of motion for a harmonic oscillator driven by the interaction $\hat{\Xi}$ between the excited electrons and the ionic degrees of freedom [8]:

$$\frac{d^2\langle\hat{Q}\rangle}{dt^2} + \Omega_0^2 = \langle\hat{\Xi}\rangle \equiv F, \tag{2.10}$$

where Ω_0 is the frequency of the coherent mode. The steady-state solution to Eq. (2.10) can be obtained by Fourier transforming and re-arranging to obtain:

$$\langle\hat{Q}(\Omega)\rangle = \frac{F(\Omega)}{\Omega_0^2 - \Omega^2} = -\frac{F(\Omega)}{(\Omega - \Omega_0)(\Omega + \Omega_0)}, \tag{2.11}$$

which has poles at $\pm\Omega_0$. The steady-state displacement can then be obtained by inverse Fourier transform of Eq. (2.11), which involves contour integration

[8] For simplicity, we ignore damping of the oscillations. It is straightforward to modify the theory to include damping.

around these two poles by the Cauchy integral formula, leading to [9]:

$$\lim_{t\to\infty}\langle\hat{Q}(t)\rangle = \frac{-i}{\sqrt{8\pi}\Omega_0}[e^{i\Omega_0 t}F(-\Omega_0) - e^{-i\Omega_0 t}F(\Omega_0)]. \tag{2.12}$$

We readily see that if $F(\Omega)$ is real, it must be an even function, which gives us $\langle\hat{Q}(t)\rangle \propto \sin(\Omega_0 t)$, corresponding to an impulsive force $F(t) \propto \delta(t)$. However, if $F(\Omega)$ is imaginary, $\langle\hat{Q}(t)\rangle \propto \cos(\Omega_0 t)$, corresponding to a displacive force $F(t) \propto \theta(t)$[10]. Furthermore, the force $F(\Omega)$ can be expressed in terms of the dielectric function of the solid $\epsilon(\omega)$ [25]

$$F(\Omega) \propto \left[\frac{d\,\mathrm{Re}(\epsilon)}{d\omega} + \frac{2i\,\mathrm{Im}\,\epsilon}{\Omega}\right]\int_{-\infty}^{\infty} e^{i\Omega t}|E(t)|^2\mathrm{d}t, \tag{2.13}$$

demonstrating that the real and imaginary parts of the force correspond to the real and imaginary parts of the dielectric function $\epsilon(\omega)$. Fourier transforming Eq. (2.13) we find that the real part of ϵ leads to $F(t) \propto |E(t)|^2$. This is a force which is non-zero precisely when the pump electric field is non-zero. In the limit where the pump pulse duration is extremely short ($\tau\Omega_0 \ll 0$), this force becomes impulsive [11].

The imaginary part of ϵ, on the other hand, leads to $F(t) \propto \int_{-\infty}^{t}|E(t')|^2\mathrm{d}t'$, which is a displacive force. This term, due to the imaginary part of the dielectric function is associated with the absorption of light by the material and an accompanying excitation of valence electrons to the conduction bands. This electronic excitation produces a change in charge density which suddenly alters the equilibrium position of the ions in the sample. This modified charge density persists for several phonon periods, exerting a displacive step-function force on the ions and launching large amplitude coherent phonon motion.

In many opaque materials $|d\,\mathrm{Re}\{\epsilon\}/d\omega| \ll 2|\mathrm{Im}\{\epsilon\}/\Omega|$, leading to a purely displacive force from the absorptive imaginary part of ϵ. In these cases, the stimulated Raman scattering picture agrees quantitatively with DECP theory. However, while DECP was unable to explain the excitation of symmetry-breaking coherent phonons, a slight modification of the transient stimulated Raman scattering (TSRS) picture can explain it.

[9] The limit $t \to \infty$ is taken to isolate the steady-state contribution to $\langle Q(t)\rangle$.

[10] $\theta(t)$ is the Heaviside step function. This function vanishes for negative t and equals unity for non-negative t.

[11] In transparent materials there is no photon absorption, meaning that this impulsive force from the real part of ϵ is the only non-zero contribution.

2.5.1 Finite lifetime charge density fluctuations

When considering the absorptive contribution to the phonon driving force, we assumed that the charge density fluctuation produced by light absorption lasted much longer than the phonon period. However, we can modify this by including a decay rate Γ for the charge density fluctuation [12]:

$$F(t) \propto \mathrm{Im}(\epsilon) \int_{-\infty}^{t} e^{-\Gamma(t-t')} |E(t')|^2 \mathrm{d}t'. \tag{2.14}$$

This is useful when considering symmetry-breaking modes, which are necessarily driven by charge density fluctuations of the same symmetry as the phonon. For example, E_g coherent phonons couple to charge fluctuations of E_g symmetry. This is nicely illustrated in Fig. 2.13 from Ref. [1], which depicts two possible photoinduced charge fluctuations in the group V semimetals and the coherent phonons that couple to these fluctuations. The symmetry of the photoinduced

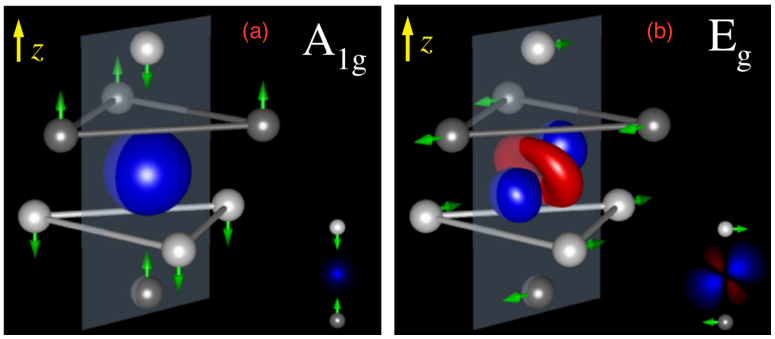

Figure 2.13: Schematic showing how photoinduced charge density fluctuations couple to coherent modes in the group V semimetals. Blue and red regions denote charge density fluctuations of opposite sign. (a): A fully symmetric charge density fluctuation couples only to the fully symmetric A_{1g} mode. (b) A charge density fluctuation with an additional E_g symmetry component will *also* drive the E_g mode, in addition to the A_{1g} mode. Figure reproduced from Ref. [1].

charge density fluctuations is determined by the polarisation of the pump pulse. In the case of the group V materials, a pump pulse polarised perpendicular to the threefold axis of the crystal will produce a charge density fluctuation with E_g symmetry (see subsection 3.17.3).

For the purposes of describing excitation of symmetry-breaking coherent phonons within the Raman theory, we can say that the symmetry-breaking modes are driven by an isosymmetric charge fluctuation which decays at a rate Γ to a fully symmetric charge fluctuation. As is indicated by Eq. (2.14), this causes the force

[12] This arises due to electrons being excited into states which rapidly decay due to scattering.

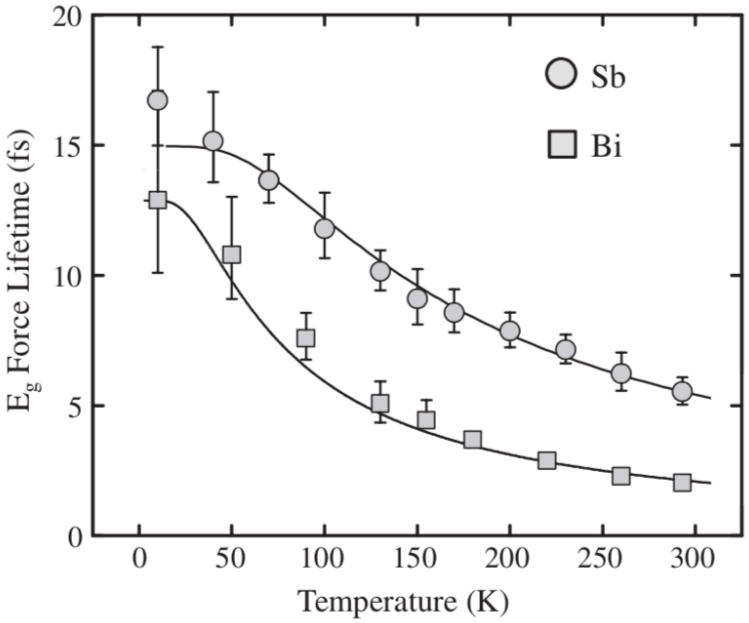

Figure 2.14: Measured lifetime of the force driving the low-symmetry E_g force in Bi and Sb. Figure reproduced from Ref. [1].

on the symmetry-breaking mode to decay at the same rate as the low-symmetry component of the charge fluctuation. In 2013, J.J Li and collaborators combined optical pump-optical probe experiments with continuous wave Raman scattering to measure the lifetime of the force driving the E_g modes in Bi and Sb. In both materials, they found that the lifetime of the force, shown in Fig.2.14, was much less than the period of the E_g mode ($\Gamma \gg \Omega_0$), causing the mode to have a small amplitude and to be proportional to $\sin(\Omega_0 t)$ consistent with an impulsive driving force. [13]. Furthermore the amplitude of the E_g mode falls off with increasing sample temperature, suggesting that the E_g force may decay by scattering involving phonons. In chapter 5, we address this question and show that electron-phonon scattering is the dominant scattering mechanism relaxing the E_g force in Bi and Sb. [30].

[13]Not to be confused with the impulsive contribution to the force due to the real (non-absorptive) part of the dielectric function, which calculations have shown to be negligible in optically pumped Bi. [50]

Chapter 3

Theoretical background and methods

3.1 Many-body Hamiltonian

In this thesis, we will be dealing primarily with solids, which are interacting many particle systems comprised of electrons and nuclei. In this context, it is important for us to consider the Hamiltonian of the entire system. The Hamiltonian is constructed as the sum of the potential and kinetic energies in the system, as follows [51]:

$$H = -\frac{\hbar^2}{2m_e}\sum_i {\nabla_i}^2 + \sum_{i<j}\frac{e^2}{|\mathbf{r_i}-\mathbf{r_j}|} + \sum_{i,I}\frac{Z_I e^2}{|\mathbf{R_I}-\mathbf{r_i}|} - \frac{\hbar^2}{2}\sum_I \frac{{\nabla_I}^2}{M_I} + \sum_{I<J}\frac{Z_I Z_J e^2}{|\mathbf{R_I}-\mathbf{R_J}|}, \tag{3.1}$$

where $\hbar$ is the reduced Planck constant, m_e, $\mathbf{r_i}$ and e are the mass, position and charge of electron i, and M_I, $\mathbf{R_I}$ and Z_I are the mass, position and atomic number of nucleus I. The first term in Eq. (3.1) is the kinetic energy operator for the electrons, the second is the electron-electron coulomb interaction, the third is the potential energy of the electrons due to coulomb interaction with the nuclei. The final two terms are the nuclear kinetic energy and the nuclear-nuclear interactions respectively.

Since the electrons move much faster than the nuclei, it is reasonable to assume that as the nuclei move, the electrons track their motion instantaneously. Within the Born-Oppenheimer approximation [52] we treat electronic and nuclear motion separately, enabling us to write the many-body wavefunction of the

system as a product of an electronic and a nuclear wavefunction:

$$\Psi_{tot}(\mathbf{r_i}, \mathbf{R_I}) = \Psi_{elec}(\mathbf{r_i}, \mathbf{R_I}) \times \Psi_{nuc}(\mathbf{R_I}). \tag{3.2}$$

We treat the nuclear degrees of freedom as fixed relative to the faster electrons. This allows us to neglect the nuclear kinetic energy. For *electronic structure* calculations, we may also neglect the nuclear-nuclear interaction energy, since it is just an additive constant in the total energy of the system. Thus we can express the Hamiltonian as:

$$H \approx -\frac{\hbar^2}{2m_e}\sum_i {\nabla_i}^2 + \sum_{i<j}\frac{e^2}{|\mathbf{r_i} - \mathbf{r_j}|} + \sum_{i,I}\frac{Q_I e^2}{|\mathbf{R_I} - \mathbf{r_i}|}, \tag{3.3}$$

$$\equiv -\frac{\hbar^2}{2m_e}\sum_i {\nabla_i}^2 + \sum_{i<j} U(\mathbf{r_i}, \mathbf{r_j}) + \sum_i V_{\text{ext}}(\mathbf{r_i}). \tag{3.4}$$

The system can be thought of as a set of N electrons evolving under the influence of an external potential V_{ext}. We can describe this evolution with the time-independent Schrödinger equation:

$$\left[\sum_{i=1}^{N}\left(-\frac{\hbar^2}{2m_e}{\nabla_i}^2 + V_{\text{ext}}(\mathbf{r_i})\right) + \sum_{i<j} U(\mathbf{r_i}, \mathbf{r_j})\right]\Psi(\mathbf{r_1}, \ldots, \mathbf{r_N}) = E\Psi(\mathbf{r_1}, \ldots, \mathbf{r_N}). \tag{3.5}$$

This is a useful way to write the Schrödinger equation of the system as it separates the contributions to the Hamiltonian of independent electrons and those of the electron-electron interaction.

3.2 Many-body fermionic wavefunction as Slater determinant

Electrons are fermions, so obey Fermi-Dirac statistics. As such, to correctly treat the many-body wavefunction we need to take into account the fermionic spin variables σ. The Pauli-exclusion principle implies that swapping the positions and spins of 2 fermions introduces an overall minus sign in the fermionic many-body wavefunction. To express this mathematically we use a composite variable of the position and spin of a fermion, $x = \{\mathbf{r}, \sigma\}$. The antisymmetry of the many-body

fermionic wavefunction can be encapsulated in the following relation:

$$\Psi(x_1, \ldots, x_i, \ldots, x_j, \ldots, x_N) = -\Psi(x_1, \ldots, x_j, \ldots, x_i, \ldots, x_N). \tag{3.6}$$

For a system of N independent electrons, the Hamiltonian can be expressed as:

$$H = \sum_{i=1}^{N} h_i, \tag{3.7}$$

with h_i being the single-particle Hamiltonian, describing the kinetic and potential energy of a single fermion. Each individual fermion evolves according to the single-particle Schrödinger equation:

$$h_i \phi_j(x_i) = \varepsilon_j \phi_j(x_i), \tag{3.8}$$

which can be solved to obtain the complete set of eigenfunctions. These single-particle eigenfunctions are usually referred to as spin-orbitals. The many-body wavefunction can then be expressed in terms of these spin-orbitals as:

$$\Psi(x_1, \ldots, x_i, \ldots, x_j, \ldots, x_N) = \frac{1}{\sqrt{N!}} \begin{vmatrix} \phi_1(x_1) & \phi_2(x_1) & \ldots & \phi_N(x_1) \\ \phi_1(x_2) & \phi_2(x_2) & \ldots & \phi_N(x_2) \\ \vdots & \vdots & \ddots & \vdots \\ \phi_1(x_N) & \phi_2(x_N) & \ldots & \phi_N(x_N) \end{vmatrix}. \tag{3.9}$$

This way of expressing a many-body wavefunction is called a Slater determinant [53]. It encodes the antisymmetry of the many-body fermionic wavefunction, since exchanging any 2 rows will introduce an overall minus sign in Ψ. If any 2 rows are equal, Ψ vanishes, reflecting the fact that 2 fermions of the same spin cannot sit at the same location. Thus, Slater determinant wavefunctions fully obey the Pauli exclusion principle by construction.

For completeness, it is worth noting that a many-body *boson* wavefunction can be expressed in an analogous way. However, since bosons do not obey an exclusion principle, and hence have a wavefunction which is symmetric under the exchange of 2 particles, the many-body wavefunction is expressed as a *permanent* rather than a determinant. Permanents can be computed using the standard methods for computing determinants, but replacing every instance of a negative sign with a positive sign. For instance, a 2×2 matrix will have the

following permanent:

$$\text{Perm}\begin{pmatrix} a & b \\ c & d \end{pmatrix} = ad + bc. \tag{3.10}$$

3.3 Variational principle and Hartree-Fock theory

For a given system described by a Hamiltonian H, the expectation value of H calculated with any trial wavefunction is bounded below by the true ground state energy of the system E_0:

$$E_0 \leq \langle \psi_{\text{trial}} | H | \psi_{\text{trial}} \rangle . \tag{3.11}$$

Thus we can define the true wavefunction of the system as that which *globally* minimises the expectation value of H. This wavefunction will also yield the correct ground state energy E_0.

The procedure for finding Ψ_0 is to choose a trial wavefunction ψ_{trial} with parameters $\{x_1, \ldots, x_N\}$ and then minimise $\langle \psi_{\text{trial}} | H | \psi_{\text{trial}} \rangle$ with respect to these parameters. The functional form of the trial wavefunction has to be carefully chosen to ensure that the *global* minimum is accessible by varying its parameters.

In order to show the utility of the variational principle, we re-introduce the electron-electron interactions in a mean-field fashion. This means that the electrons are still treated as independent, but act under the influence of an addtiional potential due to the presence of the other electrons. Rather than all electrons interacting with each other, each electron interacts with an *average* configuration of all other electrons in the system. In this mean-field approximation, we can use the variational principle to optimise the spin-orbitals in Eq. (3.9) and obtain the ground state energy of the many-body system. This is the approach of Hartree-Fock theory.

The Hartree-Fock equations are derived using the variational principle for ψ_{trial} a Slater determinant (Eq. (3.9)). The individual spin-orbitals comprising the determinant are varied under the constraint of orthonormality:

$$\langle \phi_i(x_k) | \phi_j(x_l) \rangle = \delta_{ij}\delta_{kl}. \tag{3.12}$$

We arrive at a set of equations which are solved iteratively, leading to an approach

known as the Self-Consistent Field (SCF) method. These equations are:

$$\left[\frac{-\hbar^2}{2m}\nabla^2 + V_{\text{ext}}(\mathbf{r}) + V_H(\mathbf{r})\right]\psi_i(\mathbf{r}) + \hat{V}_{\text{ex}}(\mathbf{r})\psi_i(\mathbf{r}) = \varepsilon_i\psi_i(\mathbf{r}). \tag{3.13}$$

The potentials $V_{\text{ext}}(\mathbf{r})$, $V_H(\mathbf{r})$ and the operator $\hat{V}_{\text{ex}}(\mathbf{r})$ are defined as:

$$V_{\text{ext}}(\mathbf{r}) = -e^2\sum_{I=1}^{M}\frac{Z_I}{|\mathbf{r}-\mathbf{R}_I|}, \tag{3.14}$$

$$V_H(\mathbf{r}) = -e^2\sum_{j=1}^{N}\int\frac{|\phi_j(\mathbf{r}')|^2}{|\mathbf{r}-\mathbf{r}'|}\mathrm{d}\mathbf{r}', \tag{3.15}$$

$$\hat{V}_{\text{ex}}(\mathbf{r})\phi_i(\mathbf{r}) = -e^2\sum_{j=1}^{N}\phi_j(\mathbf{r})\int\frac{{\phi_j}^*(\mathbf{r}')\phi_i(\mathbf{r}')}{|\mathbf{r}-\mathbf{r}'|}\mathrm{d}\mathbf{r}'. \tag{3.16}$$

The first two potentials are the external electron-nucleus interaction and the Hartree electrostatic interaction respectively. The operator $\hat{V}_{\text{ex}}$ corresponds to the *exchange* energy. This term accounts for the mutual repulsion of electrons with parallel spin, due to the Pauli exclusion principle. Its inclusion results in a depletion of parallel spin electrons in the region surrounding a given electron. This region of depletion is commonly referred to as an exchange hole.

Eq. (3.13) is solved self consistently. An initial guess is chosen for the spin-orbitals $\phi_I(\mathbf{r})$. These are then used to compute the potentials and the variational principle is applied to obtain the ground state energy and new spin-orbitals. This process is repeated with the new spin-orbitals, until the changes in ground state energy between consecutive steps in the iterative process are sufficiently small.

The Hartree-Fock method is a very successful method, but it does have some shortcomings. Most notably, while the electron exchange interaction is fully accounted for, the mean-field approximation neglects Coulomb correlation of electrons. This can be best understood by considering 2 electrons of antiparallel spin. The Coulomb interaction between them is repulsive and so will tend to cause the electrons to be well separated. Adding more electrons will introduce screening, but ultimately we would expect electrons of antiparallel spin to be well separated in space. Since Hartree-Fock theory doesn't account for this effect, if we take our Hartree-Fock system and increase the distance between antiparallel spins, we will reduce the energy. As a result, the energy computed in Hartree-Fock theory via the variational principle overestimates the true energy of the many-body electronic system by an amount E_{corr}, which is typically referred to as the electron correlation energy [54].

3.4 Density functional theory

Density functional theory is a reformulation of quantum mechanics which allows us to map the $3N$ dimensional problem of solving for the many-body wavefunction to a 3 dimensional problem of solving for the electron density $n(\mathbf{r})$. It relies on 2 theorems, which were proved by Hohenberg and Kohn [55].

Theorem 1: The external potential V_{ext} acting on the electrons is a unique functional [1] of the ground-state electron density $n(\mathbf{r})$. Thus, the external potential and all other ground state properties can be determined if we know $n(\mathbf{r})$.

Theorem 2: A universal functional of the ground-state electron density, $E[n(\mathbf{r})]$ exists which satisfies a variational principle in which it's global minimum is the exact ground state energy of the many-body system:

$$E_{\text{GS}} = \min_{n(\mathbf{r})} E[n] \quad \text{s.t} \quad \int n(\mathbf{r}) \mathrm{d}\mathbf{r} = N. \tag{3.17}$$

The term 'universal' refers to the fact that the functional is system independent, for a fixed number of electrons N. The electron density of the many-body system can be written as an integral over the many-body wavefunctions as follows [56]:

$$n(\mathbf{r}) = N \int \mathrm{d}\mathbf{r_2} \ldots \mathrm{d}\mathbf{r_{N_e}} \Psi^*(\mathbf{r}, \mathbf{r_2}, \ldots, \mathbf{r_{N_e}}) \Psi(\mathbf{r}, \mathbf{r_2}, \ldots, \mathbf{r_N}) \tag{3.18}$$

Hohenberg and Kohn explained that there is a one-to-one mapping between the external potential experience by the electrons, V_{ext} and the non-degenerate many-electron ground state wavefunction Ψ, and that there is also a one-to-one mapping between Ψ and the ground state density $n(\mathbf{r})$ of an N electron system.

Since the electronic density determines all ground state properties of a system, the total energy may be expressed as a functional of $n(\mathbf{r})$:

$$E[n(\mathbf{r})] = T[n] + U[n] + V_{\text{ext}}[n] \tag{3.19}$$

$$= T[n] + U[n] + \int n(\mathbf{r}) V_{\text{ext}}(\mathbf{r}) \mathrm{d}\mathbf{r} \tag{3.20}$$

$$= F[n] + \int n(\mathbf{r}) V_{\text{ext}}(\mathbf{r}) \mathrm{d}\mathbf{r}, \tag{3.21}$$

where $F[n]$ is universal and fully includes electron correlation effects, such as exchange, non-classical electron-electron self energy and Coulomb correlation.

[1] A functional is a mathematical object which takes a function as its argument and assigns to it a complex number. A simple example is the definite integral of a function: $\mathbb{I}[f(x)] = \int_a^b f(x') \mathrm{d}x'$.

We have established that all ground state properties can be determined from a knowledge of $n(\mathbf{r})$. However, this still requires solving the many-body Schrödinger equation, which is really the problem we were trying to avoid with this approach. Fortunately, Kohn and Sham found an alternative approach which circumvents this issue.

3.4.1 Kohn-Sham equations

A major issue with using the electronic density $n(\mathbf{r})$ directly, arises in the calculation of the kinetic energy of the electrons. The component of the kinetic energy due to non-interacting electrons is simple to evaluate in terms of single particle wavefunctions, but impossible to compute from knowledge of the electron density $n(\mathbf{r})$ alone. Thomas [57] and Fermi [58] suggested an approximate formula for the non-interacting kinetic energy in terms of the electron density $n(\mathbf{r})$:

$$T_{\text{TF}} = \frac{3\hbar^2}{10m_e}(3\pi^2)^{\frac{3}{2}} \int [n(\mathbf{r})]^{\frac{5}{3}} \mathrm{d}\mathbf{r}. \tag{3.22}$$

However, the Thomas-Fermi approximation to the kinetic energy produces a larger error than neglecting the effects of exchange and correlation altogether. In 1965, Kohn and Sham suggested a solution to this problem by re-phrasing the problem of solving the many-body Schrödinger equation as one of solving an *auxiliary* system of non-interacting electrons, which have the same density, but move in a mean field [59]. To do so, they proposed the following decomposition of the universal functional $F[n]$:

$$F[n] = T_s[n] + \frac{1}{2} \int n(\mathbf{r})\Phi(\mathbf{r})\mathrm{d}\mathbf{r} + E_{\text{xc}}[n], \tag{3.23}$$

where $T_s[n]$ is the kinetic energy of a gas of non-interacting electrons, $\Phi(\mathbf{r}) = e^2 \int \frac{n(\mathbf{r}')\mathrm{d}\mathbf{r}'}{|\mathbf{r}-\mathbf{r}'|}$ is the classical electrostatic interaction between an electron at position $\mathbf{r}$ and the charge density of the entire non-interacting electron gas and $E_{\text{xc}}[n]$ is the exchange-correlation energy. This is essentially the term into which we lump all of the unknowns, typically due to electron correlations [2]. As such it can trivially be defined as the exact energy minus the terms that we *do* know

[2] In 1972, Feynman referred to E_{xc} as the "stupidity energy", since it is the term which encompasses our ignorance about the details of the many-body problem.

how to calculate:

$$E_{\text{xc}}[n] = \left(\langle \hat{T}[n] \rangle - T_s[n]\right) + \left(\langle \hat{U}[n] \rangle - \frac{1}{2}\int n(\mathbf{r})\Phi(\mathbf{r})\mathrm{d}\mathbf{r}\right), \tag{3.24}$$

where $\hat{T}$ and $\hat{U}$ correspond to the first 2 terms in Eq. (3.4). It thus corresponds to the energy difference between the fully-interacting many-electron system and a non-interacting system of electrons with the same charge density $n(\mathbf{r})$.

Within this framework, assuming the system is non-magnetic, the charge density $n(\mathbf{r})$ can be expressed in terms of single particle Kohn-Sham orbitals ψ_i as follows:

$$n(\mathbf{r}) = 2\sum_{i=1}^{N/2} |\psi_i(\mathbf{r})|^2. \tag{3.25}$$

The lowest energy configuration will generally be achieved by electrons doubly occupying the $N/2$ lowest energy states with antiparallel spin electrons. This allows us to express the non-interacting part of the electron kinetic energy simply in terms of these orbitals:

$$T_s[n] = 2\left(\frac{-\hbar^2}{2m_e}\right)\sum_{i=1}^{N/2} \langle \psi_i | \nabla_i^2 | \psi_i \rangle \tag{3.26}$$

Our goal is to minimise the ground state energy. This is achieved by solving the variational problem, requiring that the following functional derivative vanish:

$$\frac{\delta\Omega}{\delta {\psi_i}^*} = 0, \tag{3.27}$$

where Ω is the energy functional, modified to include a Lagrange multipliers which constrain the Kohn-Sham orbitals ψ_i to remain orthonormal throughout the minimisation process:

$$\Omega[n] = E[n] - \sum_j \varepsilon_j \left(\langle \psi_i | \psi_j \rangle - \delta_{ij}\right). \tag{3.28}$$

The numbers ε_j are Lagrange multipliers constraining the single particle wavefunctions ψ_i to be orthonormal. Imposing $\delta\Omega/\delta\psi_i^* = 0$, we obtain the following equation:

$$\left[\frac{\hbar^2}{2m}\nabla^2 + V_{\text{eff}}(\mathbf{r})\right]\psi_i(\mathbf{r}) = \varepsilon_i \psi_i(\mathbf{r}), \tag{3.29}$$

which has the mathematical form of a single particle Schrödinger equation, but in terms of *auxilliary* Kohn-Sham orbitals. The effective potential $V_{\text{eff}} =$

$V_{\text{ext}} + \Phi(\mathbf{r}) + V_{\text{xc}}(\mathbf{r})$. The exchange-correlation potential is obtained from the functional derivative of the exchange-correlation energy with respect to the electron density:

$$V_{\text{xc}}(\mathbf{r}) = \frac{\delta E_{\text{xc}}(\mathbf{r})}{\delta n(\mathbf{r})}. \tag{3.30}$$

Equations (3.29) and (3.25) are known as the Kohn-Sham equations. They are solved iteratively until self-consistency is achieved between $n(\mathbf{r})$ and $V_{\text{eff}}(\mathbf{r})$. The total energy of the system can then be expressed in terms of the Kohn-Sham orbitals as follows [60]:

$$E[n] = 2\sum_{i=1}^{N/2} \varepsilon_i - \frac{1}{2}\int n(\mathbf{r})\Phi(\mathbf{r})\mathrm{d}\mathbf{r} + E_{\text{xc}}[n] - \int n(\mathbf{r})V_{\text{xc}}[n]\mathrm{d}\mathbf{r}. \tag{3.31}$$

This transforms the problem into one of solving the single particle Schrödinger equation, which is numerically simple. However there's a catch: we need to know the exchange-correlation functional, and in reality, although an exact exchange-correlation functional has been computed for some simple models [61, 62], it is in general not known. As a result, Kohn-Sham DFT relies on making simple, but effective approximations to $V_{\text{xc}}[n]$. We will discuss this further in section 3.5.1.

Once self-consistency is reached, the charge density $n(\mathbf{r})$ can be used to calculate the Kohn-Sham eigenvalue ε_i of any given state ψ_i. In the periodic systems that we are typically interested in, the state index i can be considered a composite index of electron wavevector $\mathbf{k}$, and band index n. Thus, the eigenvalues of the Kohn-Sham Hamiltonian $\varepsilon_{n\mathbf{k}}$ superficially resemble electronic state energies which you would find in a typical band structure. However, $\varepsilon_{n\mathbf{k}}$ entered the derivation as Lagrange multipliers constraining the *auxiliary* Kohn-Sham orbitals to be orthonormal, so it is not immediately obvious how one would connect them to the electronic state energies.

3.5 Physical interpretation of Kohn-Sham eigenvalues

In 1934, Tjalling Koopmans proved a theorem which states that the eigenvalue of the highest occupied Hartree-Fock orbital (HOMO) is equal to the first ionisation energy of the system [63]. In 1978, J.F Janak extended this theorem to Kohn-Sham DFT by showing that the Kohn-Sham eigenvalues are equal to the change in

total energy when the occupation of a given Kohn-Sham orbital is changed [64]:

$$\frac{\partial E}{\partial f_{n\mathbf{k}}} = \varepsilon_{n\mathbf{k}}. \tag{3.32}$$

This is true, independent of the exact form of the exchange-correlation functional. While this theorem makes a connection between the Kohn-Sham eigenvalues and some physical energies, there is still no rigorous connection between the Kohn-Sham eigenvalues and the electronic band structure energies. However, comparisons with experiment as well as Hartree-Fock theory, where the single particle orbitals do have well defined band structure energies, have shown that treating $\varepsilon_{n\mathbf{k}}$ as the true band structure energies is a good approximation for many materials.

3.5.1 Approximations to exchange and correlation

For realistic systems, the exchange-correlation functional E_{xc} is not known. Therefore, in order to solve the Kohn-Sham equations and compute the total energy of a system, we need to suitably approximate E_{xc}. Today, there is a diverse selection of approaches aimed at generating accurate approximations to the exchange-correlation functional. However, the simplest method, which was originally suggested by Paul Dirac [65], and employed in the context of Kohn-Sham DFT by Kohn and Sham [59], is the so-called local density approximation (LDA).

To introduce this approximation, we first define the Wigner-Seitz radius r_s as the mean radius of a sphere which contains precisely 1 electron:

$$r_s = \left(\frac{3}{4\pi n}\right)^{\frac{1}{3}}, \tag{3.33}$$

where n is the number of electrons per unit volume. We also define r_0 as the typical length over which there is an appreciable change in electron density. The local density approximation states that if the electron density $n(\mathbf{r})$ is sufficiently slowly varying, such that $r_s/r_0 \ll 1$, we can make the following approximation to the exchange-correlation functional:

$$E_{\text{xc}}^{\text{LDA}}[n] = \int n(\mathbf{r})\varepsilon_{\text{xc}}^{\text{LDA}}(n(\mathbf{r}))\mathrm{d}\mathbf{r}, \tag{3.34}$$

where $\varepsilon_{\text{xc}}^{\text{LDA}}$ is the exchange-correlation energy per electron of an homogeneous

electron gas of density $n(\mathbf{r})$. At each point in space $\mathbf{r}$, the exchange-correlation functional is given by the exchange-correlation energy of a homogeneous electron gas with density $n(\mathbf{r})$.

The LDA is known to give remarkably accurate results, far beyond the restricted context in which it was originally proposed [66, 67]. There is known to be a systematic error cancellation caused by an underestimation of the exchange energy but an overestimation of the correlation energy. For many purposes, the LDA is a perfectly adequate approach. However, calculations that require a higher degree of accuracy often need to go beyond this level of approximation.

One way to improve upon the LDA is to develop a sequence of approximations, where each approximation builds upon the previous one. For instance, the LDA can be built upon by the inclusion of progressively higher spatial derivatives of the electron density $n(\mathbf{r})$. The most common approach along these lines is the generalised gradient approximation (GGA) of Perdew, Burke and Ernzerhof [68], which builds upon the LDA by including a dependence of the exchange-correlation energy on the gradient of the electron density.

$$E_{\text{xc}}^{\text{GGA}}[n] = \int n(\mathbf{r})\varepsilon_{\text{xc}}^{\text{GGA}}(n(\mathbf{r}), |\boldsymbol{\nabla} n(\mathbf{r})|)\mathrm{d}\mathbf{r}. \tag{3.35}$$

Further improvements can be gained by introducing a portion of exact exchange from Hartree-Fock theory into E_{xc}. In these hybrid-functional approaches [69], E_{xc} is formed as a linear combination of the exact exchange functional E_x^{HF} and a GGA exchange-correlation functional:

$$E_{\text{xc}}^{\text{hyb}} = \alpha E_x^{\text{HF}} + (1-\alpha)E_{\text{xc}}^{\text{GGA}} \quad \text{with} \quad \alpha \in [0,1]. \tag{3.36}$$

An obvious drawback here is that the mixing parameter α is not known a-priori, but rather must be determined by fitting to experiment. Hybrid-functional DFT is therefore a semi-empirical framework. Nonetheless, hybrid-functional methods are a popular choice for electronic structure calculations.

For our purposes in this thesis, the LDA is more than adequate. Unless otherwise stated, LDA is used for all electronic structure calculations presented in this thesis.

3.5.2 Plane-wave based methods

Though the Kohn-Sham method reduces the many-body problem down to self-consistent solution of a single particle Schrödinger equation, there is still the issue of having to solve for an infinite number of electrons evolving under a potential generated by an infinite number of nuclei. To approach this problem, notice that crystalline materials with a periodic lattice have potentials which are invariant under translation by a Bravais lattice vector: $V(\mathbf{r}+\mathbf{R}) = V(\mathbf{r})$. As a result, Bloch's theorem allows us to express wavefunctions of the crystal system as the product of a plane-wave and a lattice periodic function $u_{n\mathbf{k}}(\mathbf{r}) = u_{n\mathbf{k}}(\mathbf{r}+\mathbf{R})$ as follows:

$$\psi_{n\mathbf{k}}(\mathbf{r}) = \frac{1}{\sqrt{N_p}} u_{n\mathbf{k}}(\mathbf{r}) e^{i\mathbf{k}\cdot\mathbf{r}}. \tag{3.37}$$

where N_p is the number of primitive cells in the system. This can be equivalently stated as:

$$\psi_{n\mathbf{k}}(\mathbf{r}+\mathbf{R}) = e^{i\mathbf{k}\cdot\mathbf{R}} \psi_{n\mathbf{k}}(\mathbf{r}), \tag{3.38}$$

where $\mathbf{R}$ is a Bravais lattice vector. This allows the electronic wavefunction of a periodic structure to be represented by a plane-wave expansion. We begin by expressing $u_{n\mathbf{k}}(\mathbf{r})$ as the Fourier transform of a function in reciprocal space:

$$u_{n\mathbf{k}}(\mathbf{r}) = \int \tilde{u}_{n\mathbf{k}}(\mathbf{g}) e^{i\mathbf{g}\cdot\mathbf{r}} \mathrm{d}\mathbf{g}, \tag{3.39}$$

and noticing that the periodicity of $u_{n\mathbf{k}}(\mathbf{r})$ requires that:

$$\int \tilde{u}_{n\mathbf{k}}(\mathbf{g}) e^{i\mathbf{g}\cdot\mathbf{r}} \mathrm{d}\mathbf{g} = \int e^{i\mathbf{g}\cdot\mathbf{R}} \left[\tilde{u}_{n\mathbf{k}}(\mathbf{g}) e^{i\mathbf{g}\cdot\mathbf{r}}\right] \mathrm{d}\mathbf{g}. \tag{3.40}$$

This is only satisfied if $e^{i\mathbf{g}\cdot\mathbf{R}} = 1$, which occurs precisely when $\mathbf{g}$ is a reciprocal lattice vector, $\mathbf{G}$. The Fourier transform therefore reduces to a Fourier series over plane-waves of wavevector $\mathbf{G}$ in the reciprocal lattice:

$$u_{n\mathbf{k}}(\mathbf{r}) = \frac{1}{\sqrt{\Omega_0}} \sum_{\mathbf{G}} c_{n\mathbf{k}}(\mathbf{G}) e^{i\mathbf{G}\cdot\mathbf{r}}, \tag{3.41}$$

where Ω_0 is the volume of the primitive cell and $c_{n\mathbf{k}}(\mathbf{G})$ are plane-wave coefficients. Combining Eqs. (3.37) and (3.41), we can write the total wavefunction in terms of these plane-wave coefficients as follows:

$$\psi_{n\mathbf{k}}(\mathbf{r}) = \frac{1}{\sqrt{N_p \Omega_0}} \sum_{\mathbf{G}} c_{n\mathbf{k}}(\mathbf{G}) e^{i(\mathbf{k}+\mathbf{G})\cdot\mathbf{r}}. \tag{3.42}$$

Within the Kohn-Sham approach, we can Fourier transform the Eq. (3.29) to obtain the following matrix equation in terms of our plane wave coefficients:

$$\sum_{\mathbf{G}'}\left[\frac{\hbar^2}{2m}|\mathbf{k}+\mathbf{G}|^2\delta_{\mathbf{G}\mathbf{G}'}+V_{\text{eff}}(\mathbf{G}-\mathbf{G}')\right]c_{n\mathbf{k}}(\mathbf{G})=\varepsilon_{n\mathbf{k}}c_{n\mathbf{k}}(\mathbf{G}), \tag{3.43}$$

where $\delta_{\mathbf{G}\mathbf{G}'}$ is the Kronecker delta function. We have now written the first Kohn-Sham equation in a form which is amenable to some reasonable approximations. For large systems, $\mathbf{k}$ is a quasi-continuous variable, but the cell-periodic part of the electronic wavefunctions will be very similar at $\mathbf{k}$ points very near to each other (ie. $u_{n\mathbf{k}} \approx u_{n\mathbf{k}+\delta\mathbf{k}}$). This allows the electronic wavefunction to be represented over a small region of reciprocal space by a single $\mathbf{k}$ point. Thus, we can calculate the total energy of the system from electronic states computed on a finite k-point grid, as long as the grid is fine enough to capture variations in the electron density. The most common method for generating this finite grid is the Monkhorst and Pack scheme [70].

Additionally, the Fourier series for the electronic wavefunctions can be truncated by setting an upper bound on the kinetic energy as follows:

$$\frac{\hbar^2}{2m}|\mathbf{k}+\mathbf{G}|^2 < E_{\text{cut}}. \tag{3.44}$$

This truncation is viable because plane-waves with higher energies contribute less to the wavefunction. Calculations are typically performed within the first Brillouin zone, which is the highest-symmetry reciprocal space primitive cell. Bloch's theorem tells us that knowing the wavefunction in the first Brillouin zone completely characterises a periodic solid. However, we must numerically converge the total energy with respect to the number of points in the $\mathbf{k}$ grid and the value of the plane-wave cutoff E_{cut}.

3.6 Pseudopotentials

The Kohn-Sham orbitals have now been written as a Fourier series in plane waves. However, due to the high kinetic energy of core electrons, their wavefunctions have very sharp oscillations near the nuclei. Thus, the number of plane-waves required to describe these core wavefunctions will be very large. Fortunately, since all chemically relevant physical processes depend primarily on the valence states, we can safely ignore the core states. This is achieved by replacing the full

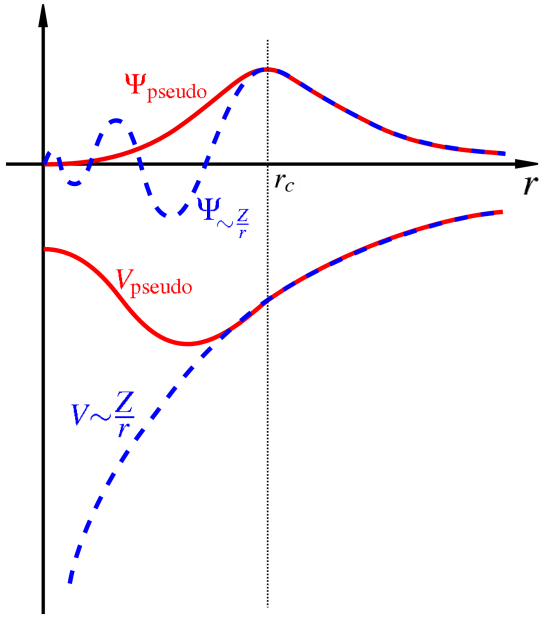

Figure 3.1: Schematic of the full Coulomb potential and real wavefunction in blue, compared with the pseudopotential and pseudowavefunction in red. They match up exactly beyond the cutoff radius. Picture taken from wikicommons.

external potential with an effective potential which is smoother in the core region but which exactly matches the full potential beyond a certain cutoff radius. As long as all valence states are outside this radius, the chemically relevant physics should be well represented. This is called the pseudopotential approximation, it is explained schematically in Fig. 3.1.

Pseudopotentials are typically constructed with 2 constituent components: a local and a non-local potential:

$$V_{\text{ps}} = V_{\text{loc}}(r) + \sum_{lm} V_{lm}(r) \left|Y_{lm}\right\rangle \left\langle Y_{lm}\right| , \tag{3.45}$$

where Y_{lm} are the spherical harmonics of orbital angular momentum number l and magnetic number m, and r is the radial distance from the nucleus. The local potential $V_{\text{loc}}(r)$ acts on all single-particle states in the same way. The operator $\left|Y_{lm}\right\rangle \left\langle Y_{lm}\right|$ projects the single-particle state onto the angular momentum coordinates $\{l, m\}$ and then the potential $V_{lm}(r)$ acts on the projected component. Thus, states with different angular momentum *feel* different potentials. It is in this respect that the second term in Eq. (3.45) is a nonlocal potential.

There is a lot of freedom in choosing a particular psuedopotential. A common choice, which is used exclusively throughout this thesis, is the norm-conserving pseudopotential. Norm-conserving psuedopotentials are constructed to satisfy

the following 2 conditions [71]:

1. Inside the cutoff radius r_c, the pseudowavefunction $\tilde{\psi}_i$ must have the same norm as the true all-electron wavefunction ψ_i:

$$\int_{r<r_c} \tilde{\psi_i}^*(\mathbf{r})\tilde{\psi_i}(\mathbf{r})\mathrm{d}\mathbf{r} = \int_{r<r_c} \psi_i^*(\mathbf{r})\psi_i(\mathbf{r})\mathrm{d}\mathbf{r}, \tag{3.46}$$

2. Outside the cutoff radius, the pseudowavefunction must be **identical** to the true all-electron wavefunction.

Certain types of pseudopotentials also allows the inclusion of relativistic effects, such as spin-orbit coupling, which would normally be omitted from the inherently non-relativistic Kohn-Sham approach. This is of particular importance for heavier atoms, such as bismuth, where relativistic effects are usually very important.

Throughout this thesis, norm-conserving, fully relativistic pseudopotentials are used for all DFT calculations. When using the Quantum Espresso code [72], Vanderbilt norm-conserving [73] pseudopotentials are used and when using the ABINIT code [74], Hartwigsen-Goedecker-Hutter (HGH) [75] pseudopotentials are employed.

3.7 Lattice dynamics in three-dimensional crystals

In this section, we will derive the equations describing lattice dynamics for a three-dimensional crystal in terms of interatomic force constants. We follow the treatment in Ref. [76] and begin by considering a crystal containing p atoms per unit cell . We consider displacements of the α^{th} atom in the l^{th} unit cell of amplitude $u^{l\alpha}$. If we assume that the total potential energy V of the crystal is a function of the instantaneous position of all atoms, we can expand V in a Taylor series in powers of the atomic displacement $u^{\alpha l}$:

$$\begin{aligned} V = V_0 + \sum_{l\alpha}\sum_{i} \left.\frac{\partial V}{\partial u_i^{l\alpha}}\right|_0 u_i^{l\alpha} + \frac{1}{2}\sum_{l\alpha,l'\alpha'}\sum_{ij} \left.\frac{\partial^2 V}{\partial u_i^{l\alpha}\partial u_j^{l'\alpha'}}\right|_0 u_i^{l\alpha}u_j^{l'\alpha'} \\ + \frac{1}{3!}\sum_{l\alpha,l'\alpha',l''\alpha''}\sum_{ijk} \left.\frac{\partial^3 V}{\partial u_i^{l\alpha}\partial u_j^{l'\alpha'}\partial u_k^{l''\alpha''}}\right|_0 u_i^{l\alpha}u_j^{l'\alpha'}u_k^{l''\alpha''} + \quad \ldots\ldots, \end{aligned} \tag{3.47}$$

where i, j and k are cartesian directions and V_0 is a constant which we may set to zero for convenience. Since the energy is zero at equilibrium, the first derivatives in the second term of Eq. (3.47) must all vanish. This leaves us

with two terms containing second and third derivatives of the crystal potential respectively. The second term is the harmonic contribution to the potential and has force constants defined by:

$$\Phi_{i,j}^{l\alpha,l'\alpha'} = \left.\frac{\partial^2 V}{\partial u_i^{l\alpha}\partial u_j^{l'\alpha'}}\right|_0. \tag{3.48}$$

The third order anharmonic terms result from the interaction of three vibrational modes and has a force constant defined by:

$$\Phi_{ijk}^{l\alpha,l'\alpha',l''\alpha''} = \left.\frac{\partial^3 V}{\partial u_i^{l\alpha}\partial u_j^{l'\alpha'}\partial u_k^{l''\alpha''}}\right|_0 \tag{3.49}$$

This allows us to re-write the crystal potential energy more compactly in terms of these force constants, yielding:

$$V = \underbrace{\frac{1}{2}\sum_{l\alpha,l'\alpha'}\sum_{ij}\Phi_{i,j}^{l\alpha,l'\alpha'}u_i^{l\alpha}u_j^{l'\alpha'}}_{V_{\text{harm}}} + \underbrace{\frac{1}{3!}\sum_{l\alpha,l'\alpha',l''\alpha''}\sum_{ijk}\Phi_{ijk}^{l\alpha,l'\alpha',l''\alpha''}u_i^{l\alpha}u_j^{l'\alpha'}u_k^{l''\alpha''}}_{V_{\text{anharm}}} + \quad \ldots\ldots \tag{3.50}$$

3.7.1 Dynamical matrix

The harmonic approximation treats a crystal as a system of independent harmonic oscillators that do not interact. The displacements corresponding to the harmonic potential V_{harm} can be expressed as a linear combination of decoupled normal vibrational modes. From elementary considerations we see that a crystal with N atoms and 3 spatial degrees of freedom will have $3N$ normal modes of vibration. The equation of motion for the system is:

$$m_\alpha\frac{\partial^2 u_i^{l\alpha}}{\partial t^2} = -\frac{\partial V_{\text{harm}}}{\partial u_i^{l\alpha}} = -\sum_{l'\alpha'}\sum_j \Phi_{ij}^{l\alpha,l'\alpha'}u_j^{l'\alpha'}. \tag{3.51}$$

The translational invariance of the force constants mean that they only depend on the relative displacement between unit cells. This allows us to re-write the equations of motion as:

$$m_\alpha\frac{\partial^2 u_i^{l\alpha}}{\partial t^2} = -\sum_{l'\alpha'}\sum_j \Phi_{ij}^{0\alpha,l-l'\alpha'}u_j^{l'\alpha'}. \tag{3.52}$$

We solve this equation with the anstaz that the solutions are plane waves of the form:

$$u_i^{l\alpha} = \frac{1}{\sqrt{m_\alpha}} \sum_{\mathbf{q}\lambda} e_{i\alpha}^{\lambda}(\mathbf{q}) e^{i(\mathbf{q}\cdot\mathbf{R}_l - \omega_{\mathbf{q}\lambda} t)}, \tag{3.53}$$

where $\omega_{\mathbf{q}\lambda}$ is the frequency of the vibrational mode with wavevector $\mathbf{q}$ and polarisation λ in the first Brillouin zone. $\mathbf{e}_\alpha^\lambda(\mathbf{q})$ is an eigenvector characterising the polarisation of the motion of atom α in mode λ. Substituting Eq. (3.53) into Eq. (3.52) yields:

$$\omega_{\mathbf{q}\lambda}^2 e_{i\alpha}^{\lambda}(\mathbf{q}) = \sum_{\alpha' j} D_{ij}^{\alpha\alpha'}(\mathbf{q}) e_{j\alpha'}^{\lambda}(\mathbf{q}), \tag{3.54}$$

where $D_{ij}^{\alpha\alpha'}(\mathbf{q})$ is the Dynamical matrix defined as:

$$D_{ij}^{\alpha\alpha'}(\mathbf{q}) = \frac{1}{\sqrt{m_\alpha m_{\alpha'}}} \sum_{l'} \Phi_{ij}^{0\alpha, l'\alpha'} e^{i\mathbf{q}\cdot\mathbf{R}_{l'}}. \tag{3.55}$$

Eq. (3.54) is an eigenvalue equation. We can find its eigenvalues by solving the secular equation:

$$\left| D_{ij}^{\alpha\alpha'}(\mathbf{q}) - \omega_{\mathbf{q}\lambda}^2 \delta_{ij}\delta_{\alpha\alpha'} \right| = 0 \tag{3.56}$$

This indicates that diagonalisation of the Dynamical matrix will yield the square of the normal mode frequencies, $\omega_{\mathbf{q}\lambda}^2$ and the normal mode eigenvectors $\mathbf{e}_\alpha^\lambda(\mathbf{q})$ for each $\mathbf{q}$. We refer to these normal modes of the harmonic crystal as phonon modes, with momentum $\mathbf{q}$ and branch index λ. For a system of N atoms, the phonon branch takes values $\lambda = 1, \ldots, 3N$.

These phonon eigenvectors form a complete, orthonormal basis for atomic motion within the crystal:

$$\sum_{\alpha i} e_{i\alpha}^{*\lambda}(\mathbf{q}) e_{i\alpha}^{\lambda'}(\mathbf{q}) = \delta_{\lambda\lambda'}, \tag{3.57}$$

$$\sum_{\lambda} e_{j\alpha'}^{*\lambda}(\mathbf{q}) e_{i\alpha}^{\lambda}(\mathbf{q}) = \delta_{ij}\delta_{\alpha\alpha'}. \tag{3.58}$$

We will now discuss the interaction between electrons and phonons and outline the main theoretical tools involved in treating this physical process.

3.8 Electron-phonon scattering

The interaction between electrons and phonons are responsible for a number of interesting and important phenomena in condensed matter and materials physics. For instance, they explain why the electronic band structure of materials change as a function of sample temperature [77, 78, 79], limit carrier mobility in semiconductors [80, 81] and provide the mechanism for conventional superconductivity [82, 83]. In the past, electron-phonon interactions have been calculated with empirical methods [84], frozen-phonon methods [85] or with the use of model Hamiltonians [86, 43]. However, the recent development of density functional perturbation theory (DFPT) has enabled the study, from first principles, of the coupling of electrons to phonons of arbitrary wavelength with primitive cell calculations (See Sec. 3.14). The computation of electron-phonon coupling matrix elements using DFPT is now possible using several standard electronic structure codes. (eg. Quantum Espresso [72] and ABINIT [74]). In sections 3.9-3.12 we will introduce the theory of electron-phonon scattering. These sections are primarily based on the following textbooks and reviews: [87, 88, 89, 90]. In section 3.13, we show how atomic forces can be computed from the diagonal part of the electron-phonon matrix. In section D, we outline the numerical implementation of electron-phonon rate equations and in section E.1 we compare electron-phonon matrix elements obtained in DFPT with those obtained using the frozen-phonon method. We will begin by introducing the Hamiltonian for the electron-phonon interaction.

3.9 Hamiltonian for electron-phonon interaction

Consider a large box containing N unit cells, each containing A atoms. An electron at the position $\mathbf{r}$, is acted upon by the Coulomb potentials of nuclei at positions $\{\mathbf{R}_{I\alpha}\} = \{\mathbf{R}_I + \tau_\alpha\}$, where $\{\mathbf{R}_I\}$ is the set of vectors pointing to each of the N unit cells and $\{\tau_\alpha\}$ is the set of vectors pointing from a reference point in each unit cell to the atomic positions in that cell. We write the self-consistent potential as $V(\mathbf{r}, \{\mathbf{R}_{I\alpha}\})$, to emphasise its parametric dependence on the ionic positions. Expanding this potential up to terms linear in the ionic coordinates we get:

$$V(\mathbf{r}, \{\mathbf{R}_{I\alpha}\}) \approx V\left(\mathbf{r}, \{\mathbf{R}^0_{I\alpha}\}\right) + \sum_{I\alpha} \nabla_{\mathbf{R}_{I\alpha}} V\left(\mathbf{r}, \{\mathbf{R}^0_{I\alpha}\}\right) \cdot \Delta\mathbf{R}_{I\alpha}, \tag{3.59}$$

where $\mathbf{R}^0_{I\alpha}$ and $\Delta\mathbf{R}_{I\alpha}$ are the equilibrium position and displacement of the α^{th} atom in unit cell I. The second term, summed over all electronic coordinates in the system gives the full electron-phonon Hamiltonian, H_{eph}. Second quantisation of the electronic coordinates allows us to express this sum as:

$$H_{\text{eph}} = \sum_{I\alpha} \Delta\mathbf{R}_{I\alpha} \cdot \sum_{\mathbf{k},\mathbf{k}'} \sum_{n,m} \frac{\langle m\mathbf{k}'|\nabla_{\mathbf{R}_{I\alpha}} V|n\mathbf{k}\rangle}{N} c^\dagger_{m\mathbf{k}'} c_{n\mathbf{k}} \tag{3.60}$$

where $\mathbf{k}$ and $\mathbf{k}'$ are the wavevectors of the electronic states, n and m are band indices, $c^\dagger_{m\mathbf{k}'}$ is the creation operator for the state $|m\mathbf{k}'\rangle$ and $c_{n\mathbf{k}}$ is the annihilation operator for the state $|n\mathbf{k}\rangle$. The electronic wavefunctions $\psi_{n\mathbf{k}}(\mathbf{r})$ are normalised to the unit cell volume *not* the volume of the overall system, hence the factor of $1/N$ in this sum.

The response of the potential to atomic displacement is invariant under translation by a lattice vector, allowing us to write

$$\nabla_{\mathbf{R}_{I\alpha}} V(\mathbf{r} + \mathbf{R}_I) = \nabla_{\mathbf{R}_{I\alpha} - \mathbf{R}_I} V(\mathbf{r}) = \nabla_{\tau_\alpha} V(\mathbf{r}), \tag{3.61}$$

where we omit explicit reference to the ionic coordinates $\{\mathbf{R}^0_{I\alpha}\}$ in the potential V. This enables us to simplify the matrix elements appearing in Eq. (3.60) as follows:

$$\langle m\mathbf{k}'|\nabla_{\mathbf{R}_{I\alpha}} V(\mathbf{r})|n\mathbf{k}\rangle = \int_{\mathbb{R}^3} \psi^*_{m\mathbf{k}'}(\mathbf{r}) \nabla_{\mathbf{R}_{I\alpha}} V(\mathbf{r})\, \psi_{n\mathbf{k}}(\mathbf{r}) \mathrm{d}^3 r \tag{3.62}$$

$$= \int_{\mathbb{R}^3} \psi^*_{m\mathbf{k}'}(\mathbf{r} + \mathbf{R}_I) \nabla_{\mathbf{R}_{I\alpha}} V(\mathbf{r} + \mathbf{R}_I)\, \psi_{n\mathbf{k}}(\mathbf{r} + \mathbf{R}_I) \mathrm{d}^3 r \tag{3.63}$$

$$= e^{-i\mathbf{k}'\cdot\mathbf{R}_I} e^{i\mathbf{k}\cdot\mathbf{R}_I} \int_{\mathbb{R}^3} \psi^*_{m\mathbf{k}'}(\mathbf{r}) \nabla_{\tau_\alpha} V(\mathbf{r})\, \psi_{n\mathbf{k}}(\mathbf{r}) \mathrm{d}^3 r \tag{3.64}$$

$$= e^{i(\mathbf{k}-\mathbf{k}')\cdot\mathbf{R}_I} \langle m\mathbf{k}'|\nabla_{\tau_\alpha} V(\mathbf{r})|n\mathbf{k}\rangle \tag{3.65}$$

Eq. (3.63) follows from equation (3.62) because the integral is taken over all space, so shifting all the functions by $\mathbf{R}_I$ does not affect the result. It is also clear that $\int_{\mathbb{R}^3} \mathrm{d}^3 r = \int_{\mathbb{R}^3} \mathrm{d}^3(r + \mathbf{R}_I)$ so I have eschewed the latter notation. Equation (3.64) follows from equation (3.63) using equation (3.61) along with Bloch's theorem (See Eq. (3.37)). Equation (3.65) follows trivially from (3.64). The

resulting matrix element in equation (3.65) depends only on the positions, $\boldsymbol{\tau}_\alpha$ of atoms within a particular unit cell.

It is useful for us to expand atomic displacements as a linear combination of the vibrational normal modes of the system. In these so-called normal coordinates, we can write the ionic displacements, $\Delta\mathbf{R}_{I\alpha}$ as follows:

$$\Delta\mathbf{R}_{I\alpha} = \frac{1}{\sqrt{NM_\alpha}} \sum_{\mathbf{q}\lambda} Q_{\mathbf{q}\lambda} \mathbf{e}_\alpha^{\mathbf{q}\lambda} e^{i\mathbf{q}\cdot\mathbf{R}_I}, \tag{3.66}$$

where $\mathbf{q}$ and λ denote phonon wavevector and branch index respectively. The associated phonon eigenvector, which specifies the polarisation of the vibrational mode, is denoted by $\mathbf{e}_\alpha^{\mathbf{q}\lambda}$ and $Q_{\mathbf{q}\lambda}$ are the expansion coefficients indicating the amplitude of each normal mode in the linear combination.

3.9.1 Quantising the Phonon Coordinates

Having expressed the atomic displacements in normal mode coordinates, the next step is to quantise the phonon coordinates. This can be done simply by representing each normal mode as a quantum harmonic oscillator. For each mode, λ we get:

$$H_\lambda = \frac{1}{2} \sum_{\mathbf{q}} P^*_{\mathbf{q}\lambda} P_{\mathbf{q}\lambda} + \omega^2_{\mathbf{q}\lambda} Q^*_{\mathbf{q}\lambda} Q_{\mathbf{q}\lambda} \tag{3.67}$$

where $P^*_{\mathbf{q}\lambda} = P_{-\mathbf{q}\lambda}$, $Q^*_{\mathbf{q}\lambda} = Q_{-\mathbf{q}\lambda}$ and $\omega^*_{\mathbf{q}\lambda} = \omega_{\mathbf{q}\lambda}$. Where, for that last equality I have used that in time-reversal symmetric systems $\omega_{-\mathbf{q}\lambda} = \omega_{\mathbf{q}\lambda}$. Factorising this Hamiltonian - for each value of $\mathbf{q}$ - we arrive at the standard definition for phonon creation and annihilation operators, $a^\dagger_{\mathbf{q}\lambda}$ and $a_{\mathbf{q}\lambda}$:

$$\begin{aligned} a^\dagger_{\mathbf{q}\lambda} &= \left(\frac{1}{2\hbar\omega_{\mathbf{q}\lambda}}\right)^{\frac{1}{2}} \left(\omega_{\mathbf{q}\lambda} Q^*_{\mathbf{q}\lambda} - iP_{\mathbf{q}\lambda}\right) \\ a_{\mathbf{q}\lambda} &= \left(\frac{1}{2\hbar\omega_{\mathbf{q}\lambda}}\right)^{\frac{1}{2}} \left(\omega_{\mathbf{q}\lambda} Q_{\mathbf{q}\lambda} + iP^*_{\mathbf{q}\lambda}\right). \end{aligned} \tag{3.68}$$

Rearranging these expressions allows us to express the normal mode amplitudes $Q_{\mathbf{q}\lambda}$ as a combination of these creation and annihilation operators as follows:

$$Q_{\mathbf{q}\lambda} = \left(\frac{\hbar}{2\omega_{\mathbf{q}\lambda}}\right)^{\frac{1}{2}} \left(a^\dagger_{-\mathbf{q}\lambda} + a_{\mathbf{q}\lambda}\right). \tag{3.69}$$

Combining equations (3.60), (3.65), (3.66) and (3.69) enables us to express the full quantum mechanical electron-phonon Hamiltonian as follows:

$$H_{\text{eph}} = \left(\frac{\hbar}{2N}\right)^{\frac{1}{2}} \sum_{\mathbf{q},\lambda} \frac{a^{\dagger}_{-\mathbf{q}\lambda} + a_{\mathbf{q}\lambda}}{\sqrt{\omega_{\mathbf{q}\lambda}}} \sum_{\mathbf{k},\mathbf{k}'} \sum_{n,m} c^{\dagger}_{m\mathbf{k}'} c_{n\mathbf{k}} \left(\sum_{\alpha} \frac{\mathbf{e}^{\mathbf{q}\lambda}_{\alpha}}{\sqrt{M_{\alpha}}} \cdot \langle m\mathbf{k}' | \nabla_{\tau_{\alpha}} V | n\mathbf{k} \rangle \right), \tag{3.70}$$

where we have used that:

$$\sum_{I} e^{i(\mathbf{k}-\mathbf{k}'+\mathbf{q})\cdot\mathbf{R}_I} = N \sum_{\mathbf{G}} \delta_{\mathbf{k}',\mathbf{k}+\mathbf{q}+\mathbf{G}} \quad \text{for} \quad \mathbf{G} \in \text{Reciprocal lattice}, \tag{3.71}$$

and that as long as we consider all possible pairs $\{\mathbf{k}, \mathbf{k}'\}$ in the first Brillouin zone, we need not explicitly distinguish between normal ($\mathbf{G} = 0$) and Umklapp ($\mathbf{G} \neq 0$) scattering. So we adopt the convention that $\mathbf{k}' - \mathbf{k}$ is folded into the first Brillouin zone and we unambiguously set $\mathbf{k}' = \mathbf{k} + \mathbf{q}$, by conservation of momentum. This enables us to rewrite the last sum on the r.h.s of equation (3.70) in the following way:

$$\sum_{\alpha} \frac{\mathbf{e}^{\mathbf{q}\lambda}_{\alpha}}{\sqrt{M_{\alpha}}} \cdot \langle m\mathbf{k}' | \nabla_{\tau_{\alpha}} V | n\mathbf{k} \rangle = \sum_{\alpha} \frac{\mathbf{e}^{\mathbf{q}\lambda}_{\alpha}}{\sqrt{M_{\alpha}}} \cdot \langle m\mathbf{k}+\mathbf{q} | \nabla_{\tau_{\alpha}} V | n\mathbf{k} \rangle \equiv g^{\mathbf{q}\lambda}_{\mathbf{k}nm}, \tag{3.72}$$

allowing us to re-express the full quantum mechanical electron-phonon Hamiltonian as follows:

$$H_{\text{eph}} = \left(\frac{\hbar}{2N}\right)^{\frac{1}{2}} \sum_{\mathbf{q},\lambda} \frac{1}{\sqrt{\omega_{\mathbf{q},\lambda}}} \left(a^{\dagger}_{-\mathbf{q}\lambda} + a_{\mathbf{q}\lambda}\right) \sum_{\mathbf{k}} \sum_{n,m} c^{\dagger}_{m\mathbf{k}+\mathbf{q}} c_{n\mathbf{k}} g^{\mathbf{q}\lambda}_{\mathbf{k}nm}. \tag{3.73}$$

The term $g^{\mathbf{q}\lambda}_{\mathbf{k}nm}$ is the matrix element representing scattering from state $|n\mathbf{k}\rangle$ to $|m\mathbf{k}+\mathbf{q}\rangle$ by the emission or absorption of a phonon of momentum $\mathbf{q}$ and branch index λ. Throughout this thesis, I calculate these matrix elements within the framework of DFPT (see Sec. 3.14). To validate this choice of method, I compare DFPT with the frozen-phonon approach for the coupling of the valence band at T to the conduction band at L in Bismuth via an X phonon in Sec. E.1.

3.10 Electronic scattering rate

Fermi's golden rule describes the transition rate from electronic state $|i\rangle$ to state $|f\rangle$ as a result of a weak periodic perturbation of the Hamiltonian, H' of

frequency ω:

$$R\left(i \to f\right) = \frac{2\pi}{\hbar} \left| \langle f|H'|i\rangle \right|^2 \delta\left(\varepsilon_f - \varepsilon_i \pm \hbar\omega\right). \tag{3.74}$$

We need to consider the action of the perturbing electron-phonon Hamiltonian on both the electrons and the phonons. For this reason, we adopt the notation of composite electron/phonon states in the occupation number representation. An electronic transition from a state with momentum $\mathbf{k}$, to one with momentum $\mathbf{k}+\mathbf{q}$, can either occur due to the absorption of a phonon of momentum $\mathbf{q}$ or emission of a phonon of momentum $-\mathbf{q}$. Thus, for phonon absorption, our initial composite state is $|i_a\rangle = |f_{m\mathbf{k}+\mathbf{q}}, f_{n\mathbf{k}}; n_{\mathbf{q},\lambda}\rangle$ and for emission it is $|i_e\rangle = |f_{m\mathbf{k}+\mathbf{q}}, f_{n\mathbf{k}}; n_{-\mathbf{q},\lambda}\rangle$. The final states are $|f_a\rangle = |f_{m\mathbf{k}+\mathbf{q}}+1, f_{n\mathbf{k}}-1, n_{\mathbf{q},\lambda}-1\rangle$ and $|f_e\rangle = |f_{m\mathbf{k}+\mathbf{q}}+1, f_{n\mathbf{k}}-1, n_{-\mathbf{q},\lambda}+1\rangle$ respectively. We will work out the matrix element $\langle f|c^\dagger_{m\mathbf{k}+\mathbf{q}}c_{n\mathbf{k}}(a^\dagger_{-\mathbf{q}\lambda}+a_{\mathbf{q}\lambda})|i\rangle$ in each case. In the case of scattering by the absorption of a phonon, the relevant product of fermion and boson creation and annihilation operators is $c^\dagger_{m\mathbf{k}+\mathbf{q}}c_{n\mathbf{k}}a_{\mathbf{q}\lambda}$. The matrix element formed by this product and the states $|i_a\rangle$, $|f_a\rangle$ is

$$\langle f_a|c^\dagger_{m\mathbf{k}+\mathbf{q}}c_{n\mathbf{k}}a_{\mathbf{q}\lambda}|i_a\rangle = \sqrt{(1-f_{m\mathbf{k}+\mathbf{q}})f_{n\mathbf{k}}n_{\mathbf{q}\lambda}}. \tag{3.75}$$

This gives us the relevant occupation factors for scattering from state $|n\mathbf{k}\rangle$ to state $|m\mathbf{k}+\mathbf{q}\rangle$ via the emission of a phonon in mode $|\mathbf{q}\lambda\rangle$. Note the emergence of the Pauli blocking factor $f_{n\mathbf{k}}(1-f_{m\mathbf{k}+\mathbf{q}})$, which prevents scattering into a full state or out of an empty state, in line with the Pauli exclusion principle. This scattering process obeys the following conservation of energy condition:

$$\varepsilon_{m\mathbf{k}+\mathbf{q}} - \varepsilon_{n\mathbf{k}} = \hbar\omega_{\mathbf{q}\lambda}. \tag{3.76}$$

which will be enforced by the usual delta function appearing in Fermi's golden rule. The other case is that of scattering by the emission of a phonon of the opposite momentum. This involves computing the matrix element:

$$\begin{aligned}\langle f_e|c^\dagger_{m\mathbf{k}+\mathbf{q}}c_{n\mathbf{k}}a^\dagger_{-\mathbf{q}\lambda}|i_e\rangle &= \sqrt{(1-f_{m\mathbf{k}+\mathbf{q}})f_{n\mathbf{k}}(n_{-\mathbf{q}\lambda}+1)} \\ &= \sqrt{(1-f_{m\mathbf{k}+\mathbf{q}})f_{n\mathbf{k}}(n_{\mathbf{q}\lambda}+1)},\end{aligned} \tag{3.77}$$

where I have used that $n_{-\mathbf{q}\lambda} = n_{\mathbf{q}\lambda}$, which follows from time-reversal symmetry. This scattering process obeys the following conservation of energy condition:

$$\varepsilon_{n\mathbf{k}} - \varepsilon_{m\mathbf{k}+\mathbf{q}} = \hbar\omega_{\mathbf{q}\lambda}. \tag{3.78}$$

Having worked out these matrix elements, we can now express the scattering rate from electronic state $|n\mathbf{k}\rangle$ to $|m\mathbf{k}+\mathbf{q}\rangle$ using Fermi's golden rule as follows:

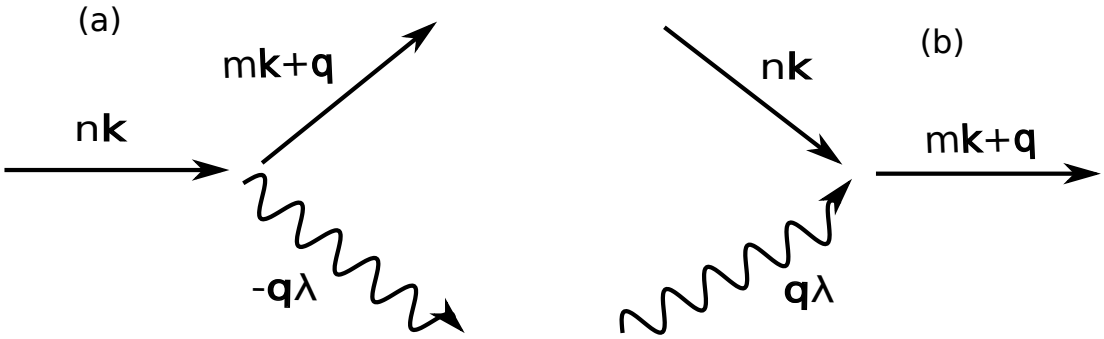

Figure 3.2: Feynman diagrams showing the allowed first order electron-phonon scattering processes. Scattering of an electron from state $|n\mathbf{k}\rangle$ to $|m\mathbf{k}+\mathbf{q}\rangle$ via (a): The emission of a phonon of momentum $-\mathbf{q}$ and polarisation λ or (b): The absorption of a phonon of momentum $\mathbf{q}$ and polarisation λ.

$$R_{\lambda}^{\pm}\left(n\mathbf{k}, m\mathbf{k}+\mathbf{q}\right) = \frac{\pi}{N}\frac{\left|g_{\mathbf{k}nm}^{\mathbf{q}\lambda}\right|^2}{\omega_{\lambda}(\mathbf{q})} f_{n\mathbf{k}}\left(1-f_{m\mathbf{k}+\mathbf{q}}\right)\left(n_{\mathbf{q},\lambda}+\frac{1}{2}\pm\frac{1}{2}\right)\delta^{\pm} \tag{3.79}$$

where the $+1/2$ term corresponds to scattering by phonon emission and the $-1/2$ term corresponds to scattering by phonon absorption (see Figs. 3.2 (a) and (b) respectively), and the energy conserving Dirac delta distributions are defined as follows:

$$\delta^{\pm} = \delta\left(\varepsilon_{m\mathbf{k}+\mathbf{q}} - \varepsilon_{n\mathbf{k}} \pm \hbar\omega_{\mathbf{q}\lambda}\right) \tag{3.80}$$

3.10.1 Change in electron and phonon occupations

To calculate the change in population of the electronic state $|n\mathbf{k}\rangle$ per unit time we must sum over contributions from scattering to and from all other electronic states $|m\mathbf{k}+\mathbf{q}\rangle$. We then sum over each of the phonon branches. The rate of change of occupation of state $|n\mathbf{k}\rangle$ is then:

$$\frac{\partial f_{n\mathbf{k}}}{\partial t} = \sum_{m\mathbf{q}\lambda\xi}\left[R_{\lambda}^{\xi}\left(m\mathbf{k}+\mathbf{q}, n\mathbf{k}\right) - R_{\lambda}^{\xi}\left(n\mathbf{k}, m\mathbf{k}+\mathbf{q}\right)\right], \tag{3.81}$$

where the integer ξ distinguishes between phonon emission and absorption.

Of course, electron-phonon scattering also affects the occupation of phonon modes $|\mathbf{q}\lambda\rangle$. We account for this by evaluating the difference between the number of phonons emitted and absorbed by electron-phonon scattering, summing over

initial and final electronic states which differ in momentum by $\mathbf{q}$:

$$\frac{\partial n_{\mathbf{q}\lambda}}{\partial t} = \sum_{\mathbf{k},n,m} \left[R^{+}_{\lambda} \left(m\mathbf{k}+\mathbf{q}, n\mathbf{k} \right) - R^{-}_{\lambda} \left(n\mathbf{k}, m\mathbf{k}+\mathbf{q} \right) \right]. \tag{3.82}$$

It should be noted that we neglect anharmonic phonon-phonon interactions here, and in principle these can play a significant role. However, in this thesis we are mostly interested in evolving these distributions for tens of femtoseconds to see the initial evolution of photo-induced atomic forces. These timescales are much shorter than the fastest phonon period in most systems and hence too short for anharmonic phonon-phonon coupling to significantly change phonon occupations.

3.11 Equilibrium lifetime of electronic state

A common approximation to Eq. (3.81) is to assign a time-independent relaxation time to each electronic state due to electron-phonon scattering. The electrons and phonons are initially in thermal equilibrium, we then perturb the occupation of a given state $|n\mathbf{k}\rangle$ from its equilibrium value $f^{0}_{n\mathbf{k}}$ by a small amount $\Delta f_{n\mathbf{k}}$ and ask how long it takes for the occupation of this state to decay back to its equilibrium value. (ie. $\Delta f_{n\mathbf{k}} \longrightarrow 0$). Since the occupations of states do not change in equilibrium, we know that $\frac{\partial f^{0}_{n\mathbf{k}}}{\partial t} = 0$. If we further assume that $\Delta f_{n\mathbf{k}}$ exponentially decays to 0, which is valid for sufficiently small perturbations $\Delta f_{n\mathbf{k}}$, we obtain:

$$\frac{\partial f_{n\mathbf{k}}}{\partial t} = \frac{\partial (\Delta f_{n\mathbf{k}})}{\partial t} = \Delta f_{n\mathbf{k}}(0) \frac{\partial}{\partial t} e^{-\frac{t}{\tau_{n\mathbf{k}}}} = -\frac{\Delta f_{n\mathbf{k}}}{\tau_{n\mathbf{k}}}, \tag{3.83}$$

where $\tau_{n\mathbf{k}}$ is the relaxation time of the state $|n\mathbf{k}\rangle$. Noting that $f_{m\mathbf{k}+\mathbf{q}}[(1-f^{0}_{n\mathbf{k}}) - \Delta f_{n\mathbf{k}}] = f_{m\mathbf{k}+\mathbf{q}}(1-f^{0}_{n\mathbf{k}}) - f_{m\mathbf{k}+\mathbf{q}}\Delta f_{n\mathbf{k}}$, we can separate out all of the terms from Eq. (3.79) and (3.81) which correspond to $\frac{\partial f^{0}_{n\mathbf{k}}}{\partial t}$ and set them to 0. This leaves us with:

$$\begin{aligned} -\frac{\Delta f_{n\mathbf{k}}}{\tau_{n\mathbf{k}}} = -\frac{\pi}{N} \sum_{\lambda m \mathbf{q}} \frac{\left| g^{\mathbf{q}\lambda}_{\mathbf{k}nm} \right|^2}{\omega_{\lambda\mathbf{q}}} \Big[& \Big\{ \Delta f_{n\mathbf{k}}(1-f_{m\mathbf{k}+\mathbf{q}}) n_{\lambda\mathbf{q}} + f_{m\mathbf{k}+\mathbf{q}} \Delta f_{n\mathbf{k}} (1+n_{\lambda\mathbf{q}}) \Big\} \delta^{+} \\ & + \Big\{ \Delta f_{n\mathbf{k}}(1-f_{m\mathbf{k}+\mathbf{q}})(1+n_{\lambda\mathbf{q}}) + f_{m\mathbf{k}+\mathbf{q}} \Delta f_{n\mathbf{k}} n_{\lambda\mathbf{q}} \Big\} \delta^{-} \Big]. \end{aligned} \tag{3.84}$$

Dividing both sides by $\Delta f_{n\mathbf{k}}$ and expanding the occupation factors yields:

$$\frac{1}{\tau_{n\mathbf{k}}} = \frac{\pi}{N}\sum_{\lambda m\mathbf{q}} \frac{\left|g^{\mathbf{q}\lambda}_{\mathbf{k}nm}\right|^2}{\omega_{\lambda\mathbf{q}}}\Big[(f_{m\mathbf{k}+\mathbf{q}} + n_{\lambda\mathbf{q}})\delta^+ + (1 - f_{m\mathbf{k}+\mathbf{q}} + n_{\lambda\mathbf{q}})\delta^-\Big]. \tag{3.85}$$

This expression for the equilibrium lifetime of electronic state $|n\mathbf{k}\rangle$ is related to the imaginary part of the electron self-energy due to electron-phonon scattering, which appears in the many-body Green's function approach, as follows: $2\,\mathrm{Im}\{\Sigma_{n\mathbf{k}}\}/\hbar = 1/\tau_{n\mathbf{k}}$.

3.12 Validity on short time scales

Eqs. (3.79) and (3.81) represent the collisional term in the semiclassical Boltzmann equation (scBE). They describe a scattering process which is Markovian (memoryless) and in which every scattering event conserves energy exactly. The equations are Markovian if the scattering rates at time t only depend on the electronic occupations at the same time t. This picture makes sense on long time scales, but is a limiting case of a more general non-Markovian equation which deviates significantly from the scBE on short time scales. This equation is the so-called quantum kinetic equation, which in the case of electron-phonon scattering can be written [90]:

$$\begin{aligned} R^{\pm}_{\lambda}\left(n\mathbf{k}, m\mathbf{k}+\mathbf{q}\right)(t) = \left|g^{\mathbf{q}\lambda}_{\mathbf{k}nm}\right|^2 \int_0^t \cos\Big(\Delta\varepsilon^{nm}_{\mathbf{kq}}(t-t')\Big) e^{-\gamma^{nm}_{\mathbf{kq}}(t-t')} \\ \times f_{n\mathbf{k}}(t')\left(1 - f_{m\mathbf{k}+\mathbf{q}}(t')\right)\left(n_{\mathbf{q},\lambda}(t') + \frac{1}{2} \pm \frac{1}{2}\right), \end{aligned} \tag{3.86}$$

where $\Delta\varepsilon^{nm}_{\mathbf{kq}} = \varepsilon_{m\mathbf{k}+\mathbf{q}} - \varepsilon_{n\mathbf{k}} \pm \hbar\omega_{\mathbf{q}\lambda}$ and $\gamma^{nm}_{\mathbf{kq}} = \gamma_{m\mathbf{k}+\mathbf{q}} + \gamma_{m\mathbf{k}+\mathbf{q}}$ is the sum of the inverse lifetimes of the initial and final states involved in the scattering. These lifetimes can be approximated by the equilibrium lifetimes as calculated within the relaxation time approximation (Sec. 3.11). Notice that in this equation, in order to calculate the scattering rate at time t, we need to have knowledge of the occupation functions at earlier times t'. This is the memory structure of the quantum kinetic equation and it conserves the system's total energy exactly, without imposing a delta function in energy for each scattering event.

However, the explicit numerical evaluation of this equation is extremely demanding for all but simple model systems [38], so we would like to approximate this by a Markovian equation. To do this, we need to make the following

approximations:

1. The memory depth of the memory kernel is extremely small, so that we can pull the occupation functions outside at time t. This is usually referred to as the limit of completed collisons.

2. We are at long times, compared with the lifetime of the states involved in the scattering i.e $\gamma^{nm}_{\mathbf{kq}} t \gg 1$.

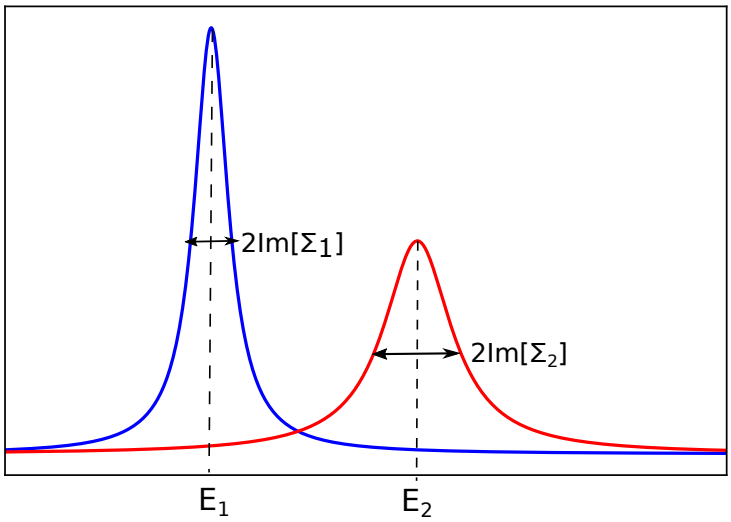

Figure 3.3: Illustration of energy conservation violation in a scattering event between states with energy E_1 and E_2 and linewidths $2\,\mathrm{Im}\{\Sigma_1\}$ and $2\,\mathrm{Im}\{\Sigma_2\}$. One can see that the uncertainty in energy of the initial and final state introduces an uncertainty in the energy difference between the two states.

Approximation 1 allows us to express Eq. (3.86) as:

$$R^{\pm}_{\lambda}\left(n\mathbf{k}, m\mathbf{k}+\mathbf{q}\right)(t) \approx \left|g^{\mathbf{q}\lambda}_{\mathbf{k}nm}\right|^2 f_{n\mathbf{k}}(t)\left(1-f_{m\mathbf{k}+\mathbf{q}}(t)\right)\left(n_{\mathbf{q},\lambda}(t)+\frac{1}{2}\pm\frac{1}{2}\right) \times \int_0^t \cos\Big(\Delta\varepsilon^{nm}_{\mathbf{kq}}(t-t')\Big)e^{-\gamma^{nm}_{\mathbf{kq}}(t-t')}. \tag{3.87}$$

Making use of the definition of $\cos x = (e^{ix}+e^{-ix})/2$, the integral in Eq. (3.87) is easily solved giving the following:

$$R^{\pm}_{\lambda}\left(n\mathbf{k}, m\mathbf{k}+\mathbf{q}\right)(t) \approx \left|g^{\mathbf{q}\lambda}_{\mathbf{k}nm}\right|^2 f_{n\mathbf{k}}(t)\left(1-f_{m\mathbf{k}+\mathbf{q}}(t)\right)\left(n_{\mathbf{q},\lambda}(t)+\frac{1}{2}\pm\frac{1}{2}\right) \times \frac{1}{2}\left[\frac{1-e^{(i\Delta\varepsilon^{nm}_{\mathbf{kq}}-\gamma^{nm}_{\mathbf{kq}})t}}{\gamma^{nm}_{\mathbf{kq}}-i\Delta\varepsilon^{nm}_{\mathbf{kq}}}+\frac{1-e^{(-i\Delta\varepsilon^{nm}_{\mathbf{kq}}-\gamma^{nm}_{\mathbf{kq}})t}}{\gamma^{nm}_{\mathbf{kq}}+i\Delta\varepsilon^{nm}_{\mathbf{kq}}}\right]. \tag{3.88}$$

Applying approximation 2, we arrive at a fully Markovian equation:

$$R_{\lambda}^{\pm}\left(n\mathbf{k}, m\mathbf{k}+\mathbf{q}\right)(t) \approx \left|g_{\mathbf{k}nm}^{\mathbf{q}\lambda}\right|^{2} f_{n\mathbf{k}}(t)\left(1-f_{m\mathbf{k}+\mathbf{q}}(t)\right)\left(n_{\mathbf{q},\lambda}(t)+\frac{1}{2}\pm\frac{1}{2}\right) \times \frac{\gamma_{\mathbf{kq}}^{nm}}{\left(\Delta\varepsilon_{\mathbf{kq}}^{nm}\right)^{2}+\left(\gamma_{\mathbf{kq}}^{nm}\right)^{2}}. \tag{3.89}$$

This equation is equivalent to the scBE, but with the energy conserving delta function replaced with a Lorentzian distribution taking into account the apparent violation of energy conservation when scattering between 2 states of finite lifetime. The heuristic explanation for this is that energy can not be perfectly conserved scattering between two states which have uncertain energies, as shown schematically in Fig. 3.3. However, the real reason why energy is not conserved in Eq. (3.89) is that we are imposing a Markovian structure on a physical system whose behaviour is non-Markovian on these timescales. In the real physical system, energy will be conserved on arbitrarily short timescales.

3.13 Atomic forces from electron-phonon matrix elements

Janak's theorem relates the DFT total energy, E_{DFT} to the energy and occupation of orbital $|n\mathbf{k}\rangle$ [67, 64]:

$$\frac{\partial E_{\text{DFT}}}{\partial f_{n\mathbf{k}}} = \varepsilon_{n\mathbf{k}} = \langle n\mathbf{k}|\hat{H}|n\mathbf{k}\rangle\,. \tag{3.90}$$

To first order in $\Delta f_{n\mathbf{k}}$, the change in the DFT total energy per unit cell is as follows:

$$\begin{aligned}\Delta E_{\text{DFT/cell}} &\approx \frac{1}{N}\sum_{n,\mathbf{k}}\Delta f_{n\mathbf{k}}\,\langle n\mathbf{k}|\hat{H}|n\mathbf{k}\rangle \\ &= \frac{1}{N}\sum_{n,\mathbf{k}}\left(f_{n\mathbf{k}}-f_{n\mathbf{k}}^{(0)}\right)\,\langle n\mathbf{k}|\hat{H}|n\mathbf{k}\rangle\end{aligned} \tag{3.91}$$

where $f_{n\mathbf{k}}^{(0)}$ is the equilibrium electronic occupation of the state $|n\mathbf{k}\rangle$ at the instantaneous temperature of the lattice and N is the number of unit cells in the system. If we are interested in short timescales (~ 10 fs), we can set $f_{n\mathbf{k}}^{(0)}$ equal to the initial equilibrium occupation of state $|n\mathbf{k}\rangle$ because the lattice temperature

will not change substantially over this timescale. The force $\mathbf{F}_\alpha$ on atom α is then:

$$\mathbf{F}_\alpha = -\nabla_{\boldsymbol{\tau}_\alpha}[\Delta E_{\text{DFT}}/\text{cell}] \tag{3.92}$$

$$= -\frac{1}{N}\sum_{n,\mathbf{k}} \nabla_{\boldsymbol{\tau}_\alpha}\left[\Delta f_{n\mathbf{k}} \langle n\mathbf{k}|\hat{H}|n\mathbf{k}\rangle\right] \tag{3.93}$$

$$\approx -\frac{1}{N}\sum_{n,\mathbf{k}} \Delta f_{n\mathbf{k}} \nabla_{\boldsymbol{\tau}_\alpha}\left[\langle n\mathbf{k}|\hat{H}|n\mathbf{k}\rangle\right] \tag{3.94}$$

If we assume that the single-particle states $|n\mathbf{k}\rangle$ are eigenstates of $\hat{H}$, then we can apply the Hellman-Feynman theorem [91]. This allows us to express the forces in terms of the diagonal electron-phonon matrix elements and the occupations of the electronic states:

$$\mathbf{F}_\alpha = -\frac{1}{N}\sum_{n,\mathbf{k}} \Delta f_{n\mathbf{k}} \langle n\mathbf{k}|\nabla_{\boldsymbol{\tau}_\alpha}\hat{H}|n\mathbf{k}\rangle\,. \tag{3.95}$$

This is a useful method for computing atomic forces, as it does not require a self-consistent calculation. However, in materials where there is a non-zero carrier density in equilibrium, the value we choose for $f^0_{n\mathbf{k}}$ can have a large effect on the atomic forces. [3]

3.14 Density functional perturbation theory

In this thesis, in addition to electronic band structure, we need to be able to calculate properties relating to phonons and their coupling to the electrons in the system from first-principles. Namely, we need to compute phonon frequencies $\omega_{\mathbf{q}\lambda}$ and electron-phonon coupling matrix elements $g^{\mathbf{q}\lambda}_{\mathbf{k}nm}$, as defined in Eq. (3.72). An extremely efficient method of computing these quantities is provided by density functional perturbation theory (DFPT) [60, 92].

DFPT combines DFT with standard quantum perturbation theory, extending the Kohn-Sham formalism to enable the *ab initio* calculation of derivatives of the total energy with respect to variations of some physical parameters of the system. Here, we outline the basic formalism of DFPT and show how it can be

[3] This is especially true for the high-symmetry forces, such as the force on the A_{1g} mode in Bi, Sb and As. For this reason, whenever we compute high-symmetry forces, we instead use constrained DFT. For low-symmetry forces, Eq. (3.95) is adequate, since only low-symmetry contributions to $f_{n\mathbf{k}}$ produce a non-zero force, and errors in choosing $f^0_{n\mathbf{k}}$ will usually be fully symmetric.

used to calculate phonon frequencies $\omega_{\mathbf{q}\lambda}$ and electron-phonon matrix elements $g^{\mathbf{q}\lambda}_{\mathbf{k}nm}$. For our purposes, we need to calculate derivatives of the total energy with respect to atomic displacements. However, for the sake of generality, we will initially treat the external potential acting on the electrons as a differentiable function of a set of parameters $\{\lambda_i\}$. When the potential is being perturbed by atomic displacements, we have that $\lambda_i = \boldsymbol{\tau}_{\boldsymbol{\alpha}}$. The Hellmann-Feynman theorem allows us to express the first and second derivatives of the total energy as:

$$\frac{\partial E}{\partial \lambda_i} = \int n_\lambda(\mathbf{r}) \frac{\partial V_\lambda(\mathbf{r})}{\partial \lambda_i} \mathrm{d}\mathbf{r}, \tag{3.96}$$

$$\frac{\partial^2 E}{\partial \lambda_i \partial \lambda_j} = \int n_\lambda(\mathbf{r}) \frac{\partial^2 V_\lambda(\mathbf{r})}{\partial \lambda_i \partial \lambda_j} \mathrm{d}\mathbf{r} + \int \frac{\partial n_\lambda(\mathbf{r})}{\partial \lambda_i} \frac{\partial V_\lambda(\mathbf{r})}{\partial \lambda_j} \mathrm{d}\mathbf{r}. \tag{3.97}$$

The solution of these equations requires computation of the ground state electron density $n_\lambda(\mathbf{r})$ and its linear response to a nuclear distortion $\partial n_\lambda(\mathbf{r})/\partial\lambda$. The first of these can be calculated from standard DFT, as outlined in the previous sections. To compute the latter, we first need to linearise Eq. (3.25) with respect to the Kohn-Sham orbitals $\psi_m(\mathbf{r})$, where m runs from 1 to the number of orbitals in the system. This is achieved by expanding both sides of the equation as a Taylor series in the set of variables $\{\lambda_i\}$ and then truncating at linear order. We arrive at the following equation:

$$\delta^\lambda n(\mathbf{r}) = 4\,\mathrm{Re} \sum_{n=1}^{N/2} \psi_n^*(\mathbf{r}) \delta^\lambda \psi_n(\mathbf{r}), \tag{3.98}$$

where δ^λ is an operator which computes the linear term of a Taylor series. We refer to it as a finite-difference operator, and it is defined as follows:

$$\delta^\lambda = \sum_i \frac{\partial}{\partial \lambda_i} \Delta\lambda. \tag{3.99}$$

Since both the unperturbed and perturbed external potential are real, the Kohn-Sham eigenvalues can be made real, allowing us to eschew the prescription of only keeping the real part of the sum in Eq. (3.98). We can use first order perturbation theory to re-write $\delta^\lambda \psi_m(\mathbf{r})$ in terms of the linear variation of the self-consistent potential $\delta^\lambda V_{\mathrm{KS}}$ as follows:

$$\delta^\lambda n(\mathbf{r}) = 4 \sum_{n=1}^{N/2} \sum_{m \neq n} \psi_n^*(\mathbf{r}) \psi_m(\mathbf{r}) \frac{\langle \psi_m | \delta^\lambda V_{\mathrm{KS}} | \psi_n \rangle}{\varepsilon_m - \varepsilon_n}. \tag{3.100}$$

The variation of the Kohn-Sham orbitals, $\delta^\lambda\psi_n$, is described by the so-called Sternheimer equation of first order perturbation theory:

$$(\hat{H}_{\text{KS}} - \varepsilon_n)\left|\delta^\lambda\psi_n\right\rangle = -(\delta^\lambda V_{\text{KS}} - \delta^\lambda\varepsilon_n)\left|\psi_n\right\rangle, \tag{3.101}$$

where $\langle\psi_n|\delta^\lambda\varepsilon_n|\psi_n\rangle$ is the first order variation of the Kohn-Sham eigenvalue due to the perturbing potential, and the first-order variation of the self consistent potential is given as:

$$\delta^\lambda V_{\text{KS}}(\mathbf{r}) = \delta^\lambda V_{\text{ext}}(\mathbf{r}) + e^2\int\frac{\delta^\lambda n(\mathbf{r}')}{|\mathbf{r}-\mathbf{r}'|}\mathrm{d}\mathbf{r}' + \left.\frac{dV_{\text{xc}}[n]}{dn}\right|_{n=n(\mathbf{r})}\delta^\lambda n(\mathbf{r}) \tag{3.102}$$

The set of Eqs. (3.98) - (3.102), form a self consistent system for the perturbed system which is analogous to the Kohn-Sham equations, Eqs. (3.29) and (3.25), for solving the ground state problem.

Since this approach yields the linear variation of the charge density $\partial n(\mathbf{r})/\partial\lambda$, it gives us everything we need to evaluate the mixed second derivatives of the total energy via Eq. (3.97), which gives us the dynamical matrix. Diagonalisation of the dynamical matrix then yields the phonon frequencies and eigenvectors as shown in Eq. (3.56).

In order to calculate the electron-phonon matrix elements, we wish to re-write Eq. (3.101) in terms of exclusively lattice periodic functions. This can be done by decomposing the perturbing potential into Fourier components:

$$\delta^\lambda V_{\text{KS}}(\mathbf{r}) = \sum_{\mathbf{q}}\delta^\lambda\tilde{V}^{\mathbf{q}}_{\text{KS}}(\mathbf{r})e^{i\mathbf{q}\cdot\mathbf{r}}, \tag{3.103}$$

and expressing the Kohn-Sham orbitals as Bloch waves $\psi_{n\mathbf{k}} \propto u_{n\mathbf{k}}e^{i\mathbf{k}\cdot\mathbf{r}}$, yielding the following equation:

$$(\hat{H}^{\mathbf{k}+\mathbf{q}}_{\text{KS}} - \varepsilon_n)\left|\delta^\lambda\psi_n\right\rangle = -\delta^\lambda\tilde{V}^{\mathbf{q}}_{\text{KS}}\left|u_{n\mathbf{k}}\right\rangle + \langle u_{n\mathbf{k}}|\delta^\lambda\tilde{V}^{\mathbf{0}}_{\text{KS}}|u_{n\mathbf{k}}\rangle_{\text{uc}}\left|u_{n\mathbf{k}}\right\rangle, \tag{3.104}$$

where $\hat{H}^{\mathbf{k}+\mathbf{q}}_{\text{KS}} = e^{-i(\mathbf{k}+\mathbf{q})\cdot\mathbf{r}}\hat{H}_{\text{KS}}e^{i(\mathbf{k}+\mathbf{q})\cdot\mathbf{r}}$ and the Dirac notation $\langle\ldots|\ldots|\ldots\rangle_{\text{uc}}$ refers to the usual inner product, with integration over a single unit cell rather than over all space. This equation gives us the perturbing potential acting on the wavefunctions $u_{n\mathbf{k}}$ for perturbations of arbitrary $\mathbf{q}$ in terms of quantities which can be computed within a single unit cell.

This is the power of DFPT, which unlike finite difference based approaches, enables the evaluation of a system's response to perturbations of arbitrary

wavelength with a primitive cell calculation. As such, calculations of phonon frequencies, eigenvectors and electron-phonon matrix elements of any phonon wavevector $\mathbf{q}$ can be performed, without having to resort to large supercell calculations, significantly reducing the computational load. For this reason, throughout this thesis, all phonon related quantities will be computed within the framework of DFPT.

3.14.1 Conventions within the ABINIT code

I will now describe a convention used by some first-principles codes, to express electron-phonon matrix elements calculated within DFPT. For example, the legacy code ABINIT has a post-processing tool called ANADDB which can, with some modifications, be used to access the electron-phonon matrix elements as computed in ABINIT [4]. If we denote the electron-phonon matrix element for moving atom τ in *reduced* direction α by $G^{\mathbf{q},\tau,\alpha}_{\mathbf{k},n,m}$, we can describe ANADDB's convention by first considering a quadratic form as follows:

$$\Xi^{\mathbf{q},\tau,\alpha,\kappa,\beta}_{\mathbf{k},n,m} = \pi \left\langle m\mathbf{k}+\mathbf{q}|\nabla_{\tau_\alpha}V|n\mathbf{k}\right\rangle \left\langle n\mathbf{k}|\nabla_{\kappa_\beta}V|m\mathbf{k}+\mathbf{q}\right\rangle = \pi G^{\mathbf{q},\tau,\alpha}_{\mathbf{k},n,m}\overline{G^{\mathbf{q},\kappa,\beta}_{\mathbf{k},n,m}} \quad (3.105)$$

Then for each fixed value of $\mathbf{k}$, $\mathbf{q}$, n , m we get (for 2 atoms per unit cell) a 6×6 matrix $\Gamma_{p,p'}$, where p is a composite index of τ,α and p' is a composite index of κ,β. For each fixed $\mathbf{q}$ we can also define a 6×6 matrix $U_{\lambda p}$ made up of the phonon displacement vectors of momentum $\mathbf{q}$. ANADDB then does the following:

$$\tilde{\Gamma}_{\lambda,\lambda'} = \sum_{p,p'} U_{\lambda p}\Gamma_{p,p'}\overline{U_{\lambda' p'}}. \quad (3.106)$$

For fixed $\mathbf{k}$, $\mathbf{q}$, n , m the diagonal elements $\tilde{\Gamma}_{\lambda=\lambda'}/\pi$ correspond to the squared electron-phonon matrix elements in normal mode coordinates, $\left|g^{\mathbf{q}\lambda}_{\mathbf{k}nm}\right|^2$ (see equation (3.72)).

[4] The name ABINIT references the first-principles (or **ab**-**init**io) nature of the calculations that it performs. The name ANADDB refers to the fact that it is used to **ana**lyse the **d**erivative **d**ata**b**ase (DDB); a large data structure containing the spatial derivatives of the total energy obtained within perturbation theory (DFPT).

3.15 Wannier interpolation

We have seen that DFPT can be used to evaluate electron-phonon matrix elements of arbitrary wavelength within a single unit cell. However, for our purposes we will need to perform double integrals over the Brillouin zone in electron and phonon momentum $\mathbf{k}$ and $\mathbf{q}$ respectively. In order to converge these integrals numerically, we will need to evaluate $g^{\mathbf{q}\lambda}_{nm\mathbf{k}}$ on reasonably fine $\mathbf{k}$ and $\mathbf{q}$ grids. Explicit evaluation of these matrix elements on a fine grid can be very computationally expensive. Fortunately, Marzari and Vanderbilt developed an extremely effective method of interpolating electronic structure quantities from a coarse grid to a finer grid using Maximally Localised Wannier functions (MLWF). This allows us to compute electronic energies, phonon frequencies and electron-phonon matrix elements on coarse grids, and inexpensively interpolate them to arbitrarily fine grids. In the following subsections, I will introduce the main concepts of MLWFs and how they are used for interpolation of electronic structure quantities. This section is largely based on the original paper on Maximally localised Wannier functions [93], and also on the later review [94]. For more details, consult these references.

3.15.1 Maximally localised Wannier functions

Electronic structure calculations are typically carried out with periodic boundary conditions. The invariance of the crystal under translation by a Bravais lattice vector means that the translation operator commutes with the system's Hamiltonian $[H, T_{\mathbf{R}}] = 0$. As a result, the eigenstates we obtain from an electronic structure are Bloch waves which satisfy:

$$\psi_{n\mathbf{k}} = \frac{1}{\sqrt{N_p}} u_{n\mathbf{k}} e^{i\mathbf{k}\cdot\mathbf{r}}, \tag{3.107}$$

where $u_{n\mathbf{k}}$ is a lattice-periodic function. An advantage of these Bloch waves are that they are localised in momentum, since they are eigenstates of H. The flip side of this coin is that Bloch waves are completely delocalised in space. By the same token, we can construct orbitals which are spatially localised, but they will not be eigenstates of H, as they will be delocalised in momentum. These functions are called Wannier functions, and we will now discuss their construction.

We will begin by considering the simplified case of an isolated band. This means that the band is separated in energy from all other bands for each value of electron momentum $\mathbf{k}$. Since Bloch functions of different electron wavevector have different envelope functions $e^{i\mathbf{k}\cdot\mathbf{r}}$, it is intuitively clear that we can construct a localised wave packet from a linear combination of Bloch functions. Since $\mathbf{k}$ resides in the periodic Brillouin zone, we can construct a Wannier function in the "home" unit cell as follows:

$$w_0(\mathbf{r}) = \frac{\Omega_0}{(2\pi)^3}\int_{\mathrm{BZ}} \psi_{n\mathbf{k}}(\mathbf{r})\mathrm{d}\mathbf{k}, \tag{3.108}$$

where Ω_0 is the real-space primitive cell volume. The integral is evaluated within the first Brillouin zone. More generally, a phase factor $e^{-i\mathbf{k}\cdot\mathbf{R}}$ can be inserted into Eq. (3.108). Since phase factors in momentum space produce translations in real space, this has the affect of translating the "home" cell Wannier function into other unit cells. Switching to Dirac's bra-ket notation, we can express the Wannier function for band n in unit cell $\mathbf{R}$ as:

$$|\mathbf{R}n\rangle = \frac{\Omega_0}{(2\pi)^3}\int_{\mathrm{BZ}} e^{-i\mathbf{k}\cdot\mathbf{R}}\,|\psi_{n\mathbf{k}}\rangle\,\mathrm{d}\mathbf{k}. \tag{3.109}$$

The Wannier functions satisfy orthonormality $\langle\mathbf{R}'m|\mathbf{R}n\rangle = \delta_{nm}\delta(\mathbf{R}'-\mathbf{R})$ and can be transformed into one another by translation through the vector $\mathbf{R}'-\mathbf{R}$. It is clear that Eq. (3.109) is a Fourier transform from momentum space to real space. The inverse transform maps Wannier functions to Bloch functions and is written as follows:

$$|\psi_{n\mathbf{k}}\rangle = \sum_{\mathbf{R}} e^{i\mathbf{k}\cdot\mathbf{R}}\,|\mathbf{R}n\rangle\,. \tag{3.110}$$

Thus, any of the Bloch functions can be constructed as a superposition of Wannier functions with appropriate phases $e^{i\mathbf{k}\cdot\mathbf{r}}$. Eqs. (3.109) and (3.110) constitute unitary transformations between Bloch and Wannier states. As such, both sets of functions provide equally valid descriptions of the states within the isolated band under consideration, which we will refer to as the band subspace. Another way to show the equivalence between the Wannier and Bloch representations is to show the band projection operator as expressed in both pictures:

$$P = \frac{\Omega_0}{(2\pi)^3}\int_{\mathrm{BZ}} |\psi_{n\mathbf{k}}\rangle\,\langle\psi_{n\mathbf{k}}|\,\mathrm{d}\mathbf{k} = \sum_{\mathbf{R}} |\mathbf{R}n\rangle\,\langle\mathbf{R}n|\,. \tag{3.111}$$

This operator takes an arbitrary state and projects it onto the n^{th} band. Therefore, it is clear that Wannier functions both carry the same information as Bloch func-

tions, and are localised in space. As such, they are an attractive option for many applications such as visualising bonding, construction of model Hamiltonians and, as I will focus on here, interpolation of electronic structure quantities.

3.15.2 Gauge freedom

The construction of Wannier functions is greatly impacted by the fact that Bloch functions exhibit a gauge freedom. We can replace

$$\left|\tilde{\psi}_{n\mathbf{k}}\right\rangle = e^{i\varphi_n(\mathbf{k})}\left|\psi_{n\mathbf{k}}\right\rangle \tag{3.112}$$

$$\Rightarrow \quad \left|\tilde{u}_{n\mathbf{k}}\right\rangle = e^{i\varphi_n(\mathbf{k})}\left|u_{n\mathbf{k}}\right\rangle \tag{3.113}$$

without changing any physical properties of the system under study. The phase $\varphi_n(\mathbf{k})$ can be any real valued function which is periodic in reciprocal space. A particularly useful choice of gauge for us is to impose that $\nabla_{\mathbf{k}} u_{n\mathbf{k}}$ is well defined for all wavevectors $\mathbf{k}$. Such gauges are referred to as *smooth*, and will tend to produce localised Wannier functions, since smoothness in Fourier space reflects localisation in real space.

This is an important consideration because the gauge indeterminacy in Bloch functions can lead to the corresponding wavefunctions having different shapes and spreads. Therefore, ensuring smoothness in the gauge of the Bloch functions is crucial for us to obtain well localised Wannier functions.

3.15.3 Generalisation to multiple bands

We now generalise to the more realistic situation of a manifold $\mathbb{M}$ of J bands which are well separated in energy from higher and lower lying bands outside $\mathbb{M}$. We allow the bands within the manifold to be degenerate with each other and to cross one another. Traces over the states within $\mathbb{M}$ are invariant under unitary transformations among the J bands at any wavevector $\mathbf{k}$. Therefore, we may generalise the notion of a gauge transformation to the action of a unitary matrix $U^{\mathbf{k}}_{mn}$ of dimension J which is periodic in reciprocal space:

$$\left|\tilde{\psi}_{n\mathbf{k}}\right\rangle = \sum_{m=1}^{J} U^{\mathbf{k}}_{mn}\left|\psi_{m\mathbf{k}}\right\rangle . \tag{3.114}$$

The gauge transformation described in Eq. (3.113) then corresponds to the diagonal part of the unitary matrix $U^{\mathbf{k}}_{nn}$. We see that the projection operator onto $\mathbb{M}$ at wavevector $\mathbf{k}$ is gauge invariant

$$P_{\mathbf{k}} = \sum_{n=1}^{J} \left|\tilde{\psi}_{n\mathbf{k}}\right\rangle \left\langle\tilde{\psi}_{n\mathbf{k}}\right| = \sum_{n=1}^{J} \left|\psi_{n\mathbf{k}}\right\rangle \left\langle\psi_{n\mathbf{k}}\right| \tag{3.115}$$

despite the fact that $\left|\tilde{\psi}_{n\mathbf{k}}\right\rangle$ is no longer an energy eigenstate and n is no longer a true band index.

This generalisation to the multiband case poses a major problem in terms of constructing Wannier functions. Namely, degeneracies within the manifold $\mathbb{M}$ mean that $\nabla_{\mathbf{k}} u_{n\mathbf{k}}$ is not well defined for all wavevectors $\mathbf{k}$, leading to a non-smooth gauge and thus Wannier functions which are not well localised. Fortunately, the introduction of the unitary transformations $U^{\mathbf{k}}_{mn}$ provides a solution to this issue. Applying a suitable choice of $U^{\mathbf{k}}_{mn}$ to the states within $\mathbb{M}$ can remove these discontinuities in $\nabla_{\mathbf{k}} u_{n\mathbf{k}}$ such that smoothness of gauge is ensured. Thus, we modify the construction of Wannier functions in Eq. (3.109) as follows:

$$|\mathbf{R}n\rangle = \frac{\Omega_0}{(2\pi)^3} \int_{\mathrm{BZ}} e^{-i\mathbf{k}\cdot\mathbf{R}} \left[\sum_{m=1}^{J} U^{\mathbf{k}}_{mn} \left|\psi_{m\mathbf{k}}\right\rangle\right] \mathrm{d}\mathbf{k}. \tag{3.116}$$

The choice of $U^{\mathbf{k}}_{mn}$ is still somewhat non-unique. We will address this by requiring our Wannier functions to be "Maximally localised". To do this we need to introduce a method by which we can define the degree of localisation of a Wannier functional:

3.15.4 The spread functional in real space

To describe the total delocalisation or spread of the Wannier functions, we introduce the following functional:

$$\Omega = \sum_{n} \left[\left\langle r^2\right\rangle_n - \left\langle r\right\rangle_n^2\right] \tag{3.117}$$

We then construct maximally localised Wannier functions by minimising Ω with respect to the unitary transformations $U^{\mathbf{k}}_{mn}$. There are other ways to construct localised Wannier functions, but for reasons which I will not explain here, we will follow the method of minimising Ω. It is worth noting that a similar functional appears in chemistry as one possible criterion for construction of "localised

molecular orbitals": the Foster-Boys scheme [95]. The spread functional can be decomposed into 2 terms:

$$\Omega = \Omega_I + \tilde{\Omega}, \tag{3.118}$$

where the two terms on the right hand side of Eq. (3.118) are defined as follows:

$$\Omega_I = \sum_n \left[\left\langle r^2 \right\rangle_n - \sum_{\mathbf{R}m} |\left\langle \mathbf{R}m|r|\mathbf{0}n\right\rangle|^2 \right], \tag{3.119}$$

$$\tilde{\Omega} = \sum_n \sum_{\mathbf{R}m\neq\mathbf{0}n} |\left\langle \mathbf{R}m|r|\mathbf{0}n\right\rangle|^2. \tag{3.120}$$

The second term $\tilde{\Omega}$ is a sum over $|\ldots|^2$ terms, so is clearly positive definite. Though less obvious, it may also be shown that Ω_I is positive definite, moreover it is gauge-invariant, meaning that it does not depend on the choice of unitary transformation among the bands $U^{\mathbf{k}}_{mn}$. Thus, the minimisation of Ω will be achieved through the minimisation of $\tilde{\Omega}$ only.

At the minimum of Ω, the off-diagonal matrix elements $|\left\langle \mathbf{R}m|r|\mathbf{0}n\right\rangle|^2$ are each as small as possible, giving the best compromise in the simultaneous diagonalisation, within the subspace of Bloch bands considered, of the position operators in each direction x, y and z, which are in general non-commuting when projected on to such a subspace.

3.15.5 Reciprocal space representation

The position operator can be written in reciprocal space as $i\nabla_{\mathbf{k}}$. This means that we can express the required matrix elements in terms of Bloch states as follows:

$$\left\langle \mathbf{R}n|\mathbf{r}|\mathbf{0}m\right\rangle = i\frac{\Omega_0}{(2\pi)^3}\int e^{i\mathbf{k}\cdot\mathbf{R}}\left\langle u_{n\mathbf{k}}|\nabla_{\mathbf{k}}|u_{m\mathbf{k}}\right\rangle \mathrm{d}\mathbf{k}, \tag{3.121}$$

and

$$\left\langle \mathbf{R}n|r^2|\mathbf{0}m\right\rangle = -\frac{\Omega_0}{(2\pi)^3}\int e^{i\mathbf{k}\cdot\mathbf{R}}\left\langle u_{n\mathbf{k}}|\nabla^2_{\mathbf{k}}|u_{m\mathbf{k}}\right\rangle \mathrm{d}\mathbf{k}. \tag{3.122}$$

These expressions permit us to express the spread functional Ω in terms of the matrix elements of $\nabla_{\mathbf{k}}$ and $\nabla^2_{\mathbf{k}}$, allowing us to compute the effects of localisation of a given unitary transformation without needing to recalculate expensive scalar products. We can evaluate the above reciprocal space derivatives using a finite

difference method,

$$\nabla f(\mathbf{k}) = \sum_{\mathbf{b}} w_b \mathbf{b}[f(\mathbf{k}+\mathbf{b}) - f(\mathbf{k})] + \mathcal{O}(b^2), \tag{3.123}$$

and

$$\nabla^2 f(\mathbf{k}) = \sum_{\mathbf{b}} w_b b^2[f(\mathbf{k}+\mathbf{b}) - f(\mathbf{k})]^2 + \mathcal{O}(b^3), \tag{3.124}$$

calculated for shells of near-neighbour points surrounding the wavevectors $\mathbf{k}$. The vector $\mathbf{b}$ connects the $\mathbf{k}$-point with its neighbours and w_b is a weighting term which depends on the geometry of the near-neighbour shells.

This finite difference method allows us to compute the matrix elements required for evaluating $\langle r^2 \rangle_n$ and $\langle r \rangle_n^2$, which enables the expression of the spread functional in terms of the overlap matrix elements $M_{nm}^{\mathbf{kb}} = \langle u_{m\mathbf{k}} | u_{n\mathbf{k}+\mathbf{b}} \rangle$ as follows:

$$\Omega_I = \frac{1}{N} \sum_{\mathbf{k},\mathbf{b}} w_b \left(J - \sum_{m,n} \left| M_{nm}^{\mathbf{kb}} \right|^2 \right) \tag{3.125}$$

and

$$\tilde{\Omega} = \frac{1}{N} \left[\sum_{\mathbf{k},\mathbf{b}} w_b \sum_{m \neq n} \left| M_{nm}^{\mathbf{kb}} \right|^2 + \sum_{\mathbf{k},\mathbf{b}} w_b \sum_{n} \left(- \operatorname{Im}\{\ln M_{nm}^{\mathbf{kb}}\} - \mathbf{b} \cdot \langle \mathbf{r} \rangle_n \right)^2 \right]. \tag{3.126}$$

This means that once the overlaps $\mathbf{M}_{nm}^{\mathbf{kb}}$ have been computed, no further interaction with an electronic structure code is necessary. As a result, Wannier interpolation is electronic structure method-independent. All that remains is to minimise the non-gauge invariant component of the spread functional $\tilde{\Omega}$ with respect to unitary transformations $U_{mn}^{\mathbf{k}}$.

This minimisation procedure is carried out by changing the unitary transformation by a small amount $U_{mn}^{\mathbf{k}} \longrightarrow U_{mn}^{\mathbf{k}} + \delta W_{mn}^{\mathbf{k}}$, step-by-step. These changes proceed in the direction of steepest descent until $\tilde{\Omega}$ has been minimised. For more details of the minimisation procedure, see Ref. [94].

3.15.6 Entangled bands

The methods for obtaining MLWFs described above were derived under the assumption that the group of bands of interest were isolated in energy from all other bands throughout the Brillouin zone. However, in many cases, the bands of interest are not isolated. In these cases, the desired bands lie within a

fixed energy range, but overlap and hybridise with other, unwanted bands which extend further up (or down) in energy. We refer to these bands as *entangled*.

In the case of isolated bands our task was to select a gauge which would produce optimally smooth Bloch functions $|\tilde{u}_{n\mathbf{k}}\rangle$ and hence maximally localised Wannier functions $|\mathbf{R}n\rangle$. However, for entangled bands we must first select a J-dimensional Bloch subspace which varies smoothly in $\mathbf{k}$-space. As shown in Eq. (3.118), the spread functional can be decomposed into a gauge-invariant component Ω_I and a gauge-dependent component $\tilde{\Omega}$. Since Ω_I is gauge-invariant, it is not important for the selection of an optimally smooth gauge. However, since it is a part of the spread functional, it must describe $\mathbf{k}$-space smoothness in some other sense. As it turns out, Ω_I is a measure of the *intrinsic* smoothness of the underlying Hilbert space. To see this, we re-express Eq. (3.125) as

$$\Omega_I = \frac{1}{N}\sum_{\mathbf{k},\mathbf{b}} w_b \mathcal{T}_{\mathbf{kb}} \tag{3.127}$$

with

$$\mathcal{T}_{\mathbf{kb}} = \mathrm{Tr}[P_{\mathbf{k}} Q_{\mathbf{k}+\mathbf{b}}] \tag{3.128}$$

where $P_{\mathbf{k}} = \sum_{n=1}^{J} |\tilde{u}_{n\mathbf{k}}\rangle\langle\tilde{u}_{n\mathbf{k}}|$ is the projector onto the Bloch subspace at wavevector $\mathbf{k}$ and $Q_{\mathbf{k}} = \mathbb{I} - P_{\mathbf{k}}$, where $\mathbb{I}$ is the identity operator. The quantity $\mathcal{T}_{\mathbf{kb}}$ measures the degree of mismatch between Bloch subspaces at neighbouring points $\mathbf{k}$ and $\mathbf{k}+\mathbf{b}$. Since Ω_I is a weighted sum of $\mathcal{T}_{\mathbf{kb}}$ over the Brillouin zone, we say that Ω_I corresponds to the average mismatch between neighbouring subspaces. Thus, minimisation of Ω_I would result in the smoothest possible subspace selection as a function of $\mathbf{k}$.

Therefore, the procedure for selection of an optimally smooth Bloch subspace is as follows:

1. A set of $\mathcal{J}_{\mathbf{k}} \geq J$ Bloch functions is identified at each $\mathbf{k}$-point in the Brillouin zone. This is typically given by a range of energies or bands, and is referred to as the "disentanglement window".

2. An iterative procedure is then employed to identify self-consistently at each $\mathbf{k}$-point the J-dimensional Bloch subspace that, when integrated over the Brillouin zone, will give the smallest value of Ω_I.

This procedure will yield the smoothest possible Bloch subspace, as a function of $\mathbf{k}$. The process of choosing the optimally smooth Bloch subspace essentially amounts to a linear transformation from $\mathcal{J}_{\mathbf{k}}$ initial eigenstates to J smooth

Bloch-like states as follows:

$$\left|\tilde{\psi}_{n\mathbf{k}}\right\rangle = \sum_{m=1}^{\mathcal{J}_{\mathbf{k}}} \left|\psi_{m\mathbf{k}}\right\rangle V_{\mathbf{k},mn}. \tag{3.129}$$

This algorithm can be modified so that a certain subset of states within the disentanglement window are preserved identically. This subset can also be specified as a range of bands or energies, and is commonly referred to as the "frozen window". Often, successful interpolation of electronic structure quantities can hinge on choosing suitable disentanglement and frozen windows.

One of the major uses of Maximally localised Wannier functions is for efficient interpolation of various electronic and phonon quantities. The method is extremely useful in situations where a quantity is required on a fine grid. In these cases, it is often impractical to compute these quantities directly on such a fine grid. One such example is that of electron-phonon matrix elements. The computation of these matrix elements directly from DFPT is extremely heavy for all but relatively coarse grids. However, interpolating these matrix elements from a coarse grid to a fine grid using MLWFs in very efficient.

I will now introduce the theory of Wannier interpolation, beginning with the interpolation of electronic band structure and then going on to explain the interpolation of electron-phonon matrix elements.

3.15.7 Interpolation of electronic band structure

The Wannier interpolation procedure is shown schematically in Fig. 3.4. The first principles calculation is carried out on a relatively coarse uniform BZ grid, where the quantity of interest $f(\mathbf{q})$ is evaluated in terms of Bloch states. These states are then transformed into Wannier functions, which transforms the function into real space in the Wannier representation: $f(\mathbf{q}) \longrightarrow F(\mathbf{R})$. The localisation of the Wannier functions ensure that the function $F(\mathbf{R})$ decays rapidly with increasing $|\mathbf{R}|$. Thus we have a short-range real-space representation allowing the quantity f to be interpolated onto an arbitrarily fine grid $f(\mathbf{k})$. This method will correctly capture variations in $f(\mathbf{k})$ over reciprocal distances shorter than Δq provided that the linear dimensions of the equivalent real-space supercell $L = 2\pi/\Delta q$ are significantly larger than the decay lengths of the Wannier functions. The simplest quantity to interpolate using Wannier functions is the electronic band structure. We will briefly describe the procedure here. If we have a set of Wannier functions

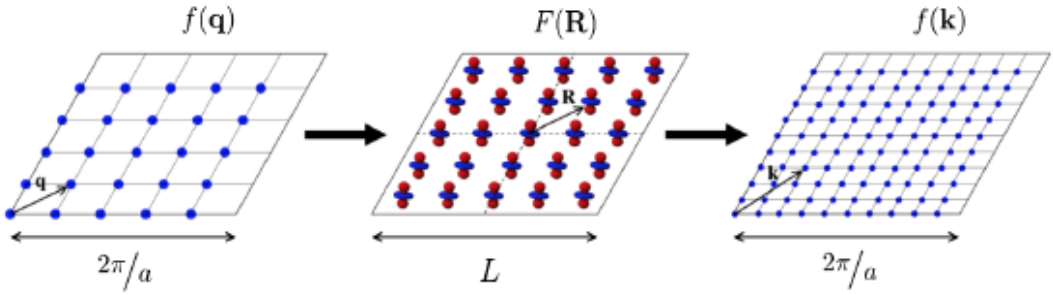

Figure 3.4: Schematic of the Wannier interpolation procedure. The left panel shows the coarse BZ grid on which the function $f(\mathbf{q})$ is explicitly calculated. The middle panel shows the resulting function $F(\mathbf{R})$ in real-space following a Wannier transform. Due to the localisation process, the function $F(\mathbf{R})$ is strongly localised at the lattice points,. The right panel shows the quantity $f(\mathbf{q})$ following an inverse Wannier transform onto a much finer grid in the BZ. Figure reproduced from Ref. [94]

which span a Bloch subspace of J bands, we can construct Bloch-like states as follows:

$$\left|\psi^W_{n\mathbf{k}}\right\rangle = \sum_{\mathbf{R}} e^{i\mathbf{k}\cdot\mathbf{R}} \left|\mathbf{R}n\right\rangle \quad \text{for} \quad (n = 1, \ldots, J), \tag{3.130}$$

where the W superscript indicates that the Bloch functions are not in general eigenstates of the Hamiltonian. We shall refer to them as belonging to the Wannier gauge. We can define a non-diagonal Hamiltonian matrix as follows:

$$H^W_{\mathbf{k}nm} = \left\langle \psi^W_{n\mathbf{k}} \middle| H \middle| \psi^W_{m\mathbf{k}} \right\rangle = \sum_{\mathbf{R}} e^{i\mathbf{k}\cdot\mathbf{R}} \left\langle \mathbf{0}n \middle| H \middle| \mathbf{R}m \right\rangle . \tag{3.131}$$

One can diagonalise this matrix to evaluate the interpolated eigenstate energies $\tilde{\varepsilon}_{n\mathbf{k}}$:

$$H^H_{\mathbf{k}nm} = [U^\dagger_{\mathbf{k}} H^W_{\mathbf{k}} U_{\mathbf{k}}]_{nm} = \delta_{nm}\tilde{\varepsilon}_{n\mathbf{k}}. \tag{3.132}$$

We now drop the explicit band notation and consider matrix multiplication to be implicit. We then find that Eq. (3.132) gives us the transformation law for Bloch states:

$$\left|\psi^H_{\mathbf{k}}\right\rangle = \left|\psi^W_{\mathbf{k}}\right\rangle V_{\mathbf{k}}, \tag{3.133}$$

where $V_{\mathbf{k}}$ is the unitary matrix defined in Eq. (3.129). If we insert a wavevector from the first principles grid into Eqs. (3.131) and (3.132), we get the original first principles eigenstate energies. However, in principle we can insert arbitrary $\mathbf{k}$, resulting in eigenstate energies which interpolate smoothly between the first principles values. As a result, once the matrix elements $\langle \mathbf{0}|H|\mathbf{R}\rangle$ are known, the band structure can be computed very inexpensively by Fourier transforming and diagonalising this matrix. The matrix elements are themselves acquired by

inversion of Eq. (3.131) as follows:

$$\langle \mathbf{0}|H|\mathbf{R}\rangle = \frac{1}{N}\sum_{\mathbf{q}} e^{-i\mathbf{q}\cdot\mathbf{R}} \left\langle \psi^W_{\mathbf{q}} \middle| H \middle| \psi^W_{\mathbf{q}} \right\rangle , \tag{3.134}$$

where N is the number of grid points. The calculation of electronic band structure by Wannier interpolation is extremely accurate. The exponential localisation of the Wannier functions within the periodic supercell, means that the magnitude of the matrix elements $\langle \mathbf{0}|H|\mathbf{R}\rangle$ decrease very rapidly with increasing $|\mathbf{R}|$. Since the number of lattice vectors included in the summation in Eq. (3.131) is the same as the number of first-principles grid points, we see that beyond a certain density of first-principles grid points, the error incurred by interpolation decreases exponentially.

3.15.8 Interpolation of electron-phonon matrix elements.

The main motivation for us to utilise Wannier interpolation in this thesis, is for the efficient interpolation of electron-phonon matrix elements. We recall that the electron-phonon matrix element for scattering of an electron from state $|\psi_{n\mathbf{k}}\rangle$ to $|\psi_{m\mathbf{k+q}}\rangle$ by the emission or absorption of a phonon from the mode of wavevector $\mathbf{q}$ and branch λ is:

$$g^{\mathbf{q}\lambda}_{\mathbf{k}nm} = \langle \psi_{m\mathbf{k+q}} | \partial_{\mathbf{q}\lambda} V | \psi_{n\mathbf{k}} \rangle , \tag{3.135}$$

where $\partial_{\mathbf{q}\lambda} V$ is the derivative of the self-consistent potential with respect to displacement of the phonon mode $|\mathbf{q}\lambda\rangle$. Evaluation of these matrix elements is the main computational bottleneck to the first-principles treatment of electron-phonon interactions and scattering. This is primarily due to the dependence of these matrix elements on both the electronic and phonon wavevectors $\mathbf{k}$ and $\mathbf{q}$. Thus calculations of $g^{\mathbf{q}\lambda}_{\mathbf{k}nm}$ scale with BZ mesh density as the product of the number of $\mathbf{k}$ and $\mathbf{q}$ points $N_{\mathbf{k}}N_{\mathbf{q}}$.

It should be noted that the Wannier interpolation of electronic bands and the Fourier interpolation of phonon dispersions share a degree of similarity. This suggests the possibility of interpolating electron-phonon matrix elements in both the electron and phonon momenta [96]. The pre-requisite, of course, is the computation of $g^{\mathbf{q}\lambda}_{\mathbf{k}nm}$ on a relatively course grid using DFPT or some other first-principles method.

We begin by defining some notation for the lattice dynamics. We write the instantaneous nuclear positions as $\mathbf{R} + \boldsymbol{\tau}_\alpha + \mathbf{u}_{\mathbf{R}\alpha}(t)$, where $\mathbf{R}$ is the Bravais

lattice vector, $\boldsymbol{\tau}_\alpha$ is the vector joining the position of nucleus $\alpha \in \{1, \ldots, A\}$ to the reference point within its unit cell and $\mathbf{u}_{\mathbf{R}\alpha}(t)$ denotes the instantaneous displacement due to phonon motion. The normal modes can then be written in the following form:

$$u^{\mathbf{q}\lambda}_{\mathbf{R}\alpha}(t) = \mathbf{u}^{\mathbf{q}\lambda}_{\alpha} e^{i(\mathbf{q}\cdot\mathbf{R} - \omega_{\mathbf{q}\lambda}t)}, \tag{3.136}$$

where $\mathbf{u}^{\mathbf{q}\lambda}_{\alpha}$ is the mode amplitude vector of mode $|\mathbf{q}\lambda\rangle$, which is obtained as the product of the mode eigenvector with the amplitude of the mode. Both the phonon frequencies $\omega_{\mathbf{q}\lambda}$ and the mode amplitude vectors are obtained by diagonalisation of the dynamical matrix $[D_{\mathbf{q}}]^{i,j}_{\alpha,\beta}$, where i and j denote spatial directions. If we introduce the composite indices $\mu = \{\alpha, i\}$ and $\lambda = \{\beta, j\}$, the eigenvalue equation can be written as:

$$[e^{\dagger}_{\mathbf{q}} D_{\mathbf{q}} e_{\mathbf{q}}]_{\mu\lambda} = \delta_{\mu\lambda}\omega^2_{\mathbf{q}\lambda}, \tag{3.137}$$

where $e_{\mathbf{q}}$ is a unitary $3A \times 3A$ matrix whose columns $e_{\mathbf{q},\mu,\lambda}$ are the phonon eigenvectors. We can express the complex phonon amplitudes by scaling by $(m_0/m_\alpha)^{-1/2}$ where m_0 is a reference mass and m_α is the mass of the α^{th} nucleus in the unit cell. These vectors are then denoted as $U^{\text{ph}}_{\mathbf{q},\mu,\lambda}$ in matrix form. We can now express the derivative of the self-consistent potential appearing in the electron-phonon matrix element as follows:

$$\partial_{\mathbf{q}\lambda} = \frac{\partial}{\partial\eta} V(\mathbf{r}; \{\mathbf{R} + \boldsymbol{\tau}_\alpha + \eta\mathbf{u}_{\mathbf{R}\alpha}\}) \tag{3.138}$$

$$= \sum_{\mathbf{R},\mu} e^{i\mathbf{q}\cdot\mathbf{R}} \partial_{\mathbf{R}\mu} V(\mathbf{r}) U^{\text{ph}}_{\mathbf{q},\mu\lambda}. \tag{3.139}$$

In analogy with the interpolation of electronic band structure, these single-atom displacements can be viewed as maximally localised "lattice Wannier functions". As such, these lattice Wannier functions can be defined within the Wannier gauge or within the "eigenmode-gauge". In the Wannier gauge, we can express the phonon perturbation to the self-consistent potential as:

$$\partial^W_{\mathbf{q}\mu} V(\mathbf{r}) = \sum_{\mathbf{R}} e^{i\mathbf{q}\cdot\mathbf{R}} \partial_{\mathbf{R}\mu} V(\mathbf{r}), \tag{3.140}$$

which is related to its eigenmode-gauge counterpart as follows:

$$\partial_{\mathbf{q}\lambda} V(\mathbf{r}) = \sum_{\mu} \partial^W_{\mathbf{q}\mu} V(\mathbf{r}) U^{\text{ph}}_{\mathbf{q},\mu\lambda}. \tag{3.141}$$

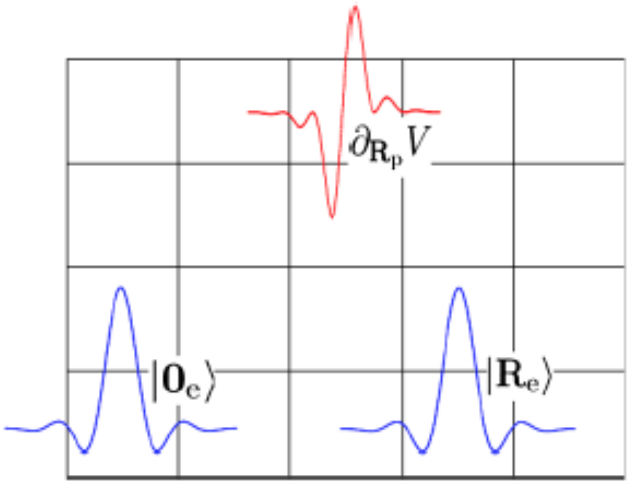

Figure 3.5: The real space representation of the electron-phonon matrix element $\langle \mathbf{0}_e | \partial_{\mathbf{q}\mu} V | \mathbf{R}_e \rangle$ in the basis of Wannier functions. The squares represent the Bravais lattice. This schematic illustrates that we need $|\mathbf{0}_e\rangle$, $|\mathbf{R}_e\rangle$ and $\partial_{\mathbf{q}\mu} V$ to be well localised. Matrix elements where any two of these functions are centred on distant lattice sites, will be vanishingly small. Figure reproduced from Ref. [94]

Now that we have generalised the notion of Wannier gauge to lattice Wannier functions, we may express the electron-phonon matrix elements $g^{\mathbf{q}\lambda}_{\mathbf{k}nm}$ in this gauge. If we drop explicit reference to band indices from our notation, we can evaluate $g^W_\mu(\mathbf{k},\mathbf{q}) = \left\langle \psi^W_{\mathbf{k}+\mathbf{q}} \middle| \partial^W_{\mathbf{q}\mu} V \middle| \psi^W_{\mathbf{k}} \right\rangle$ by combining Eqs. (3.130) and (3.140) as follows:

$$g^W_\mu(\mathbf{k}',\mathbf{q}') = \sum_{\mathbf{R}_e,\mathbf{R}_p} e^{i(\mathbf{k}'\cdot\mathbf{R}_e + \mathbf{q}'\cdot\mathbf{R}_p)} \langle \mathbf{0}_e | \partial_{\mathbf{R}_p\mu} V | \mathbf{R}_e \rangle \,, \tag{3.142}$$

where the subscripts e and p denote electronic and phonon quantities respectively, and where we have used the primed wavevectors $\mathbf{k}'$ and $\mathbf{q}'$ to indicate that g^W_μ can be interpolated to arbitrary wavevectors $(\mathbf{k}',\mathbf{q}')$ throughout the BZ.

The different constituents of the electron-phonon matrix element in the Wannier representation $\langle \mathbf{0}_e | \partial_{\mathbf{q}\mu} V | \mathbf{R}_e \rangle$ are shown schematically in Fig. 3.5. The localisation in real space of $|\mathbf{0}_e\rangle$, $|\mathbf{R}_e\rangle$ and $\partial_{\mathbf{q}\mu} V$ ensure smooth interpolation of the electron-phonon matrix elements with respect to both the electron and phonon wavevectors. The final step in the interpolation procedure is to transform both the electronic and lattice Wannier functions back to the Hamiltonian

and eigenmode gauges respectively:

$$g^H_\lambda(\mathbf{k}',\mathbf{q}') = \left\langle \psi^H_{\mathbf{k}'+\mathbf{q}'} \middle| \partial_{\mathbf{q}'\lambda} V \middle| \psi^H_{\mathbf{k}'} \right\rangle \tag{3.143}$$

$$= U^\dagger_{\mathbf{k}'+\mathbf{q}'} \left[\sum_\mu g^W_\mu(\mathbf{k}',\mathbf{q}') U^{\mathrm{ph}}_{\mathbf{q}',\mu\lambda} \right] U_{\mathbf{k}'}. \tag{3.144}$$

Therefore, once the matrix elements $\langle \mathbf{0}_e | \partial_{\mathbf{R}_p\mu} V | \mathbf{R}_e \rangle$ are known, the electron-phonon matrix elements can be interpolated to arbitrary wavevectors $(\mathbf{k}', \mathbf{q}')$, by combining the previous 2 equations.

In analogy with the computation of $\langle \mathbf{0}|H|\mathbf{R}\rangle$ for the interpolation of the band structure, the matrix elements $\langle \mathbf{0}_e | \partial_{\mathbf{R}_p\mu} V | \mathbf{R}_e \rangle$ can be obtained by inverting Eq. (3.142) over the first-principles (coarse) mesh and using Eqs. (3.141) and (3.129).

Throughout this thesis, where electron-phonon matrix elements are required with mesh density greater than $N_{\mathbf{k}} = N_{\mathbf{q}} = 8 \times 8 \times 8$, this method has been used to interpolate electron-phonon matrix elements from DFPT to a finer grid. All Wanner interpolations of electronic band structure and electron-phonon matrix elements are performed using the open source EPW (**e**lectron-**p**honon **W**annier) code [97], developed at the University of California at Berkeley. This is a code that takes first-principles electronic structure quantities from the Quantum Espresso code [72] as input, and interpolates them to a fine grid. It also performs transport calculations.

Having discussed equilibrium electronic structure theory methods in detail, we will now introduce some useful methods for simulating photoexcited electronic systems.

3.16 Photoexcited electrons: Constrained DFT

Within Standard DFT, the occupation of electrons is given by a *zero-temperature* Fermi-Dirac distribution in which all states below the Fermi-level are completely filled and all those above are completely empty. An extension of DFT by Mermin [98] allowed for the occupations of electronic states to be extended to a finite temperature Fermi-Dirac distribution. This assumes that the electrons are in thermal equilibrium with their environment as well as with all other degrees

of freedom in the system. More precisely, it assumes that the total free energy of the system is minimised with respect to the occupations of the electronic states. This approach allows us to use finite temperature equilibrium electrons to approximate the physics of photoexcited electrons.

A caveat is that in photoexcited systems, some of the above assumptions may not be valid, particularly on short (sub-picosecond) timescales. The dynamics of ions in photoexcited systems are driven by electrons which are far from equilibrium. The relaxation of photoexcited electrons can be divided into intra-band relaxation and inter-band relaxation. Intra-band relaxation, which at the photoexcited carrier densities of interest in most experiments ($\sim 10^{20}$ cm^{-3}), is dominated by electron-electron scattering, proceeds in tens of femtoseconds [11]. However, inter-band relaxation (eg. electron-hole recombination) may take much longer, particularly in semiconductors [99].

There are two approximations which are commonly used to treat electronic occupations following photoexcitation. Both approaches assume that intraband electron-electron scattering proceeds extremely fast. However, they differ in their assumptions about the rate of electron-hole recombination.

3.16.1 Fast electron-hole recombination

The excited electrons and holes are assumed to come into thermal equilibrium with one another via rapid electron-hole recombination. They form a hot Fermi-Dirac distribution,

$$f_{n\mathbf{k}}(T,\mu) = \frac{1}{e^{(\varepsilon_{n\mathbf{k}}-\mu)/k_BT}+1}, \tag{3.145}$$

whose temperature T is determined by the amount of energy deposited in the system by photons during photoexcitation:

$$\Delta E \equiv E(T,\mu) - E(T=0,\mu) = n_{\text{ph}}\hbar\omega_{\text{ph}}, \tag{3.146}$$

where n_{ph} and $\hbar\omega_{\text{ph}}$ are the number of photons and the photon energy respectively. This occupation scheme is illustrated in Fig. 3.6.

The Kohn-Sham equations are then solved within Mermin's finite temperature DFT, constraining the occupations to remain fixed at the values given by Eqs. (3.145) and (3.146) at each step of the self-consistent process.

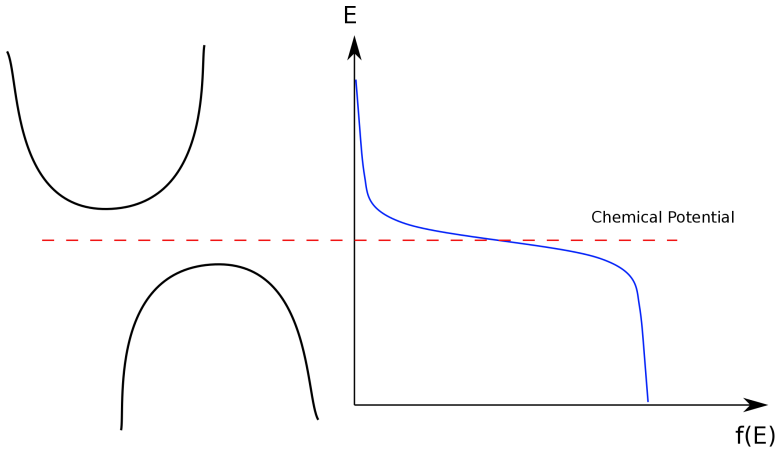

Figure 3.6: Schematic of photoexcited electronic occupations assuming that the electrons are in a hot Fermi-Dirac distribution with a single chemical potential for all bands.

3.16.2 Slow electron-hole recombination

Another way of approaching the problem is to assume that the electrons thermalise separately from the holes. This approach, which was introduced by Tangney and Fahy [3, 100] to study photoexcited tellurium, amounts to assuming that electron-hole recombination proceeds very slowly. This approach was motivated by the long electron-hole recombination times (up to multiple ns) in semiconductors [99]. However, it has also been used successfully to study photoexcited Bi, a semimetal [20]. The slow rate of electron-hole recombination results in electrons which have a different chemical potential to the holes, but are at the same temperature:

$$f^{\mathrm{vb}}_{n\mathbf{k}}(T,\mu_{\mathrm{vb}}) = \frac{1}{e^{(\varepsilon_{n\mathbf{k}}-\mu_{\mathrm{vb}})/k_BT}+1}, \quad f^{\mathrm{cb}}_{n\mathbf{k}}(T,\mu_{\mathrm{cb}}) = \frac{1}{e^{(\varepsilon_{n\mathbf{k}}-\mu_{\mathrm{cb}})/k_BT}+1}. \tag{3.147}$$

These schemes for treating photoexcited electrons will be utilised in chapter 4, where we will be investigating the excited dynamics of the A_{1g} coherent mode. They are suitable for this purpose under the assumption that the electrons and holes form Fermi-Dirac distributions on timescales much shorter than the A_{1g} mode period (~ 300 fs in Bi) which is usually satisfied. We give more details on its implementation in that chapter. However, it must be stressed that these methods for treating the excited electrons will be useless when we are concerned with symmetry-breaking coherent modes such as the E_g modes in Bi, Sb and As. This is because thermal occupations by definition have the same symmetry as the underlying crystal, so the forces produced by a thermal distribution of electrons cannot break the symmetry of the lattice (see section 2.5.1). For this

reason, we will introduce a more appropriate method for computing the dynamic occupations of electronic states following photoexcitation in section 3.17.

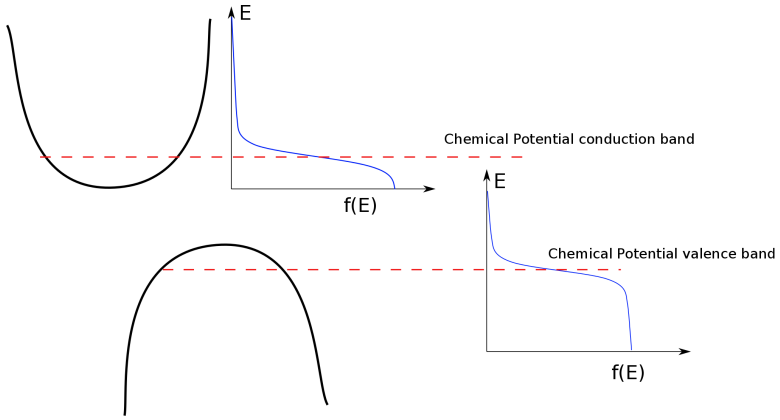

Figure 3.7: Schematic of photoexcited electronic occupations assuming that the electrons have hot Fermi-Dirac distributions with equal temperatures, but with different chemical potentials for electrons(conduction bands) and holes(valence bands).

3.16.3 Two-temperature model

A similar approach is applied to the problem of excited electrons coupled to phonons. It assumes that the electrons and phonons thermalise among themselves very quickly and remain in thermal distributions with well defined temperatures due to electron-electron and phonon-phonon scattering, such that they can at all times be described by two temperatures, T_e for the electrons and T_{ph} for the phonons. The electrons and lattice are then assumed exchange heat at a rate determined by the electron-phonon coupling constant G_0, often, but not always [34], assumed to be independent of temperature. The temperatures of the electrons and phonons as a function of time are determined by the following two equations :

$$C_e \frac{\partial T_e}{\partial t} = \kappa \Delta^2 T_e - G_0(T_e - T_{ph}) + P_0(\mathbf{r}, t), \tag{3.148}$$

$$C_{ph} \frac{\partial T_{ph}}{\partial t} = G_0(T_e - T_{ph}), \tag{3.149}$$

where the first term on the right hand side of Eq. (3.148) takes account of thermal conductivity losses and the third term is a source term taking account of laser heating from the pump pulse. The coupling constant G_0 is usually determined from comparison with experiment [101]. The two-temperature

model has proved a very useful tool for studying many different photoexcited systems [102, 101, 34, 103].

3.17 Photoexcitation: Electron-Photon interaction

A major focus of this work will be to study the excitation of electrons by the absorption of photons from polarised pulses of light. This means we need to directly consider the interactions of electrons with photons. In particular, we are interested in those interactions in which electrons are excited into higher single-particle states via the absorption of a photon. In principle, there can be nonlinear processes where more than one photon is absorbed/emitted per electronic excitation, but here we restrict ourselves to *single* photon processes. We will also restrict ourselves to direct processes where electrons and photons are the only particles involved. Indirect processes typically involve phonons providing an additional momentum $\mathbf{q}$ and are a method of photon absorption in indirect gap materials, such as silicon [104]. This section is largely based on Ref. [87].

Conservation of energy and momentum imply that the transition energy $\varepsilon_{m\mathbf{k}'} - \varepsilon_{n\mathbf{k}}$ must be equal to the photon energy $\hbar\omega$ and that the change in electron momentum during the transition $\mathbf{k}' - \mathbf{k}$ must be equal to the photon momentum $\boldsymbol{\kappa}$. We describe the incident light (photons) with its magnetic vector potential as follows:

$$\mathbf{A}(\mathbf{r}, t) = A_0 e^{i(\boldsymbol{\kappa}\cdot\mathbf{r} - \omega t)}\hat{\mathbf{e}} + \text{c.c}, \tag{3.150}$$

where c.c denotes the complex conjugate of the first term and $\hat{\mathbf{e}}$ is a unit vector pointing in the direction of polarization of the light. By recognising that the total momentum of the electromagnetic field is $\mathbf{p}_{\text{tot}} = \mathbf{p} + e\mathbf{A}$, where $\mathbf{p}$ is the electron momentum operator, we can write the Hamiltonian as:

$$H_{\text{tot}} = H_0 + H' = V(\mathbf{r}) + \frac{1}{2m_e}(\mathbf{p} + e\mathbf{A})^2 \tag{3.151}$$

$$= V(\mathbf{r}) + \frac{1}{2m_e}\mathbf{p}^2 + \frac{e}{m_e}\mathbf{p}\cdot\mathbf{A} + e^2\mathbf{A}^2. \tag{3.152}$$

We make the dipole approximation by disregarding the terms which are quadratic in $\mathbf{A}$, since they are much smaller than the linear term, we can

now write the Schrödinger equation of the system as follows:

$$\left[\frac{1}{2m_e}\mathbf{p}^2 + \frac{e}{m_e}\mathbf{p}\cdot\mathbf{A} + V(\mathbf{r})\right]\Psi = i\hbar\frac{\partial\Psi}{\partial t}. \tag{3.153}$$

Expanding Ψ in terms of the solutions to the unperturbed system $H_0\Psi_0 = i\hbar\dot{\Psi}$, and assuming that these solutions are single-particle Bloch waves, we get:

$$\Psi = \sum_{n\mathbf{k}} a_{n\mathbf{k}}(t)\exp\left[-\frac{i}{\hbar}\varepsilon_{n\mathbf{k}}t\right]|\psi_{n\mathbf{k}}\rangle \tag{3.154}$$

Inserting the form of the wavefunction in Eq. (3.154) into the Schrödinger equation given by Eq. (3.153) and multiplying by $\exp[(i/\hbar)\varepsilon_{mk'}t]\,\langle\psi_{m\mathbf{k}}|$ we reach the following differential equation for the coefficients:

$$\dot{a}_{m\mathbf{k}'}(t) = \frac{1}{i\hbar}\sum_{n\mathbf{k}} a_{n\mathbf{k}}(t)\exp\left(\frac{i}{\hbar}[\varepsilon_{m\mathbf{k}'} - \varepsilon_{n\mathbf{k}}]t\right)\,\langle\psi_{m\mathbf{k}'}|H'|\psi_{n\mathbf{k}}\rangle\,. \tag{3.155}$$

Next we impose the initial condition that at $t = 0$, the probability amplitude to be in state $\psi_{n\mathbf{k}}$ is 1 if the state is occupied before the arrival of the photons, and 0 if not. This gives to first degree of approximation:

$$\dot{a}_{j'\mathbf{k}'}(t) = \frac{1}{i\hbar}\exp\left(\frac{i}{\hbar}[\varepsilon_{j'\mathbf{k}'} - \varepsilon_{j\mathbf{k}}]t\right)\,\langle\psi_{j'\mathbf{k}'}|H'|\psi_{j\mathbf{k}}\rangle\,. \tag{3.156}$$

The probability $W(j,\mathbf{k},j',\mathbf{k}',\omega,t)$, that at time t, the electron in $\psi_{j\mathbf{k}}$ will have scattered to $\psi_{j'\mathbf{k}'}$ is given by $|a_{j'\mathbf{k}}(t)|^2$. Integrating Eq. (3.156) over time:

$$W(j,\mathbf{k},j',\mathbf{k}',\omega,t) = -\frac{1}{\hbar^2}\left|\int_0^t \exp\left(\frac{i}{\hbar}[\varepsilon_{j'\mathbf{k}'} - \varepsilon_{j\mathbf{k}}]t'\right)\,\langle\psi_{j'\mathbf{k}'}|H'|\psi_{j\mathbf{k}}\rangle\,\mathrm{d}t'\right|^2. \tag{3.157}$$

If we substitute in H' and expand the vector potential $\mathbf{A}$ in terms of its definition in Eq. (3.150), we can express the matrix element appearing in Eq. (3.157) as follows:

$$\langle\psi_{j'\mathbf{k}'}|H'|\psi_{j\mathbf{k}}\rangle = \frac{e\hbar A_0}{im_e}\left[e^{-i\omega t}\,\langle\psi_{j'\mathbf{k}'}|e^{i\boldsymbol{\kappa}\cdot\mathbf{r}}\hat{\mathbf{e}}\cdot\nabla|\psi_{j\mathbf{k}}\rangle + e^{i\omega t}\,\langle\psi_{j'\mathbf{k}'}|e^{-i\boldsymbol{\kappa}\cdot\mathbf{r}}\hat{\mathbf{e}}\cdot\nabla|\psi_{j\mathbf{k}}\rangle\right]. \tag{3.158}$$

Only the first term contributes to processes involving the excitation of an electron via the absorption of a photon. The second term corresponds to processes with the emission of a photon and an electron being demoted, which we are not interested in here, so we neglect it. We can restrict the integration in the matrix element to a single unit cell by utilising Bloch's theorem $\psi_{n\mathbf{k}}(\mathbf{r}+\mathbf{R}_l) =$

$\psi_{n\mathbf{k}}(\mathbf{r})\exp(i\mathbf{k}\cdot\mathbf{R}_l)$ as follows:

$$\begin{aligned} M_{j'j}(\mathbf{k},\mathbf{k}') &= \langle\psi_{j'\mathbf{k}'}|e^{i\boldsymbol{\kappa}\cdot\mathbf{r}}\hat{\mathbf{e}}\cdot\nabla|\psi_{j\mathbf{k}}\rangle \\ &= \langle u_{j'\mathbf{k}'}|e^{i(\boldsymbol{\kappa}+\mathbf{k}-\mathbf{k}')\cdot\mathbf{r}}\hat{\mathbf{e}}\cdot\nabla|u_{j\mathbf{k}}\rangle \\ &= \langle u_{j'\mathbf{k}'}|e^{i(\boldsymbol{\kappa}+\mathbf{k}-\mathbf{k}')\cdot\boldsymbol{\tau}}\hat{\mathbf{e}}\cdot\nabla|u_{j\mathbf{k}}\rangle_{\text{uc}}\sum_l e^{i(\boldsymbol{\kappa}+\mathbf{k}-\mathbf{k}')\cdot\mathbf{R}_l}. \end{aligned} \tag{3.159}$$

The sum in Eq. (3.159) is only non-zero if $\boldsymbol{\kappa}+\mathbf{k}-\mathbf{k}'$ is a reciprocal lattice vector

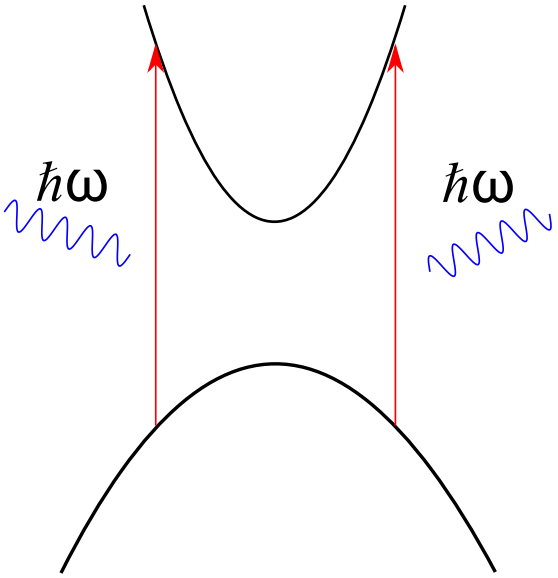

Figure 3.8: A schematic of a direct transition involving the absorption of a photon of energy $\hbar\omega$.

G. Since $\mathbf{k}$ and $\mathbf{k}'$ lie in the first Brillouin zone, and the photon momentum $|\boldsymbol{\kappa}|$ is much smaller than any reciprocal lattice vector, this condition is equivalent to $\mathbf{k}' = \mathbf{k}+\boldsymbol{\kappa}$. If we further assume that $|\boldsymbol{\kappa}|$ is *negligible* compared with the dimensions of the first Brillouin zone, then the scattering follows the approximate conservation of momentum condition:

$$\boldsymbol{\kappa} = 0 \quad , \quad \mathbf{k} = \mathbf{k}'. \tag{3.160}$$

The excitation of electrons by photon absorption takes place with no change in electron wavevector (direct transition). We can now re-express the optical transition matrix elements as:

$$M_{j'j}(\mathbf{k}) = \langle u_{j'\mathbf{k}}|\hat{\mathbf{e}}\cdot\nabla|u_{j\mathbf{k}}\rangle_{\text{uc}} = \frac{\hbar}{i}\langle u_{j'\mathbf{k}}|\hat{\mathbf{e}}\cdot\mathbf{p}|u_{j\mathbf{k}}\rangle_{\text{uc}}. \tag{3.161}$$

This allows us to express the probability that an electron will scatter from $\psi_{j\mathbf{k}}$ to $\psi_{j'\mathbf{k}'}$ in the following simplified form:

$$W(j,j',\mathbf{k},\omega,t) = -\frac{e^2A_0^2}{m_e^2}\left|M_{j'j}(\mathbf{k})\int_0^t \exp\Big(\frac{i}{\hbar}[\varepsilon_{j'\mathbf{k}} - \varepsilon_{j\mathbf{k}} - \hbar\omega]t'\Big)\mathrm{d}t'\right|^2 \quad (3.162)$$

If we define, $\Omega = (\varepsilon_{j'} - \varepsilon_j + \hbar\omega)/2\hbar$, the integral over time can be evaluated as follows:

$$\left|\int_0^t e^{(2i\Omega t)}\right|^2 = \left|\frac{e^{2i\Omega t}-1}{2i\Omega}\right|^2 = \frac{\sin^2(\Omega t)}{\Omega^2}$$

$$\sim \pi t\delta(\Omega) \quad \text{for} \quad \Omega t \gg 1.$$

The probability $W(j,j',\mathbf{k},\omega,t)$ is now linear with respect to time, so taking a single time-derivative, we arrive at a time-independent scattering rate:

$$R(j,j',\mathbf{k},\omega) = \dot{W}(j,j',\mathbf{k},\omega,t) = 2\pi\hbar\frac{e^2A_0^2}{m_e^2}|M_{jj'}(\mathbf{k})|^2\delta(\varepsilon_{j'\mathbf{k}} - \varepsilon_{j\mathbf{k}} - \hbar\omega), \quad (3.163)$$

which is essentially just Fermi's golden rule for direct transitions. One drawback of this theoretical treatment of the problem is our assumption that the single-particle states were stationary states with infinite lifetime. We address this in the following subsection:

3.17.1 Modification due to finite lifetime of electronic states.

We have modelled the problem of electronic excitation as direct transitions between states which have infinite lifetimes. In reality, the excited electronic states will be undergoing scattering, such as electron-phonon or electron-electron, which give them a finite lifetime. To treat this, we include a damping term in the integral of Eq (3.162) which reflects the finite lifetime of the electronic states involved in the scattering:

$$W(j,j',\mathbf{k},\omega,t) = -\frac{e^2A_0^2}{m_e^2}\left|M_{j'j}(\mathbf{k})\int_0^t \exp\Big(\frac{i}{\hbar}[\varepsilon_{j'\mathbf{k}} - \varepsilon_{j\mathbf{k}} - \hbar\omega]t'\Big)\exp\big(-\gamma_{\mathbf{k}}^{jj'}t'\big)\mathrm{d}t'\right|^2, \quad (3.164)$$

where $\gamma_{\mathbf{k}}^{jj'} = \gamma_{j\mathbf{k}} + \gamma_{j'\mathbf{k}}$ is the sum of the inverse lifetimes of the states. Performing the integral with this extra damping term and taking the limit $\gamma_{\mathbf{k}}^{jj'}t \gg 1$, we obtain something similar to Fermi's golden rule, but with a Lorentzian in place

of a Dirac delta distribution:

$$R(j, j', \mathbf{k}, \omega) \propto |M_{jj'}(\mathbf{k})|^2 \frac{\hbar\gamma_{\mathbf{k}}^{jj'}}{\left(\Delta\varepsilon_{\mathbf{k}}^{jj'}\right)^2 + \left(\hbar\gamma_{\mathbf{k}}^{jj'}\right)^2}. \tag{3.165}$$

For a similar derivation in the case of electron-phonon scattering, see section 3.12. It is with this formula that we calculate the rates of scattering from conduction to valence bands during electronic excitation. We typically put an average inverse lifetime into this formula rather than calculating the lifetimes of every individual state. Other than being more physically justified, this method is advantageous when performing calculations on a finite Brillouin zone grid, where exact energy conservation is not possible.

3.17.2 Computing photoinduced driving forces on coherent modes

We are particularly interested in the forces which are exerted on the atoms by the photoexcited electrons. These are the forces which drive coherent mode oscillations following photoexcitation. Throughout this thesis, we compute photoinduced atomic driving forces using the method described in Ref. [50]. The distribution of photoexcited electrons in the conduction bands and holes in the valence bands are proportional to

$$g_{n\mathbf{k}}^{\mathrm{opt}} \equiv \sum_{m \in \mathrm{vb}} |M_{nm}(\mathbf{k})|^2 \delta(\varepsilon_{n\mathbf{k}} - \varepsilon_{m\mathbf{k}} - \hbar\omega) \quad \text{for} \quad n \in \mathrm{cb}, \tag{3.166}$$

and

$$g_{m\mathbf{k}}^{\mathrm{opt}} \equiv -\sum_{n \in \mathrm{cb}} |M_{nm}(\mathbf{k})|^2 \delta(\varepsilon_{n\mathbf{k}} - \varepsilon_{m\mathbf{k}} - \hbar\omega) \quad \text{for} \quad m \in \mathrm{vb}. \tag{3.167}$$

This allows us to compute the rate of change of force on a coherent mode with coordinate u_i as:

$$\frac{\partial F_i}{\partial t} \sim \sum_{n \in \text{ all bands}} \int_{\mathrm{BZ}} \frac{\partial \varepsilon_{n\mathbf{k}}}{\partial u_i} g_{n\mathbf{k}}^{\mathrm{opt}} \mathrm{d}\mathbf{k} \tag{3.168}$$

3.17.3 Polarization dependence and symmetry-breaking

As seen in Eq. (3.161), the optical transition matrix elements $M_{jj'}(\mathbf{k})$ depend upon the scalar product $\hat{\mathbf{e}} \cdot \mathbf{p}$ between the electron momentum and the direction of polarisation of the incident light. This can result in symmetry-equivalent states $|\psi_{n\mathbf{k}}\rangle$ and $\left|\psi_{n\hat{R}(\mathbf{k})}\right\rangle$ becoming differently occupied during photoexcitation if the scalar product is not invariant under the symmetry operation $\hat{R}$. An illustrative

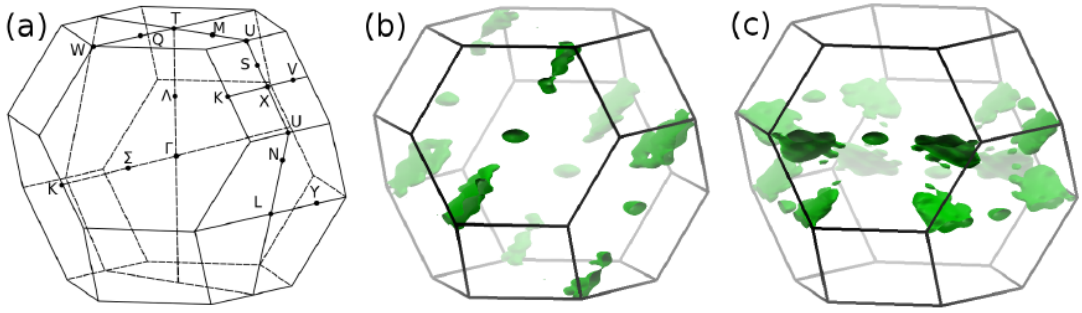

Figure 3.9: (a): The first Brillouin zone of the A7 rhombohedral structure. This is the structure of Bi, Sb and As. (b): The regions of the Brillouin Zone with the greatest concentration of excited electrons and holes when bismuth is excited by 1.5 eV photons polarized in the x-direction and (c) polarized in the z-direction. The fading of the isosurfaces indicates depth. Figure reproduced from Ref. [50]

example is that of bismuth, which has 3-fold rotational symmetry about its z-axis ($\Gamma - T$ line in Fig. 3.9). When the incident light is polarised parallel to the z-axis, the scalar product $\hat{\mathbf{e}} \cdot \mathbf{p}$ is invariant under rotation by $\pi/3$, so the excited distribution of electrons has 3-fold rotational symmetry (See Fig. 3.9 (c)). However, when the light is polarised perpendicular to this, the scalar product is not invariant, and the excited electrons have a broken 3-fold rotational symmetry (See Fig. 3.9 (b)), producing a force on the symmetry-breaking E_g mode.

A large part of this thesis is devoted to understanding the mechanism for generation and relaxation of the photo-induced driving forces on symmetry-breaking coherent phonon modes. It is important to note that such symmetry-breaking forces only arise when the photoexcited electron-hole plasma breaks one of the point group symmetries of the crystal. In fact, if the coherent mode breaks a particular point group symmetry, the excited electron distribution must also break this symmetry. This is referred to as isosymmetry between photoexcited electrons and photo-induced atomic driving forces. It should be noted that the two-temperature model and other constrained DFT approaches cannot be used to probe symmetry-breaking forces on coherent modes. These models give photoexcited electron distributions which have full crystal symmetry, so will

always produce 0 force on symmetry-breaking modes.

Chapter 4

Photoinduced reversal of Peierls distortion in Antimony

4.1 Introduction

A key challenge in condensed matter physics is the control of collective transformations of materials with light. Recently, it has been shown that optical excitation can drive collective structural transformations to phases that do not exist on the equilibrium phase diagram of materials as diverse as transition metal oxides [105], transition metal chalcogenides [106], and main group semimetals [6]. Finding alternate structural phases using optical excitation offers a route to understanding the fundamental driving forces behind the ground states of materials. Understanding of nonequilbrium structural phases at high excitation density requires both an understanding of how the structure of the ground state is defined, and how photoexcitation modifies the interatomic forces holding the crystal together [44, 45]. Experimentally reaching many of these states requires a high degree of photoexcitation, with a significant fraction (1-5%) of the valence electrons excited to the conduction bands [15, 14]. Often, materials photoexcited to this degree undergo irreversible changes, making traditional stroboscopic pump-probe methods challenging. This is because these pump-probe experiments require the system to relax back to its ground state between pump-probe pairs. For irreversible processes, such as photoinduced structural phase transitions, this assumption breaks down. However, recently the single-shot pump-probe approach was developed allowing information to be gathered about these irreversible processes. This method involves the division of the

probe beam into several pulses, each separated by a short time interval, which can probe the systems evolution for up to 10 ps following the absorption of the pump pulse. I will not describe the experimental details here, but the reader is directed to the review in Ref. [107].

In this chapter, we calculate the potential energy of Sb as a function of both the A_{1g} coordinate and the density of photoexcited carriers. We show that the A_{1g} mode undergoes softening as a function of the number of electrons excited to the conduction bands and that at high levels of photoexcitation, Sb can undergo a domain reversal in which the Peierls distortion is reversed. These results are in good agreement with single shot pump-probe results carried out by our experimental collaborators, which also show some evidence for this domain reversal. Finally, we calculate the third order anharmonic decay rate of the A_{1g} mode in Sb as a function of pump fluence and compare against pump-probe measurements.

4.2 Constrained DFT calculations of photoexcited potential energy of A_{1g} mode in Antimony

The constrained DFT method, as outlined in section 3.16, enables us to calculate total energies of systems with excited electrons and holes. This can be combined with the frozen-phonon method [108], which entails approximating atomic motion by computing the total energy of the system for several snapshots of the atomic positions, to calculate the potential energy surface of a given coherent phonon as a function of the photoexcited carrier density n_c. We typically give n_c as the percentage of valence electrons excited to the conduction bands. We work in the limit of slow electron-hole recombination (see subsection 3.16.2), where the electrons and the holes are assumed to have thermalised among themselves, but not with each other [1] [3, 100, 20]. This creates an electron-hole plasma in which the electrons and holes have different chemical potentials. For this reason, we will refer to this as the two chemical potential model.

The total energy calculations were performed using a version of the ABINIT code [74], which had been modified to allow the use of constrained DFT [2]. This

[1] In appendix A, we show that our results would not change substantially if we had assumed the limit of fast electron-hole recombination.

[2] This modification was performed by Eamonn Murray.

modification involved including options to define the electronic occupations according to two Fermi-Dirac distributions with different chemical potentials. However, since we will be using the frozen-phonon method and displacing the atoms from their equilibrium positions, we also need to impose dynamical constraints on the excited electronic occupations.

4.2.1 Isentropic dynamics

Electrons move much faster than ions in a solid, meaning that throughout phonon motion the electrons can be assumed to track the ions and remain in quasi-equilibrium. This means that the electrons undergo a quasistatic reversible process and satisfy [109]:

$$\delta Q = T_e \mathrm{d}S_e, \tag{4.1}$$

where δQ is a small heat exchange between the electrons and the lattice, T_e is the electronic temperature and S_e is the electronic entropy per unit cell defined by:

$$S_e = -\frac{k_\mathrm{B}}{\Omega_\mathrm{BZ}} \int_\mathrm{BZ} \sum_n f_{n\mathbf{k}} \ln f_{n\mathbf{k}} + (1 - f_{n\mathbf{k}}) \ln(1 - f_{n\mathbf{k}}) \mathrm{d}\mathbf{k}, \tag{4.2}$$

where Ω_BZ is the volume of the Brillouin zone and $f_{n\mathbf{k}}$ is the occupation of the n^th electronic band at wavevector $\mathbf{k}$. The exchange of heat between the excited electrons and the lattice in antimony has been shown to proceed on timescales much longer ($\sim$ few ps) than the period of the A_{1g} mode (~ 220 fs) [110]. If we assume that the electrons do not exchange heat with the lattice throughout the atomic motion, Eq. (4.1) dictates that the entropy be a constant of motion. This idea of constraining entropy to be a constant of motion was first introduced by Stampfli and Benneman [111], and has since been used in several theoretical studies of photoinduced coherent phonon motion [34, 112].

Combining the two chemical potential model with isentropic dynamics leads to the following set of constraints for the excited electrons:

$$n_c(x_0) = n_\mathrm{ph}; \quad \Delta E(x_0) = n_\mathrm{ph} \hbar\omega_\mathrm{ph}; \quad S_e(x) = S_e(x_0), \tag{4.3}$$

where $n_c(x_0)$ is the number of photoexcited carriers at the equilibrium phonon coordinate x and $\Delta E(x)$ is the change in total energy as a function of phonon displacement.

4.2.2 Numerical approach

The first step is to calculate the electronic entropy at the ground state equilibrium A_{1g} mode coordinate $S(x_0)$. To achieve this, we note from Eq. (4.3) that the first two constraints imply that the energy per electron-hole pair is equal to the pump photon energy. We choose a photon energy of 1.5 eV [3], and set the electronic temperature to 5365 K (or ~ 0.462 eV), which is the energy that gives the correct energy per electron-hole pair. [4] The entropy $S_e(x_0)$ is then calculated for each n_c using the bisection method to vary the valence band (μ_v) and conduction band (μ_c) chemical potentials until the number of excited electrons is n_c.

Constrained DFT calculations were then performed for several values of n_c and several atomic displacements. They were carried out on four shifted uniform $8 \times 8 \times 8$ k-point grids, generated with the Monkhorst-Pack scheme. We used the local density approximation (LDA) [59] to exchange and correlation (see section 3.5.1), and a Hartwigsen-Goedecker-Hutter (HGH) pseudopotential [75]. The wavefunctions were represented by a plane wave expansion with a kinetic energy cut off of 30 Hartree. The results of these calculations are then fitted to a bivariate polynomial in $x - \frac{1}{2}$ and n_c as follows:

$$E(x, n_c) = \sum_{i=0}^{9} \sum_{j=0}^{3} a_{ij} n_c^j \left(x - \frac{1}{2} \right)^{2i}. \tag{4.4}$$

For each value of n_c, the potential energy of the A_{1g} mode is an even function about $x = 1/2$, allowing us to omit odd powers of $x - 1/2$. [5].

4.2.3 Results

Fig. 4.1 shows the fitted potential energy surface of the A_{1g} mode, showing clearly the progression from a double well potential [6] to a single well with increasing photoexcited carrier concentration, which is accompanied by a structural phase transition from the Peierls distorted A7 rhombohedral to one which

[3] The typical pump photon energy used in experiments, which corresponds to a wavelength of ~ 800 nm.

[4] Here we use hot thermal electrons to mimic the effect of excited electrons. This temperature gives an electron-hole pair energy 1.5 eV for $n_c = 1\%$. The relevant temperature changes slightly with changing n_c, but the effect is small so we neglect it here.

[5] We include up to 18^{th} powers of $x - 1/2$, for reasons of fit convergence, as opposed to any physical reason.

[6] The potential is a double well because there are two energetically equivalent equilibrium separations x_0 of the two atoms in the unit cell.

is similar to simple cubic, but with rhombohedral angles which differ slightly from $60°$ [7]. For ease of comparison, the energies have been shifted such that $E(x_0, n_c) = 0$ for all n_c. This structural phase transition can be understood by

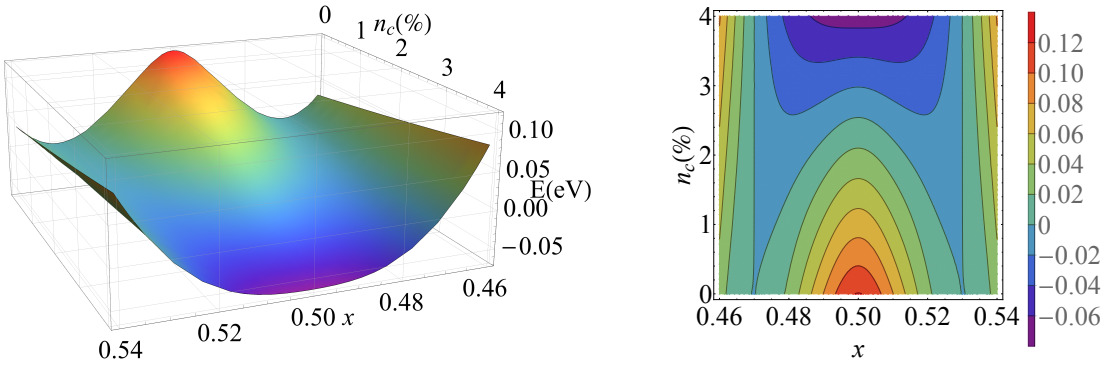

Figure 4.1: The surface describing the potential of the A_{1g} mode in Sb as a function of photoexcited carrier density n_c, represented by a three dimensional surface plot (left) and a contour plot (right). It is readily seen that as n_c is increased, the double well potential energy transforms steadily into a single well.

plotting the A_{1g} mode frequency. Since the potential energy surface is highly anharmonic for large phonon displacement, the harmonic frequency is defined for small amplitude motion about the (excited) equilibrium position where the potential energy approaches harmonicity as:

$$\omega_H = 2\pi\nu_H = \sqrt{\frac{1}{\mu}\frac{\partial^2 E}{\partial x^2}}, \tag{4.5}$$

where ν_H and ω_H are the harmonic mode frequency and angular frequency respectively, and μ is the reduced mass.

To better understand large amplitude atomic motion on the anharmonic double well potential, we can also define an anharmonic frequency. We define this as the inverse of the period of motion of a classical particle which starts at $x = x_0$, travels to the next point x_1 such that $E(x_0) = E(x_1)$, and oscillates back to x_0. We assume that the particle loses no energy as it moves along the potential curve, which amounts to neglecting damping of the A_{1g} mode. Later in this chapter, we will explicitly account for the effects of damping by numerically solving the classical equations of motion for the potential energy surface shown in Fig. 4.1.

To derive an explicit expression for the period, we consider a mass μ which is

[7] The angles will eventually adjust to $60°$, but the timescale for this is defined by the period of long wavelength acoustic modes. On the timescales of our simulations, the rhombohedral angles remain roughly constant.

constrained to move along a curve such that its energy is described by $E(x)$ [8]. The mass moves between points x_0 and x_1 such that $E(x_0) = E(x_1)$. Conservation of energy implies that any changes in the particle's potential energy must be balanced by a change in its kinetic energy:

$$E(x_0) - E(x) = T(x) = \frac{1}{2}\mu v(x)^2 = \frac{1}{2}\mu\left(\frac{\mathrm{d}x}{\mathrm{d}t}\right)^2, \tag{4.6}$$

where $T(x)$ is the kinetic energy of the particle. Re-arranging Eq. (4.6) allows us to express the period of motion:

$$P = 2\int_{x_0}^{x_1}\mathrm{d}t = 2\int_{x_0}^{x_1}\frac{\mathrm{d}x}{\sqrt{\frac{2}{\mu}[E(x_0) - E(x)]}}, \tag{4.7}$$

where the factor of 2 is to take account of both the outward and return journeys, which take the same amount of time by symmetry.

The harmonic frequency was calculated by taking the second derivative of the fitted function from Eq. (4.4) and evaluating it at the points where $E(x, n_c)$ was minimum for each value of n_c. The anharmonic frequency was obtained by performing the integral from Eq. (4.7) on the same fitted function. [9] Fig. 4.2

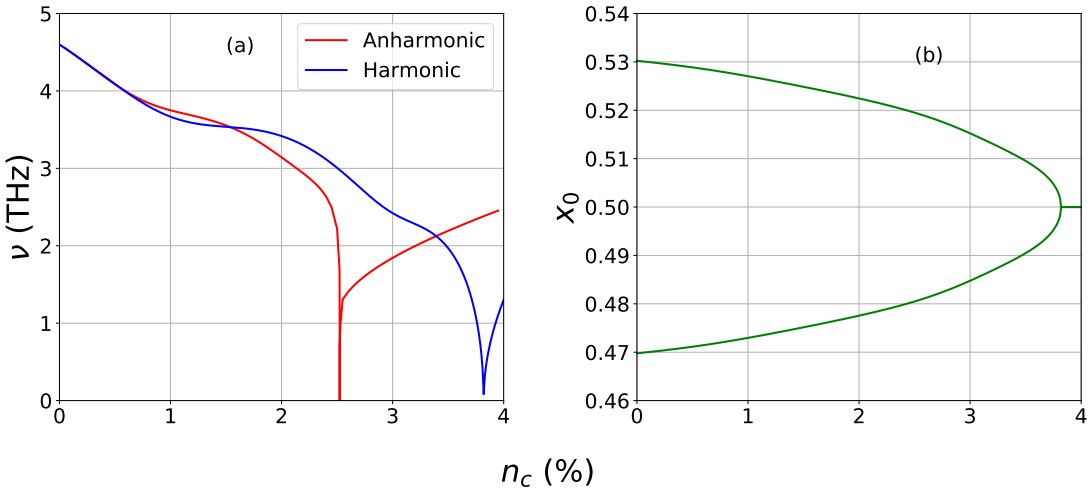

Figure 4.2: (a) Shows the harmonic and anharmonic frequencies and (b) shows the equilibrium value(s) of the A_{1g} mode coordinate x_0 as a function of photoexcited carrier concentration.

(a) shows the calculated harmonic and anharmonic frequency of the A_{1g} mode as a function of n_c. The wobbles in the curves arise due to oscillations in the

[8] In the case where x describes the displacement of an optical mode, such as the A_{1g} mode in Sb, μ is the reduced mass of the mode.

[9] These operations were carried out using Wolfram Mathematica [113].

second derivative of high order polynomial fits to data. Increasing the order of the polynomial causes these oscillations to shift location, but they cannot be removed by including higher terms. However, the ground state frequency as well as the locations of the roots are insensitive to these wobbles.

We note that as we decrease n_c, the amplitude of motion goes to 0 and the harmonic and anharmonic frequencies become equal. The harmonic frequency goes to 0 at $n_c \sim 3.8\%$, accompanied by the two equivalent A_{1g} equilibrium coordinates x_0 and x_0' becoming degenerate, as shown in Fig. 4.2 (b). This occurs because the harmonic frequency is proportional to the curvature of the potential energy near its minimum, which changes sign when $x_0 \to x_0'$ so must go through 0. Physically, this corresponds to a second order displacive phase transition [114, 115] from the A7 rhombohedral structure to a simple cubic structure, as depicted in Fig 4.3. However, Fig. 4.3 also shows that above a

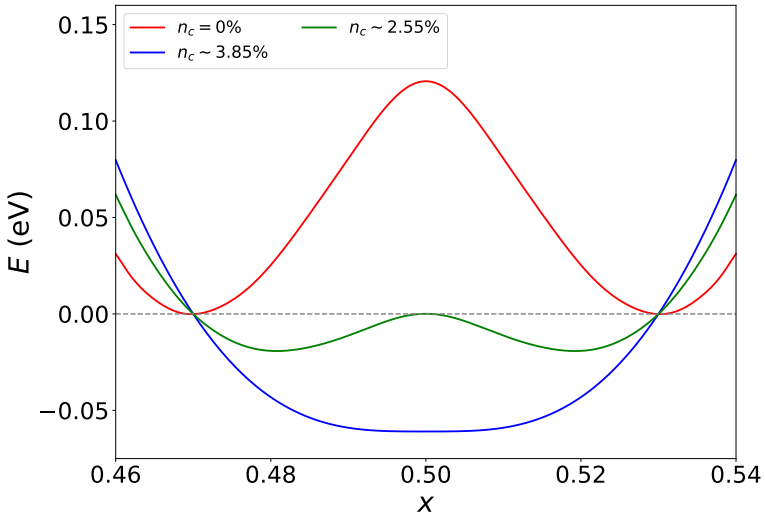

Figure 4.3: Potential energy curves of the A_{1g} mode for three important values of photoexcited carrier concentration n_c. Upon photoexcitation, the A_{1g} coordinate will start off at its equilibrium position x and oscillate between endpoints x_0 and x_0'. The green curve gives the carrier concentration at which the central barrier energy becomes equal to $E(x_0)$. Above this excitation, the A_{1g} coordinate can cross the barrier. The blue curve gives the value of n_c at which the double well potential energy of the A_{1g} mode becomes a single well.

certain threshold for the photoexcited carrier concentration ($n_c \sim 2.55\%$), the atoms are given enough energy to overcome the potential barrier separating the two wells centred on x_0 and x_0'. At this threshold carrier concentration, the initial energy of the atoms is equal to the barrier height, resulting in the atoms being displaced to the location of the potential barrier without returning. The anharmonic frequency goes to 0 (infinite period), as shown in Fig. 4.2 (a).

For higher carrier concentrations, the mode coordinate travels over the barrier and oscillates between the two ground state minima (x_0 and x_0'). If the mode coordinate is driven to traverse the central energy barrier an odd number of times, photoexcitation can permanently shift the equilibrium position from one well to the other, reversing the Peierls distortion. Whether this occurs depends on both the pump pulse energy and the damping of the mode [116]. One possible scenario is that the damping rate of the mode exceeds its frequency, leading to a mode coordinate which is driven over the barrier and does not return. In ferroelectric materials, which are characterised by the development of a permanent nonzero phonon displacement below a critical temperature T_c [117], this can lead to permanent ferroelectric domain reversal [116, 118, 119].

4.3 Comparison with experiment

The work described in this chapter was undertaken in collaboration with Keith Nelson, Sam Teitelbaum and their colleagues at the Massachusetts Institute of Technology (MIT). Single-shot optical pump-optical probe spectroscopy was carried out on a 30 nm thick polycrystalline thin film of Sb which was thermally evaporated on a sapphire $[0001]$ substrate and cryogenically cooled to a temperature of 80 K. The pump and probe were both taken from the fundamental wavelength (800 nm) of the Ti:Sapphire laser. Single-shot measurements were carried out using a dual-echelon single-shot spectrometer, described in more detail in Ref. [107].

The single-shot approach allows the probing of reflectivity oscillations following photoexcitation by a high fluence pump pulse [107]. It is useful at this point to explain the conversion between incident fluence and the number of carriers excited to the conduction bands. The film is 30 nm thick, and the ambipolar diffusivity of free carriers in semimetals is $\sim 30\mathrm{cm}^2/\mathrm{s}$ [120], meaning that the time required for the excited electrons to diffuse to the back of the film is ~ 100 fs, which is significantly less than a single phonon period. Thus, we may assume that the photoinduced carriers are uniformly distributed over the film thickness and can be related to the incident pump fluence as follows:

$$F = \frac{Nd\hbar\omega}{1-R}, \tag{4.8}$$

where d is the film thickness, N is the number of excited carriers per unit volume,

$\hbar\omega$ is the pump photon energy and R is the reflectivity. [10] A photoexcited carrier concentration of $n_c = 1\%$ corresponds to one electron being excited per 10 primitive cells on average [11], so to calculate N, we merely invert the volume (in cm^3) of 10 primitive cells, giving us $N = 1.7 \times 10^{21}\mathrm{cm}^{-3}$. The Reflectivity R is 0.7 for p-polarised light at a wavelength of 800 nm incident at a 10° angle. Eq. (4.8) then tells us that an incident fluence of ~ 4.2 mJ/cm^2 will excite 1% of the valence electrons to the conduction band.

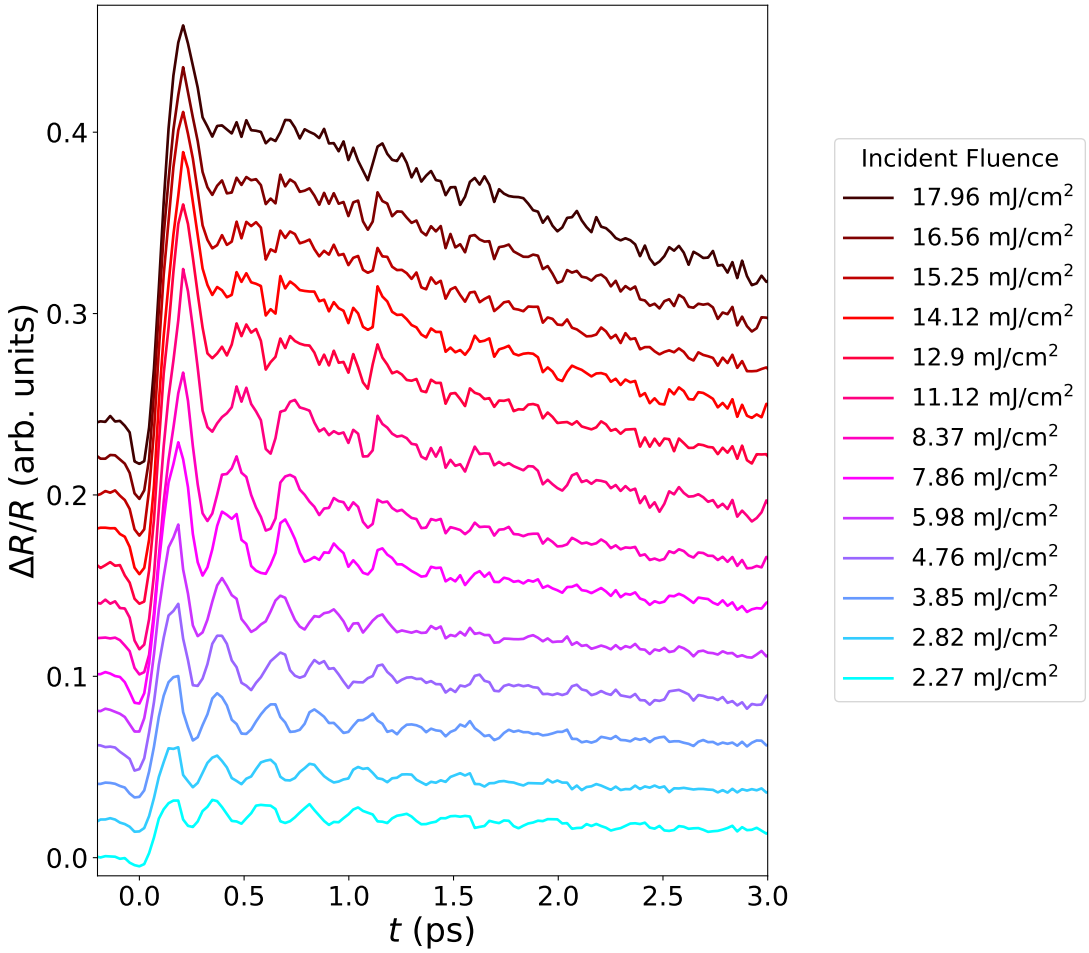

Figure 4.4: Time traces of transient reflectivity $\Delta R/R$ from single shot optical pump-optical probe measurements. The different colours correspond to different incident pump fluences.

Fig 4.4 shows the time trace of the transient reflectivity from the single shot measurements. The traces are offset for clarity and the different colours correspond to different pump fluences ranging from 2.27 to 17.96 meV/cm^2. This

[10] Note that this is the incident fluence. To calculate the absorbed fluence, we would omit the factor of $(1 - R)^{-1}$

[11] This is because Sb has 10 valence electrons.

means the photoexcited carrier concentration varies from ~ 0.54 to $\sim 4.28\%$ of the valence electrons excited to the conduction bands. We can see that the traces show clear signs of A_{1g} mode oscillations, which increase in amplitude but become increasingly damped as the fluence is increased. At pump fluences of ~ 14 mJ/cm^2 and above, there are no visible oscillations of the transient reflectivity.

The individual single shot traces were fit to a decaying exponential term plus an offset to account for electronic and thermal contributions to the transient reflectivity. These terms were then subtracted from the pump-probe trace and the remaining oscillatory component was fit to a single damped oscillation of the form

$$\left(\frac{\Delta R}{R}\right)_{\mathrm{osc}} = A\cos(\omega t + \phi)e^{-\Gamma t}, \tag{4.9}$$

where ω is the angular frequency of the A_{1g} mode, ϕ is its initial phase and Γ is its decay rate. Fig. 4.5 shows the resulting A_{1g} mode frequency as a function of pump fluence alongside the values we calculated using constrained DFT. The spurious oscillations of the A_{1g} mode harmonic frequency which arise from the global high-order polynomial fitting of the potential energy surface make comparison with experiment more challenging. However, these frequencies can also be computed by locally fitting the potential energy curves near their minima with a quadratic function. We computed the harmonic frequency this way for 8 values of n_c evenly spaced between 0 and 2.8% and the results were fit to a cubic function of the form:

$$\nu(n_c) = \nu(0) + an_c + bn_c^2 + cn_c^3, \tag{4.10}$$

where a, b and c are fitting coefficients. The agreement between theory and experiment is reasonably good, providing good evidence for photoinduced phonon softening in antimony.

4.3.1 Reversal of Peierls distortion

Fig. 4.6 (a) shows the anharmonic frequency ν_{AN} and the range of motion of the A_{1g} mode in Sb as calculated using constrained DFT. The anharmonic frequencies are computed using Eq. (4.7) and the range of motion is computed by subtracting the endpoints of motion and scaling by the length c of the trigonal axis in picometers. As the initial energy given to the mode by the pump pulse

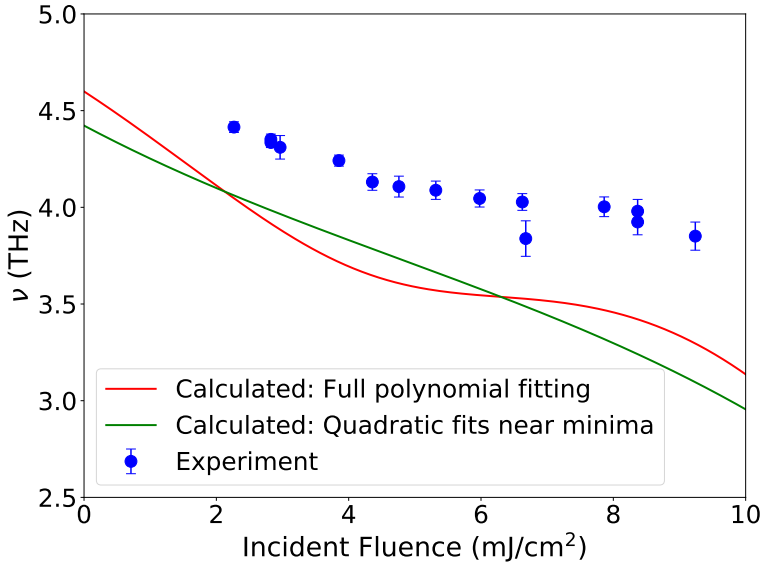

Figure 4.5: Comparison between the experimental and calculated harmonic frequency of the Sb A_{1g} mode. The red line was obtained by taking second derivatives of the polynomial fit in Eq. (4.4). The green line comes from fitting quadratic curves near the minimum for several values of n_c.

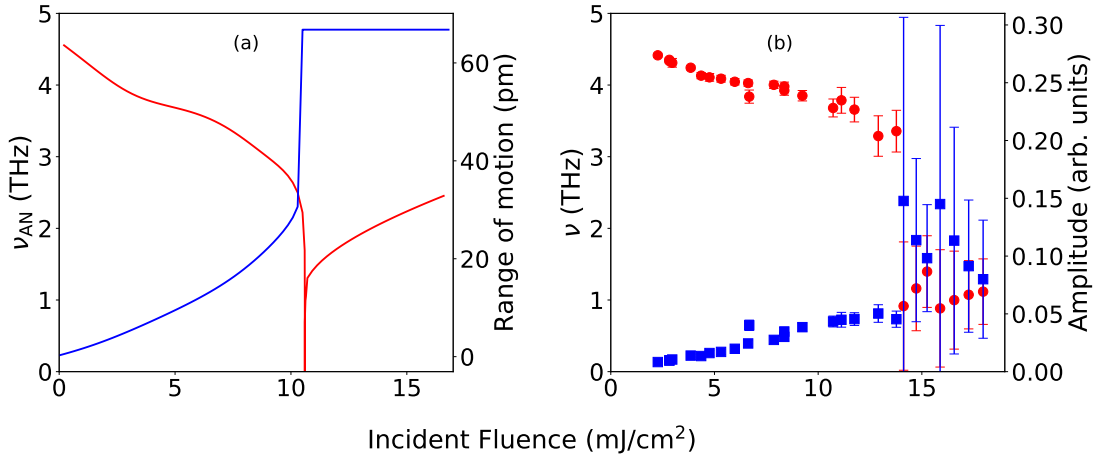

Figure 4.6: (a): The computed anharmonic frequency in THz (red line) as well as the range of motion in pm (blue line) as a function of pump fluence, showing a barrier crossing at ~ 10.5 mJ/cm^2. (b): The experimentally measured frequency in THz (red circles) along with the amplitude of reflectivity oscillations (blue squares) plotted for several pump fluences. At a fluence of ~ 14 mJ/cm^2, the fitting of the reflectivity data becomes unreliable.

is increased beyond the barrier height between the two wells, the anharmonic frequency goes to zero and the range of motion jumps discontinuously to the value $c(x_0' - x_0)$, where the mode oscillates between the two well minima, crossing the barrier each time. Fig. 4.6 (b) shows the fitted frequencies ν and amplitudes of $\Delta R/R$ from the single shot pump probe experiment as a function of incident pump fluence. The frequency and amplitude display similar qualitative

behaviour as seen in the calculations, albeit at a slightly higher fluence, providing a hint that barrier crossing may be occuring at fluences higher than $F \sim 14$ mJ/cm^2. However, the lack of visible oscillations in $\Delta R/R$ along with the large

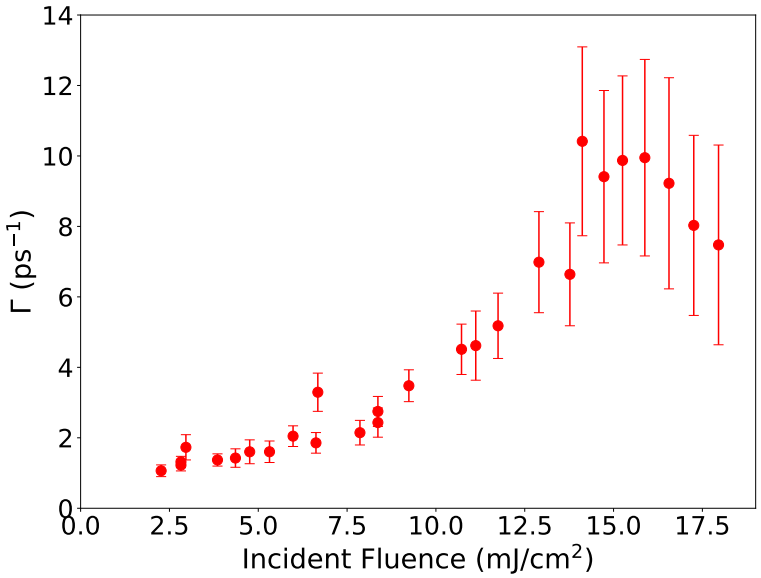

Figure 4.7: Experimentally measured A_{1g} mode decay for several values of incident fluence. At a fluence of ~ 14 mJ/cm^2, the fitting of the reflectivity data breaks down and the damping rate jumps from ~ 6 ps^{-1} to 10 ps^{-1}.

damping of the mode at these fluences (see Fig. 4.7) prevent us from concluding definitively that the experiment sees a barrier crossing. To further explore this, we need to include some damping in our theoretical treatment. To do this, we solve the classical equations of motion for a particle of mass μ moving under the time-dependent potential energy $E(x, n(t))$:

$$\mu\ddot{x}(t) + \lambda\dot{x}(t) + \frac{\partial E(x, n_c(t))}{\partial x} = 0, \quad n_c(t) = n_c(0)e^{-\gamma_c t} \tag{4.11}$$

where λ/μ is the damping constant, which reduces to the damping rate when using dimensionless displacements. At each time, the potential energy $E(x, n_c(t))$ is obtained from the fitting to constrained DFT described in Eq. (4.4). The carrier concentration n_c decays over time as excited electrons relax back to their ground states. We set the lifetime $(1/\gamma_c)$ of these excited electrons to be ~ 3.7 ps, in line with two-temperature model calculations carried out by our collaborators. We use the experimental values of the mode decay rate for each carrier concentration (see Fig. 4.7). The initial conditions are given by setting $x(0)$ to be one of the two equivalent ground state equilibrium positions and $\dot{x}(0) = 0$, which amounts to assuming cosine-like motion. The transient reflectivity is then proportional to

the squared atomic displacement from the centre of the unit cell:

$$\Delta R \propto \left(x(t) - \frac{1}{2}\right)^2 - \left(x_0 - \frac{1}{2}\right)^2, \tag{4.12}$$

where x_0 is the equilibrium mode coordinate and $x(t)$ is the time-dependent displacement of the A_{1g} mode. The resulting simulated transient reflectivity traces are shown in Fig. 4.8 for several fluences ranging from 2.27 - 17.96 mJ/cm^2. These simulations agree well with the pump-probe data from Fig. 4.4 and show evidence of a barrier crossing for a fluence of 17.96 mJ/cm^2. The signature of barrier crossing is seen in the initial bump in ΔR in the first ~ 100 fs of time-evolution. Fig. 4.9 shows the time-dependent displacement $x(t)$, instead of

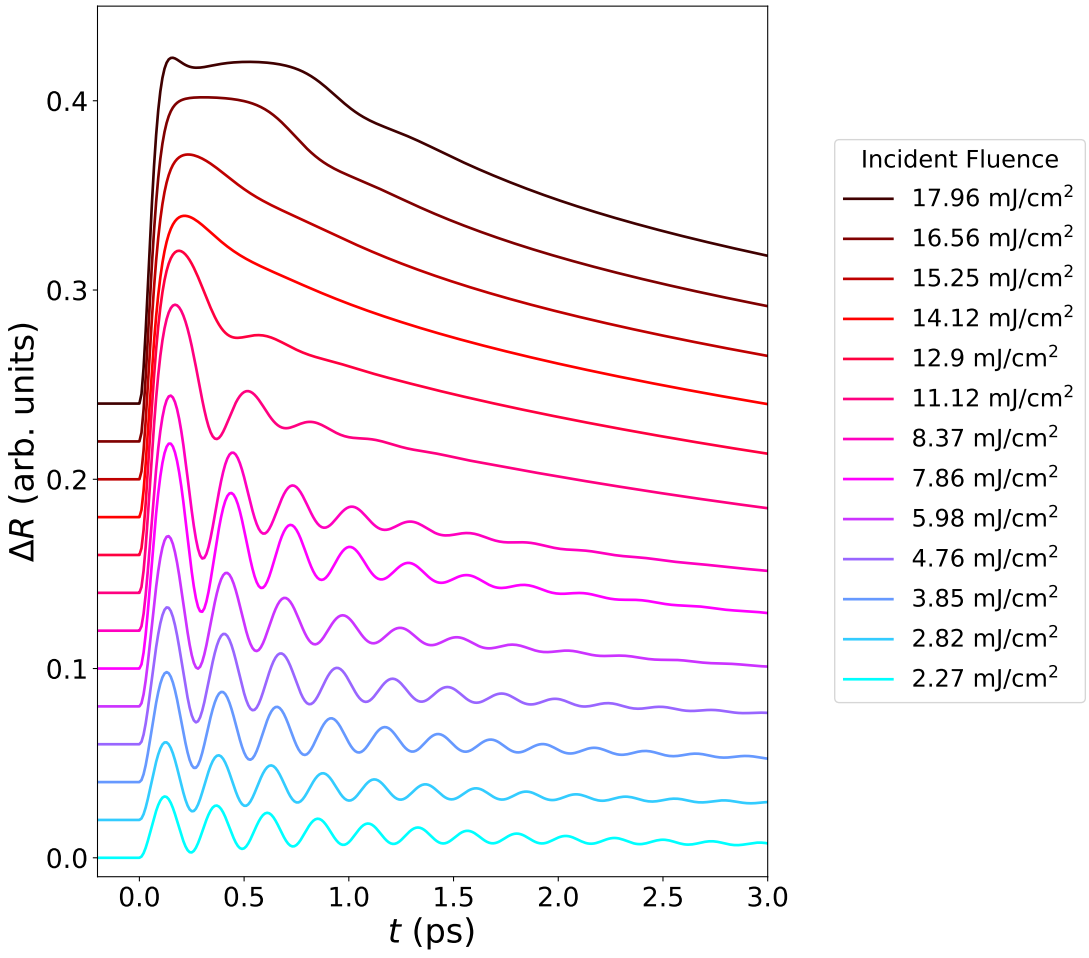

Figure 4.8: Simulations of the coherent A_{1g} mode component of the transient reflectivity obtained by solving the classical equations of motion in a time-dependent potential as described in Eq. (4.11). The traces have been offset for clarity and scaled such that the overall range is similar to that of Fig. 4.4. At a fluence of 17.96 mJ/cm^2, the bump occuring over the first ~ 100 fs indicates a barrier crossing.

its square, which shows the barrier crossing at this fluence more directly. In this

plot, the barrier position is described by a horizontal dashed line which is crossed for a fluence of 17.96 mJ/cm^2, but not for the slightly lower fluence of 16.56 mJ/cm^2. However, the precise value of the mode damping will influence these thresholds so we cannot precisely pinpoint the fluence at which this is expected to occur. However, it is true that both the calculations and the experiment are consistent with a reversal of the Peierls distortion for a pump fluence of ~ 17 mJ/cm^2.

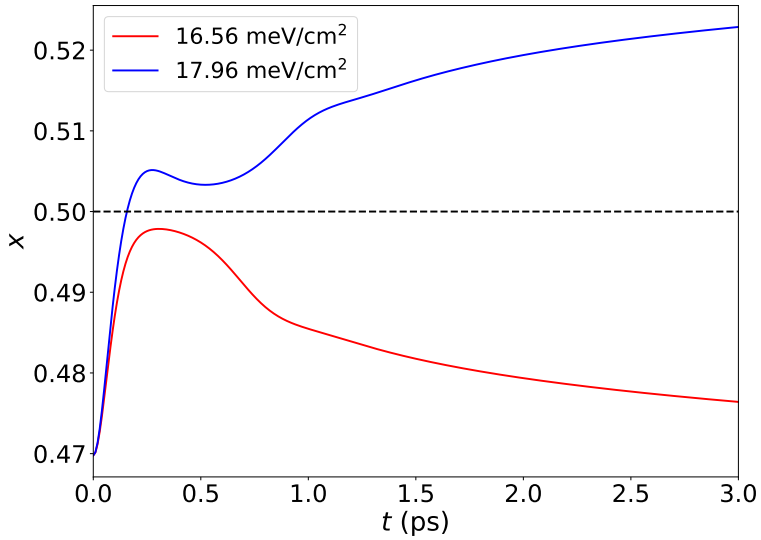

Figure 4.9: Simulated time-dependent A_{1g} mode displacement for the two highest fluences in the experiment. The dashed line marks the position of high-symmetry, where the potential barrier sits. At a fluence of 17.96 mJ/cm^2, the atoms cross the barrier and do not return, suggesting a reversal of the Peierls distortion.

One drawback of the methods that we have used here is our reliance on the experimental A_{1g} mode decay rates. The question arises as to whether we can calculate this decay rate from first principles. In the following section, we will address this question and attempt to compute the room temperature (300 K) fluence dependent decay rate of this mode in Sb.

4.4 Calculations of anharmonic decay of A_{1g} mode in Sb.

Coherent phonons can in principle dissipate their energy in a number of ways. A primary mechanism for this is anharmonic decay [39], whereby the coherent phonon couples to other phonon modes throughout the Brillouin zone.

These many-body phonon-phonon interactions can be expanded in a perturbation series, the lowest order anharmonic terms being so-called 3 phonon processes [121, 122]. The most relevant three phonon process here involves the coherent phonons losing energy by coupling to pairs of acoustic modes with momenta $\mathbf{q}_1 + \mathbf{q}_2 = 0$ and energies which satisfy

$$\hbar\omega_{\mathbf{q}_1\lambda_2} + \hbar\omega_{\mathbf{q}_2\lambda_2} = \hbar\Omega_0, \tag{4.13}$$

where λ_1 and λ_2 denote phonon branches and Ω_0 is the frequency of the coherent mode. For low pump-fluences, it has been demonstrated both theoretically [40] and experimentally [44] that the dominant decay channel for the A_{1g} mode in photoexcited Bi involves it decaying into pairs of acoustic modes with frequencies which satisfy $\Omega_0 = 2\omega_{\mathbf{q}}$. This anharmonic decay is accompanied by a modulation of the mean square displacements $\langle x^2_{\mathbf{q}}\rangle$ of the target modes at twice their harmonic frequency [40, 44, 123]; a process known as resonant squeezing [124] or downconversion [44].

Here we follow the method of Fahy and collaborators [40], calculating the decay rate of the A_{1g} mode in antimony within a classical simulation of third order anharmonicity. To do this, we first compute the 6×6 (2 atoms/cell) dynamical matrix $\mathbf{D}_{\mathbf{q}}(x_0, n_c)$ of Sb as a function of the A_{1g} mode coordinate x_0 as well as the photoexcited carrier concentration using constrained DFT within the single chemical potential approximation, where the photoexcited electrons are assumed to occupy a hot Fermi-Dirac distribution (see section 3.16.1) [12]. The dynamical matrices were computed on a uniform $8 \times 8 \times 8$ Brillouin zone using DFPT and then Fourier interpolated to a $20 \times 20 \times 20$ grid using the ANADDB code [125]. They were computed for excited carrier concentrations of 0 and 1%, and for the equilibrium A_{1g} mode coordinates evaluated at these carrier concentrations. The calculated dynamical matrix elements are then interpolated using linear functions in x_0 and n_c. The energy per unit cell, as a function of x_0 and n_c for the photoexcited system is as described by the fitting in Eq. (4.4) and shown in Fig. 4.1. The A_{1g} mode coordinate x_0 and the correlation functions of the target modes $\langle Q^*_{\lambda\mathbf{q}} Q_{\lambda'\mathbf{q}}\rangle$ obey the coupled equations

$$\ddot{x}_0 = -\frac{1}{Mc^2}\frac{\partial E_0(x_0, n_c)}{\partial x_0} - \frac{1}{N}\sum_{\lambda\lambda'\mathbf{q}} \frac{\mathrm{d}\mathbf{D}_{\lambda\lambda'\mathbf{q}}}{\mathrm{d}x_0}\langle Q^*_{\lambda\mathbf{q}} Q_{\lambda'\mathbf{q}}\rangle, \tag{4.14}$$

[12] We use the single chemical potential because it is possible to perform such calculations in ABINIT without modification. In appendix A, we show that the single chemical potential model gives similar photoexcited frequencies to the two chemical potential model

where λ and λ' are phonon branch indices, c is the lattice constant along the trigonal axis and M is the reduced mass per unit cell for the A_{1g} mode. These equations are then integrated numerically using the Euler-Cromer ("leap-frog") method with a time step of $dt = 5$ fs. For more details on the method, see Ref. [40]. We also need to account for the heat exchange between the excited hot electrons and the lattice as a function of time. This is approximated by Newton's law of cooling, taking the lattice heat capacity to be its Dulong-Petit value of $C_l = 6N_{\rm at}k_{\rm B}$ and assuming that the electron-hole plasma has a heat capacity $C_p = 3N_{\rm el}k_{\rm B}$, where $N_{\rm el}$ and $N_{\rm at}$ denote the number of excited electron-hole pairs and atoms in the system respectively. This allows us to relate the changes in the temperatures of the plasma and the lattice as follows:

$$-C_l\frac{{\rm d}T_l}{{\rm d}t} = \frac{\rm d}{{\rm d}t}Q_{l\to p} = \alpha(T_l - T_p) = C_p\frac{{\rm d}T_p}{{\rm d}t}, \tag{4.15}$$

where T_l is the lattice temperature, T_p is the temperature of the excited electron-hole plasma, $Q_{l\to p}$ is the heat transfer from the lattice to the plasma and α is a constant of proportionality. These equations can be re-arranged to give:

$$\frac{{\rm d}T_l}{{\rm d}t} = -\frac{\alpha}{C_l}(T_l - T_p), \quad \frac{{\rm d}T_p}{{\rm d}t} = -\frac{\alpha}{C_p}(T_p - T_l). \tag{4.16}$$

We define the average energy decay rate of the excited electrons due to electron-phonon scattering as $\gamma_{\rm el} = (1/E_{\rm el})({\rm d}E_{\rm el}/{\rm d}t)$ and the corresponding energy decay rate of the phonons to the electrons as $\gamma_{\rm ph} = (1/E_{\rm ph})({\rm d}E_{\rm ph}/{\rm d}t)$. Since T_l and T_p are proportional to the average of $E_{\rm ph}$ and $E_{\rm el}$ respectively, we can re-write Eqs. (4.17) to give the rate of change of the temperature difference as a function of $\gamma_{\rm ph}$ and $\gamma_{\rm el}$:

$$\frac{\rm d}{{\rm d}t}(T_p - T_l) = -(\gamma_{\rm ph} + \gamma_{\rm el})(T_p - T_l). \tag{4.17}$$

The fact that the electrons are initially at a much higher temperature ($\sim$ few thousand K) than the lattice (300 K) means that the $\gamma_{\rm el}$ terms dominates here. In parent element Bi, this term has been estimated to be $\sim 0.5\ {\rm ps}^{-1}$. We adopt this as an approximate electron cooling rate in Sb due to its similarities between Bi and Sb.

This method for simulating the coupled dynamics of the coherent and target modes is expected to be reliable only for low levels of excitation, since for higher levels of excitation the coherent mode coordinate spends a lot of time near the barrier, where other modes in the Brillouin zone are expected to go unstable. These unstable modes exhibit imaginary frequencies and will not behave well

within this model. For this reason we restrict ourselves to photoexcited carrier densities less or equal to 1% of valence electrons excited, or an incident fluence of ~ 4.2 mJ/cm^2 in the experiment.

Fig. 4.10 (a) shows the calculated evolution of the A_{1g} coordinate for an initial lattice temperature of 300 K when $n_c = 1\%$ of valence electrons are excited to the conduction bands. The results show a damped oscillation with a decay rate of ~ 0.65 ps^{-1}. This time evolution was repeated for $n_c = 0.1, 0.2, \ldots 1\%$ as well as a low concentration run for $n_c = 0.01\%$ and the resulting decay rates were interpolated to produce a smooth curve as shown in Fig. 4.10 (b).

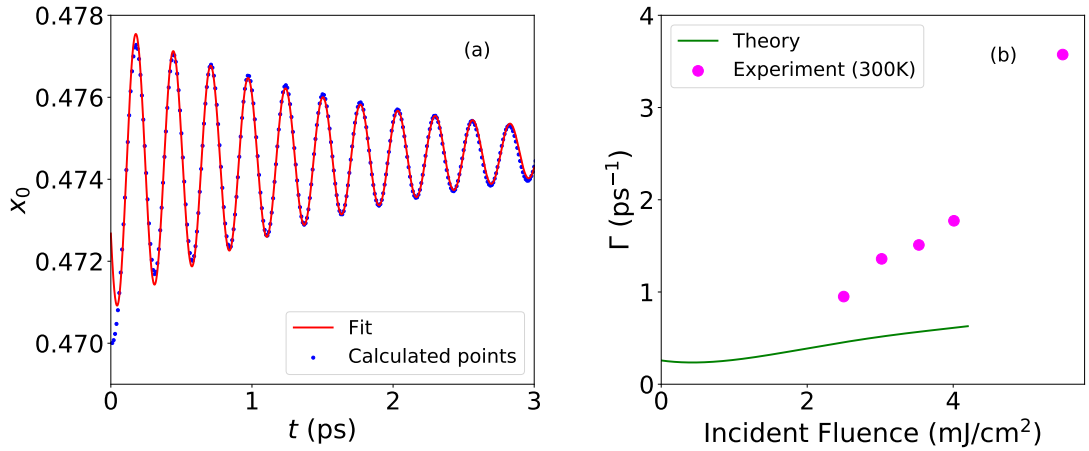

Figure 4.10: (a): Calculated time evolution of the A_{1g} mode coordinate x_0 at an excitation density of $n_c = 1\%$ valence electrons excited to the conduction bands, showing damped oscillations. These oscillations are fit to a decaying cosine term plus a constant shift. (b): Calculated and measured A_{1g} mode decay rates as a function of fluence. The experimental values clearly rise more steeply with increasing incident fluence.

Interestingly, the experimental decay rates are higher at all pump fluences and they follow a much steeper trend with increasing fluence. This discrepancy between the calculated and measured A_{1g} mode decay rates in Sb has also been reported in Ref. [126], where they performed molecular dynamics calculations in a supercell of 576 Sb atoms and saw no significant dependence of the A_{1g} mode decay rate on the electronic temperature in their simulation. Their calculation was non-perturbative, suggesting that 4 phonon processes and higher are likely not the source of our discrepancy with experiment.

Despite the growing discrepancy between theory and experiment with increasing fluence, our simulations do achieve good agreement with experiment for the low fluence limit of the A_{1g} mode decay rate. Fig. 4.11 shows the room temperature pump-probe traces for Sb from Ref. [1], fit to a decaying cosine, an offset due

to the shift in the equilibrium mode coordinate and a decaying exponential to capture the effects of electronic decay. The fitting produces an experimental

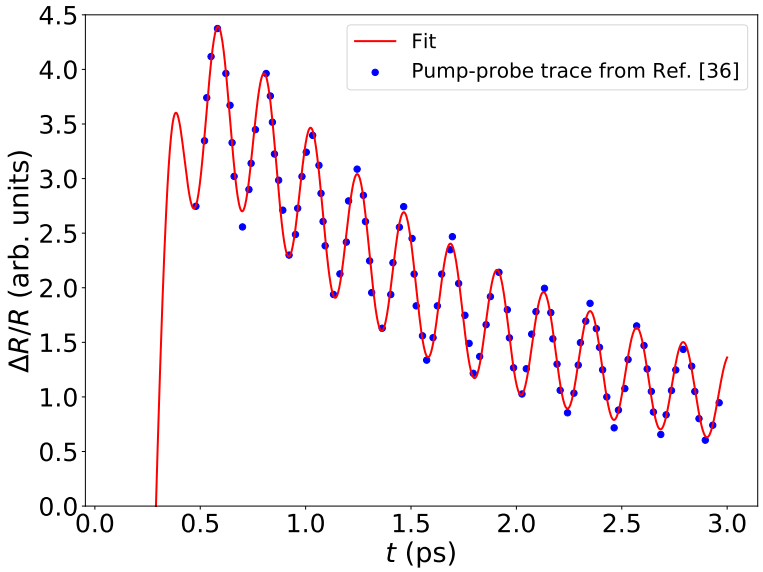

Figure 4.11: Transient reflectivity trace from pump-probe measurements in Ref. [1]. The experimental data was fit to a decaying cosine, a constant shift and a decaying exponential (electronic decay).

decay rate of $0.28\ \mathrm{ps}^{-1}$, which is in excellent agreement with the low fluence limit of our calculations: $\Gamma \approx 0.25\ \mathrm{ps}^{-1}$. We can also extract the same number from the Raman spectra in Ref. [1]. The full width at half maximum gives the energy decay rate of the mode to be $0.62\ \mathrm{ps}^{-1}$. The energy of a damped harmonic oscillator decays twice as fast as its amplitude. This is apparent when we consider that the energy E of the oscillator is proportional to its amplitude squared as follows:

$$E \propto |A|^2 = \left|A_0 e^{-\Gamma t}\right|^2 = |A_0|^2 e^{-2\Gamma t} = E_0 e^{-2\Gamma t}, \tag{4.18}$$

where A is the amplitude of the mode and Γ is the amplitude decay rate. Thus, the energy of the mode decays with a decay rate of 2Γ. This means that the amplitude decay rate implied by the Raman spectra is $0.62/2 = 0.31\ \mathrm{ps}^{-1}$, also in good agreement with our calculated value.

Overall, the calculations of the A_{1g} mode decay rate agree well with experiment at low pump fluence, but increasingly depart from the experimental results with increasing fluence. Since the nonperturbative approach employed by Ref. [126] also fails to capture the steep trend in decay rate with increasing fluence, this discrepancy cannot be explained by higher-order phonon-phonon scattering

processes. The electron-phonon interaction could in principle explain this trend, especially since its scattering rate is highly fluence dependent. However, due to time constraints, we have not yet been able to pursue this. Therefore, it remains an open question.

4.5 Summary

We have calculated the potential energy and harmonic frequency of the A_{1g} mode as a function of photoexcited carrier concentration, and hence pump-fluence. These calculations are in good agreement with single shot pump-probe experiments which carried out by our collaborators. We simulate pump-probe traces of the transient reflectivity, which agree well with the experimental traces, and show that Sb undergoes a reversal of its Peierls distortion at an incident fluence of 17.96 mJ/cm^2. We calculate the decay rate of the A_{1g} mode due to third order anharmonic coupling, which agree well with low fluence experimental measurements, but depart significantly from measurements at higher fluence. Comparison of our calculations with those of Ref. [126], who use a nonperturbative approach, rule out the possibility that higher order anharmonicity could explain this discrepancy. We suggest that electron-phonon scattering may provide an explanation, since its rates depend strongly on the density of excited carriers, and hence the pump-fluence. However, this remains an open question.

Chapter 5

Ultrafast relaxation of symmetry-breaking photo-induced atomic forces

Abstract

In this chapter, we present a first-principles method for the calculation of the temperature-dependent relaxation of symmetry-breaking atomic driving forces in photoexcited systems. We calculate the phonon-assisted decay of the photoexcited force on the low-symmetry E_g mode following absorption of an ultrafast pulse in Bi, Sb and As. The force decay lifetimes for Bi and Sb are of the order of 10 fs and in agreement with recent experiments, demonstrating that electron-phonon scattering is the primary mechanism relaxing the symmetry-breaking forces. Calculations for a range of absorbed photon energies suggest that larger amplitude, symmetry-breaking atomic motion may be induced by choosing a pump photon energy which maximises the product of the initial E_g force and its lifetime. The high-symmetry A_{1g} force undergoes a partial decay to a non-zero constant on similar timescales, which has not yet been measured in experiments, suggesting that the A_{1g} mode is driven by a combination of impulsive and displacive forces. The average imaginary part of the electron self-energy over the photoexcited carrier distribution provides a crude indication of the decay rate of symmetry-breaking forces. The work described in this chapter has been published in Physical Review Letters. [30]

5.1 Introduction

Photoexcitation with a laser pulse of duration much less than the fastest phonon period can be used to launch large amplitude coherent atomic motion in a variety of materials and molecules [14]. However, symmetry-breaking coherent atomic motion has been shown experimentally to have an amplitude orders of magnitude less than that of symmetry-preserving coherent atomic motion in a variety of materials [1, 22, 23, 24]. Furthermore, the amplitudes of symmetry-breaking modes decrease strongly with increasing sample temperature, whereas high-symmetry mode amplitude is relatively insensitive to temperature, indicating very different aspects of the ultrafast dynamics affecting the two cases. If we understand the limiting mechanisms, it may be possible to suppress them and drive larger amplitude symmetry-breaking coherent atomic motion.

We will focus on the group V semimetals: Bi, Sb and As. Bi and Sb have proven to be useful model systems for pump-probe reflectivity experiments due to their large vibrational response to optical excitation [25, 26, 27, 28]. As has not been widely used in these experemients, presumably due to the safety concerns associated with hitting a poisonous material with an intense burst of light. High-symmetry coherent A_{1g} phonons can be generated in these materials through a mechanism termed displacive excitation of coherent phonons (DECP, see section 2.4) [31], related to the absorptive part of the Raman response [21]. Additionally, when the pump pulse is polarised perpendicular to the 3-fold rotational axis of the crystal, the symmetry-breaking E_g mode has also been detected [15, 1], but with a much lower amplitude that falls off strongly with increasing sample temperature. In fact, symmetry-breaking modes often go undetected unless the sample temperature has been reduced below a certain threshold and specialized, polarization-sensitive measurements are used to detect the reflected probe radiation.

In this work, we provide a quantitative understanding of how incoherent electron-phonon scattering limits the generation of symmetry-breaking coherent atomic motion. We combine density functional perturbation theory (DFPT) [60], and electron-phonon scattering rate equations [127, 35, 128] to calculate the evolution on fs timescales of a photoexcited electronic distribution generated by optical absorption and compute the resulting time-dependent atomic forces in the group-V semimetals, Bi, Sb and As. We find that electron-phonon scattering dominates in determining the lifetime of the E_g driving force in photoexcited Bi

and Sb, with calculated lifetimes in good agreement with recent experiments [1], and we predict similar behavior in As. We calculate the dependence of the initial atomic driving forces and their lifetimes on the photon energy of the pump pulse and suggest how variation of the incident photon energy may be used to maximise the impact on low-symmetry atomic motion.

Our method goes beyond standard time-dependent density functional theory (TDDFT) [129] approaches by explicitly considering the coupling of the excited electron-hole plasma to the continuum of thermal phonon modes throughout the Brillouin zone and can be used to compute the lifetime of symmetry-breaking photo-induced atomic forces on ultrafast timescales in a variety of materials.

At room temperature, the E_g mode in bismuth (antimony) was observed to have an amplitude ~ 10 (30) times smaller than the high-symmetry A_{1g} mode [15, 1]. In 2015, Murray et. al. calculated the initial photoexcited distribution of electrons in Bi from first principles, taking into account the optical transition matrix elements, and computed the resulting atomic forces with constrained DFT (see sections 3.17 and 3.16), showing that the initial driving forces exerted on the A_{1g} and E_g modes are comparable. [50]. Therefore, the highly reduced amplitude of the E_g mode indicates that the E_g driving force is extremely short lived. Recent experimental work utilised a combination of optical pump-optical probe and continuous-wave (cw) Raman scattering to indirectly determine the lifetime of the E_g driving force in Bi and Sb as a function of temperature. The E_g force lifetime in bismuth (antimony) was found to vary from 13 ± 4 fs (17 ± 2 fs) at 10 K to 2 ± 0.4 fs (5.5 ± 0.5 fs) at room temperature [1]. It was suggested that the rapid, temperature-dependent relaxation of this force was due to the initial low-symmetry excited electron-hole plasma rapidly regaining full symmetry via electron-phonon scattering. A similar conclusion was reached in other experimental work [15], where the E_g driving force in bismuth was shown to have a decay time of ~ 4 fs at room temperature. A study of the coherent modes in topological insulator Bi_2Te_3 showed similar behaviour of the symmetry-breaking E_g modes, whose relatively small amplitude compared with the fully symmetric A_{1g} modes was attributed to short-lived photoexcited electronic states with lifetimes ~ 10 fs [22]. A recent calculation [37] found the timescale for equilibration of L valley occupations in photoexcited silicon via electron-phonon scattering to be 180 fs, but did not consider the consequences for the generation of symmetry-breaking coherent atomic motion. As discussed in subsection 2.3.1, the group-V semimetals crystallise in the A7 rhombohedral structure, with 2 atoms per unit cell. One atom is at the origin and the other displaced a distance

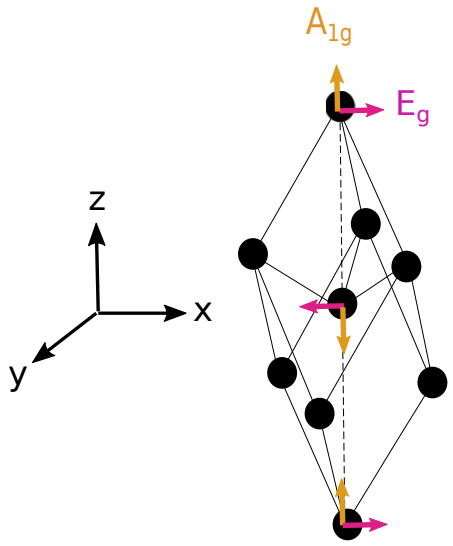

Figure 5.1: The crystal structure of the A7 rhombohedral structures Bi, Sb and As. The dashed vertical line corresponds to the c-axis of the crystal. The coherent A_{1g} and E_g modes are marked with arrows.

zc along the trigonal axis (c-axis), which is represented by a dashed line in the inset of Fig. 5.1. The internal atomic displacement parameter, z, is highly sensitive to excitation of electrons to the conduction bands. This alters the equilibrium value of z and generates oscillations of the symmetry-preserving A_{1g} mode. In contrast, the symmetry-breaking E_g mode involves motion of the atoms perpendicular to the c-axis and is thus not driven by the conventional DECP mechanism, which assumes occupations of excited electron states that preserve crystal symmetry. The E_g mode is driven by unbalanced occupation of symmetry-equivalent regions of the Brillouin zone following photoexcitation by a pump polarised perpendicular to the 3-fold axis of the crystal [1, 50]. In fact, we will also show that even the A_{1g} mode is not fully explained by the DECP model, but rather has a second component which is impulsive.

5.2 Theoretical framework and methodology

We compute electron states $|n\mathbf{k}\rangle$ with energy $\epsilon_{n\mathbf{k}}$ for band n at momenta $\mathbf{k}$, and phonon normal modes $\mathbf{e}^{\lambda}(\mathbf{q})$ with frequency $\omega_{\lambda\mathbf{q}}$ at momenta $\mathbf{q}$ on a uniform grid in the Brillouin zone and find the electron-phonon matrix elements , $g^{\lambda\mathbf{q}}_{\mathbf{k}nm}$ as defined in Ref. [89], on the same grid using DFPT [60] [1]. These quantities are

[1] In appendix E we cross check the electron-phonon matrix elements obtained with DFT against those obtained using the frozen-phonon method.

then interpolated to a finer grid using maximally localised Wannier functions [94]. See sections 3.4, 3.14 and 3.15 for details on these methods. We generate the initial non-equilibrium photoexcited distribution in the same manner as Ref. [50], using the optical transition probabilities computed within the dipole approximation. The distribution of photoexcited carriers in the conduction (cb) and valence (vb) bands are proportional to:

$$g^{\text{opt}}_{n\mathbf{k}} \equiv \sum_{m\in\text{cb}} |\langle\psi_{n\mathbf{k}}|\mathcal{E}\cdot\mathbf{p}|\psi_{m\mathbf{k}}\rangle|^2\delta(\varepsilon_{n\mathbf{k}}-\varepsilon_{m\mathbf{k}}-\hbar\omega), \quad \text{for } n\in\text{cb}, \tag{5.1}$$

and

$$g^{\text{opt}}_{m\mathbf{k}} \equiv -\sum_{n\in\text{cb}} |\langle\psi_{n\mathbf{k}}|\mathcal{E}\cdot\mathbf{p}|\psi_{m\mathbf{k}}\rangle|^2\delta(\varepsilon_{n\mathbf{k}}-\varepsilon_{m\mathbf{k}}-\hbar\omega), \quad \text{for } m\in\text{vb}, \tag{5.2}$$

where $\mathcal{E}$ is the polarisation of the pump pulse and ω is the radiation frequency. This enables us to generate initial distributions of photoexcited electrons which have a broken 3-fold symmetry by choosing $\mathcal{E}$ is aligned perpendicular to the z-axis, producing a non-zero force on the symmetry-breaking E_g mode, as discussed in section 3.17.3. The excited electronic occupations are then evolved in time using electron-phonon rate equations at the level of the semi-classical Boltzmann equation [127, 35, 128]:

$$\frac{\partial f_{n\mathbf{k}}}{\partial t} = \sum_{m,\mathbf{q},\lambda,\xi}\left[R^{\xi}_{\lambda}\left(m\mathbf{k}+\mathbf{q},n\mathbf{k}\right)-R^{\xi}_{\lambda}\left(n\mathbf{k},m\mathbf{k}+\mathbf{q}\right)\right] \tag{5.3}$$

$$\frac{\partial n_{\mathbf{q}\lambda}}{\partial t} = \sum_{\mathbf{k},n,m}\left[R^{+}_{\lambda}\left(m\mathbf{k}+\mathbf{q},n\mathbf{k}\right)-R^{-}_{\lambda}\left(n\mathbf{k},m\mathbf{k}+\mathbf{q}\right)\right], \tag{5.4}$$

where $\xi =$ phonon emission $(+)$ or phonon absorption $(-)$, $f_{n\mathbf{k}}$ ($f_{m\mathbf{k}+\mathbf{q}}$) is the occupation of electronic state $|n\mathbf{k}\rangle$ ($|m\mathbf{k}+\mathbf{q}\rangle$), $n_{\mathbf{q},\lambda}$ are the phonon occupations for branch λ, and R^{ξ}_{λ} are the electron-phonon scattering rates defined by Fermi's golden rule:

$$R^{\pm}_{\lambda}\left(n\mathbf{k},m\mathbf{k}+\mathbf{q}\right) = \frac{1}{N}\frac{1}{\omega_{\lambda\mathbf{q}}}\left|g^{\lambda\mathbf{q}}_{\mathbf{k}nm}\right|^2 f_{n\mathbf{k}} \quad \times \tag{5.5}$$

$$\left(1-f_{m\mathbf{k}+\mathbf{q}}\right)\left(n_{\lambda\mathbf{q}}+\frac{1}{2}\pm\frac{1}{2}\right)\delta(\varepsilon_{m\mathbf{k}+\mathbf{q}}-\varepsilon_{n\mathbf{k}}\pm\hbar\omega_{\lambda\mathbf{q}}), \tag{5.6}$$

where N is the number of wave vectors $\mathbf{k}$ (or $\mathbf{q}$) in the uniform Brillouin zone grid, $\omega_{\mathbf{q}\lambda}$ are the phonon frequencies and $\delta(\varepsilon_{m\mathbf{k}+\mathbf{q}}-\varepsilon_{n\mathbf{k}}\pm\hbar\omega_{\lambda\mathbf{q}})$ are the energy conserving delta functions for emission and absorption of a phonon. Finite lifetimes give the electronic states a Lorentzian line shape in energy and the

energy conservation delta-function broadens to a Lorentzian whose width is the sum of the linewidths of the initial and final state in the scattering process [38]:

$$P^{\pm} = \frac{\mathrm{Im}\{\Sigma_{m\mathbf{k}+\mathbf{q}} + \Sigma_{n\mathbf{k}}\}}{[\Delta\varepsilon^{nm}_{\mathbf{k},\mathbf{k}+\mathbf{q}} \pm \hbar\omega_{\lambda\mathbf{q}}]^2 + [\mathrm{Im}\{\Sigma_{m\mathbf{k}+\mathbf{q}} + \Sigma_{n\mathbf{k}}\}]^2}, \tag{5.7}$$

where $\Delta\varepsilon^{nm}_{\mathbf{k},\mathbf{k}+\mathbf{q}} = \varepsilon_{m\mathbf{k}+\mathbf{q}} - \varepsilon_{n\mathbf{k}}$ and $\mathrm{Im}\{\Sigma_{n\mathbf{k}}\}$ is the imaginary part of the electron self-energy for state $|n\mathbf{k}\rangle$:

$$\mathrm{Im}\{\Sigma_{n\mathbf{k}}\} = \frac{\hbar}{2N}\frac{1}{\omega_{\lambda\mathbf{q}}}\sum_{m,\mathbf{q}\lambda}\left|g^{\lambda\mathbf{q}}_{\mathbf{k}nm}\right|^2\Big[(f_{m\mathbf{k}+\mathbf{q}} + n_{\lambda\mathbf{q}})\delta(\varepsilon_{m\mathbf{k}+\mathbf{q}} - \varepsilon_{n\mathbf{k}} - \hbar\omega_{\lambda\mathbf{q}}) \tag{5.8}$$

$$+ (1 + n_{\lambda\mathbf{q}} - f_{m\mathbf{k}+\mathbf{q}})\delta(\varepsilon_{m\mathbf{k}+\mathbf{q}} - \varepsilon_{n\mathbf{k}} + \hbar\omega_{\lambda\mathbf{q}})\Big] \tag{5.9}$$

It is temperature-dependent and related to the equilibrium lifetime of the state

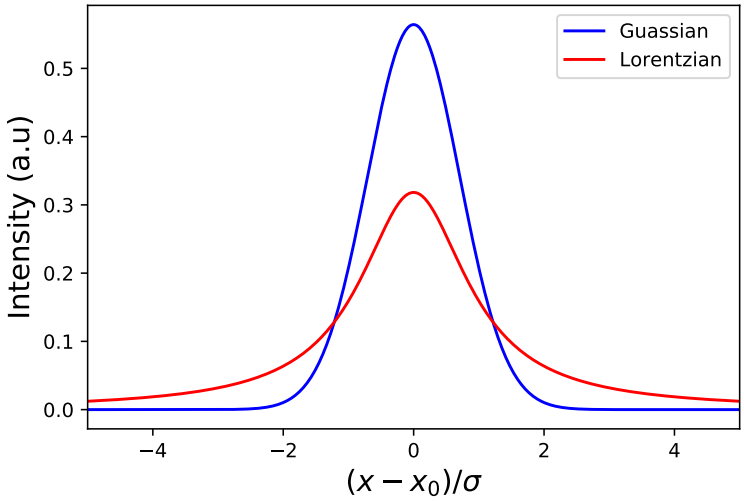

Figure 5.2: Comparison of Gaussian and Lorentian lineshapes of the same spectral weight. The gaussian is expressed as $\frac{1}{\sigma\sqrt{\pi}}\exp\{-(\frac{x-x_0}{\sigma})^2\}$, whereas the corresponding Lorentzian is expressed as $\frac{1}{\pi}\frac{\sigma}{(x-x_0)^2+\sigma^2}$. The Lorentzian is significantly more tailed than the corresponding Gaussian.

via $1/\tau_{n\mathbf{k}}(T) = 2\,\mathrm{Im}\{\Sigma_{n\mathbf{k}}(T)\}/\hbar$ [89]. Although the physically correct form of the electronic state lineshape is Lorentzian (as in Eq. (5.7)), it is numerically convenient for us to instead treat it as a Gaussian lineshape. As illustrated in Fig. 5.2, the tails of a Gaussian distribution die off more quickly than those of the corresponding Lorentzian. We have verified that this choice of lineshape does not appreciably affect our results. In practice, we calculate $\mathrm{Im}\{\Sigma_{n\mathbf{k}}\}$ by replacing the energy conserving delta function with a Gaussian. However, the calculated E_g force lifetimes are insensitive to the width of this Gaussian. The replacement of an exact energy conserving dirac delta function with a lineshape

brings our rate equations into agreement with the completed-collisions limit of the Kadanoff-Baym equations [37]. This limit is also equivalent to a density matrix approach in the limit of Markovian scattering. This means that the scattering is memoryless, so that the scattering probabilities at time t depend on the occupations at the same time, and not on the occupations at times earlier than t.

The atomic force $\boldsymbol{F_\alpha}$ on atom α in the unit cell is computed at each time step using the diagonal part of the electron-phonon matrix:

$$\boldsymbol{F_\alpha} = -\frac{1}{N}\sum_{n,\mathbf{k}} \Delta f_{n\mathbf{k}} \langle n\mathbf{k}|\nabla_{\boldsymbol{\tau_\alpha}}\hat{H}|n\mathbf{k}\rangle \,, \tag{5.10}$$

where $\Delta f_{n\mathbf{k}} = f_{n\mathbf{k}} - f^0_{n\mathbf{k}}$ is the change in occupation of state $|n\mathbf{k}\rangle$ from its equilibrium value [2] and $\boldsymbol{\tau_\alpha}$ is the displacement of atom α from equilibrium. [3]

5.3 Results

The time evolution of both the E_g and the A_{1g} driving forces are shown in Fig. 5.3, demonstrating that the E_g force exponentially decays to zero, as expected, while the A_{1g} force undergoes a more complex time evolution. In Bi and Sb, the A_{1g} force undergoes a partial decay from its initial value to a non-zero constant. In As, the A_{1g} force increases slightly before decaying to a non-zero constant. This is not surprising, since the evolution of the A_{1g} force depends on the precise distribution of photoexcited electrons. In fact, at some other photon energies, the evolution of the A_{1g} forces in Bi and Sb also depart from purely exponential behaviour. There has been debate as to whether the A_{1g} mode is driven by an impulsive or a displacive force [25, 130]. The calculated partial decay of the A_{1g} force tells us that the A_{1g} mode is in fact driven by a combination of the two. The component of the force that does not decay on these timescales corresponds to a displacive force. The term that decays on a timescale much shorter than the

[2] The equilibrium distribution should be given by a Fermi-Dirac distribution at the instantaneous temperature of the lattice. However, since the lattice temperature does not change appreciably on tens-of-femtoseconds timescales, we can safely set this equal to the initial electronic distribution before photoexcitation.

[3] We have also computed the atomic forces self consistently within the framework of CDFT [3] using the ABINIT package [74]. We find that the E_g force computed both ways agree very well, so we use the approach in Eq. (5.10) as it is more efficient. The A_{1g} force depends more delicately on the exact values of the equilibrium electronic occupations, $f^0_{n\mathbf{k}}$, so we compute it within CDFT.

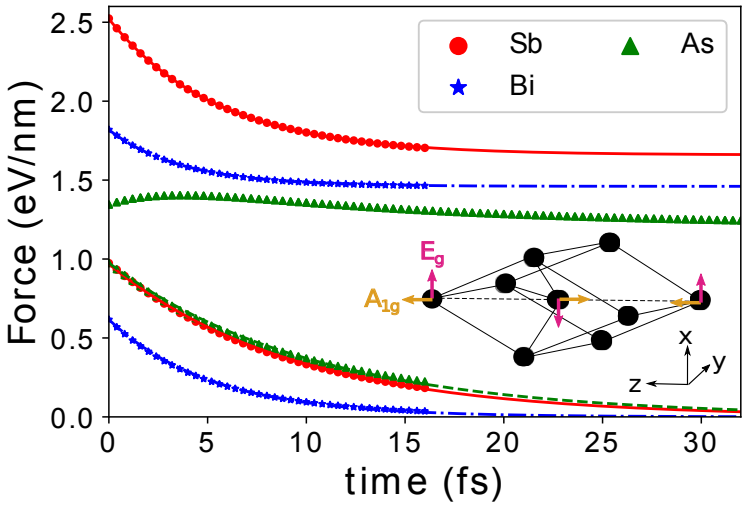

Figure 5.3: The E_g and A_{1g} driving forces in Bi, Sb and As as functions of time-delay, following the absorption of 0.1 photons of energy $\hbar\omega = 1.5$ eV per unit cell. The three upper plots show the A_{1g} force, the three lower show the E_g force. The solid lines are fittings to the explicitly calculated data points. F_{E_g} is fit to a decaying exponential $F_{E_g}(t=0)\exp\{-t/\tau_{E_g}\}$ and $F_{A_{1g}}$ is fit to a decaying exponential plus a constant term: $F^1_{A_{1g}}\exp\left\{-t/\tau_{A_{1g}}\right\} + F^2_{A_{1g}}$ as discussed in the main text. Inset: The unit cell of the group-V semimetals. The pink (gold) arrows indicate atomic motion corresponding to the E_g (A_{1g}) modes.

pump pulse duration is impulsive, since it gives a sudden kick to the A_{1g} mode.

The final values of the A_{1g} forces in Bi and Sb are obtained by fitting the calculated time-dependent values to a decaying exponential plus a constant term, as explained in the caption of Fig. 5.3. In As, we extract the final A_{1g} force by fitting the same function to the tail of the calculated values. In Table 5.1, we see that the final A_{1g} forces in all three materials are slightly higher than that which would be obtained in constrained DFT (CDFT) by assuming a hot thermal distribution of electrons and holes, with different chemical potentials [3]. The one chemical potential method produces forces which are in excellent agreement with those produced by the two chemical potential model, as shown in the fourth column of table 5.1. It should be noted that the A_{1g} force must eventually relax to 0 when the excited electronic occupations return to equilibrium i.e. $\Delta f_{n\mathbf{k}} = 0$, as indicated by Eq. (5.10). However, this requires the excited electrons to reach the same temperature as the lattice and for all electrons and holes to recombine. This process occurs on much longer timescales (> 10 ps) [120] and is beyond the scope of this work.

Table 5.1: Comparison of initial (F^i_{A1g}) and final A_{1g} force (F^f_{A1g}) with those obtained in a two-chemical potential CDFT calculation ($F^{2\mu}_{A1g}$) [3] and those obtained in a one-chemical potential calculation ($F^{1\mu}_{A1g}$). The forces are computed assuming an absorbed fluence of 0.1 photons of energy 1.5 eV per unit cell.

Material	F^i_{A1g} (eV/nm)	F^f_{A1g} (eV/nm)	$F^{2\mu}_{A1g}$ (eV/nm)	$F^{1\mu}_{A1g}$ (eV/nm)
Bismuth	1.82	1.46	1.34	1.40
Antimony	2.52	1.66	1.38	1.35
Arsenic	1.35	1.21	1.13	1.02

5.3.1 Reinterpretation of experimental results given partial decay of A_{1g} force.

As we explain in chapter 1, Li et. al. [1] determined the E_g force lifetime indirectly, by comparing the ratio of the E_g to A_{1g} mode amplitude in an optical pump-optical probe experiment with cross-sections obtained in a cw Raman scattering experiment. The experimental E_g force lifetimes in Ref. [1] were derived, assuming that the A_{1g} force does not change over the duration of the pump-pulse (~ 70 fs). However, our calculations show a decay of the A_{1g} force from $F_0 \rightarrow sF_0$ in much less than 70 fs for Bi ($s \sim 0.80$) and Sb ($s \sim 0.65$), as shown in Fig. 5.3. Therefore, in order to make a quantitative comparison with our theoretical results, we need to adjust the experimental analysis of [1] to account for this partial decay.

To estimate the impact of this on the experimentally derived E_g force lifetime, we need to understand the amount by which this partial decay modifies the initial amplitude of the A_{1g} mode. At times much greater than the pump pulse duration ($t \gg \tau_p$) and assuming that the pump pulse duration is much less than the phonon period ($\Omega\tau_p \ll 1$), we can describe the A_{1g} mode by a harmonic oscillator subject to 2 driving forces, a step function which decays at a rate Γ, and one which does not decay. This gives the following equation of motion :

$$\ddot{Q} + \Omega^2 Q = \frac{F_0}{\mu}[s + (1-s)e^{-\Gamma t}], \tag{5.11}$$

where s is a dimensionless parameter, F_0 is the initial driving force and μ is the effective mass. Making the substitution $Q \rightarrow \mu Q/F_0$, we arrive at the simpler equation:

$$\ddot{Q} + \Omega^2 Q = s + (1-s)e^{-\Gamma t}, \tag{5.12}$$

which has a general solution of the form:

$$Q(t) = A\cos(\Omega t + \phi) + \frac{s}{\Omega^2} + \frac{1-s}{\Gamma^2+\Omega^2}e^{-\Gamma t}. \tag{5.13}$$

The initial conditions are that $Q(0) = 0$ and that $\dot{Q}(0) = 0$, which give us the following:

$$-A\cos(\phi) = \frac{s}{\Omega^2} + \frac{1-s}{\Gamma^2+\Omega^2} \tag{5.14}$$

$$-A\sin(\phi) = \frac{1-s}{\Gamma^2+\Omega^2}\left(\frac{\Gamma}{\Omega}\right). \tag{5.15}$$

Taking the ratio of these we obtain the phase:

$$\tan\phi = \frac{\Omega\Gamma(1-s)}{s\Gamma^2+\Omega^2}. \tag{5.16}$$

We see that the partial decay of the A_{1g} force has implications for the initial phase of the coherent A_{1g} mode. Under the assumption that the A_{1g} force remains constant over the duration of the pump pulse ($s = 1$), we would expect that the A_{1g} oscillations would be purely cosine-like (DECP theory), in contrast to the E_g mode which, having a force that quickly decays to zero ($s = 0$), is sine-like (assuming $\Gamma \gg \Omega$). The partial decay of the A_{1g} mode modifies the phase away from purely cosine-like behaviour. Since the A_{1g} mode decays more in Sb than Bi, we find that Bi and Sb should have different phase differences between their A_{1g} and E_g modes. This has been observed by Misochko et. al. [131], who measured this phase difference in Bi to be $\phi_{E_g} - \phi_{A_{1g}} = 108 \pm 24^o$ and pointed out that Merlin and co-workers [26] measured the analogous phase difference in Sb to be $\phi_{E_g} - \phi_{A_{1g}} = 66 \pm 19^o$ at room temperature. The Bi measurements were carried out at several different temperatures and did not show a clear dependence on temperature. However, the error bars were large enough to accommodate a weak dependence on temperature, which we see in our calculations. Although the agreement between experimental measurement and calculations of these phases are not in quantitative agreement, partly due to our overestimation of the E_g force lifetimes, we do qualitatively reproduce the result that $\phi_{E_g} - \phi_{A_{1g}}$ differs between Bi and Sb.

Summing the squares of Eq. (5.14) and Eq. (5.15), we find that the amplitude,

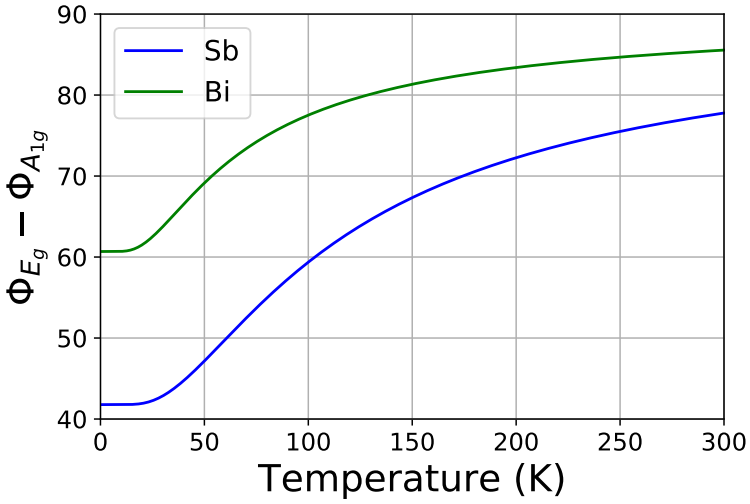

Figure 5.4: Phase difference between A_{1g} and E_g mode of Bi and Sb as a function of temperature.

$A = \Lambda/\Omega^2$, where Λ is defined by:

$$\Lambda^2 \equiv \left[\frac{s^2}{\frac{\Omega^2}{\Gamma^2}+1} + \frac{1}{\frac{\Gamma^2}{\Omega^2}+1}\right], \tag{5.17}$$

leading to the following equation of motion for the A_{1g} mode:

$$Q(t) = \frac{1-s}{\Gamma^2+\Omega^2}e^{-\Gamma t} + \frac{\Lambda}{\Omega^2}\left[\frac{s}{\Lambda} - \cos(\Omega t + \phi)\right] \tag{5.18}$$

If we compare this with the equation of motion for the A_{1g} mode driven by a **time-independent** force:

$$Q(t) = \frac{1}{\Omega^2}\left[1 - \cos(\Omega t + \phi)\right], \tag{5.19}$$

we see that the primary effect of the force decaying from $F_0 \to sF_0$ is to reduce the amplitude of the A_{1g} mode by the factor Λ.

Li et. al. gives the following expression for the E_g force relaxation rate [1]:

$$\Gamma_{E_g} = \Omega_{E_g}\sqrt{\frac{{g_{PP}}^4}{{g_{RS}}^4} - 1}, \tag{5.20}$$

where ${g_{PP}}^4 = (A_{A_{1g}}\tilde{A}_{A_{1g}}/A_{E_g}\tilde{A}_{E_g})^2$ is the "effective electron-phonon coupling" from the optical pump-optical probe experiment and ${g_{RS}}^4 = (A_{A_{1g}}/A_{E_g})^4$ is the corresponding coupling deduced from cw Raman scattering cross sections which are fairly insensitive to electronic decay of the mode driving forces. The

amplitudes are assumed to be of the form [1]:

$$A_{E_g} = \frac{F^0_{E_g}}{\mu {\Omega_{E_g}}^2} \tag{5.21}$$

$$\tilde{A}_{E_g} = \frac{F^0_{E_g}}{\mu {\Omega_{E_g}}^2 \sqrt{1 + \frac{{\Gamma_{E_g}}^2}{{\Omega_{E_g}}^2}}} \tag{5.22}$$

$$A_{A_{1g}} = \frac{F^0_{A_{1g}}}{\mu {\Omega_{A_{1g}}}^2}. \tag{5.23}$$

The amplitude $\tilde{A}_{A_{1g}}$ is assumed to be approximately equal to $A_{A_{1g}}$, which amounts to assuming that the A_{1g} driving force remains constant over the duration of the pump pulse (~ 70 fs). Since our calculations show a partial decay of the A_{1g} driving force in Bi and Sb, we make the following modification:

$$\tilde{A}_{A_{1g}} = \frac{F^0_{A_{1g}} \Lambda}{\mu {\Omega_{A_{1g}}}^2}, \tag{5.24}$$

which implies a change to the derived values of the E_g force lifetime by a factor of:

$$\tau_{E_g} = \frac{\sqrt{\frac{{g_{PP}}^4}{{g_{RS}}^4} - 1}}{\sqrt{\Lambda^2 \frac{{g_{PP}}^4}{{g_{RS}}^4} - 1}}. \tag{5.25}$$

Fig. 5.5 shows the resulting modifications to the experimentally derived E_g force lifetimes for Bi and Sb.

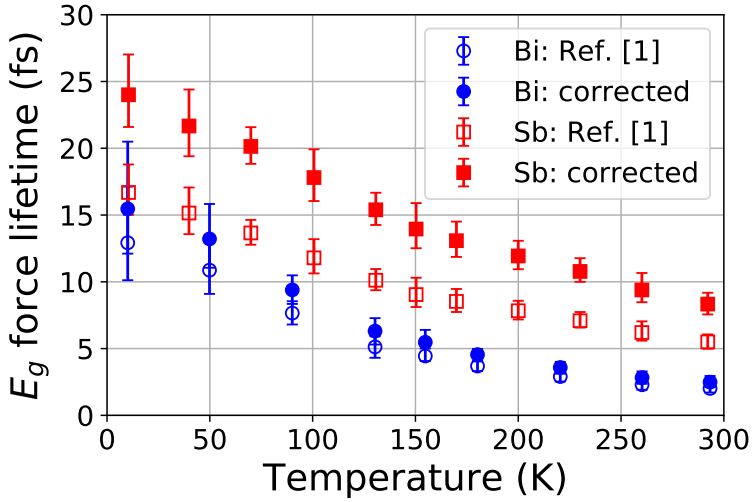

Figure 5.5: Corrections to the experimentally derived E_g force lifetimes reported in Ref. [1]. The open points are the experimental values reported in Ref. [1], the solid points are the experimental values after taking into account the calculated partial decay of the A_{1g} driving force.

5.3.2 Comparison with experimental E_g force lifetimes.

In Fig. 5.6, the calculated and experimental E_g force lifetime are shown as functions of temperature for Bi and Sb, and only the calculated values for As, where no experimental measurements are available. The electronic band energies, phonon frequencies and electron-phonon matrix elements were computed on a $6 \times 6 \times 6$ grid using Quantum Espresso [72] and interpolated to a $14 \times 14 \times 14$ grid using the EPW code. [97], as discussed in section 3.15. The pump pulse photon energy in the calculations is 1.5 eV, as in the experiment in Ref. [1].

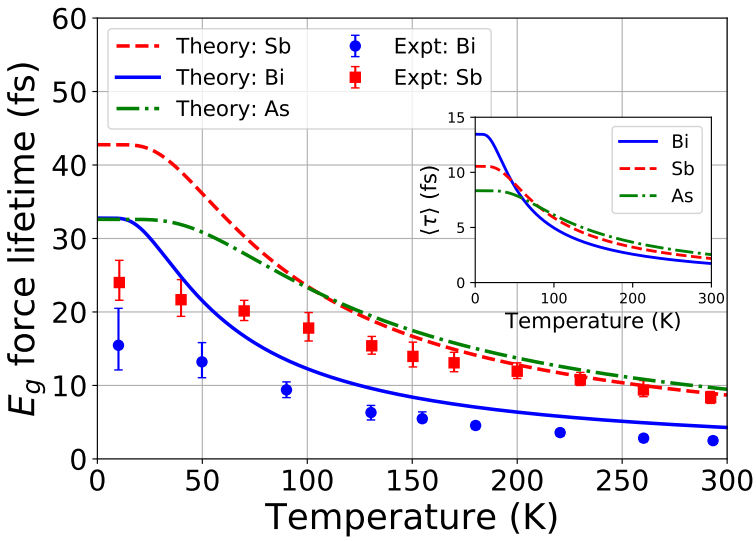

Figure 5.6: Lifetime of driving force on E_g mode as a function of lattice temperature for Bi, Sb and As for a pump photon energy of 1.5 eV. The curves are theoretical results, the points are the experimentally inferred values [1] re-derived taking into account the partial decay of the A_{1g} force. Inset: the average lifetime of states within the excited electron-hole plasma, as defined in Eq. (5.27). Both $\langle\tau\rangle$ and τ_{E_g} were computed for 16 temperatures in the interval $[0.1, 300]$ K and fitted with the function $f(T) = f(0)/[1 + 2n_B(T, \Omega_0)]$, where $n_B(T, \Omega_0)$ is the Bose-Einstein occupation number for a mode frequency Ω_0 at temperature T and Ω_0 is a fitting parameter: $\hbar\Omega_0(\text{Bi}) \approx 6.8$ meV, $\hbar\Omega_0(\text{Sb}) \approx 10.7$ meV and $\hbar\Omega_0(\text{As}) \approx 15.5$ meV.

The agreement between theory and experiment is very good. However, there is some degree of discrepancy. A useful indicator of this discrepancy can be gained from adding a hypothetical temperature-independent scattering rate (for example, as might be expected due to static defect scattering) to the calculated E_g force decay rate Γ_{E_g}:

$$\Gamma_{E_g}(T) \longrightarrow \Gamma_{E_g}(T) + \Gamma', \tag{5.26}$$

and then using Γ' as an adjustable parameter to bring theory and experiment

into agreement. The results of this process are shown in Fig. 5.7. We see that the calculated E_g force relaxation rate in antimony differs from experiment by a constant scattering rate of $\Gamma \sim 12.5\,\mathrm{ps}^{-1}$, consistent with a temperature-independent scattering mechanism due to static imperfections in the sample, such as impurities or grain boundaries. The Bismuth results do not differ from experiment by a temperature-independent scattering rate, but rather by a roughly uniform factor of ~ 1.5. This small discrepancy could be due to some additional scattering mechanism not considered here, such as electron-electron scattering. However, given the challenging nature of the experiment, the agreement is good and confirms that electron-phonon scattering is the dominant relaxation mechanism for the E_g driving force in both materials. Calculations of the E_g force lifetime, keeping the phonon populations fixed at their initial values, differ from the full calculations by less than 1% , indicating that evolution of the phonon populations is not important for the relaxation of the E_g force. Thus the E_g force relaxation is primarily due to coupling between the excited electron-hole plasma and the pre-existing thermal disorder (or quantum disorder at zero temperature) present at the time of photoexcitation. Further insight can be

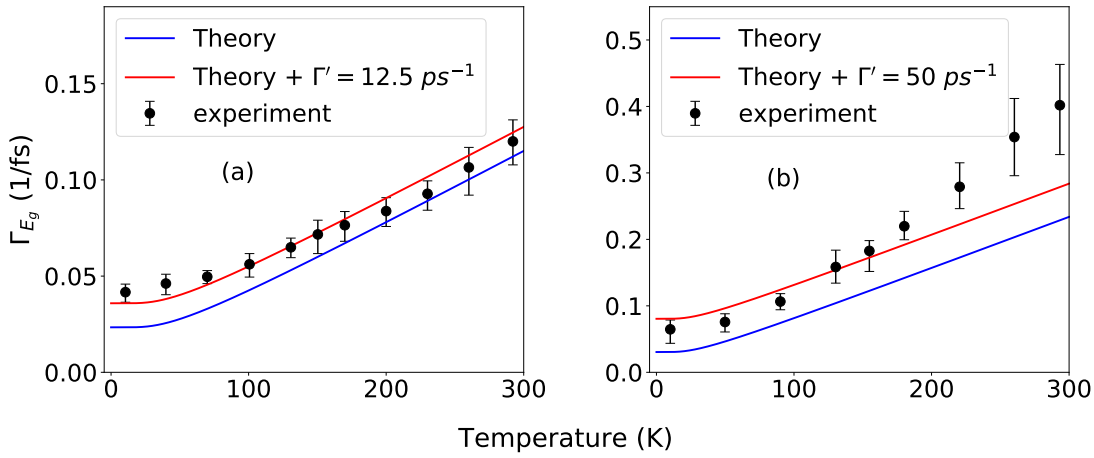

Figure 5.7: The E_g force decay rate with and without the addition of a corrective temperature-independent scattering rate via Matthiessen's rule for (a): Sb and (b): Bi. These results show that the Sb E_g force decay rate differs from experiment by a constant, but Bi does not.

gained by defining the average lifetime of states within the excited electron-hole plasma due to electron-phonon scattering:

$$\frac{1}{\langle \tau(T) \rangle} = \frac{\sum_{n\mathbf{k}\in \mathrm{vb}} \gamma_{n\mathbf{k}}(T)(1-f_{n\mathbf{k}})}{\sum_{n\mathbf{k}\in \mathrm{vb}} (1-f_{n\mathbf{k}})} + \frac{\sum_{n\mathbf{k}\in \mathrm{cb}} \gamma_{n\mathbf{k}}(T) f_{n\mathbf{k}}}{\sum_{n\mathbf{k}\in \mathrm{cb}} f_{n\mathbf{k}}}, \tag{5.27}$$

where $f_{n\mathbf{k}}$ are the initial photoexcited electronic occupations following absorption of 1.5 eV photons and $\gamma_{n\mathbf{k}}$ are the equilibrium inverse relaxation times of the electronic states $|n\mathbf{k}\rangle$ [88], which are plotted as a function of energy for Bi, Sb and As in Fig. 5.8 (a). There is a significant spread of values in the numerical results at each energy, but we have removed this noise by binning the electronic state decay rates. It is apparent that the electronic state inverse relaxation times are quite similar overall in all 3 materials. However, since the scattering which gives rise to $\gamma(E)$ is almost elastic (phonons don't carry much energy), the shape of $\gamma(E)$ follows the shape of the electronic density of states very closely, as can be readily seen by comparison with Fig. 5.8 (b).

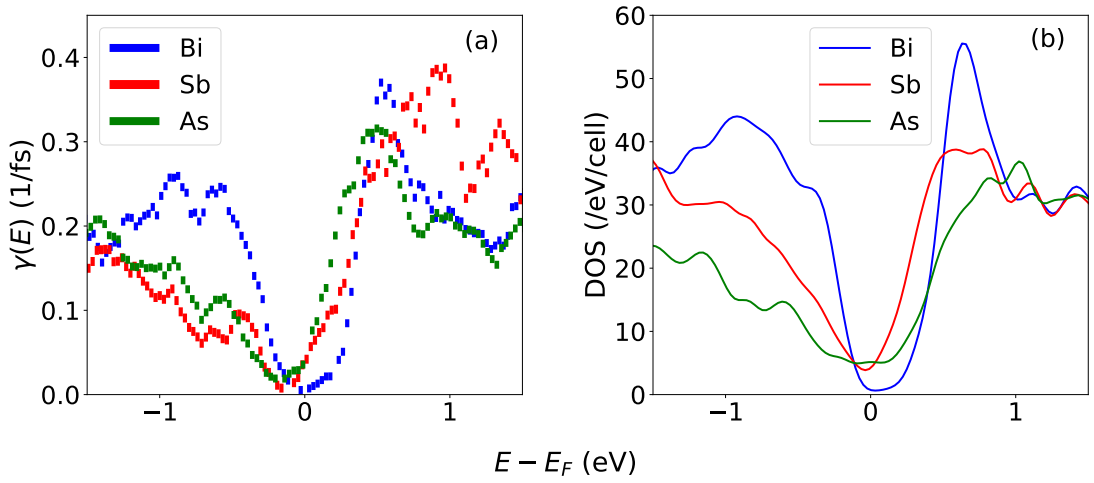

Figure 5.8: (a) shows the inverse electronic lifetimes of Bi, Sb and As as a function of energy at 300 K, binned to reduce noise. (b) is the electronic density of states for the same 3 materials.

In the inset of Fig. 5.6, we plot $\langle\gamma(T)\rangle$ for Bi, Sb and As. We see that it is similar to, but less than the E_g force lifetime in all three materials, since not all electron-phonon scattering events degrade the E_g force, but all relax the states within the electron-hole plasma. This quantity could be useful in more structurally complex systems where a full simulation of atomic force decay would be computationally demanding. A large value of $\langle\tau\rangle$ means that the excited electronic states have long lifetimes, which could potentially facilitate the generation of long lived symmetry-breaking atomic forces. We further note that the temperature dependence of the E_g force lifetime is very similar to that of $\langle\tau\rangle$. Thus, if we compute the lifetime of the E_g force at low-temperature, we can estimate $\tau_{E_g}(T)$ by computing $\langle\tau(T)\rangle$, which is computationally much less demanding. In more structurally complex materials, where a full simulation of the force decay might be very difficult, $\langle\tau\rangle$ should provide a reasonable

approximation of the lifetime of symmetry-breaking atomic driving forces.

The similarity between $\langle\tau\rangle$ and the lifetime of the E_g force underlines the importance of the coupling between the excited electron-hole plasma and the continuum of thermal vibrations in determining the behaviour of symmetry-breaking atomic driving forces. This is in contrast to the A_{1g} driving force, which decays to a value similar to the force we would obtain by assuming two separate thermal distributions for the photoexcited electrons and holes, on timescales less than 100 fs (as shown in Fig. 5.3 and Table 5.1). This underlines that the dynamics affecting symmetry-breaking forces are quite different to those determining symmetry-preserving forces. A natural question to ask is how

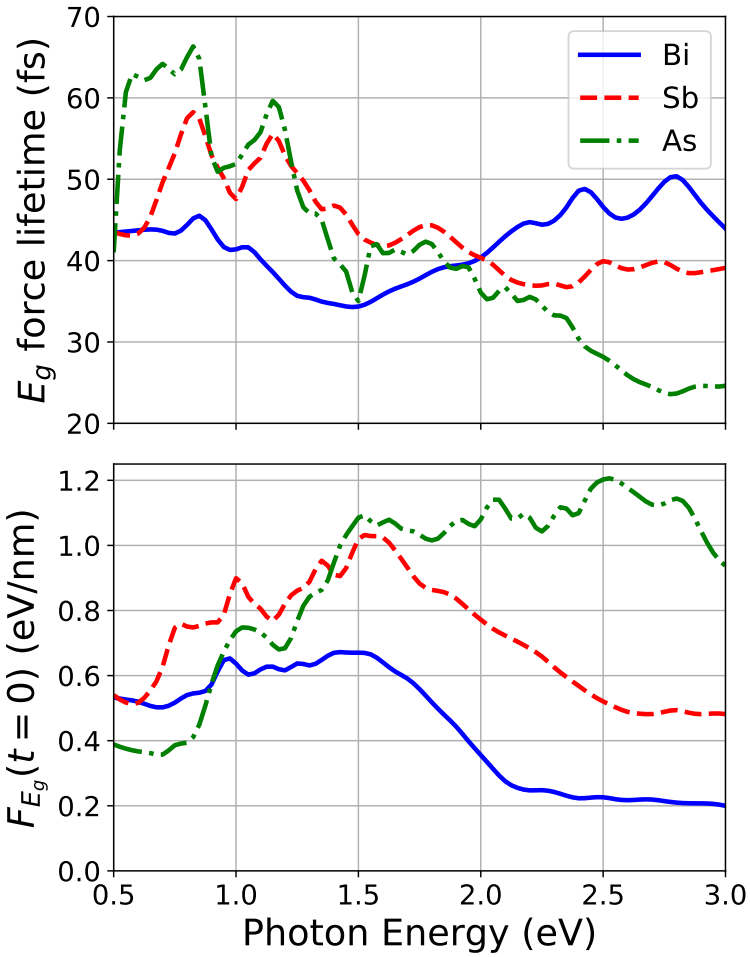

Figure 5.9: Upper: Low temperature (0.1 K) driving force lifetime of the E_g photoexcited force in Bi, Sb and As, as functions of the pump photon energy. Lower: Initial E_g driving force as functions of pump photon energy, assuming 0.1 photons absorbed per unit cell.

might we vary the conditions of the experiment to maximise the impact on symmetry-breaking modes. Perhaps the most obvious way is to decrease the

sample temperature, thereby decreasing the phonon populations and hence the rate of decay of the E_g force by electron-phonon scattering. Aside from lowering temperature [4], we can vary the photon energy of the pump pulse. Due to the strong energy dependence of the electron lifetimes, arising from the electronic density of states, varying the photon energy will have a significant effect on both the initial E_g force $F_{E_g}(t=0)$ and the E_g force lifetime τ_{E_g}.

In Fig. 5.9, we show that both the initial E_g force and the E_g force lifetime vary substantially with the pump photon energy in all three materials [5]. The amplitude of the E_g mode depends on both the initial value and the lifetime of the E_g force as follows:

$$A_{E_g} \propto \frac{F_{E_g}(t=0)}{\sqrt{1+\frac{1}{\tau_{E_g}^2 \Omega_{E_g}^2}}}. \tag{5.28}$$

In the limit where the lifetime of the E_g force is much shorter than the period of the E_g mode, $\tau_{E_g}\Omega_{E_g} \ll 1$, this simplifies to $A_{E_g} \propto F_{E_g}(t=0)\tau_{Eg}$. [6] This tells us that to maximise the impact of photoexcitation on symmetry-breaking modes, we should pump at a photon energy which maximises the product of the initial driving force, and its lifetime. Within the energy range considered, this indicates

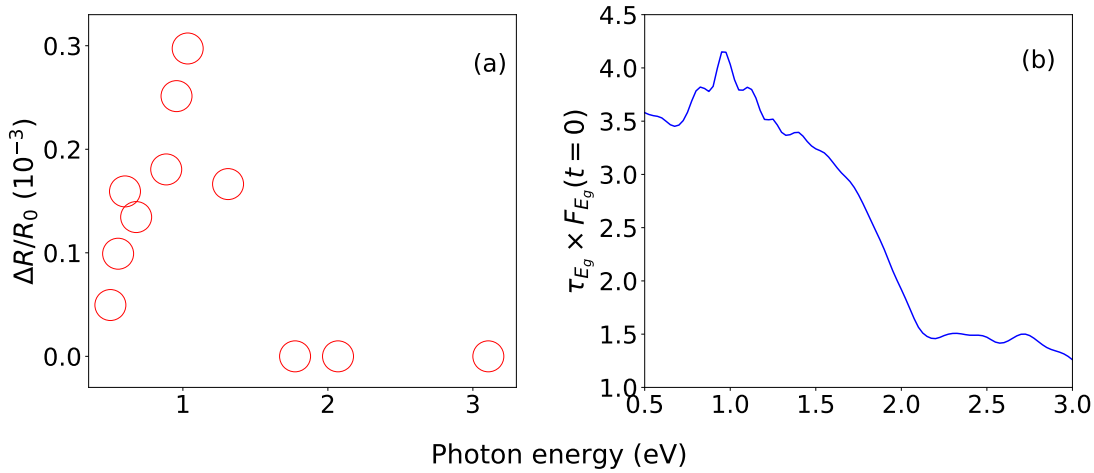

Figure 5.10: (a): Plot of experimentally measured amplitude of reflectivity oscillations corresponding to the E_g mode in Bi for several different pump photon energies [130]. (b): Calculated product of initial value and lifetime of E_g driving force vs photon energy. Both of these quantities are directly proportional to the E_g mode amplitude. They show similar trends and are both maximised at a photon energy of ~ 1 eV.

[4] Another way to increase the E_g mode amplitude is to increase the pump fluence, thereby increasing the photoexcited carrier density. However, this would increase the A_{1g} mode amplitude by the same factor.

[5] These calculations were performed on a $16 \times 16 \times 16$ grid

[6] This limit is mostly satisfied, although at very low temperatures, where Ω_{E_g} can become comparable to Γ_{E_g}, it may be necessary to evaluate Eq. (5.28) directly.

that bismuth should be pumped with photons of energy ~ 0.9 eV, antimony with photons of energy in the interval $[1.0, 1.5]$ eV and arsenic with photons of energy in the interval $[1.0, 2.5]$ eV to maximise the E_g mode amplitude.

Room temperature experiments have been carried out in Bi for several pump wavelengths [130]. Fig. 5.10 (a) shows the photon energy dependence of the amplitude of the E_g component of transient reflectivity oscillations for several different pump photon energies. Since both this quantity, and $\tau_{E_g} F_{E_g}(t = 0)$ (plotted in Fig. 5.10 (b)) are proportional to the amplitude of the E_g mode, we can compare the trends of these two quantities. We find that they agree reasonably well, and most importantly, both the experiment and our calculations indicate that pumping at ~ 1 eV will maximise the impact on the E_g mode.

This argument that varying photon energy can be used to maximise impact on symmetry-breaking modes is not restricted to Bi, Sb and As, but rather generalises to any other material in which electron-phonon scattering plays a significant role in limiting the generation of large amplitude symmetry-breaking coherent modes. This means that in a variety of other materials, choosing a photon energy which maximises $\tau_{E_g} F_{E_g}(t = 0)$ would enable us to increase the amplitude of symmetry-breaking coherent modes, which could permit investigation into the possibility of inducing structural phase transitions which lower crystal symmetry. [15]

5.4 Conclusions

In conclusion, we have developed a new first principles method for calculating the generation and relaxation of low-symmetry photo-induced forces, which goes beyond conventional TDDFT approaches by explicitly considering coupling between the excited electron-hole plasma and the continuum of thermal vibrations, enabling us to accurately describe the ultrafast excitation and relaxation of the symmetry-breaking E_g driving force in Bi, Sb and As. We have shown that electron-phonon scattering is the primary relaxation mechanism of the E_g force in Bi, Sb and As. The symmetry-preserving A_{1g} force undergoes a partial decay to a non-zero value on similar timescales to the E_g force decay, demonstrating that the excitation of the A_{1g} mode is not fully explained by the simple DECP model, but also has an impulsive component. We have defined a non-equilibrium average lifetime of states within the electron-hole plasma and shown that it pro-

vides a crude indication of the E_g force lifetime and has the same temperature dependence as the E_g force lifetime in all three materials, making it a computationally useful diagnostic for the lifetime of low-symmetry photo-induced forces in more structurally complex materials. We have demonstrated that the lifetimes of the E_g forces in Bi, Sb and As vary substantially with the photon energy of the pump pulse, and suggest that similar effects would occur in other materials, providing a path to generating larger amplitude symmetry-breaking atomic motion by suitable choice of pump photon energy.

Chapter 6

Conclusions

Important conclusions can be drawn on this basis of the work presented in this thesis. On the subject of photoinduced structural phase transitions, our calculations, along with the experimental measurements of our collaborators, provide good evidence that the Peierls distortion in Sb can be reversed by optical excitation above a certain fluence threshold. The calculated frequency of the A_{1g} mode agrees well with the experiments at moderate fluence ($<$ 10 mJ/cm^2). We have shown that the measured decay rate of the A_{1g} mode agrees well with our calculations of third order anharmonic decay at low pump fluence. However, the experiment displays a steep trend with respect to increasing pump fluence, which is not fully captured by our calculations. Comparison of our calculations with those of Ref. [126], who use a nonperturbative approach, rule out the possibility that higher order anharmonicity could explain this discrepancy. We suggest that electron-phonon scattering may provide an explanation, since its rates depend strongly on the density of excited carriers, and hence the pump-fluence. However, this remains an open question.

Symmetry-breaking coherent modes are driven by excited electrons which initially occupy symmetry-equivalent regions of the Brillouin zone unequally. The experimentally measured amplitude of these modes are much smaller than those of fully symmetric coherent modes. A recent experimental study [1] has shown that the comparatively low amplitude of the E_g modes in Bi and Sb, compared with the fully symmetric A_{1g} mode, is due to the driving force on the E_g mode being very short lived ($\sim$ 10 fs $\ll$ phonon period). Our first principles calculations of the time evolution of the E_g mode driving force by electron-phonon scattering, showed excellent agreement with these experimental measurements,

demonstrating that electron-phonon scattering is the primary mechanism that relaxes the E_g force in Bi and Sb [30]. We have also made a theoretical prediction for the lifetime of the E_g force in As. The calculations also show that the high-symmetry A_{1g} mode undergoes a partial decay from its initial value, to a smaller but nonzero value on timescales similar to the decay of the E_g force. This demonstrates that the force driving the A_{1g} mode is not purely displacive, but rather has a significant impulsive component.

We have shown that a crude indication of the lifetime of symmetry-breaking modes can be obtained from an average of the electronic state lifetimes over the excited electron distribution, providing a useful diagnostic for identifying materials which may have long-lived symmetry-breaking forces. We have demonstrated that the E_g force lifetimes in Bi, Sb and As vary substantially with pump photon energy. This is likely due to the energy dependence of the electronic density of states, because electron-phonon scattering rates will be proportional to the density of available final states. We suggest a method for increasing the impact of optical excitation on symmetry-breaking modes in all materials by choosing a photon energy which maximises the product of the initial E_g force and its lifetime.

More generally, these results underline the importance of correctly treating incoherent electron-phonon scattering, particularly when studying electronic distributions which have a lower symmetry than the underlying crystal. Theoretical frameworks which are widely used to study ultrafast processes, such as conventional time-dependent density functional theory (TDDFT) [129], do not include this mechanism so would not capture the physics of the ultrafast decay of symmetry-breaking atomic forces in *any* material.

Chapter 7

Outlook: Ultrafast thermalisation of non-equilbrium excited electronic distributions.

Photoexcitation of a materials causes its electrons to be excited into a the conduction bands. The optical transitions are determined by the pulse photon energy polarisation, and the dipole matrix elements (see section 3.17), resulting in a non-equilibrium excited electronic distribution which does not have a well defined temperature. The excited electrons then scatter among themselves and with lattice vibrations, forming a Fermi-Dirac distribution. [1] The timescale for this process is often assumed to be on the order of tens to hundreds of femtoseconds, an assumption which is crucial to the two temperature model (see subsection 3.16.3) [102, 101, 34, 103].

The question then arises as to whether we can simulate this ultrafast thermalisation process from first-principles. Fig. 7.1 shows the evolutions of the photoexcited electronic distribution following photoexcitation, including only electron-phonon scattering, as implemented in chapter 5 and Ref. [30]. The initial photoexcited distribution was computed using the optical transition matrix elements as described in Eqs. (5.1) and (5.2). One striking feature of the time evolution in Fig. 7.1, is that the occupation goes from initially having a wide range of values at each energy to being a function of energy only after $\sim 10 - 15$ fs, a timescale similar to the decay of the E_g force. This makes sense, because

[1] Or, for systems in which electron-hole recombinations is slow, the electrons and holes form separate Fermi-Dirac distributions, as is assumed in two chemical potential constrained DFT(see subsection 3.16.2).

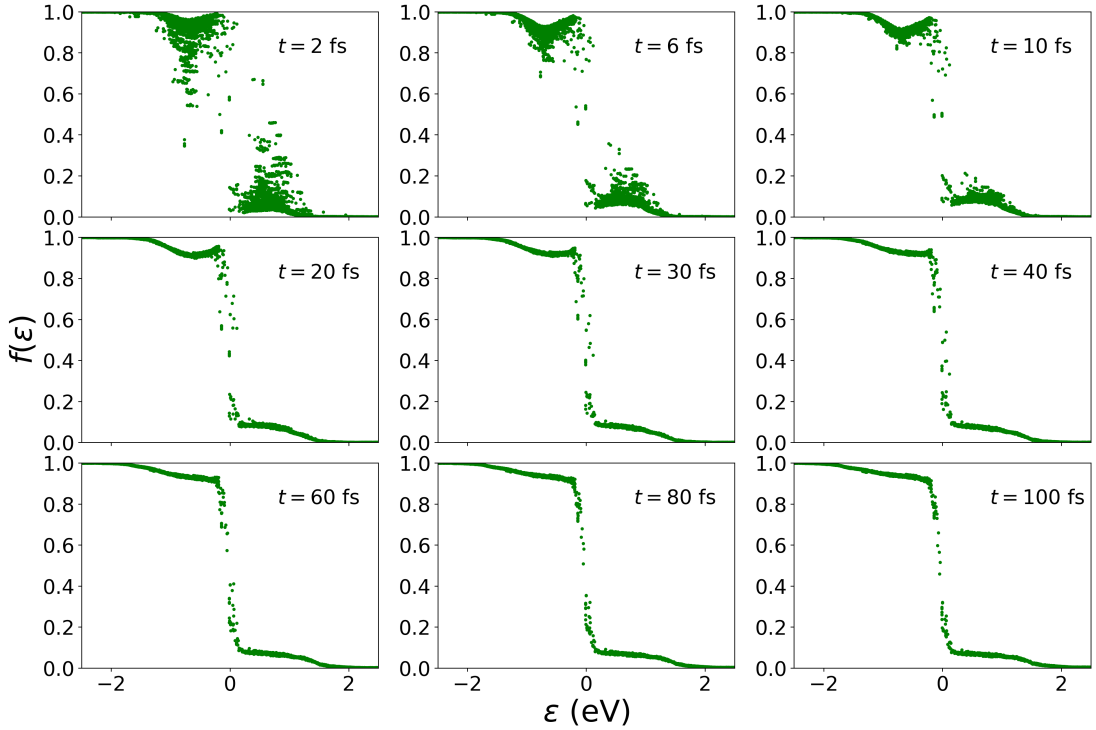

Figure 7.1: Snapshots of excited electronic distribution in Bi, evolving under the influence of electron-phonon scattering. The excited distribution was calculated assuming 0.1 x-polarised photons of energy $\hbar\omega = 1.5$ eV were absorbed per unit cell.

in order for the electronic occupation to be a function of energy, symmetry-equivalent regions of the Brillouin zone must be equally occupied [2]. The results also conform to the intuitive argument that electron-phonon scattering is effective at scrambling momentum, while electron-electron scattering is effective at scrambling energy. However, the electrons do not form a thermal distribution through electron-phonon scattering alone.

This suggests that if we want to simulate the thermalisation of non-equilibrium excited electrons, we must include electron-electron scattering in our calculations. Marini and collaborators have simulated electron thermalisation in silicon, including both electron-phonon and electron-electron scattering [36, 38]. However, they treat the Coulomb interaction between the electrons as statically screened, which simplifies their approach. This is well motivated in semiconductors and insulators, since an electronic gap of 1 eV corresponds to a timescale of 0.66 fs through the Heisenberg uncertainty principle, which is a very short timescale compared with the time required for thermalisation (tens to hundreds of fs). However, in semimetals like Bi, Sb and As, this is not a reasonable

[2] Recall that the E_g force is only non-zero if there is an unbalanced occupation of symmetry-equivalent regions of the Brillouin zone.

approximation.

The simulation, from first principles, of electron thermalisation in photoexcited semimetals by a combination of electron-phonon and dynamically screened electron-electron scattering is an interesting open problem. Although time constraints prohibited us from pursuing this problem fully, we briefly lay out our proposed approach here, along with the relevant equations.

7.1 Coulomb matrix elements

Electrons interact with one another by the Coulomb interaction. Therefore, in order to calculate electron-electron scattering rates, we need to define Coulomb matrix elements. The coulomb matrix element for electrons in states $|\mathbf{k}\rangle$ and $|\mathbf{k}'\rangle$ scattering to states $|\mathbf{k}+\mathbf{q}\rangle$ and $|\mathbf{k}'-\mathbf{q}\rangle$ is defined [3]

$$M(\mathbf{k},\mathbf{k}',\mathbf{q}) = \int\int \mathrm{d}\mathbf{r}\mathrm{d}\mathbf{r}'\psi_{\mathbf{k}}(\mathbf{r})\psi_{\mathbf{k}'}(\mathbf{r}')\frac{\mathbf{1}}{|\mathbf{r}-\mathbf{r}'|}\psi_{\mathbf{k}'-\mathbf{q}}(\mathbf{r}')\psi_{\mathbf{k}+\mathbf{q}}(\mathbf{r}). \tag{7.1}$$

Recall that Bloch's theorem allows us to express the electron wavefunctions as a product of a plane wave and a cell-periodic function $u_{\mathbf{k}}(\mathbf{r})$

$$\psi_{\mathbf{k}}(\mathbf{r}) = \frac{1}{\sqrt{N_p}}u_{\mathbf{k}}(\mathbf{r})e^{i\mathbf{k}\cdot\mathbf{r}}. \tag{7.2}$$

Expanding the periodic part in a Fourier series allows us to express the wavefunction as follows:

$$\psi_{\mathbf{k}}(\mathbf{r}) = \frac{1}{\sqrt{N_p\Omega_0}}\sum_{\mathbf{G}} c_{\mathbf{k}}(\mathbf{G})e^{i(\mathbf{k}+\mathbf{G})\cdot\mathbf{r}}. \tag{7.3}$$

[3] In the following expressions, $\mathbf{k}$ is a composite variable for electronic wavevector and band.

If we also Fourier transform the Coulomb potential, we can now write Eq. (7.1) in the following form:

$$\begin{aligned} M(\mathbf{k},\mathbf{k}',\mathbf{q}) =& \frac{1}{N_p^2}\int V(\mathbf{Q})\left[\int_{\mathbb{R}} u_{\mathbf{k}}(\mathbf{r})u_{\mathbf{k}+\mathbf{q}}(\mathbf{r})e^{i(\mathbf{Q}+\mathbf{q})\cdot\mathbf{r}}\mathrm{d}\mathbf{r}\right] \\ & \left[\int_{\mathbb{R}} u_{\mathbf{k}'}(\mathbf{r}')u_{\mathbf{k}'-\mathbf{q}}(\mathbf{r}')e^{-i(\mathbf{Q}+\mathbf{q})\cdot\mathbf{r}'}\mathrm{d}\mathbf{r}'\right]\mathrm{d}\mathbf{Q}. \\ =& \frac{1}{N_p^2{\Omega_0}^2}\sum_{\mathbf{G_1}} u^*_{\mathbf{k}}(\mathbf{G_1})\sum_{\mathbf{G_2}} u_{\mathbf{k}+\mathbf{q}}(\mathbf{G_2})\sum_{\mathbf{G_3}} u^*_{\mathbf{k}'}(\mathbf{G_3})\sum_{\mathbf{G_4}} u_{\mathbf{k}'-\mathbf{q}}(\mathbf{G_4})\times \\ & N_p\Omega_0\int V(\mathbf{Q})\delta(\mathbf{Q}-(\mathbf{G_1}-\mathbf{G_2}-\mathbf{q}))\delta(\mathbf{Q}-(\mathbf{G_4}-\mathbf{G_3}-\mathbf{q}))\mathrm{d}\mathbf{Q}. \end{aligned}$$

The first delta function picks out the term $V(\mathbf{G_1}-\mathbf{G_2}-\mathbf{q})$ from the integral over $\mathbf{Q}$ and leaves us with a delta function which imposes that $\mathbf{G_1}-\mathbf{G_2}=\mathbf{G_4}-\mathbf{G_3}\equiv\mathbf{G}$. This allows us to rewrite our matrix element as:

$$M(\mathbf{q}) = \frac{1}{N_p\Omega_0}\sum_{\mathbf{G}}\frac{4\pi e^2}{|\mathbf{q}-\mathbf{G}|^2}\left[\sum_{\mathbf{G}'} u^*_{\mathbf{k}}(\mathbf{G}')u_{\mathbf{k}+\mathbf{q}}(\mathbf{G}'+\mathbf{G})\right]\left[\sum_{\mathbf{G}''} u^*_{\mathbf{k}'}(\mathbf{G}'')u_{\mathbf{k}'-\mathbf{q}}(\mathbf{G}''-\mathbf{G})\right]. \tag{7.4}$$

However, the appropriate interaction potential for carrier-carrier scattering is the *screened* Coulomb interaction $W(\mathbf{q},\omega)$ defined by:

$$W(\omega,\mathbf{q}) = \frac{\mathbf{V}(\mathbf{q})}{\varepsilon(\omega,\mathbf{q})} \approx \frac{\mathbf{V}(\mathbf{q})}{\varepsilon(\omega)}, \tag{7.5}$$

where $\varepsilon(\omega,\mathbf{q})$ is the carrier dielectric function.

7.2 Dielectric function in the random phase approximation

A reasonable approximation to the screening due to a gas of interacting electrons is to compute the screening as if the electrons were non-interacting. This is the so-called random phase approximation, and it allows us to write the electronic susceptibility tensor as [51]:

$$\chi_{\mathbf{G}\mathbf{G}'}(\mathbf{q},\omega) = \sum_{n,m,\mathbf{k}}\frac{(f_{n\mathbf{k}}-f_{m\mathbf{k}+\mathbf{q}})\left\langle\psi_{n\mathbf{k}}|e^{-i(\mathbf{q}+\mathbf{G})\cdot\mathbf{r}}|\psi_{m\mathbf{k}+\mathbf{q}}\right\rangle\left\langle\psi_{m\mathbf{k}+\mathbf{q}}|e^{i(\mathbf{q}+\mathbf{G}')\cdot\mathbf{r}}|\psi_{n\mathbf{k}}\right\rangle}{\Omega_0(\varepsilon_{n\mathbf{k}}-\varepsilon_{m\mathbf{k}+\mathbf{q}}+\hbar\omega+i\delta)}, \tag{7.6}$$

where δ is a term which is inserted to move the poles of the function into the complex plane; a standard practice in complex analysis. Typically, we would

take the limit as $\delta \longrightarrow 0^+$. However, since we know that the electronic states have a finite lifetime due to their interactions phonons and other electrons, we set this term equal to the average linewidth of the electronic states in the system: $\delta = \langle \hbar/\tau_{n\mathbf{k}} \rangle \equiv \langle \lambda \rangle$.

The dielectric tensor can be divided into the head ($\mathbf{G} = \mathbf{G}' = 0$), the body ($\mathbf{G} \neq 0$ and $\mathbf{G}' \neq 0$) and the wings ($\mathbf{G} = 0$ or $\mathbf{G}' = 0$)) [132]. A common assumption is to neglect the body and wings of the dielectric function. In doing so, one neglects so-called local field effects [51]. This assumption is exact under the assumption that the system is homogeneous, which is typically not the case for electrons in semiconductors and semimetals. However, it turns out that for the *intraband* ($n = m$) contributions to the dielectric function, the body and wings vanish as $\mathbf{q} \longrightarrow 0$ [132]. This means that within the long wavelength limit ($\mathbf{q} \longrightarrow 0$), local field effects can be safely ignored.

Since it is not computationally feasible to compute all possible combinations of $\mathbf{G}$ and $\mathbf{G}'$, we restrict our attention for now to the intraband contributions to the electronic dielectric function and consider only the head ($\mathbf{G} = \mathbf{G}' = 0$). If we do this, and utilise Bloch's theorem, we get:

$$\chi_{\text{intra}}(\mathbf{q}, \omega) = \frac{1}{N_p \Omega_0} \sum_{n,\mathbf{k}} \frac{(f_{n\mathbf{k}} - f_{n\mathbf{k}+\mathbf{q}}) |\langle u_{n\mathbf{k}} | u_{n\mathbf{k}+\mathbf{q}} \rangle|^2}{\varepsilon_{n\mathbf{k}} - \varepsilon_{n\mathbf{k}+\mathbf{q}} + \hbar\omega + i\langle \lambda \rangle}. \tag{7.7}$$

This expression enables us to calculate the real and imaginary parts of the intraband dielectric function, $\epsilon = 1 - (4\pi e^2/q^2)\chi$. Defining $\Delta\varepsilon^{\mathbf{k}}_{nn'}(\omega) = \varepsilon_{n\mathbf{k}} - \varepsilon_{n\mathbf{k}+\mathbf{q}} + \hbar\omega$, we arrive at the following expressions for the real and imaginary parts of the dielectric function:

$$\epsilon^{(1)}_{\text{intra}}(\mathbf{q}, \omega) = 1 - \frac{4\pi e^2}{N_p \Omega_0 |\mathbf{q}|^2} \sum_{n,\mathbf{k}} (f_{n\mathbf{k}} - f_{n\mathbf{k}+\mathbf{q}}) |\langle u_{n\mathbf{k}} | u_{n\mathbf{k}+\mathbf{q}} \rangle|^2 \frac{\Delta\varepsilon^{\mathbf{k}}_{nn'}(\omega)}{[\Delta\varepsilon^{\mathbf{k}}_{nn'}(\omega)]^2 + \langle \lambda \rangle^2}, \tag{7.8}$$

$$\epsilon^{(2)}_{\text{intra}}(\mathbf{q}, \omega) = -\frac{4\pi e^2}{N_p \Omega_0 |\mathbf{q}|^2} \sum_{n,\mathbf{k}} (f_{n\mathbf{k}} - f_{n\mathbf{k}+\mathbf{q}}) |\langle u_{n\mathbf{k}} | u_{n\mathbf{k}+\mathbf{q}} \rangle|^2 \frac{\langle \lambda \rangle}{[\Delta\varepsilon^{\mathbf{k}}_{nn'}(\omega)]^2 + \langle \lambda \rangle^2}. \tag{7.9}$$

Approximating the interband terms of the dielectric function in a way which is both computationally tractable and physically sensible is a more difficult proposition. However, a first step may be to assume that all interband electron-electron interactions are screened in the long wavelength limit. Within that

scheme, the interband dielectric function can be obtained from the OPTIC code (part of the ABINIT package) [74].

Having computed the screened Coulomb matrix elements, the electron-electron scattering rates can be evaluated using Fermi's golden rule:

$$R_{\mathbf{k},\mathbf{k}',\mathbf{q}} = \frac{2\pi}{\hbar}|W(\mathbf{q})|^2 f_{\mathbf{k}} f_{\mathbf{k}'}(1-f_{\mathbf{k}+\mathbf{q}})(1-f_{\mathbf{k}'-\mathbf{q}})\delta(E_{\mathbf{k}+\mathbf{q}}+E_{\mathbf{k}'}-E_{\mathbf{k}'}-E_{\mathbf{k}'-\mathbf{q}}), \quad (7.10)$$

where $\mathbf{k}$ is again a composite variable of electronic wavevector and band. As a result of this, electron-electron scattering can be incorporated in a straightforward way, into the code we have written to evolve excited electrons (and the E_g force) in time. The calculation of electron-electron scattering rates involves three nested loops over all available states, so is computationally heavy. However, the coupling between many states is negligible, suggesting that sparse matrix methods might be capable of reducing the computation time. [4]

[4] We are still working on implementing this numerically.

Appendix A

Comparison of slow and fast electron-hole recombination within constrained DFT

There are two competing approximations for treating excited electrons and holes within constrained DFT. The first of these assumes that electron-hole recombination proceeds on a timescale much longer than a coherent phonon period, leading to electrons and holes which thermalise separately into two Fermi-Dirac distributions with a common temperature, but different chemical potentials. This is referred to as the two chemical potential model. The other approach is to assume that electron-hole recombinations proceeds instantaneously, leading to a single hot thermal distribution of electrons. This second approach is referred to as the one (or single) chemical potential model. For more details, see section 3.16. Despite corresponding to opposite assumptions about the rate of electron-hole recombination. The two approaches give harmonic frequencies and equilibrium displacements in good agreement with each other, implying that the rate of electron-hole recombination is not very important form the perspective of studying coherent phonon motion within constrained DFT. This justifies our choice of the two chemical potential model in chapter 4.

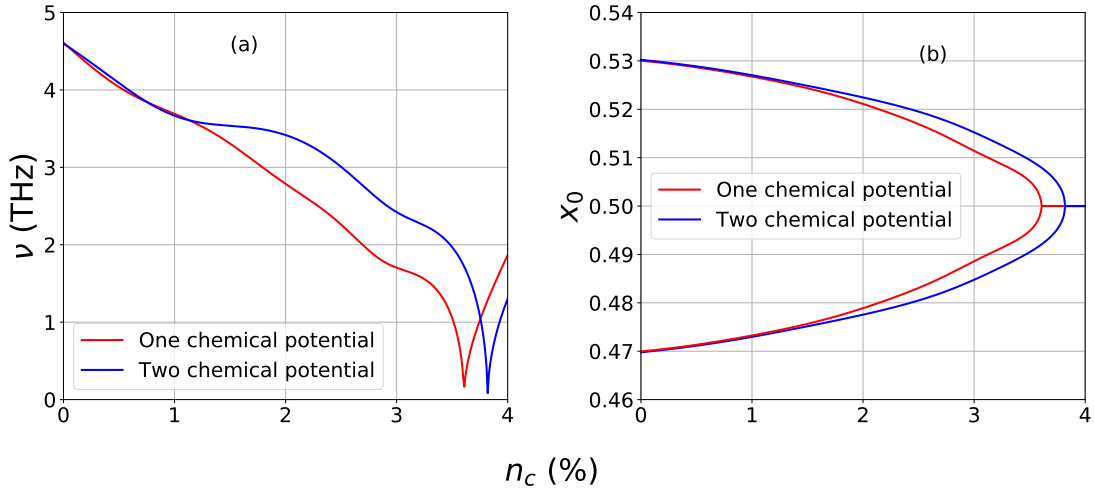

Figure A.1: Comparison of the effects of slow and fast electron-hole recombination on the harmonic frequency and the equilibrium coordinate of the A_{1g} mode as a function of photoexcited carrier concentration.

Appendix B

Wannier interpolation of Group V semimetal bandstructures

The electronic bandstructure, phonon dispersion and electron-phonon coupling matrix elements used in chapter 5 were calculated on a uniform $6 \times 6 \times 6$ Brillouin zone grid within the framework of density functional perturbation theory. We used a 25 hartree plane wave energy cutoff and the local density approximation to exchange and correlation. Norm-conserving pseudopotentials including spin orbit coupling were used for all three materials (Bi, Sb and As). These quantities were then interpolated to finer grids using maximally localised Wannier functions (MLWF) as implemented in the EPW code [97]. These were performed using 14 Wannier orbitals for Bi and 16 Wannier orbitals for Sb and As. Since we consider photoexcited pump pulse photons between 0.5 eV and 3.0 eV, we are interested in states within ~ 2 eV of the Fermi level, which are well represented by this Wannier interpolation for all three materials.

The electron-phonon matrix elements are interpolated from a coarse $6 \times 6 \times 6$ grid to finer grids.

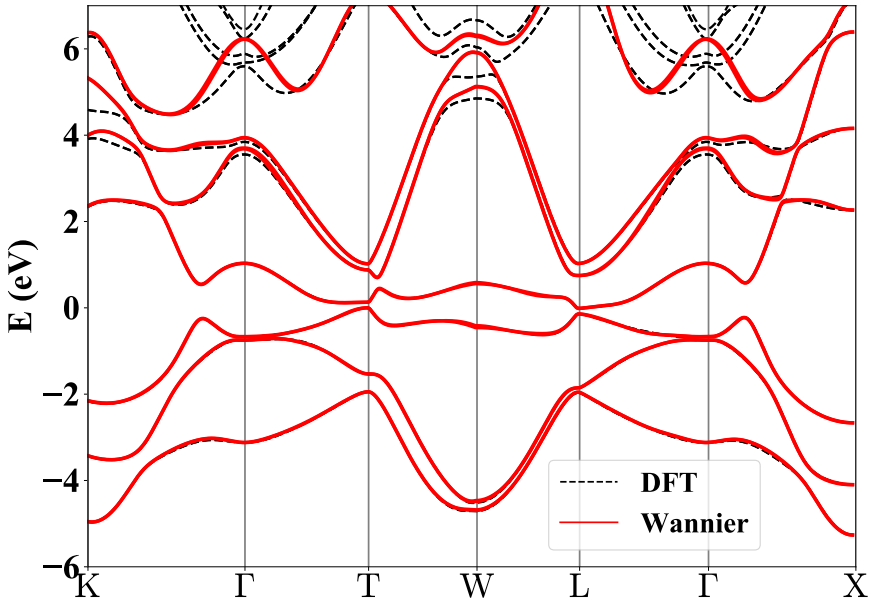

Figure B.1: Comparison of Bi DFT bands with those obtained by Wannier interpolation. 14 Wannier orbitals were used to interpolate the bandstructure from a coarse $6 \times 6 \times 6$ grid.

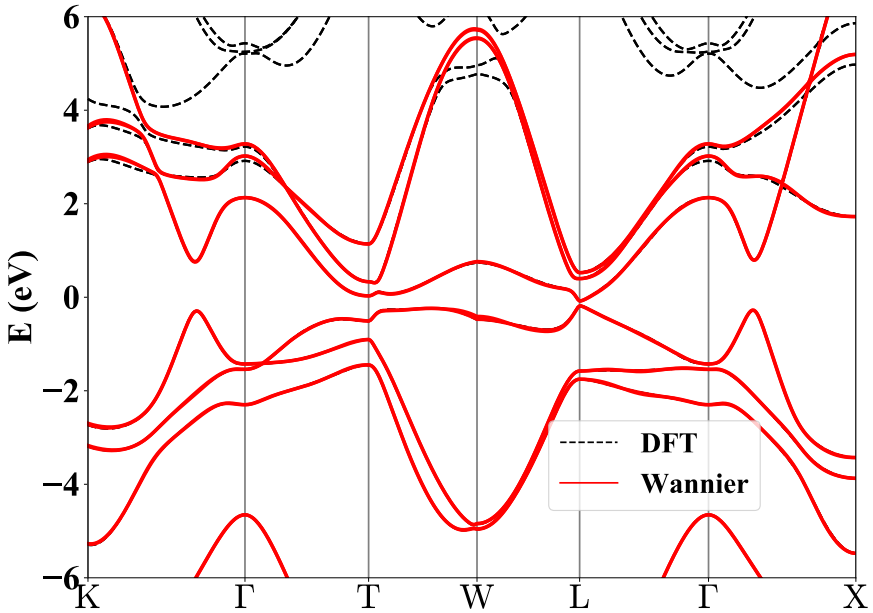

Figure B.2: Comparison of Sb DFT bands with those obtained by Wannier interpolation. 16 Wannier orbitals were used to interpolate the bandstructure from a coarse $6 \times 6 \times 6$ grid.

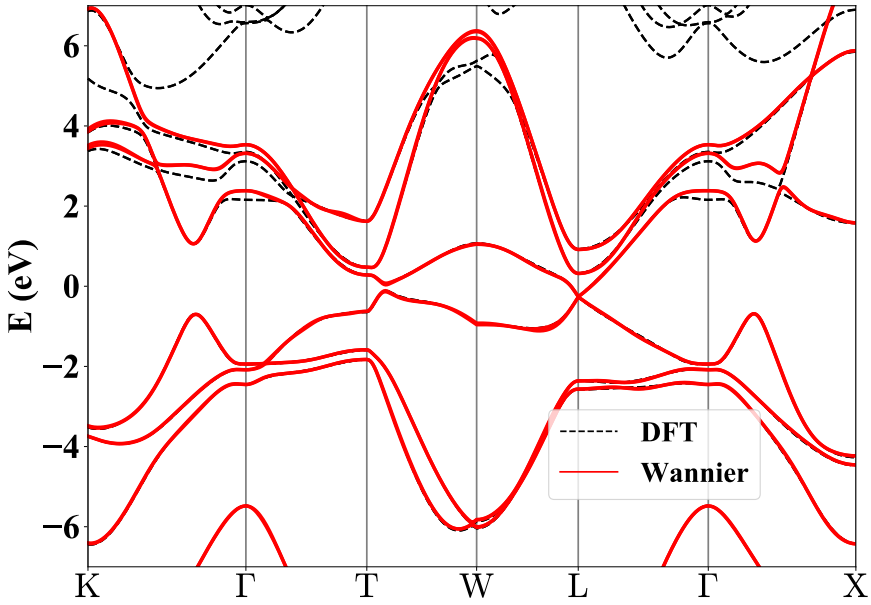

Figure B.3: Comparison of As DFT bands with those obtained by Wannier interpolation. 16 Wannier orbitals were used to interpolate the bandstructure from a coarse $6 \times 6 \times 6$ grid.

Appendix C

Convergence of E_g force lifetime.

The E_g force lifetime has two convergence parameters, the number of k(and q) points in the uniform Brillouin zone grid (N_k) and the Gaussian smearing, σ, used to compute $\mathrm{Im}\{\Sigma_{n\mathbf{k}}\}$ (see Eq. 4 of main text.). As shown in Fig. $C.1$, the low-temperature (0.1 K) E_g force lifetime at the experimental pump-pulse energy (1.5 eV) is insensitive to σ and is converged at a Brillouin zone grid of $N_k = 12 \times 12 \times 12$. At a grid density of $N_k = 14 \times 14 \times 14$, the E_g force lifetime converges in all 3 materials and at all temperatures considered, so we perform our calculations on that grid.

At excitation energies where the electronic density of states is very low, the convergence with respect to grid sampling becomes more demanding. However, for the energy range shown in Fig. 3 of the main text, going from a $14 \times 14 \times 14$ grid to a $16 \times 16 \times 16$ grid makes at most a difference of $\sim 20\%$.

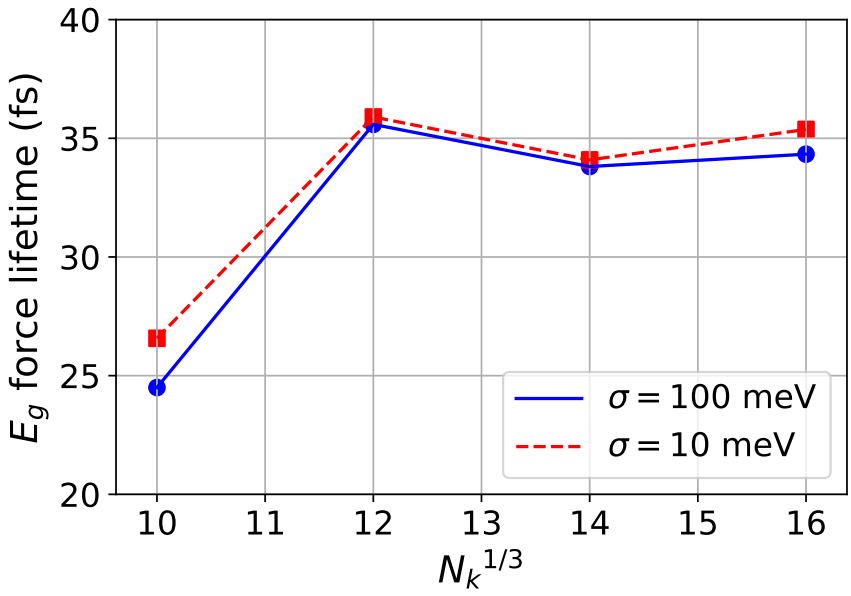

Figure C.1: Convergence of low-temperature (0.1 K) E_g force lifetime in Bi with respect to N_k and σ assuming an absorbed photon energy of 1.5 eV.

Appendix D

Numerical Implementation

In this appendix we will briefly explain our implementation of electron-phonon rate equations. The purpose of these calculations is to calculate the time evolution of electronic and phonon occupations due to electron-phonon scattering. We calculate the change in population of *each* electronic state $|n\mathbf{k}\rangle$ over many time steps, each of duration Δt. The change over a single time step can be computed as follows:

$$\Delta f_{n\mathbf{k}} = \Delta t \sum_{\mathbf{q}} \sum_{m} \sum_{\lambda} [R_{\lambda}^{+}\left(m\mathbf{k}+\mathbf{q}, n\mathbf{k}\right) + R_{\lambda}^{-}\left(m\mathbf{k}+\mathbf{q}, n\mathbf{k}\right) - R_{\lambda}^{+}\left(n\mathbf{k}, m\mathbf{k}+\mathbf{q}\right) - R_{\lambda}^{-}\left(n\mathbf{k}, m\mathbf{k}+\mathbf{q}\right)]. \tag{D.1}$$

The phonon populations are stepped forward in time using the same numerical procedure, but applied to Eq. (3.82). For short enough time-steps, the results will converge with respect to the time-step duration. We find that a time step of ~ 100 attoseconds is suitable for studying ultrafast evolution of photoexcited carriers and atomic forces, processes which typically take place on timescales of ~ 10 femtoseconds.

D.0.1 Electron and Phonon Occupations

We assume that the phonon occupations are initially described by a Bose-Einstein distribution at the sample temperature T:

$$n_{\mathbf{q}\lambda} = \frac{1}{e^{\frac{\hbar\omega_{\mathbf{q}\lambda}}{k_{\mathrm{B}}T}} - 1}, \tag{D.2}$$

where $k_{\mathrm{B}}T$ is the thermal energy of the phonons. The initial value of the electronic occupations are those computed with the optical transition matrix elements as outlined in Sec. 3.17 and using the OPTIC code, which is an add-on to the ABINIT package [74] [1]. We then evolve the electron and phonon occupations using the electron-phonon scattering rate equations. This evolution is performed using a Fortran code that we developed, which takes electronic band structure, phonon dispersions and electron-phonon matrix elements as input and evolves the electron and phonon distributions in time. It also evaluates the atomic forces at each time step using Eq. (3.95).

D.0.2 Hartree atomic units and dimensional analysis

Throughout our calculations of the relaxation of atomic forces, we use Hartree atomic units, since these are the units used in both the ABINIT and Quantum Espresso codes. These are units in which $\hbar = k_{\mathrm{B}} = m_e = 4\pi\epsilon_0 = c/\alpha \equiv 1$, where k_{B} is Boltzmann's constant, ϵ_0 is the permittivity of free space, c is the speed of light and α is the fine structure constant. The unit of energy is the Hartree, which is twice the first ionisation energy of a Hydrogen atom and the unit of length is the Bohr radius. The corresponding unit of time is 2.418884×10^{-17} s. So, to convert the time to femtoseconds we will need to divide the time in atomic units by ≈ 41.34138.

If we re-write Eq. (3.79), without the dimensionless constants and occupation factors:

$$R^{\pm}_{\lambda}(n\mathbf{k}, m\mathbf{k}+\mathbf{q}) \propto \frac{\left|g^{\mathbf{q}\lambda}_{\mathbf{k}nm}\right|^2}{\omega_{\mathbf{q}\lambda}}\delta^{\pm}, \tag{D.3}$$

we can perform dimensional analysis as follows:

$$\begin{aligned}\left[R^{\pm}_{\lambda}(n\mathbf{k}, m\mathbf{k}+\mathbf{q})\right] &= [\text{time}]\frac{[\text{Energy}]^2}{[\text{distance}]^2[\text{mass}]}\frac{1}{[\text{Energy}]} \\ &= [\text{time}]\frac{[\text{Energy}]^2}{[\text{time}]^2[\text{Energy}]}\frac{1}{[\text{Energy}]} = \frac{1}{[\text{time}]},\end{aligned} \tag{D.4}$$

showing that our scattering rates indeed have units of inverse time.

[1] OPTIC is a post-processing tool which takes the output from the first-principles ABINIT code and computes certain **opti**cal properties of materials.

Appendix E

Comparison of DFPT and frozen-phonon methods for Bismuth

E.1 Frozen-phonon calculation of electron-phonon matrix elements

It is important to check the electron-phonon matrix elements calculated with DFPT against a more simple frozen-phonon calculation. In this section we aim to compute the electron-phonon matrix element, for each phonon branch, between the valence band at **T** and the conduction band at **L** using the frozen-phonon method. This particular electron-phonon scattering is an important channel for indirect electron-hole recombination in photoexcited bismuth. We can then compare the results with those obtained from DFPT.

E.1.1 Extracting the electron-phonon matrix elements

The full Hamiltonian, in the presence of a perturbation can be written as follows:

$$\hat{H}' = \hat{H}_0 + \Delta\hat{H}. \tag{E.1}$$

We denote the unperturbed and perturbed eigenstates for band n and wavevector $\mathbf{k}$ as $|\psi_{n\mathbf{k}}\rangle$ and $|\psi'_{n\mathbf{k}}\rangle$ respectively. This calculation will be performed in a supercell

in which $\mathbf{k}$ folds on to $\mathbf{k}+\mathbf{q}$, allowing us to express $\hat{H}'$ at the wavevector $\mathbf{k}$ as a diagonal matrix as follows [133]:

$$\hat{H}' = \hat{H}_0 + \Delta\hat{H} = \sum_{n'} \varepsilon_{n'\mathbf{k}}{}' \left|\psi'_{n'\mathbf{k}}\right\rangle \left\langle\psi'_{n'\mathbf{k}}\right| \tag{E.2}$$

Applying $|\psi_{n\mathbf{k}}\rangle$ from the right, $\langle\psi_{m\mathbf{k}}|$ from the left and subtracting the $\hat{H}_0$ term from both sides we get:

$$\langle\psi_{m\mathbf{k}}|\Delta\hat{H}|\psi_{n\mathbf{k}}\rangle = \sum_{n'} \varepsilon_{n'\mathbf{k}}{}' \langle\psi_{m\mathbf{k}}|\psi'_{n'\mathbf{k}}\rangle \langle\psi'_{n'\mathbf{k}}|\psi_{n\mathbf{k}}\rangle - \varepsilon_{n\mathbf{k}}\delta_{nm} \tag{E.3}$$

$$= \sum_{n'} \varepsilon_{n'\mathbf{k}}{}' \langle\psi_{m\mathbf{k}}|\psi'_{n'\mathbf{k}}\rangle \langle\psi'_{n'\mathbf{k}}|\psi_{n\mathbf{k}}\rangle - \varepsilon_{n\mathbf{k}}\delta_{nm}. \tag{E.4}$$

This gives us the electron-phonon matrix element to first order:

$$\begin{aligned} V^{\lambda}_{n\mathbf{k}m\mathbf{q}} &= \langle\psi_{m\mathbf{k}}|\frac{\partial\hat{H}}{\partial R_\lambda}|\psi_{n\mathbf{k}}\rangle \approx \langle\psi_{m\mathbf{k}}|\frac{\Delta\hat{H}}{\Delta R_\lambda}|\psi_{n\mathbf{k}}\rangle \\ &= \frac{1}{\Delta R_\lambda}\left[\sum_{n'} \varepsilon_{n'\mathbf{k}}{}' \langle\psi_{m\mathbf{k}}|\psi'_{n'\mathbf{k}}\rangle \langle\psi'_{n'\mathbf{k}}|\psi_{n\mathbf{k}}\rangle - \varepsilon_{n\mathbf{k}}\delta_{nm}\right], . \end{aligned} \tag{E.5}$$

allowing us to compare the squared matrix elements calculated in DFPT with $\pi\left|V^{\lambda}_{n\mathbf{k}m\mathbf{q}}\right|^2/M_\alpha$, where M_α is the mass of the α-th atom in the unit cell. However, we still need to evaluate the overlaps appearing in Eq. (E.5). For this reason, we need to examine the form of the wavefunctions in ABINIT.

E.1.2 ABINIT wavefunctions including spin-orbit interaction

Our calculations include spin-orbit coupling, so we need to account for spin in our treatment of the wavefunctions. There are two possible values of spin for a fermion: Namely spin up ($\sigma = 1$) and spin down ($\sigma = 2$). The periodic part of the Bloch wavefunction is written in ABINIT as

$$u_{n\mathbf{k}}(\mathbf{r},\sigma) = \frac{1}{\sqrt{\Omega_0}}\sum_{\mathbf{G}} c_{n\mathbf{k}}(\mathbf{G},\sigma)e^{2\pi i\mathbf{G}.\mathbf{r}}, \tag{E.6}$$

which differs from the traditional definition by a factor of 2π in the exponent. These units of $\mathbf{G}$ imply that $\exp\{i\mathbf{G}\cdot\mathbf{R}\} = 1$ for all Bravais lattice vectors $\mathbf{R}$. Using Bloch's theorem we can express the full wavefunction in terms of the periodic part times a plane wave and expand in a Fourier series (see subsection 3.5.2) as

follows:

$$\psi_{n\mathbf{k}}(\mathbf{r},\sigma) = \frac{1}{\sqrt{N_p}} u_{n\mathbf{k}}(\mathbf{r},\sigma) e^{2\pi i \mathbf{k}.\mathbf{r}} = \frac{1}{\sqrt{N_p \Omega_0}} \sum_{\mathbf{G}} c_{n\mathbf{k}}(\mathbf{G},\sigma) e^{2\pi i (\mathbf{k}+\mathbf{G}).\mathbf{r}}, \tag{E.7}$$

where N_p is the number of primitive cells in the system. These wavefunctions are normalised such that:

$$\sum_{\sigma} \langle \psi_{n\mathbf{k}}(\mathbf{r},\sigma) | \psi_{n\mathbf{k}}(\mathbf{r},\sigma) \rangle = \sum_{\sigma} \sum_{\mathbf{G}} |c_{n\mathbf{k}}(\mathbf{G},\sigma)|^2 = 1 \tag{E.8}$$

E.1.3 Overlap of ABINIT wavefunctions in terms of fourier coefficents

We need to compute overlaps of the Bloch wavefunctions in order to extract the electron-phonon matrix elements as in equation (E.5). The overlap of two Bloch wavefunctions can be expanded and simplified as follows:

$$\langle u_{m\mathbf{k}}(\mathbf{r}) | u_{n\mathbf{k}'}(\mathbf{r}) \rangle = \sum_{\sigma} \int_{\mathbb{R}^3} u^*_{m\mathbf{k}'}(\mathbf{r},\sigma) u_{n\mathbf{k}}(\mathbf{r},\sigma)\, d^3r \tag{E.9}$$

$$= \sum_{\sigma} \int_{\mathbb{R}^3} \left[\frac{1}{\sqrt{\Omega_0}} \sum_{\mathbf{G}'} c^*_{m\mathbf{k}'}(\mathbf{G}',\sigma) e^{-2\pi i \mathbf{G}'.\mathbf{r}} \right] \left[\frac{1}{\sqrt{\Omega_0}} \sum_{\mathbf{G}} c_{n\mathbf{k}}(\mathbf{G},\sigma) e^{2\pi i \mathbf{G}.\mathbf{r}} \right] d^3r \tag{E.10}$$

$$= \frac{1}{\Omega_0} \sum_{\sigma} \sum_{\mathbf{G}} \sum_{\mathbf{G}'} c^*_{m\mathbf{k}'}(\mathbf{G}',\sigma) c_{n\mathbf{k}}(\mathbf{G},\sigma) \left[\int_{\mathbb{R}^3} e^{2\pi i (\mathbf{G}-\mathbf{G}').\mathbf{r}}\, d^3r \right] \tag{E.11}$$

$$= \frac{1}{\Omega_0} \sum_{\sigma} \sum_{\mathbf{G}} \sum_{\mathbf{G}'} c^*_{m\mathbf{k}'}(\mathbf{G}',\sigma) c_{n\mathbf{k}}(\mathbf{G},\sigma) N_p \delta_{\mathbf{G},\mathbf{G}'} \left[\int_{\mathcal{PC}} e^{2\pi i (\mathbf{G}-\mathbf{G}').\tau}\, d^3\tau \right] \tag{E.12}$$

$$= N_p \sum_{\sigma} \sum_{\mathbf{G}} c^*_{m\mathbf{k}'}(\mathbf{G},\sigma) c_{n\mathbf{k}}(\mathbf{G},\sigma), \tag{E.13}$$

where $\mathcal{PC}$ is the primitive cell and the index l runs over all primitive cells in the system. However, if we are in a supercell with N_p primitive cells and the bands at $\mathbf{k}$ and $\mathbf{k}'$ are folded on to each other, we can set $\mathbf{k} = \mathbf{k}'$ and we get the following identity:

$$\langle \psi_{m\mathbf{k}}(\mathbf{r}) | \psi_{n\mathbf{k}}(\mathbf{r}) \rangle = \frac{1}{N_p} \langle u_{m\mathbf{k}}(\mathbf{r}) | u_{n\mathbf{k}}(\mathbf{r}) \rangle, \tag{E.14}$$

which allows us to express the inner product of the *full* wavefunctions as follows:

$$\langle \psi_{m\mathbf{k}}(\mathbf{r}) | \psi_{n\mathbf{k}}(\mathbf{r}) \rangle = \sum_{\sigma} \sum_{\mathbf{G}} c^*_{m\mathbf{k}}(\mathbf{G},\sigma) c_{n\mathbf{k}}(\mathbf{G},\sigma). \tag{E.15}$$

We can now express the electron-phonon matrix elements in equation (E.5) in terms of the fourier coefficients as follows:

$$V^{\lambda}_{n\mathbf{k}m\mathbf{q}} = \sum_{n'} \varepsilon_{n'\mathbf{k}}{}' \left\langle \psi_{m\mathbf{k}} | \psi'_{n'\mathbf{k}} \right\rangle \left\langle \psi'_{n'\mathbf{k}} | \psi_{n\mathbf{k}} \right\rangle - \varepsilon_{n\mathbf{k}}\delta_{nm} \tag{E.16}$$

$$= \sum_{n'} \varepsilon_{n'\mathbf{k}}{}' \left[\sum_{\tilde{\sigma}} \sum_{\tilde{\mathbf{G}}} c^{*}_{m\mathbf{k}}(\tilde{\mathbf{G}}, \tilde{\sigma}) c'_{n'\mathbf{k}}(\tilde{\mathbf{G}}, \tilde{\sigma}) \right] \left[\sum_{\sigma} \sum_{\mathbf{G}} c^{*'}_{n'\mathbf{k}}(\mathbf{G}, \sigma) c_{n\mathbf{k}}(\mathbf{G}, \sigma) \right] - \varepsilon_{n\mathbf{k}}\delta_{nm}. \tag{E.17}$$

I have implemented Equation (E.17) in a Fortran code using plane-wave coefficients from a version of the Cut3d post-processing tool [1] that I modified for this purpose.

In practice only a finite number of reciprocal lattice vectors G are summed over in the plane-wave expansion. These reciprocal lattice vectors form a sphere of radius $|\mathbf{G}_{\text{max}}(\mathbf{k})|$. This radius is determined by imposing a cut-off on the plane-wave kinetic energy as follows:

$$\frac{\hbar^2}{2m}|\mathbf{k} + \mathbf{G}|^2 < E_{\text{cut}}. \tag{E.18}$$

Although we are looking at coupling between two specific states, the presence of spin-orbit coupling doubles the number of states to four, which are two sets of doubly-degenerate states. This means that there are four possible transitions as follows:

$$\begin{aligned} |n \uparrow \mathbf{k}\rangle &\rightarrow |m \uparrow \mathbf{k} + \mathbf{q}\rangle\,, \\ |n \uparrow \mathbf{k}\rangle &\rightarrow |m \downarrow \mathbf{k} + \mathbf{q}\rangle\,, \\ |n \downarrow \mathbf{k}\rangle &\rightarrow |m \uparrow \mathbf{k} + \mathbf{q}\rangle\,, \\ |n \downarrow \mathbf{k}\rangle &\rightarrow |m \downarrow \mathbf{k} + \mathbf{q}\rangle \end{aligned} \tag{E.19}$$

Summing up $\pi \left| V^{\lambda}_{n,\mathbf{k},m,\mathbf{q}} \right|^2 / M_\alpha$ over the four couplings corresponding to these transitions gives a quantitative comparison with DFPT.

[1] Cut3D is a tool for analysing the wavefunction and charge density files produced by ABINIT. I modified it to carry out the inner products in Eq. (E.17).

E.1.4 Setting up the supercell

A supercell is a unit cell of a system which is comprised of many primitive cells. When we wish to perform DFT calculations for a given phonon displacement, the phonon wavevector $\mathbf{q}$ must be compatible with the periodic boundary conditions of the supercell. This is because the displacement of phonons of wavevector $\mathbf{q}$ has a phase factor $\exp(-i\mathbf{q}\cdot\mathbf{R})$, where $\mathbf{R}$ is a Bravais lattice vector.

We are interested in the coupling between the valence band at $\mathbf{T} = (1/2, 1/2, 1/2)$ and the conduction band at $\mathbf{L} = (1/2, 0, 0)$, which are connected by the phonon $\mathbf{X} = (0, 1/2, 1/2)$. To allow the atoms to displace in a phonon mode of this wavevector, we require a supercell with four atoms and twice the volume of the primitive cell. Further, we wish to choose supercell lattice vectors such that $\mathbf{X}$ is a reciprocal lattice vector, ensuring that the bands at $\mathbf{T}$ and $\mathbf{L}$ are folded on to each other in the first Brillouin zone. For this reason, we choose the following reciprocal lattice vectors:

$$\mathbf{b}_1{}' = \frac{1}{2}(\mathbf{b}_2 + \mathbf{b}_3)\ , \quad \mathbf{b}_2{}' = \mathbf{b}_1\ , \quad \mathbf{b}_3{}' = \frac{1}{2}(\mathbf{b}_2 - \mathbf{b}_3). \tag{E.20}$$

Within the basis of these reciprocal lattice vectors we have $\mathbf{T} = (1, 1/2, 0)$ and $\mathbf{L} = (0, 1/2, 0)$. To deduce the corresponding new direct lattice vectors, we use the following matrix equation: $\mathbf{B} = \mathbf{A}^T$, where $\mathbf{A}$ is a matrix containing the three direct lattice vectors and $\mathbf{B}$ is the matrix of reciprocal lattice vectors.

$$\mathbf{a}_1{}' = \mathbf{a}_2 + \mathbf{a}_3\ , \quad \mathbf{a}_2{}' = \mathbf{a}_1\ , \quad \mathbf{a}_3{}' = \mathbf{a}_2 - \mathbf{a}_3. \tag{E.21}$$

The cell defined by these lattice vectors has twice the volume of the primitive cell, as required. It remains to specify the positions $\boldsymbol{\tau}_\alpha$ of each of the four atoms in the supercell in terms of the lattice vectors $\mathbf{a}_i{}'$. These are as follows:

$$\begin{aligned}
&\boldsymbol{\tau}_1 = (0, 0, 0)\ , \quad \boldsymbol{\tau}_2 = (1/2 - \delta, 1/2 - \delta, 0)\ , \\
&\boldsymbol{\tau}_3 = (1/2, 0, 1/2)\ , \quad \boldsymbol{\tau}_4 = (1 - \delta, 1/2 - \delta, 1/2).
\end{aligned}$$

Having set up the supercell, we can now compute the "unperturbed" electronic wavefunctions from with a standard DFT calculation. However, to calculate the electron-phonon matrix elements we also require the perturbed wavefunctions. That is, the wavefunctions when the phonon displacement is frozen in.

E.1.5 Freezing in the X phonon

To obtain the appropriate phonon displacements we require the normalised phonon eigenvectors $\mathbf{e}_\alpha^{\mathbf{X}\lambda}$. These are calculated within the framework of DFPT. The phonon displacements can be expressed in terms of these normalised eigenvectors as follows:

$$\Delta\mathbf{R}_{I\alpha}^{\mathbf{q}\lambda} = \mathcal{A}\,\frac{\mathbf{e}_\alpha^\lambda}{\sqrt{M_\alpha}}\sin(\mathbf{q}\cdot\mathbf{R_I} - \omega t), \tag{E.22}$$

where I runs over unit cells, α runs over the two atoms in the unit cell, the amplitude of the phonon is denoted $\mathcal{A}$ and M_α is the mass of atom α. Since we are freezing in a phonon displacement, we may set $\omega t = 0$ without loss of generality. A standard DFT calculation with the atomic positions displaced according to Eq. (E.22), will yield the perturbed plane-wave coefficients in Eq. (E.17), and hence the electron-phonon matrix elements.

E.1.6 Results

The first thing we do is to compare the phonon frequencies obtained using this frozen-phonon method with DFPT. This is done to ensure that we are freezing in the correct normal modes. Recall that for a normal mode, the restoring force on every atom in each direction is the same. This fact allows us to compute the frequencies as follows:

$$\omega_{\mathbf{q}\lambda} = \left(\frac{-\Delta F_{\alpha i}}{M_\alpha \Delta\tau_{\alpha i}}\right)^{\frac{1}{2}}, \tag{E.23}$$

where $\Delta\tau_{\alpha i}$ denotes the displacement of atom α in direction i and $\Delta F_{\alpha i}$ is the corresponding change in force.Table E.1 shows a comparison of the DFPT phonon frequencies in THz with the frozen-phonon calculations. The frequencies

Table E.1: Comparison of phonon frequencies at $\mathbf{X}$ in the Brillouin zone calculated by DFPT and frozen-phonon methods.

branch	DFPT	Frozen-Phonon
1	0.67047	0.63823
2	0.763244	0.796142
3	1.00143	0.947475
4	2.48712	2.45422
5	2.77663	2.77663
6	2.84901	2.84901

obtained using either method agree to within $\sim 5\%$ for the acoustic modes, and agree even more closely for the optic modes. This confirms that we have indeed frozen in the correct mode. It now remains to compare the electron-phonon matrix elements obtained using either method. Table E.2 shows a comparison

Table E.2: Comparison of squared matrix elements calculated by DFPT and frozen-phonon method.

branch	DFPT	Frozen-Phonon
1	0	0
2	0	0
3	5.617×10^{-9}	4.76×10^{-9}
4	16.26×10^{-9}	16.12×10^{-9}
5	0	0
6	10.79×10^{-9}	9.13×10^{-9}

of the DFPT squared matrix elements with those obtained from frozen-phonon calculations. The *squared* matrix elements for all 6 branches agree to within $\sim 10\%$. This means that the magnitude of the (un-squared) matrix elements would agree to within $\sim 5\%$, which is an acceptable degree of accuracy. This validates our choice of DFPT for the computation of electron-phonon matrix elements. For a more thorough comparison between DFPT and the frozen-phonon approach to computing electron-phonon matrix elements, see Ref. [89].

References

[1] J. J. Li, J. Chen, D. A. Reis, S. Fahy, and R. Merlin, "Optical Probing of Ultrafast Electronic Decay in Bi and Sb with Slow Phonons," *Phys. Rev. Lett.*, vol. 110, p. 047401, Jan 2013.

[2] X. Gonze, J.-P. Michenaud, and J.-P. Vigneron, "First-principles study of As, Sb, and Bi electronic properties," *Phys. Rev. B*, vol. 41, pp. 11827–11836, Jun 1990.

[3] P. Tangney and S. Fahy, "Calculations of the A_1 phonon frequency in photoexcited tellurium," *Phys. Rev. Lett.*, vol. 82, no. 21, pp. 4340–4343, 1999.

[4] J. Stähler, U. Bovensiepen, M. Meyer, and M. Wolf, "A surface science approach to ultrafast electron transfer and solvation dynamics at interfaces," vol. 37, no. 10, pp. 2180–2190, 2008.

[5] S. Wall, S. Yang, L. Vidas, M. Chollet, J. M. Glownia, M. Kozina, T. Katayama, T. Henighan, M. Jiang, T. A. Miller, *et al.*, "Ultrafast disordering of vanadium dimers in photoexcited VO_2," *Science*, vol. 362, no. 6414, pp. 572–576, 2018.

[6] S. W. Teitelbaum, T. Shin, J. W. Wolfson, Y.-H. Cheng, I. J. Porter, M. Kandyla, and K. A. Nelson, "Real-time observation of a coherent lattice transformation into a high-symmetry phase," *Phys. Rev. X*, vol. 8, p. 031081, Sep 2018.

[7] M. Rini, A. Cavalleri, R. W. Schoenlein, R. López, L. C. Feldman, R. F. Haglund, L. A. Boatner, and T. E. Haynes, "Photoinduced phase transition in VO_2 nanocrystals: ultrafast control of surface-plasmon resonance," *Opt. Lett.*, vol. 30, pp. 558–560, Mar 2005.

[8] Z. Li, Y. Chen, and C. Burda, "Photoexcited dynamics in metal halide perovskites: From relaxation mechanisms to applications," *The Journal of Physical Chemistry C*, vol. 123, no. 6, pp. 3255–3269, 2019.

[9] M. Salinga, B. Kersting, I. Ronneberger, V. P. Jonnalagadda, X. T. Vu, M. Le Gallo, I. Giannopoulos, O. Cojocaru-Mirédin, R. Mazzarello, and A. Sebastian, "Monatomic phase change memory," *Nature Materials*, vol. 17, no. 8, pp. 681–685, 2018.

[10] E. Kuramochi and M. Notomi, "Phase-change memory," *Nature Photonics*, vol. 9, pp. 712 EP –, 10 2015.

[11] J. Shah, *Ultrafast Spectroscopy of Semiconductors and Semiconductor Nanostructures*. Springer, Berlin, 1996.

[12] D. Rudolf, C. La-O-Vorakiat, M. Battiato, R. Adam, J. M. Shaw, E. Turgut, P. Maldonado, S. Mathias, P. Grychtol, H. T. Nembach, *et al.*, "Ultrafast magnetization enhancement in metallic multilayers driven by superdiffusive spin current," *Nature Communications*, vol. 3, pp. 1037 EP –, 09 2012.

[13] M. Weis, K. Balin, R. Rapacz, A. Nowak, M. Lejman, J. Szade, and P. Ruello, "Ultrafast light-induced coherent optical and acoustic phonons in few quintuple layers of the topological insulator Bi_2Te_3," *Phys. Rev. B*, vol. 92, p. 014301, Jul 2015.

[14] D. M. Fritz, D. A. Reis, *et al.*, "Ultrafast bond softening in Bismuth: Mapping a solid's interatomic potential with X-rays," *Science*, vol. 315, no. 5812, pp. 633–636, 2007.

[15] S. L. Johnson, P. Beaud, E. Möhr-Vorobeva, A. Caviezel, G. Ingold, and C. J. Milne, "Direct observation of non-fully-symmetric coherent optical phonons by femtosecond x-ray diffraction," *Phys. Rev. B*, vol. 87, p. 054301, Feb 2013.

[16] M. Trigo, M. Fuchs, J. Chen, M. P. Jiang, M. Cammarata, *et al.*, "Fourier-transform inelastic X-ray scattering from time- and momentum-dependent phonon-phonon correlations," *Nature Physics*, vol. 9, no. 12, pp. 790–794, 2013.

[17] A. Stolow, A. E. Bragg, and D. M. Neumark, "Femtosecond time-resolved photoelectron spectroscopy," *Chem. Rev.*, vol. 104, no. 4, pp. 1719–1758, 2004.

[18] F. Schmitt, P. S. Kirchmann, U. Bovensiepen, R. G. Moore, L. Rettig, M. Krenz, J. H. Chu, N. Ru, L. Perfetti, D. H. Lu, M. Wolf, I. R. Fisher, and Z. X. Shen, "Transient electronic structure and melting of a charge density wave in TbTe3," *Science*, vol. 321, no. 5896, pp. 1649–1652, 2008.

[19] B. Mansart, M. J. G. Cottet, T. J. Penfold, S. B. Dugdale, R. Tediosi, M. Chergui, and F. Carbone, "Evidence for a peierls phase-transition in a three-dimensional multiple charge-density waves solid," *Proc. Natl. Acad. Sci. U.S.A*, vol. 109, no. 15, pp. 5603–5608, 2012.

[20] E. D. Murray, D. M. Fritz, J. K. Wahlstrand, S. Fahy, and D. A. Reis, "Effect of lattice anharmonicity on high-amplitude phonon dynamics in photoexcited bismuth," *Phys. Rev. B*, vol. 72, p. 060301, Aug 2005.

[21] R. Merlin, "Generating coherent THz phonons with light pulses," *Solid State Comm.*, vol. 102, no. 2-3, pp. 207–220, 1997.

[22] O. V. Misochko, A. A. Mel'nikov, S. V. Chekalin, and A. Y. Bykov, "Features of coherent phonons of the strong topological insulator Bi_2Te_3," *JETP Letters*, vol. 102, pp. 235–241, aug 2015.

[23] N. Kamaraju, S. Kumar, M. Anija, and A. K. Sood, "Large-amplitude chirped coherent phonons in tellurium mediated by ultrafast photoexcited carrier diffusion," *Phys. Rev. B*, vol. 82, p. 195202, Nov 2010.

[24] T. Huber, M. Ranke, A. Ferrer, L. Huber, and S. L. Johnson, "Coherent phonon spectroscopy of non-fully symmetric modes using resonant terahertz excitation," *Applied Physics Letters*, vol. 107, no. 9, p. 091107, 2015.

[25] T. E. Stevens, J. Kuhl, and R. Merlin, "Coherent phonon generation and the two stimulated raman tensors," *Phys. Rev. B*, vol. 65, p. 144304, Mar 2002.

[26] G. A. Garrett, T. F. Albrecht, J. F. Whitaker, and R. Merlin, "Coherent THz phonons driven by light pulses and the Sb problem: What is the mechanism?," *Phys. Rev. Lett.*, vol. 77, no. 17, pp. 3661–3664, 1996.

[27] T. K. Cheng, J. Vidal, H. J. Zeiger, G. Dresselhaus, M. S. Dresselhaus, and E. P. Ippen, "Mechanism for displacive excitation of coherent phonons in Sb, Bi, Te, and Ti_2O_3," *Appl. Phys. Lett.*, vol. 59, no. 16, pp. 1923–1925, 1991.

[28] C. E. Crespo-Hernández, B. Cohen, P. M. Hare, and B. Kohler, "Ultrafast excited-state dynamics in nucleic acids," *Chem. Rev.*, vol. 104, no. 4, pp. 1977–2019, 2004.

[29] M. Dresselhaus, G. Dresselhaus, and J. A., *Applications of Group Theory to the Physics of Solids*. Springer, 2008.

[30] S. M. O'Mahony, F. Murphy-Armando, E. D. Murray, J. D. Querales-Flores, I. Savić, and S. Fahy, "Ultrafast relaxation of symmetry-breaking photo-induced atomic forces," *Phys. Rev. Lett.*, vol. 123, p. 087401, Aug 2019.

[31] H. J. Zeiger, J. Vidal, T. K. Cheng, E. P. Ippen, G. Dresselhaus, and M. S. Dresselhaus, "Theory for displacive excitation of coherent phonons," *Physical Review B*, vol. 45, no. 2, pp. 768–778, 1992.

[32] Z. Huang and K.-J. Kim, "Review of x-ray free-electron laser theory," *Phys. Rev. ST Accel. Beams*, vol. 10, p. 034801, Mar 2007.

[33] T. Shin, J. W. Wolfson, S. W. Teitelbaum, M. Kandyla, and K. A. Nelson, "Carrier confinement and bond softening in photoexcited bismuth films," *Phys. Rev. B*, vol. 92, p. 184302, Nov 2015.

[34] Y. Giret, A. Gellé, and B. Arnaud, "Entropy driven atomic motion in laser-excited bismuth," *Phys. Rev. Lett.*, vol. 106, p. 155503, Apr 2011.

[35] P. Maldonado, K. Carva, M. Flammer, and P. M. Oppeneer, "Theory of out-of-equilibrium ultrafast relaxation dynamics in metals," *Phys. Rev. B*, vol. 96, p. 174439, Nov 2017.

[36] D. Sangalli and A. Marini, "Complete collisions approximation to the Kadanoff-Baym equation: a first-principles implementation," *Journal of Physics: Conference Series*, vol. 609, p. 012006, may 2015.

[37] D. Sangalli and A. Marini, "Ultra-fast carriers relaxation in bulk silicon following photo-excitation with a short and polarized laser pulse," *EPL*, vol. 110, 2015.

[38] A. Marini, "Competition between the electronic and phonon–mediated scattering channels in the out–of–equilibrium carrier dynamics of semiconductors: an ab-initio approach," *J. Phys. Conf. Ser*, vol. 427, p. 012003, mar 2013.

[39] P. G. Klemens, "Anharmonic decay of optical phonons," *Phys. Rev.*, vol. 148, pp. 845–848, Aug 1966.

[40] S. Fahy, E. D. Murray, and D. A. Reis, "Resonant squeezing and the anharmonic decay of coherent phonons," *Phys. Rev. B*, vol. 93, p. 134308, Apr 2016.

[41] S. W. Teitelbaum, T. Henighan, Y. Huang, H. Liu, M. P. Jiang, D. Zhu, M. Chollet, T. Sato, E. D. Murray, S. Fahy, S. O'Mahony, T. P. Bailey, C. Uher, M. Trigo, and D. A. Reis, "Direct measurement of anharmonic decay channels of a coherent phonon," *Phys. Rev. Lett.*, vol. 121, p. 125901, Sep 2018.

[42] F. Herman, C. D. Kuglin, K. F. Cuff, and R. L. Kortum, "Relativistic corrections to the band structure of tetrahedrally bonded semiconductors," *Phys. Rev. Lett.*, vol. 11, pp. 541–545, Dec 1963.

[43] R. Peierls, S. Rudolf Ernst Peierls, R. Peierls, and O. U. Press, *Quantum Theory of Solids*. International series of monographs on physics, Clarendon Press, 1955.

[44] S. W. Teitelbaum, T. C. Henighan, H. Liu, M. P. Jiang, D. Zhu, M. Chollet, T. Sato, Éamonn D. Murray, S. Fahy, S. O'Mahony, T. P. Bailey, C. Uher, M. Trigo, and D. A. Reis, "Measurements of nonequilibrium interatomic forces in photoexcited bismuth," 2019 (ArXiV preprint 1908.07161).

[45] E. D. Murray, S. Fahy, D. Prendergast, T. Ogitsu, D. M. Fritz, and D. A. Reis, "Phonon dispersion relations and softening in photoexcited bismuth from first principles," *Phys. Rev. B*, vol. 75, p. 184301, May 2007.

[46] L. M. Falicov and P. J. Lin, "Band Structure and Fermi Surface of Antimony: Pseudopotential Approach," *Phys. Rev.*, vol. 141, pp. 562–567, Jan 1966.

[47] J.-P. Issi, "Low Temperature Transport Properties of the Group V Semimetals," *Australian Journal of Physics*, vol. 32, no. 6, pp. 585–628, 1979.

[48] M. G. Priestley, L. R. Windmiller, J. B. Ketterson, and Y. Eckstein, "De Haas—Van Alphen Effect and Fermi Surface in Arsenic," *Phys. Rev.*, vol. 154, pp. 671–682, Feb 1967.

[49] D. M. Riffe and A. J. Sabbah, "Coherent excitation of the optic phonon in Si: Transiently stimulated Raman scattering with a finite-lifetime electronic excitation," *Phys. Rev. B*, vol. 76, p. 085207, Aug 2007.

[50] É. D. Murray and S. Fahy, "First-Principles Calculation of Femtosecond Symmetry-Breaking Atomic Forces in Photoexcited Bismuth," *Phys. Rev. Lett.*, vol. 114, p. 055502, feb 2015.

[51] M. L. Cohen and S. G. Louie, *Fundamentals of Condensed Matter Physics*. Cambridge University Press, 2016.

[52] M. Born and R. Oppenheimer, "Zur quantentheorie der molekeln," *Annalen der Physik*, vol. 389, no. 20, pp. 457–484, 1927.

[53] J. C. Slater, "The theory of complex spectra," *Phys. Rev.*, vol. 34, pp. 1293–1322, Nov 1929.

[54] P.-O. Löwdin, "Quantum Theory of Many-Particle Systems. III. Extension of the Hartree-Fock Scheme to Include Degenerate Systems and Correlation Effects," *Phys. Rev.*, vol. 97, pp. 1509–1520, Mar 1955.

[55] P. Hohenberg and W. Kohn, "Inhomogeneous electron gas," *Phys. Rev.*, vol. 136, pp. B864–B871, Nov 1964.

[56] R. O. Jones, "Density functional theory: Its origins, rise to prominence, and future," *Rev. Mod. Phys.*, vol. 87, pp. 897–923, Aug 2015.

[57] L. H. Thomas, "The calculation of atomic fields," *Mathematical Proceedings of the Cambridge Philosophical Society*, vol. 23, no. 5, p. 542–548, 1927.

[58] E. Fermi, "Un metodo statistico per la determinazione di alcune prioreta dell'atome," *Rend. Accad. Naz. Lincei*, vol. 6, pp. 7165–7168, Dec 1927.

[59] W. Kohn and L. J. Sham, "Self-consistent equations including exchange and correlation effects," *Phys. Rev.*, vol. 140, pp. A1133–A1138, Nov 1965.

[60] S. Baroni, S. de Gironcoli, A. Dal Corso, and P. Giannozzi, "Phonons and related crystal properties from density-functional perturbation theory," *Rev. Mod. Phys.*, vol. 73, pp. 515–562, Jul 2001.

[61] A. J. Cohen and P. Mori-Sánchez, "Landscape of an exact energy functional," *Phys. Rev. A*, vol. 93, p. 042511, Apr 2016.

[62] P. Mori-Sánchez and A. J. Cohen, "Exact Density Functional Obtained via the Levy Constrained Search," *The Journal of Physical Chemistry Letters*, vol. 9, pp. 4910–4914, 09 2018.

[63] T. Koopmans, "Über die zuordnung von wellenfunktionen und eigenwerten zu den einzelnen elektronen eines atoms," *Physica*, vol. 1, no. 1, pp. 104 – 113, 1934.

[64] J. F. Janak, "Proof that $\frac{\partial e}{\partial n_i} = \epsilon$ in density-functional theory," *Phys. Rev. B*, vol. 18, pp. 7165–7168, Dec 1978.

[65] P. A. M. Dirac, "Note on Exchange Phenomena in the Thomas Atom," *Mathematical Proceedings of the Cambridge Philosophical Society*, vol. 26, no. 3, p. 376–385, 1930.

[66] W. Kohn, "Nobel lecture: Electronic structure of matter—wave functions and density functionals," *Rev. Mod. Phys.*, vol. 71, pp. 1253–1266, Oct 1999.

[67] R. M. Martin, *Electronic Structure: Basic Theory and Practical Methods*. Cambridge University Press, 2004.

[68] J. P. Perdew, K. Burke, and M. Ernzerhof, "Generalized gradient approximation made simple," *Phys. Rev. Lett.*, vol. 77, pp. 3865–3868, Oct 1996.

[69] A. D. Becke, "A new mixing of Hartree-Fock and local density-functional theories," *The Journal of Chemical Physics*, vol. 98, no. 2, pp. 1372–1377, 1993.

[70] H. J. Monkhorst and J. D. Pack, "Special points for Brillouin-zone integrations," *Phys. Rev. B*, vol. 13, pp. 5188–5192, Jun 1976.

[71] D. R. Hamann, M. Schlüter, and C. Chiang, "Norm-conserving pseudopotentials," *Phys. Rev. Lett.*, vol. 43, pp. 1494–1497, Nov 1979.

[72] P. Giannozzi *et al.*, "QUANTUM ESPRESSO: a modular and open-source software project for quantum simulations of materials," *J. Phys. Condens. Matter*, vol. 21, p. 395502, sep 2009.

[73] D. Vanderbilt, "Optimally smooth norm-conserving pseudopotentials," *Phys. Rev. B*, vol. 32, pp. 8412–8415, Dec 1985.

[74] X. Gonze *et al.*, "ABINIT: First-principles approach to material and nanosystem properties," *Comput. Phys. Commun.*, vol. 180, no. 12, pp. 2582–2615, 2009.

[75] C. Hartwigsen, S. Goedecker, and J. Hutter, "Relativistic separable dual-space Gaussian pseudopotentials from H to Rn," *Phys. Rev. B*, vol. 58, no. 7, pp. 3641–3662, 1998.

[76] G. Srivastava, *The Physics of Phonons*. Taylor & Francis, 1990.

[77] P. B. Allen and V. Heine, "Theory of the temperature dependence of electronic band structures," *Journal of Physics C: Solid State Physics*, vol. 9, pp. 2305–2312, jun 1976.

[78] P. B. Allen and M. Cardona, "Theory of the temperature dependence of the direct gap of germanium," *Phys. Rev. B*, vol. 23, pp. 1495–1505, Feb 1981.

[79] P. B. Allen and M. Cardona, "Temperature dependence of the direct gap of si and ge," *Phys. Rev. B*, vol. 27, pp. 4760–4769, Apr 1983.

[80] K. Kaasbjerg, K. S. Thygesen, and K. W. Jacobsen, "Phonon-limited mobility in n-type single-layer mos_2 from first principles," *Phys. Rev. B*, vol. 85, p. 115317, Mar 2012.

[81] F. Meng, J. Ma, J. He, and W. Li, "Phonon-limited carrier mobility and temperature-dependent scattering mechanism of $3C$-SiC from first principles," *Phys. Rev. B*, vol. 99, p. 045201, Jan 2019.

[82] J. Bardeen, L. N. Cooper, and J. R. Schrieffer, "Microscopic theory of superconductivity," *Phys. Rev.*, vol. 106, pp. 162–164, Apr 1957.

[83] J. Bardeen, L. N. Cooper, and J. R. Schrieffer, "Theory of superconductivity," *Phys. Rev.*, vol. 108, pp. 1175–1204, Dec 1957.

[84] B. A. Sanborn, P. B. Allen, and D. A. Papaconstantopoulos, "Empirical electron-phonon coupling constants and anisotropic electrical resistivity in hcp metals," *Phys. Rev. B*, vol. 40, pp. 6037–6044, Sep 1989.

[85] P. K. Lam, M. M. Dacorogna, and M. L. Cohen, "Self-consistent calculation of electron-phonon couplings," *Phys. Rev. B*, vol. 34, pp. 5065–5069, Oct 1986.

[86] H. Fröhlich, "Electrons in lattice fields," *Advances in Physics*, vol. 3, no. 11, pp. 325–361, 1954.

[87] O. Madelung, *Introduction to Solid-State Theory*, vol. 196. 2012.

[88] G. Grimvall, *The electron-phonon interaction in metals*. Amsterdam North-Holland Pub., 1981.

[89] F. Giustino, "Electron-phonon interactions from first principles," *Rev. Mod. Phys.*, vol. 89, p. 015003, Feb 2017.

[90] H. Haug and A. Jauho, *Quantum Kinetics in Transport and Optics of Semiconductors*. Springer Series in Solid-State Sciences, Springer Berlin Heidelberg, 2007.

[91] R. P. Feynman, "Forces in molecules," *Physical Review*, vol. 56, no. 4, pp. 340–343, 1939.

[92] X. Gonze, "Adiabatic density-functional perturbation theory," *Phys. Rev. A*, vol. 52, pp. 1096–1114, Aug 1995.

[93] I. Souza, N. Marzari, and D. Vanderbilt, "Maximally localized Wannier functions for entangled energy bands," *Phys. Rev. B*, vol. 65, p. 035109, Dec 2001.

[94] N. Marzari, A. A. Mostofi, J. R. Yates, I. Souza, and D. Vanderbilt, "Maximally localized Wannier functions: Theory and applications," *Rev. Mod. Phys.*, vol. 84, pp. 1419–1475, Oct 2012.

[95] J. M. Foster and S. F. Boys, "Canonical configurational interaction procedure," *Rev. Mod. Phys.*, vol. 32, pp. 300–302, Apr 1960.

[96] F. Giustino, M. L. Cohen, and S. G. Louie, "Electron-phonon interaction using Wannier functions," *Phys. Rev. B*, vol. 76, p. 165108, Oct 2007.

[97] S. Poncé, E. Margine, C. Verdi, and F. Giustino, "EPW: Electron–phonon coupling, transport and superconducting properties using maximally localized Wannier functions," *Computer Physics Communications*, vol. 209, pp. 116 – 133, 2016.

[98] N. D. Mermin, "Thermal properties of the inhomogeneous electron gas," *Phys. Rev.*, vol. 137, pp. A1441–A1443, Mar 1965.

[99] R. Häcker and A. Hangleiter, "Intrinsic upper limits of the carrier lifetime in silicon," *Journal of Applied Physics*, vol. 75, no. 11, pp. 7570–7572, 1994.

[100] P. Tangney and S. Fahy, "Density-functional theory approach to ultrafast laser excitation of semiconductors: Application to the A_1 phonon in tellurium," *Phys. Rev. B*, vol. 65, p. 054302, Jan 2002.

[101] H. E. Elsayed-Ali, T. B. Norris, M. A. Pessot, and G. A. Mourou, "Time-resolved observation of electron-phonon relaxation in copper," *Phys. Rev. Lett.*, vol. 58, pp. 1212–1215, Mar 1987.

[102] J. G. Fujimoto, J. M. Liu, E. P. Ippen, and N. Bloembergen, "Femtosecond laser interaction with metallic tungsten and nonequilibrium electron and lattice temperatures," *Phys. Rev. Lett.*, vol. 53, pp. 1837–1840, Nov 1984.

[103] J. Chen, D. Tzou, and J. Beraun, "A semiclassical two-temperature model for ultrafast laser heating," *International Journal of Heat and Mass Transfer*, vol. 49, no. 1, pp. 307 – 316, 2006.

[104] J. Noffsinger, E. Kioupakis, C. G. Van de Walle, S. G. Louie, and M. L. Cohen, "Phonon-assisted optical absorption in silicon from first principles," *Phys. Rev. Lett.*, vol. 108, p. 167402, Apr 2012.

[105] J. Zhang, X. Tan, M. Liu, S. W. Teitelbaum, K. W. Post, F. Jin, K. A. Nelson, D. N. Basov, W. Wu, and R. D. Averitt, "Cooperative photoinduced metastable phase control in strained manganite films," *Nature Materials*, vol. 15, pp. 956 EP –, 07 2016.

[106] M. Y. C. Teo, S. A. Kulinich, O. A. Plaksin, and A. L. Zhu, "Photoinduced structural conversions of transition metal chalcogenide materials," *The Journal of Physical Chemistry A*, vol. 114, pp. 4173–4180, 04 2010.

[107] T. Shin, J. W. Wolfson, S. W. Teitelbaum, M. Kandyla, and K. A. Nelson, "Dual echelon femtosecond single-shot spectroscopy," *Review of Scientific Instruments*, vol. 85, no. 8, p. 083115, 2014.

[108] K. H. Weyrich, ""frozen" phonon calculations: Lattice dynamics and -instabilities," *Ferroelectrics*, vol. 104, no. 1, pp. 183–194, 1990.

[109] D. Schroeder, *An Introduction to Thermal Physics*, ch. 3, pp. 111–112. Addison Wesley, 2000.

[110] L. Waldecker, T. Vasileiadis, R. Bertoni, R. Ernstorfer, T. Zier, F. H. Valencia, M. E. Garcia, and E. S. Zijlstra, "Coherent and incoherent structural dynamics in laser-excited antimony," *Phys. Rev. B*, vol. 95, p. 054302, Feb 2017.

[111] P. Stampfli and K. H. Bennemann, "Dynamical theory of the laser-induced lattice instability of silicon," *Phys. Rev. B*, vol. 46, pp. 10686–10692, Nov 1992.

[112] E. S. Zijlstra, L. L. Tatarinova, and M. E. Garcia, "Laser-induced phonon-phonon interactions in bismuth," *Phys. Rev. B*, vol. 74, p. 220301, Dec 2006.

[113] W. R. Inc., "Mathematica, Version 11.0."

[114] R. James, "Displacive phase transformations in solids," *Journal of the Mechanics and Physics of Solids*, vol. 34, no. 4, pp. 359 – 394, 1986.

[115] B. N. Harmon, "Displacive Phase Transformations and Phonons. In: Turchi P.E.A., Gonis A. (eds) Statics and Dynamics of Alloy Phase Transformations.," *NATO ASI Series (Series B: Physics)*, vol. 39, 1994.

[116] S. Fahy and R. Merlin, "Reversal of ferroelectric domains by ultrashort optical pulses," *Phys. Rev. Lett.*, vol. 73, pp. 1122–1125, Aug 1994.

[117] C. Kittel, *Introduction to Solid State Physics, 6th edition, chapter 13*. Wiley, 1986.

[118] G.-h. Shao, Y.-h. Bai, G.-x. Cui, C. Li, X.-b. Qiu, D.-q. Geng, D. Wu, and Y.-q. Lu, "Ferroelectric domain inversion and its stability in lithium niobate thin film on insulator with different thicknesses," *AIP Advances*, vol. 6, no. 7, p. 075011, 2016.

[119] R. Xu, S. Liu, I. Grinberg, J. Karthik, A. R. Damodaran, A. M. Rappe, and L. W. Martin, "Ferroelectric polarization reversal via successive ferroelastic transitions," *Nature Materials*, vol. 14, no. 1, pp. 79–86, 2015.

[120] Y. M. Sheu, Y. J. Chien, C. Uher, S. Fahy, and D. A. Reis, "Free-carrier relaxation and lattice heating in photoexcited bismuth," *Phys. Rev. B*, vol. 87, p. 075429, Feb 2013.

[121] T. J. Singh and G. S. Verma, "Three-phonon processes in solids," *Phys. Rev. B*, vol. 19, pp. 1248–1253, Jan 1979.

[122] J. Ziman, *Electrons and Phonons: The Theory of Transport Phenomena in Solids*. International series of monographs on physics, OUP Oxford, 2001.

[123] S. L. Johnson, P. Beaud, E. Vorobeva, C. J. Milne, E. D. Murray, S. Fahy, and G. Ingold, "Directly observing squeezed phonon states with femtosecond x-ray diffraction," *Phys. Rev. Lett.*, vol. 102, p. 175503, Apr 2009.

[124] X. Hu and F. Nori, "Squeezed phonon states: Modulating quantum fluctuations of atomic displacements," *Phys. Rev. Lett.*, vol. 76, pp. 2294–2297, Mar 1996.

[125] X. Gonze and C. Lee, "Dynamical matrices, born effective charges, dielectric permittivity tensors, and interatomic force constants from density-functional perturbation theory," *Phys. Rev. B*, vol. 55, pp. 10355–10368, Apr 1997.

[126] S. Krylow, E. S. Zijlstra, F. C. Kabeer, T. Zier, B. Bauerhenne, and M. E. Garcia, "Nonequilibrium dynamics of the phonon gas in ultrafast-excited antimony," *Phys. Rev. Materials*, vol. 1, p. 073601, Dec 2017.

[127] O. Madelung, *Introduction to Solid-State Theory*. Springer, Berlin, 1978.

[128] S. Sadasivam, M. K. Y. Chan, and P. Darancet, "Theory of thermal relaxation of electrons in semiconductors," *Phys. Rev. Lett.*, vol. 119, p. 136602, Sep 2017.

[129] E. Runge and E. K. U. Gross, "Density-functional theory for time-dependent systems," *Phys. Rev. Lett.*, vol. 52, pp. 997–1000, Mar 1984.

[130] A. Melnikov, O. Misochko, and S. Chekalin, "Generation of coherent phonons in bismuth by ultrashort laser pulses in the visible and NIR: Displacive versus impulsive excitation mechanism," *Physics Letters A*, vol. 375, no. 19, pp. 2017 – 2022, 2011.

[131] K. Ishioka, M. Kitajima, and O. V. Misochko, "Temperature dependence of coherent A_{1g} and E_g phonons of bismuth," *Journal of Applied Physics*, vol. 100, no. 9, p. 093501, 2006.

[132] J. Harl, "The linear response function in density functional theory: Optical spectra and improved description of electron correlation.," *PhD thesis*, 2008.

[133] F. Murphy-Armando and S. Fahy, "First-principles calculation of carrier-phonon scattering in n-type $Si_{1-x}Ge_x$ alloys," *Phys. Rev. B*, vol. 78, p. 035202, Jul 2008.